

Dissertation zur Erlangung des Doktorgrades
der Fakultät für Chemie und Pharmazie
der Ludwig-Maximilians-Universität München

**Tunable Vapor Sensors and Nanostructures based on
Oxide and Phosphate Nanosheets**

Pirmin Ganter

aus

Freiburg im Breisgau, Deutschland

2018

Erklärung

Diese Dissertation wurde im Sinne von § 7 der Promotionsordnung vom 28. November 2011 von Frau Prof. Dr. Bettina V. Lotsch betreut.

Eidesstattliche Versicherung

Diese Dissertation wurde eigenständig und ohne unerlaubte Hilfe erarbeitet.

München, 16.05.2018

(Pirmin Ganter)

Dissertation eingereicht am: 18.05.2018

1. Gutachterin: Prof. Dr. Bettina V. Lotsch

2. Gutachterin: Prof. Dr. Christina Scheu

Mündliche Prüfung am: 22.06.2018

Für meine Schwester und meine Eltern

Danksagung

An erster Stelle möchte ich mich bei Prof. Dr. B. V. Lotsch für die Betreuung der Dissertation und die von ihr gewährte wissenschaftliche Freiheit bedanken.

Ich möchte mich zudem bei Prof. Dr. C. Scheu für das Übernehmen des Koreferats dieser Dissertation sowie die durchgeführten Kooperationsprojekte bedanken.

Prof. Dr. T. Bein, Prof. Dr. R. Dinnebier, Prof. Dr. A. Hartschuh und Prof. Dr. K. Karaghiosoff danke ich für ihre Bereitschaft als Teil der Prüfungskommission mitzuwirken.

Besonderer Dank gebührt Prof. Dr. L. M. Schoop für ihre Betreuung in der Zeit, in der sie am Max-Planck-Institut für Festkörperforschung als Postdoktorandin tätig war. Neben der fachlichen Betreuung, möchte ich ihr insbesondere für das Beibringen von diversen „Soft Skills“ danken. Ihre positive und strukturierte Herangehensweise an wissenschaftliche Fragestellungen war sehr motivierend und inspirierend.

Besonderer Dank gilt auch den internen und externen Kooperationspartnern Katalin Szendrei-Temesi, Dr. Christian Ziegler, Mourad Elsobky und Björn Albrecht für die erfolgreich abgeschlossenen Projekte.

Für die technische Unterstützung bei diversen Angelegenheiten, insbesondere Messungen, möchte ich mich bei Viola Duppel, Roland Eger, Willi Hölle, Claudia Kamella, Marie-Luise Schreiber, Frank Adams, Christine Stefani und Armin Schulz bedanken.

Ebenso danke ich meiner Masterandin Marie Däntl und Praktikantin Linda Wehner, die mich durch ihren Einsatz unterstützt haben. Meiner Nachfolgerin Marie Däntl wünsche ich zudem alles Gute für ihre Doktorarbeit.

Dr. Sourav Laha und Dr. Alena Folger möchte ich für das kritische Korrekturlesen dieser Arbeit danken.

Weiterer Dank gebührt Dr. Alexander Hunger, geborener Kuhn, für die Einführung in das Thema während meiner Masterarbeit und während des ersten Monats meiner Doktorarbeit sowie für seine fundamentalen Ratschläge.

Dank gebührt auch meinen Labor- und Bürokollegen Dr. Daniel Weber und Dr. Tanmay Banerjee, welche mir durch Ihre Vorschläge und Ratschläge weitergeholfen haben.

Für die gute und produktive Arbeitsatmosphäre möchte ich mich insbesondere bei allen aktuellen und ehemaligen Mitgliedern der 2D Untergruppe, aber auch dem gesamten Arbeitskreis Lotsch bedanken.

Mein allergrößter Dank gilt jedoch meinen Eltern und meiner Schwester, welche mich unterstützt und ermutigt haben meinen Weg zu gehen.

Summary

Over the last decades, millions of tons of layered materials have been produced every year as they are utilized in various everyday applications. However, only from 2004 onwards, following the discovery of graphene's exceptional properties by Geim and Novoselov, the delamination of layered materials into nanosheets gained tremendous interest. At the beginning, mainly graphene was investigated but with the awareness of graphene's limitations, the focus shifted toward the exploration of other nanosheets exhibiting complementary properties. Up to now, many nanosheets have shown outstanding properties and hence, were utilized in proof-of-concept devices. However, these nanosheet-based devices, despite excellent performances, are absent in our everyday life. With the rising awareness of this contradiction, the focus of nanosheet-based research is gradually shifting from mainly fundamental exploration of novel nanosheets toward their utilization in applications. Therefore, major research efforts are currently carried out regarding the delamination, positioning and modification of nanosheets in order to harvest their superior properties in impactful applications (see Chapter 1).

In light of the ongoing developments, the current thesis is targeted to bridge the gap toward technologically relevant applications for phosphate and oxide nanosheets by advancing and improving their delamination, positioning and modification.

In Chapter 2 and 3 the processing of $\text{H}_3\text{Sb}_3\text{P}_2\text{O}_{14}$ and HSbP_2O_8 nanosheets into thin films and Bragg stacks (BSs) as well as the extraordinary performance of these thin film vapor sensors, especially toward humidity, was demonstrated. The fast response times and high sensitivity enabled the touchless tracking of human finger motions and trace amounts of water detection. The acidic interlayer environment plays a key role for the observed high selectivity toward polar protic vapors. The difference in affinity of polar and protic vapors to the acidic interlayer environment enabled the differentiation between various polar protic vapors.

In Chapter 4, 5 and 6 non-covalent modification of the interlayer space was utilized to modify, tune and tailor nanosheet-based Fabry-Pérot vapor sensors. Methods for modifying the interlayer space include counter ion exchange and vapor-phase intercalation. The modifications of the interlayer environment result in higher sensitivities, faster response and recovery times and tunable selectivities. Both methods define the sensor response, however, the vapor-phase amine intercalation is considered more flexible and versatile compared to the ion exchange before spin-coating, being a post-film fabrication modification. More importantly, as the amines were intercalated into photonic sensors, they were distinguished based on their normalized optical shift and intercalation time. Besides amine differentiation, intercalation into photonic structure allowed the spatially and temporally resolved optical tracking of the intercalation process. This tracking enabled the localization of the amine vapor source as the intercalation into thin films starts at the area facing toward the vapor source. Moreover, the area in which intercalation takes place in the thin film was controlled by utilizing a mask-based approach. It enabled the locally resolved chemical modification with amine vapors allowing for

straightforward array design as well as nanostructuring. Due to the locally resolved chemical modification with different amines, the sensor array enabled us to distinguish several solvent vapors with the naked eye.

In Chapter 5 the concept of modifying the interlayer environment beyond sensing was demonstrated by developing a novel lithography method termed by us photocatalytic nanosheet lithography (PNL). The photocatalytic properties of the calcium niobate nanosheets in thin films were utilized to control the interlayer cation in a spatially resolved manner by applying a mask-based approach. UV illumination through the mask resulted in the decomposition of tetrabutylammonium (TBA) in the interlayer space in the exposed areas. This approach led to a patterned thin film of $\text{TBA}_x\text{H}_{1-x}\text{Ca}_2\text{Nb}_3\text{O}_{10}$ and $(\text{NH}_4)_x\text{H}_{1-x}\text{Ca}_2\text{Nb}_3\text{O}_{10}$. As the interlayer cation is controlling the swelling properties, areas which contain TBA could be easily removed in a selective etching step. Therefore, $\text{TBA}_x\text{H}_{1-x}\text{Ca}_2\text{Nb}_3\text{O}_{10}$ acted as negative photoresist allowing for sub 100 μm patterning of $(\text{NH}_4)_x\text{H}_{1-x}\text{Ca}_2\text{Nb}_3\text{O}_{10}$. Lateral patterning of $(\text{NH}_4)_x\text{H}_{1-x}\text{Ca}_2\text{Nb}_3\text{O}_{10}$ is of high interest, as it is a good high k -dielectric material even at low thicknesses and efficient lateral patterning methods are missing. As PNL is compatible with state of the art lithography processes, it paves the way for the implementation of $(\text{NH}_4)_x\text{H}_{1-x}\text{Ca}_2\text{Nb}_3\text{O}_{10}$ and related photoactive nanosheets in technical devices.

Besides the effective positioning and modification methods, the development of new exfoliation techniques is also of high interest. In Chapter 7 a novel silver assisted exfoliation route was developed. The silver exfoliation route relied on a silver ion exchange step prior to treatment with organic iodides for exfoliation. The formation of highly water insoluble silver iodide was the driving force for exfoliation. The silver assisted exfoliation route has two advantages: On the one hand, it can be achieved with a wide range of exfoliation agents (EAs) and on the other hand, it avoids the extensive use of concentrated acids, which can have detrimental effects on some transition metal oxides (TMOs). On a more fundamental level, the addition of a novel exfoliation route facilitates the general understanding of exfoliation processes.

On a broader perspective, the results obtained in the current thesis represent a significant step toward the utilization of phosphate nanosheet-based vapor sensors and oxide nanosheets into devices for commercial applications. Although this thesis could not completely solve the colossal challenges relevant for transitioning towards these applications, it nevertheless triggered significant interest from industry in this topic.

Implementation of $\text{H}_3\text{Sb}_3\text{P}_2\text{O}_{14}$ nanosheets in touchless positioning interfaces (Chapter 2)

“Touchless Optical Finger Motion Tracking Based on 2D Nanosheets with Giant Moisture Responsiveness” by Katalin Szendrei,* Pirmin Ganter,* Olalla Sánchez-Sobrado, Roland Eger, Alexander Kuhn, and Bettina V. Lotsch. Published in *Adv. Mater.* **2015**, 27, 6341-6348.

$\text{H}_3\text{Sb}_3\text{P}_2\text{O}_{14}$ is a layered material with humidity dependent swelling and hence, also proton conductivity. Therefore, $\text{H}_3\text{Sb}_3\text{P}_2\text{O}_{14}$ is a good candidate for humidity sensors relying either on a change in proton conductivity or thickness. High performance humidity sensors can be utilized in touchless positioning interfaces (TPI) because a humidity sheath surrounds the human finger. As some of the properties of layered bulk materials can be improved by delaminating them into nanosheets,

$\text{H}_3\text{Sb}_3\text{P}_2\text{O}_{14}$ nanosheets can possibly provide the ground for high performance humidity sensors. In Chapter 2 we utilize $\text{H}_3\text{Sb}_3\text{P}_2\text{O}_{14}$ nanosheets in two sorts of high performance humidity sensors:

thin films relying on the change in proton conductance as well as BSs utilizing the optical thickness change.

$\text{K}_3\text{Sb}_3\text{P}_2\text{O}_{14}$, which was obtained by solid-state synthesis, was ion exchanged to $\text{H}_3\text{Sb}_3\text{P}_2\text{O}_{14}$ and subsequently exfoliated in pure water (Figure 0.1a). $\text{H}_3\text{Sb}_3\text{P}_2\text{O}_{14}$ nanosheets were characterized by means of atomic force microscopy (AFM) (Figure 0.1b), transmission electron microscopy (TEM) (Figure 0.1c), scanning electron microscopy (SEM) and X-ray diffraction (XRD).

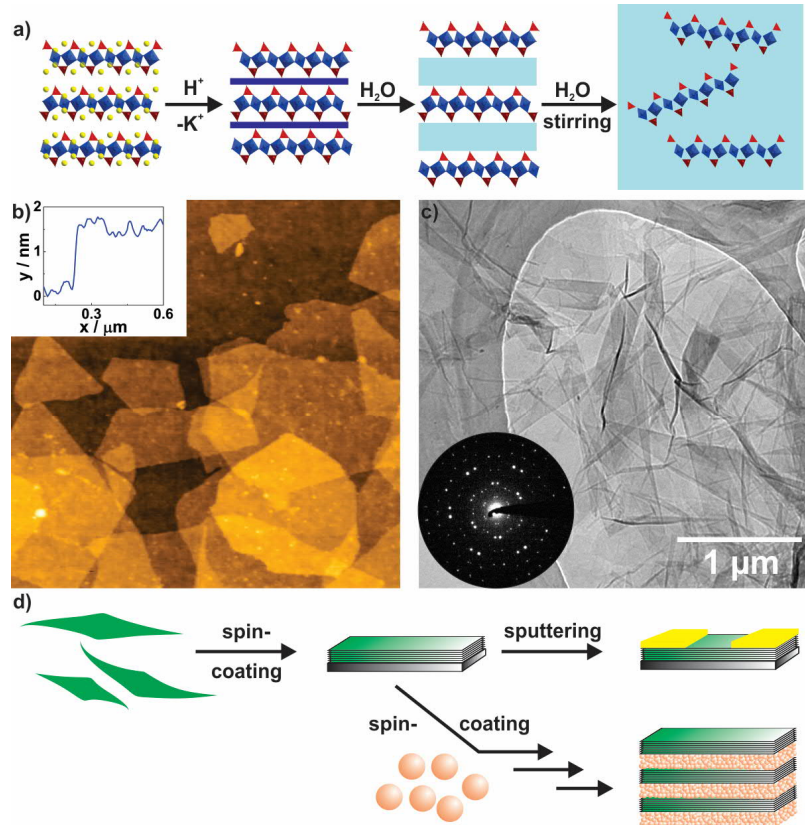


Figure 0.1. Schematic exfoliation procedure, characterization of $\text{H}_3\text{Sb}_3\text{P}_2\text{O}_{14}$ nanosheets and their assembly. a) Schematic ion exchange and exfoliation of $\text{K}_3\text{Sb}_3\text{P}_2\text{O}_{14}$ into $\text{H}_3\text{Sb}_3\text{P}_2\text{O}_{14}$ nanosheets. b) AFM image of the $\text{H}_3\text{Sb}_3\text{P}_2\text{O}_{14}$ nanosheets with a height profile of a single layer nanosheet. c) TEM image of randomly overlapping nanosheets with a selected area diffraction (SAD) from an area with two overlapping nanosheets. d) Schematic processing of $\text{H}_3\text{Sb}_3\text{P}_2\text{O}_{14}$ nanosheets into thin film resistive devices (top) and one-dimensional (1D) photonic crystals (PC, bottom).

Spin-coating was used to prepare thin films out of the nanosheets on quartz substrates as well as BSs on glass slides (Figure 0.1d). The response of these two distinct sensor systems toward relative humidity (RH) was analysed. The thin film sensors showed a change in proton conductance by five orders of magnitude over the complete humidity range (Figure 0.2a) and exhibit a fast response and recovery time (< 3 s). This results was, to the best of our knowledge, the highest sensitivity for any nanosheet-based humidity sensor and among the fastest humidity sensors reported so far. In contrast to

the $\text{H}_3\text{Sb}_3\text{P}_2\text{O}_{14}$ bulk material, we observed a continuous (rather than step like) response in the change of conductance toward humidity changes and also an increase in sensitivity for the nanosheet-based device (Figure 0.2a). Both are beneficial characteristics for sensors and can be attributed to the smaller particle size as well as to the turbostratic disorder leading to less well-defined adsorption sites between the layers and an increased water uptake. This continuous response behavior with respect

to RH was also found for the thickness changes by spectroscopic ellipsometry. The gradual but substantial and fast thickness changes were utilized in BSs for humidity sensing. An unprecedented Bragg peak (BP) shift of 513 nm within a few seconds over the entire humidity range was observed for a $\text{TiO}_2/\text{H}_3\text{Sb}_3\text{P}_2\text{O}_{14}$ BS, and reversible transparency switching was seen for a $\text{SiO}_2/\text{H}_3\text{Sb}_3\text{P}_2\text{O}_{14}$ BS. The combination of fast response times paired with ultralarge optical shift was superior to all BSs for humidity sensing reported until that point of time.

Due to their extraordinary sensing performances, both the thin films as well as the BSs could be utilized in TPI. Hereby, the large responses allowed for the detection of distances of a human finger from the device surface up to several mm, combined with fast response times for the detection of subsecond tapping events (Figure 0.2b, c). Moreover, a lateral finger motion could be tracked in a touchless fashion with a BS for the first time (Figure 0.2d). This result demonstrates the suitability of $\text{H}_3\text{Sb}_3\text{P}_2\text{O}_{14}$ nanosheets for application in touchless user interfaces, which could eliminate the current drawbacks of touchscreens such as scratches, finger prints and hygiene issues

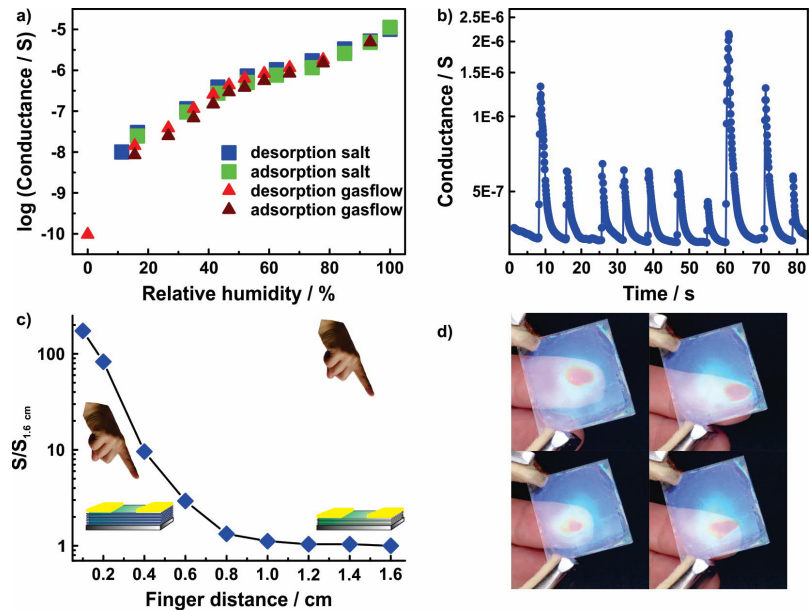


Figure 0.2. Humidity sensing characteristics of the thin film as well as touchless tracking with a $\text{SiO}_2/\text{H}_3\text{Sb}_3\text{P}_2\text{O}_{14}$ BS. a) Ionic conductance as a function of RH for the thin film. b) Response to a subsecond finger tapping. c) Normalized conductance increase as a function of finger distance from the nanosheet film. d) Touchless optical finger motion tracking with a $\text{SiO}_2/\text{H}_3\text{Sb}_3\text{P}_2\text{O}_{14}$ BS.

Utilization of HSbP_2O_8 nanosheets in trace water sensing and vapor distinction (Chapter 3)

“Towards the Nanosheet-Based Photonic Nose: Vapor Recognition and Trace Water Sensing with Antimony Phosphate Thin Film Devices” by Pirmin Ganter,* Katalin Szendrei,* and Bettina V. Lotsch. Published in *Adv. Mater.* **2016**, *28*, 7436-7442. Inside front cover image by Christoph Hohmann, Nanosystems Initiative Munich (NIM).



HSbP_2O_8 is closely related to $\text{H}_3\text{Sb}_3\text{P}_2\text{O}_{14}$ (Chapter 2) as it contains the same elements and fundamental building blocks as $\text{H}_3\text{Sb}_3\text{P}_2\text{O}_{14}$, but with different stoichiometry. Therefore, HSbP_2O_8 forms a different layered structure (see Chapter 1). This related structure results in similar fundamental properties for the bulk material, such as humidity dependent swelling and proton conductivity, but with altered characteristics. In contrast to $\text{H}_3\text{Sb}_3\text{P}_2\text{O}_{14}$, the HSbP_2O_8 bulk material is able to desorb all water molecules at very low RH, which is most likely attributed to the fact that the layer structure does not exhibit structural pores. Due to the loss of all water molecules, HSbP_2O_8 exhibits a larger change in ionic conductivity in the low humidity region. Therefore, combined with improved characteristics of a nanosheet-based sensor it is likely that trace amounts of water can be detected. Besides the trace water detection, it is also of high interest to understand the fundamental sensing response toward other vapor analytes and to evaluate the vapor discrimination capability. In Chapter 3 we show trace water detection with a HSbP_2O_8 thin film based on proton conductance. In addition, we present the vapor distinguishing capability of a $\text{TiO}_2/\text{HSbP}_2\text{O}_8$ BS relying on the dual readout of saturation time and optical shift.

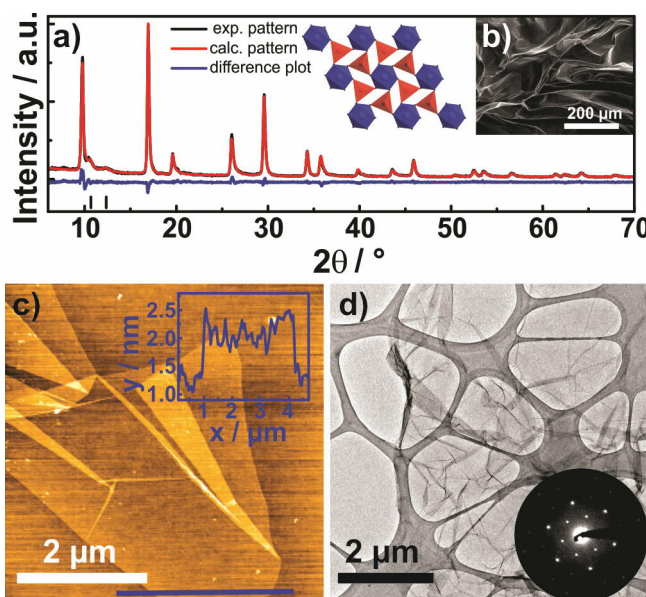


Figure 0.3. Characterization of HSbP_2O_8 nanosheets. a) Rietveld refinement of the XRD pattern of a HSbP_2O_8 nanosheet pellet showing a Warren-type peak profile (experimental pattern in black, calculated pattern in red, and difference plot in blue) with the resulting structure ([001] viewing direction, PO_4 tetrahedra red, SbO_6 octahedra blue). b) SEM image of the exfoliated and randomly restacked nanosheet pellet, exhibiting a “silk-like” morphology d) AFM image of overlapping HSbP_2O_8 single layer nanosheets e) TEM image of randomly overlapping HSbP_2O_8 nanosheets with a representative SAD of a single nanosheet (inset).

HSbP_2O_8 nanosheets, were obtained in a similar process as described for $\text{H}_3\text{Sb}_3\text{P}_2\text{O}_{14}$. The HSbP_2O_8 nanosheets were characterized with TEM, AFM, XRD, energy dispersive X-ray spectroscopy (EDX), and SEM (Figure 0.3). Thin films and BSs were prepared by spin-coating. The response of both

devices toward RH was studied. The HSbP_2O_8 thin film exhibited a change in proton conductance by five orders of magnitude and exhibited a higher sensitivity in the low humidity regime compared to the $\text{H}_3\text{Sb}_3\text{P}_2\text{O}_{14}$ nanosheet device (Chapter 2, Figure 0.4a). For the $\text{TiO}_2/\text{HSbP}_2\text{O}_8$ BS we observed similar large optical shifts (> 500 nm) compared to $\text{H}_3\text{Sb}_3\text{P}_2\text{O}_{14}$ based BS over the entire humidity range. As before, these sensitivity values are among the highest values obtained for sensing humidity with a nanosheet-based thin film or with a BS.

The high sensitivity in the low humidity regime renders the thin film device an intriguing candidate for trace water sensing based on ion conduction. The performance and selectivity was analyzed by testing

water-alcohol mixtures. We were able to detect concentrations as low as 2000 ppm of water in water-alcohol mixtures (Figure 0.4b), which are typical concentrations of water traces in organic solvents. Moreover, an exponential increase in conductance was observed between 2000 and 20000 ppm, which is highly beneficial for sensing due to the linear readout (Figure 0.4b).

The reproducibility was also confirmed by repeating the measurement with two different devices. These characteristics make HSbP_2O_8 nanosheet thin films an attractive alternative for determination of trace water in the high ppm regime compared to traditional, more time consuming techniques such as the Karl-Fischer titration.

Besides achieving a high sensitivity and selectivity toward one analyte, it is also of high interest to distinguish between several vapor analytes. For this purpose, we exposed the $\text{TiO}_2/\text{HSbP}_2\text{O}_8$ BS to several organic vapors grouped into three categories i) water, ii) polar protic as well as iii) non-protic (polar and non-polar) vapors (Figure 0.4c, d). Upon exposure, we recorded the optical shift and the saturation time. Hereby, different interactions between the analytes and materials (TiO_2 and HSbP_2O_8) were observed. For all groups of analyte vapors a fast filling of the porous TiO_2 layers was detected,

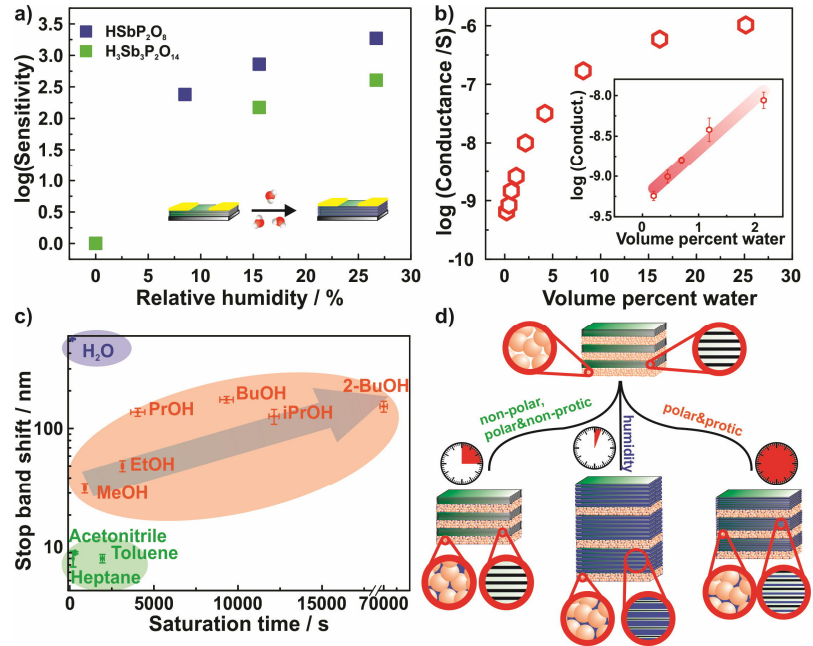


Figure 0.4. Sensitivity and selectivity features of the two devices. a) Comparison of sensitivity for HSbP_2O_8 and $\text{H}_3\text{Sb}_3\text{P}_2\text{O}_{14}$ thin film devices in the low humidity regime. b) Representative trace water sensing of a HSbP_2O_8 thin film (120 nm) for ethanol. In the inset, a close-up of the region 0 and 2.5 volume percent of water is displayed with standard deviations resulting from averaging over three thin films. c) Logarithmic stop band shifts plotted against the response times for the different solvent vapors ($\text{HSbP}_2\text{O}_8/\text{TiO}_2$ BS). d) Schematic showing the interactions of the HSbP_2O_8 nanosheet/ TiO_2 nanoparticle (NP) BS with the different types of solvent vapors, which serve as a fingerprint for analyte identification.

which led to an increase in the refractive index (RI) of the TiO₂ layer. The increase of the RI of the porous TiO₂ layers resulted in a slight redshift of the BP. The filling of the TiO₂ layer was the only response observed for the non-protic (polar and non-polar) analytes as they cannot interact with the highly acidic interlayer environment of HSbP₂O₈. The non-protic analytes can be distinguished mainly on their saturation time, which is correlated to their kinetic diameter. The other two groups, namely water and polar analytes, can interact also with polar and acidic nanosheet layers. The intercalation into the nanosheet layer led to an increase in its thickness and a slight decrease in its RI, resulting in a large redshift of the BP. Thereby, especially the molecular shape as well as the interaction with the nanosheet layer, *e.g.* the ability to form hydrogen bonds, caused significant differences in the saturation time. Water behaves in a distinct way as it showed very fast intercalation into the nanosheet layers due to its superior interaction with the hydrophilic environment. In the remaining group of protic and polar vapors, which showed a substantially longer intercalation time compared to the intercalation time of water, the vapors can clearly be distinguished to such high degree that even isomers can be differentiated. These findings demonstrate the feasibility of nanosheet-based sensors for the differentiation of vapors. Especially in comparison to other photonic noses relying on an array sensor with different functionalizations combined with sophisticated data processing, or on complex sensing structures, the presented method is a much easier approach. Moreover, as the interlayer environment in turbostratically restacked nanosheets can be tuned by various methods such as intercalation, ion exchange and covalent modification, it is likely that the sensing properties can be tuned (see Chapter 4, 5 and 6).

Revealing the influences of the interlayer cation on the sensing characteristics of photonic nanosheet-based sensors (Chapter 4)

“Toward Tunable Photonic Nanosheet Sensors: Strong Influence of the Interlayer Cation on the Sensing Characteristics” by Pirmin Ganter, Leslie M. Schoop, and Bettina V. Lotsch. Published in *Adv. Mater.* **2017**, 29, 1604884.

Enhancing and tailoring certain sensor functions, such as their sensitivity or capability to differentiate between vapors of various volatile organic compounds (VOCs), is of high practical interest. As discussed in Chapters 2 and 3, nanosheets are excellent candidates for vapor sensors due to their large surface area, small size, and good swelling capability. Current approaches to alter the characteristics of nanosheet-based vapor sensors are mainly based on covalent modification or metal NP decoration. Another approach, applicable for nanosheet-based sensors, relying on ion exchange has received no attention for vapor sensing so far, although most nanosheets are carrying a layer charge, which is compensated by exchangeable counter ions. Moreover, promising reports for the sorption characteristics of ion exchanged layered bulk materials are available. In Chapter 4 we utilize the counter-ion exchange approach to demonstrate the strong impact of the interlayer cations TBA and tetrabutylphosphonium (TBP) on the sensing characteristics in nanosheet-based Fabry-Pérot thin film devices. Fabry-Pérot devices utilize interference effects and hence mainly operate on thickness changes for nanosheet-based thin films.

KTaP₂O₈, which was obtained by solid state synthesis, was ion exchanged to HTaP₂O₈ and subsequently exfoliated into

nanosheets with TBAOH or TBPOH. The TBA_xH_{1-x}TaP₂O₈ and TBP_xH_{1-x}TaP₂O₈ nanosheets with x = 0.6 were characterized by several methods including TEM, AFM, elemental analysis, and XRD to confirm their single layer nature as well as their structural integrity. Subsequently, they were spin-coated onto Si substrates to obtain Fabry-Pérot devices and characterized by thin film out-of-plane

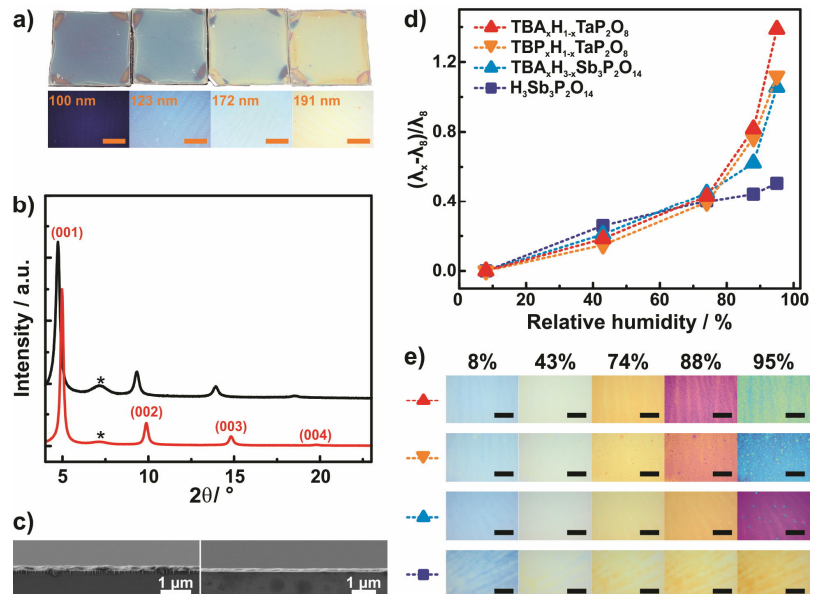


Figure 0.5. Thin film characterization and response toward humidity. a) Images of TBA_xH_{1-x}TaP₂O₈ thin films with different thicknesses that result in different interference colors (scale bar 400 μm). b) Out-of-plane XRD patterns of TBP_xH_{1-x}TaP₂O₈ (top, black) and TBA_xH_{1-x}TaP₂O₈ (bottom, red). c) SEM cross-section images of TBP_xH_{1-x}TaP₂O₈ (left) and TBA_xH_{1-x}TaP₂O₈ (right) thin films. Humidity sensing with H₃Sb₃P₂O₁₄, TBA_xH_{3-x}Sb₃P₂O₁₄, TBP_xH_{1-x}TaP₂O₈, and TBA_xH_{1-x}TaP₂O₈ thin films presented in terms of d) normalized optical shift, and e) color change.

XRD, SEM cross-section images, ellipsometry and ultraviolet-visible (UV-Vis) spectroscopy (Figure 0.5a-c). In order to clearly determine the role of the cation and as HTaP_2O_8 can only be exfoliated with a bulky organic ion, $\text{H}_3\text{Sb}_3\text{P}_2\text{O}_{14}$ and $\text{TBA}_x\text{H}_{3-x}\text{Sb}_3\text{P}_2\text{O}_{14}$ thin films were fabricated as well as references. To understand the impact of the interlayer cation, the thin films were first exposed toward varying RH values. We observed an increased sensitivity, which is exemplified by the larger redshift in the high humidity regime for all TBA or TBP containing thin films compared to the pristine $\text{H}_3\text{Sb}_3\text{P}_2\text{O}_{14}$ thin film (Figure 0.5d, e). The observation was also confirmed by optical isotherms obtained by ellipsometric porosimetry. This result is remarkable as already pristine $\text{H}_3\text{Sb}_3\text{P}_2\text{O}_{14}$ is highly moisture sensitive as shown in Chapter 2. The increase in sensitivity can be attributed to the fact that the quaternary ammonium ions easily hydrate.

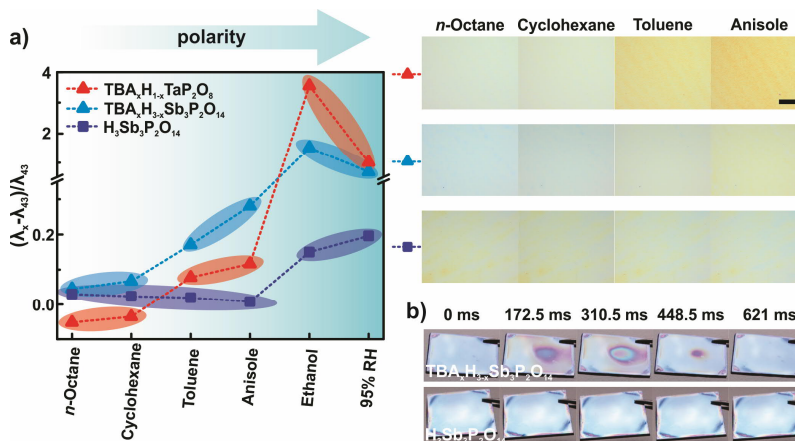


Figure 0.6. Influence of the interlayer cation on the sensing response. a) Normalized optical shifts of $\text{TBA}_x\text{H}_{1-x}\text{TaP}_2\text{O}_8$, $\text{TBA}_x\text{H}_{3-x}\text{Sb}_3\text{P}_2\text{O}_{14}$, and $\text{H}_3\text{Sb}_3\text{P}_2\text{O}_{14}$ thin films upon exposure toward vapors with different polarity (left) and corresponding light microscope images (right). b) Frames from two videos showing the response of $\text{TBA}_x\text{H}_{3-x}\text{Sb}_3\text{P}_2\text{O}_{14}$ (top) and $\text{H}_3\text{Sb}_3\text{P}_2\text{O}_{14}$ (bottom) toward a short ethanol vapor pulse illustrating the impact of the interlayer cation TBA on the response and recovery time.

To further investigate the impact of interlayer cations we studied the response of $\text{TBA}_x\text{H}_{1-x}\text{TaP}_2\text{O}_8$, $\text{TBA}_x\text{H}_{3-x}\text{Sb}_3\text{P}_2\text{O}_{14}$ and $\text{H}_3\text{Sb}_3\text{P}_2\text{O}_{14}$ Fabry-Pérot devices toward vapors of varying polarity (non-polar: cyclohexane, *n*-octane; moderate polar: toluene and anisole as well as polar: ethanol and humidity). We found that $\text{H}_3\text{Sb}_3\text{P}_2\text{O}_{14}$ thin films are only able to differentiate among polar and protic analytes due to the inability of the moderate and non-polar analytes to interact with the acidic and highly polar interlayer environment, in agreement with Chapter 3 (Figure 0.6a, dark blue). However, exchanging the interlayer cation to TBA dramatically alters the interlayer environment, as it widens the interlayer space and partially hydrophobizes it. Thereby the interaction with moderately polar and non-polar analytes is possible (Figure 0.6a, light blue and red). Consequently, TBA enables the optical differentiation of all the mentioned vapors and hence, the interlayer cation has a profound influence on the sensing response. To further characterize and evaluate the impact of the interlayer modification, we recorded time dependent responses of the samples toward short pulses of alcohol (ethanol and isopropanol) vapors. While the TBA containing samples were able to track these vapor streams in spatio-temporal resolution with subsecond response time (Figure 0.6b, top row) and extraordinary sensitivity (optical shifts of about 1400 nm within 322 ms), the $\text{H}_3\text{Sb}_3\text{P}_2\text{O}_{14}$ sample containing no TBA was not able to resolve these sensing signals owing to its slower response time as well as lower sensitivity (Figure 6b, bottom row).

In summary, we presented a viable route to tunable, low-cost sensors, which does not rely on covalent modification of the host species, but can be easily tuned through non-covalent interactions between the host and guest species on the one hand, and between the guest species and the solvent vapor on the other hand. Ultimately, introducing carefully selected cations into the nanosheet interlayer gallery may result in rationally designed sensors with tailor-made properties.

Controlling the interlayer cations in calcium niobate nanosheets thin films for sensing and μm -scale patterning (Chapter 5)

“Photocatalytic Nanosheet Lithography: Photolithography based on Organically Modified Photoactive 2D Nanosheets” Pirmin Ganter and Bettina V. Lotsch. Published in *Angew. Chem. Int. Ed.* **2017**, 56, 8389-8392.

Calcium niobate nanosheets have a very high dielectric constant ($\epsilon_r > 150$) and are photocatalytically active under UV-radiation. Due to these outstanding properties and their stability (see Chapter 1.5.2), calcium niobate nanosheets ($\text{Ca}_2\text{Nb}_3\text{O}_{10}$) have been utilized in artificial heterostructures, as photocatalysts, and as dielectric materials in ultrathin high- k capacitors. Their photocatalytic activity was found to decompose TBA, which is added in the exfoliation step. While there is a single layer control in the thickness of nanosheet-based structures, there is currently rather little control over lateral dimensions in a scalable way, despite its need for various applications. Utilizing the inherent photocatalytic activity of the calcium niobate nanosheets in combination with a mask could lead to a laterally patterned interlayer environment. As the interlayer environment controls the swelling properties of the nanosheet-based films (see Chapter 4), a development step could be used to selectively remove the areas containing one type of the interlayer cation, whereas the areas containing the other cation remain on the surface. Therefore, the calcium niobate nanosheets can act as a photoresist. In Chapter 5, we demonstrate the transferability of the interlayer cation based vapor sensing concept of Chapter 4 to calcium niobate nanosheets. We utilize this concept in combination with the inherent photocatalytic properties of the calcium niobate nanosheets to photo-pattern thin films of the nanosheets on the sub $100\ \mu\text{m}$ scale by using $\text{TBA}_x\text{H}_{1-x}\text{Ca}_2\text{Nb}_3\text{O}_{10}$ as a negative photoresist.

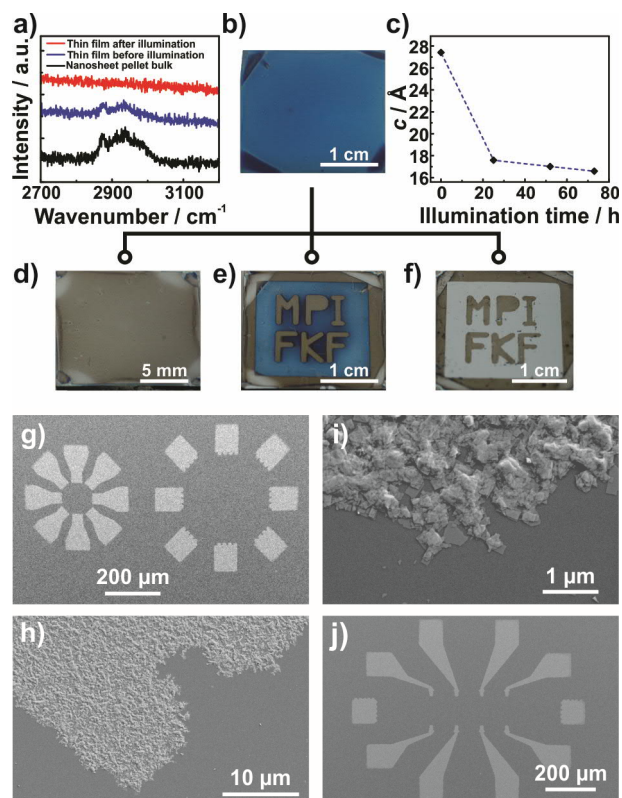


Figure 0.7. PNL with $\text{TBA}_x\text{H}_{1-x}\text{Ca}_2\text{Nb}_3\text{O}_{10}$ thin films. a) Raman spectra and c) d -spacing proving the photocatalytic decomposition under UV-radiation of TBA, which is also directly observable in the color change of the $\text{TBA}_x\text{H}_{1-x}\text{Ca}_2\text{Nb}_3\text{O}_{10}$ thin film, see b) and d). By applying a mask the thin films can be patterned, e) and f), after removing the unexposed area result in $(\text{NH}_4)_x\text{H}_{1-x}\text{Ca}_2\text{Nb}_3\text{O}_{10}$ structures. g-j) μm -scale patterning by applying a μm -scale mask. In i) the fundamental building blocks of the structures are observable, which are nanosheets.

$\text{KCa}_2\text{Nb}_3\text{O}_{10}$, which was obtained by solid state synthesis, was ion exchanged and subsequently exfoliated into $\text{TBA}_x\text{H}_{1-x}\text{Ca}_2\text{Nb}_3\text{O}_{10}$ nanosheets with TBAOH. Spin-coating was used to construct thin films on Si substrates leading to Fabry-Pérot type devices similar as described for $\text{TBA}_x\text{H}_{1-x}\text{TaP}_2\text{O}_8$ in Chapter 4. We analyzed the photonic sensing response toward different vapors (*n*-octane, cyclohexane, toluene, anisole and different levels of RH). We observed high sensitivity toward water vapor in the high humidity regime and vapor discrimination capability for vapors with different polarity. The obtained results are in close agreement with TBA modified samples discussed in Chapter 4. Consequently, the outlined concept in Chapter 4 of the interlayer cation dominating the sensing response in nanosheet-based photonic devices can be validated and generalized. In the next step, we combined this concept with the inherent photocatalytic activity of the calcium niobate nanosheets. Therefore, areas of the thin films surface are exposed to UV-light through a shadow mask (Figure 0.7b, d-f). This approach leads in the illuminated areas to the decomposition of TBA in the interlayer space and its replacement by protons ammonium cations resulting in a thickness decrease of the exposed areas of the photonic thin film and hence color change (Figure 0.7e). The decomposition of TBA was also confirmed by Raman spectroscopy as well as thin film out-of-plane XRD (Figure 0.7a, c). As the non-exposed areas containing $\text{TBA}_x\text{H}_{1-x}\text{Ca}_2\text{Nb}_3\text{O}_{10}$ substantially swell and ultimately exfoliate in polar solvents, they were washed off with an acetone-water mixture (Figure 0.7f). On the contrary, the exposed areas consisting of $(\text{NH}_4)_x\text{H}_{1-x}\text{Ca}_2\text{Nb}_3\text{O}_{10}$ do not substantially swell or even exfoliate in water due to the change of interlayer cation. Therefore, these areas remain on the substrate (Figure 0.7f). In essence, $\text{TBA}_x\text{H}_{1-x}\text{Ca}_2\text{Nb}_3\text{O}_{10}$ nanosheets can be used as a negative photoresist. With a view toward potential applications of two-dimensional (2D) materials in microelectronics, patterning on the μm -scale is key. Therefore, we applied a μm -scale mask and obtained various μm -scale features of $(\text{NH}_4)_x\text{H}_{1-x}\text{Ca}_2\text{Nb}_3\text{O}_{10}$ with high fidelity (Figure 0.7g-j). We were able to obtain feature sizes down to 10 μm so far by this technique, which we named PNL. As the $\text{TBA}_x\text{H}_{1-x}\text{Ca}_2\text{Nb}_3\text{O}_{10}$ nanosheets can be directly used as negative photoresist without requiring a sacrificial photoresist, PNL is an overall resource and economic efficient new technique. Moreover, we expect PNL to be sufficiently general to transfer it to other photoactive 2D systems and to further reduce the features sizes accessible down to the submicron scale.

Vapor-phase alkylamine intercalation: A smart, versatile and colorful way for sensor modification (Chapter 6)

“Vapor-Phase Amine Intercalation for the Rational Design of Photonic Nanosheet Sensors” by Pirmin Ganter, Leslie M. Schoop, Marie Däntl, and Bettina V. Lotsch. Published in *Chem. Mater.* **2018**, *30*, 2557-2565.

Fine-tuning of a vapor sensor’s sensitivity and selectivity over a broad analyte range is of enormous commercial interest but also a key challenge in fundamental science. Despite making progress in recent years by various approaches based on 2D materials including the ion exchange method presented in Chapter 4, in their current development state all of the demonstrated methods have certain shortcomings. In Chapter 6 we address this issue by the development of an easy, straightforward, and versatile method based on vapor-phase amine intercalation into photonic nanosheet sensors allowing for a tunable selectivity as well as sensitivity (Figure 0.8). Similar to the ion exchange method, the vapor-phase amine intercalation utilizes non-covalent modification of the interlayer space and at the same time offers several important advantages (see Figure 0.8 and Chapter 6).

$\text{H}_3\text{Sb}_3\text{P}_2\text{O}_{14}$ thin films on a Si substrates were synthesized as described in Chapter 2 and 4. The photonic thin films were afterwards intercalated with primary and tertiary alkylamines and aminoalcohols over the vapor-phase (Figure 0.8).

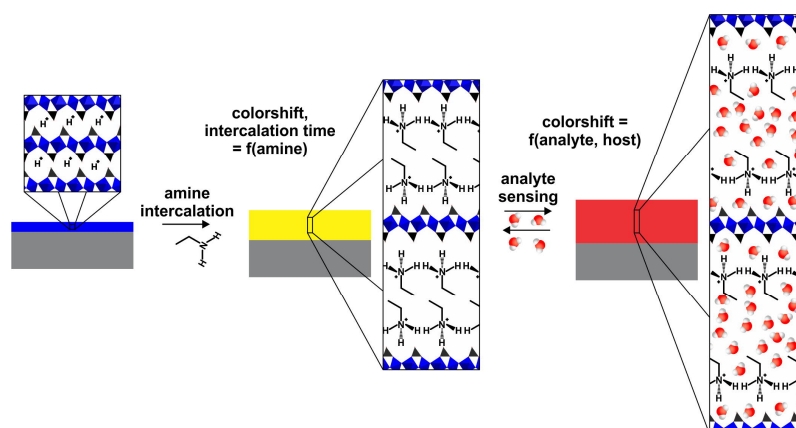


Figure 0.8. Schematic overview of the vapor-phase amine intercalation and its utilization in sensing.

Thereby, the amines are protonated to ammonium ions and hence, trapped in the interlayer space. The intercalated thin films were characterized with out-of-plane XRD and UV-Vis spectroscopy (Figure 0.9a). Hereby, a monolayer arrangement was found for the tertiary amines and a bilayer arrangement for the primary amines. As the amines are intercalated into photonic thin films, they can be differentiated based on their optical shift and intercalation time (Figure 0.9a, b). The optical shift and the intercalation time depend on the alkyl chain length as well as the properties of the amine (Figure 0.9b). Besides the differentiation of amines, this can be utilized to track the intercalation process in a time and space resolved manner (Figure 0.9b). The spatially resolved tracking makes it possible to localize the amine vapor source and to optically study the intercalation mechanism and its kinetics. Therefore, it is of practical as well as fundamental interest. As the amines are trapped as ammonium ions in the interlayer space, the intercalated and hence, functionalized, thin films can be utilized in vapor sensing (Figure 0.8, Figure 0.9c). As many amines can be intercalated over the vapor-phase, a

gradual and widely tunable sensitivity and selectivity is expected. We demonstrated the tuneability by analyzing the sensing response (optical shift) of thin films intercalated with primary alkylamines with varying alkyl chain length toward vapors of different polarity (94% RH, toluene and cyclohexane vapor). We were able to show that by varying the alkyl chain length the selectivity and sensitivity can be gradually tuned (Figure 0.9c). While we observed a large response toward polar analytes for short chained amines, a large response toward non-polar analytes for long chained alkylamines was detected. The selectivity could be further tuned by introducing an OH functional group. Besides the tuning of the selectivity and sensitivity, we were able to show for the primary alkylamine modified thin films subsecond response and recovery times, long-term stability, as well as the ability to differentiate solvent vapor mixtures. The fast response and recovery times enabled tracking of vapor streams in real-time.

As the amine intercalation occurs over the vapor-phase and is a post-film fabrication modification, we were able to intercalate various amines at different locations into a single film by applying a mask (Figure 0.9d). Compared to other approaches our work represents a significant advance, since array fabrication as well as nanostructuring is easily possible. The array sensors obtained by intercalating ethylamine, butylamine and decylamine into individual films could be used to differentiate between various vapors with the naked eye, based on the characteristic color pattern for each vapor (Figure 0.9d). Compared to other optical array sensors, which require additional sophisticated read-out methods like principal component analysis (PCA), the presented detection method is a significant improvement. Taken together, vapor-phase amine intercalation enables not only to differentiate between various amines, but also to tune the response toward vapors in a spatially resolved fashion.

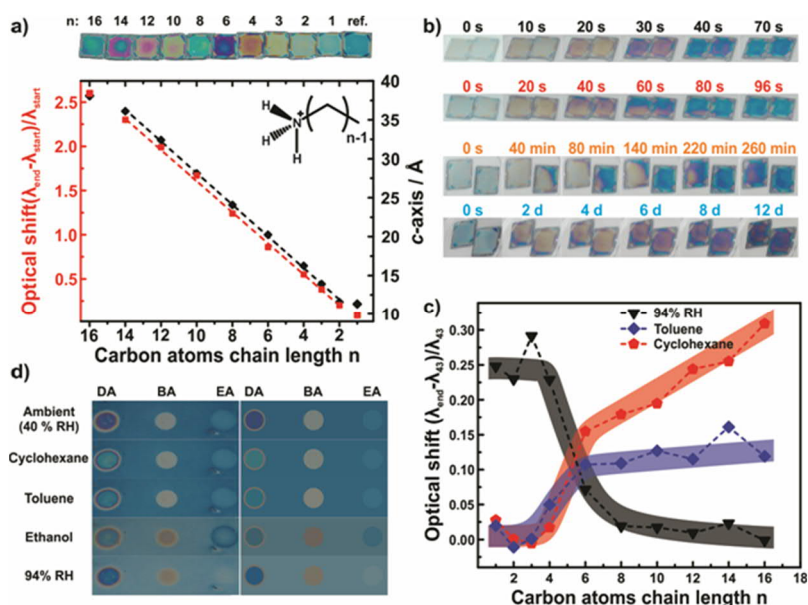
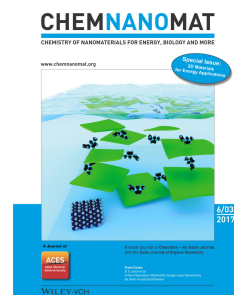


Figure 0.9. Vapor-phase alkylamine intercalation into $\text{H}_3\text{Sb}_3\text{P}_2\text{O}_{14}$ nanosheet-based thin films. a) Images of $\text{H}_{3-x}(\text{NH}_3(\text{CH}_2)_{n-1}\text{CH}_3)_x\text{Sb}_3\text{P}_2\text{O}_{14}$ intercalated thin films and their characterization. b) Temporal resolved tracking of the intercalation process for *n*-butylamine (black), *N,N*-dimethylbutylamine (red), 4-dimethylamino-1-butanol (orange) and 4-amino-1-butanol (light blue). c) Impact of the alkyl chain length of intercalated primary amines on the sensitivity and selectivity of the sensor. d) Response of an array sensor (left) obtained by intercalating *n*-decylamine, *n*-butylamine and *n*-ethylamine at different locations in a single $\text{H}_3\text{Sb}_3\text{P}_2\text{O}_{14}$ thin film. On the right averaged RGB image of the response, which can be utilized for analyte identification similar to the color coded legend of a pH-indicator paper for pH identification.

The silver exfoliation route (Chapter 7)

“A New Fabrication Method for Single-Layer Nanosheets by Silver-Assisted Exfoliation” by Pirmin Ganter,* Christian Ziegler,* Anne T. Friedrichs, Viola Duppel, Christina Scheu, and Bettina V. Lotsch. Published in *ChemNanoMat* **2017**, 3, 411-414. Front cover image by Pirmin Ganter.



The development of novel exfoliation routes of layered materials is of immense interest due to the broad range of possibilities ranging from fundamental physics to processing nanosheets into ultrathin functional devices. Moreover, as every delamination method brings its own set of advantages and limitations, the improvement of existing and the development of new exfoliation routes is highly desirable. The currently most applied exfoliation route for oxide nanosheets is based on the proton exchange route, which is limited by the requirement of acid stability of the layered material as well as the limited number of usable EAs. The enlargement of the portfolio of EAs is of high interest, as the nanosheet properties are influenced by the EA used (see Chapter 4). In addition, eliminating the requirement of acid stability can result in the novel delamination of acid-sensitive materials. In

Chapter 7, a novel silver-assisted exfoliation route is presented increasing the portfolio of EAs and dropping the requirement of acid stability (Figure 0.10a). To demonstrate the broad applicability of the silver assisted exfoliation, the method is applied to obtain three types of nanosheets, each exfoliated with three different exfoliating agents.

KLaNb_2O_8 , $\text{KCa}_2\text{Nb}_3\text{O}_{10}$ and KTaP_2O_8 were synthesized by a solid state reaction and characterized by powder XRD and EDX. Subsequently, the compounds were ion exchanged in an AgNO_3 melt to obtain $\text{AgLaNb}_2\text{O}_8$, $\text{AgCa}_2\text{Nb}_3\text{O}_{10}$ and AgTaP_2O_8 . The successful exchange was verified by EDX. The three compounds were exfoliated by stirring or shaking in 1:1 ratio with the iodide

salts of the EAs, which were TBA, choline (Ch) or 1-allyl-3-methylimidazolium (AMI) iodide (Figure 0.10a). Treatment of the silver phases with the iodides resulted in the removal Ag^+ from the interlayer space and formation of highly insoluble silver iodide. The formation of silver iodide is the driving force for the exchange of Ag^+ with the organic cations Ch, AMI and TBA in the interlayer space. This exchange most likely enables the compounds to undergo osmotic swelling, ultimately leading to

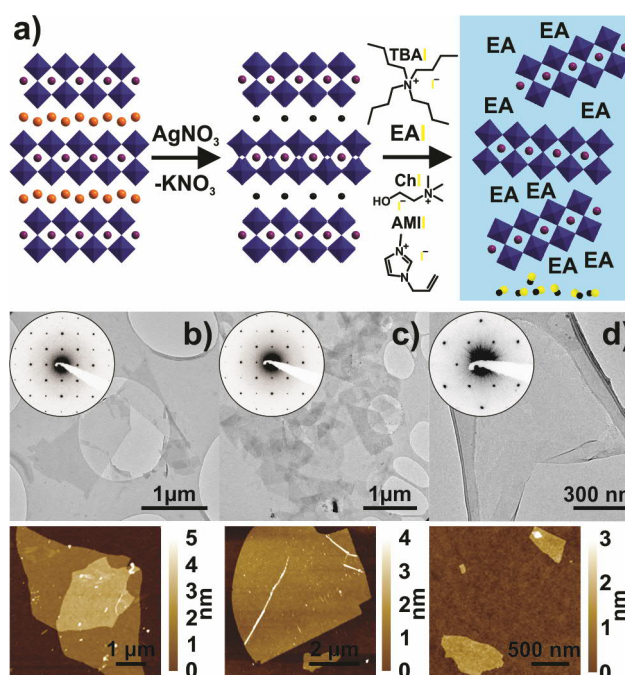


Figure 0.10. The silver-assisted exfoliation route. a) Scheme of the silver-assisted exfoliation route. TEM and AFM characterization of nanosheets obtained by exfoliating b) $\text{AgCa}_2\text{Nb}_3\text{O}_{10}$, c) $\text{AgLaNb}_2\text{O}_7$, and d) AgTaP_2O_8 with ChI.

nanosheets by applying some weak mechanical force. The process is similar to the acid-mediated exfoliation route as a reaction with a strongly negative reaction enthalpy is utilized for exfoliation. In the case of the proton-assisted exfoliation route the “hard” interlayer protons react with “hard” OH^- to form H_2O , whereas in the case of the silver assisted exfoliation route soft Ag^+ reacts with soft I^- resulting in AgI . Therefore, this points toward a more general concept for chemically inducing exfoliation based on Pearson’s concept of “hard and soft acids and bases” (HSAB).

To yield mainly single layer nanosheets a centrifugation step was applied to remove non-exfoliated bulk material. The resulting nanosheets were analyzed by TEM including selected area electron diffraction (SAED) and AFM. We were able to show by comparison with data of nanosheets obtained from $\text{HCa}_2\text{Nb}_3\text{O}_{10}$, HLaNb_2O_8 and from Chapter 4 for HTaP_2O_8 with TBAOH that the silver assisted exfoliation route yields nanosheets of similar quality with various exfoliation agents (AMII, TBAI, CHI) (Figure 0.10 b-d). Therefore, the silver exfoliation route offers an alternative to the proton exchange exfoliation route. In addition, it has the advantages of allowing the use of exotic EAs, which can be beneficial for tailoring the properties of the nanosheets. Moreover, it might be applied to acid sensitive systems and it does not require the use of organic hydroxides, which are less common compared to the iodides.

Table of contents

Erklärung	I
Eidesstattliche Versicherung	I
Danksagung	V
Summary	VII
Table of contents	XXIII
1 Introduction	1
1.1 From omnipresent layered materials to superior nanosheet-based devices	1
1.2 The many ways to nanosheets: solvent-based exfoliation methods	4
1.2.1 Liquid-phase exfoliation	5
1.2.2 Redox-mediated exfoliation	5
1.2.3 Ion exchange exfoliation	6
1.3 Assembly of nanosheets: resolving the contradiction of scalability and control	8
1.4 Tailoring of the nanosheets properties	11
1.4.1 Covalent modification	12
1.4.2 Ion exchange and intercalation	12
1.5 The layered metal phosphates $A_nM_nP_2O_{5+3n}$ and the Dion-Jacobson phase $ACa_2Nb_3O_{10}$ with $M = Sb$ ($n = 1, 3$), Ta ($n = 1$) and $A = K$ and H	14
1.5.1 The layered metal phosphates from past to present	14
1.5.2 From layered perovskite to the Dion-Jacobson phase $KCa_2Nb_3O_{10}$	17
1.6 Application and devices	20
1.6.1 Chemical sensors	20
1.6.2 Transition metal oxide nanosheets: promising high- k dielectrics	27
1.7 Objectives	29
1.8 Bibliography	31
2 Implementation of $H_3Sb_3P_2O_{14}$ nanosheets in touchless positioning interfaces	41
2.1 Touchless Optical Finger Motion Tracking Based on 2D Nanosheets with Giant Moisture Responsiveness	41
2.1.1 Introduction	42
2.1.2 Results and discussion	44

2.1.3 Conclusion	53
2.1.4 Acknowledgement	53
2.1.5 Bibliography	53
2.2 Supporting Information: Touchless Optical Finger Motion Tracking Based on 2D Nanosheets with Giant Moisture Responsiveness	56
2.2.1 Methods	56
2.2.2 Characterization	57
2.2.3 Additional data	60
2.2.4 Bibliography	72
3 Utilization of HSbP₂O₈ nanosheets in trace water sensing and vapor distinction	73
3.1 Towards the Nanosheet-Based Photonic Nose: Vapor Recognition and Trace Water Sensing with Antimony Phosphate Thin Film Devices	73
3.1.1 Introduction	75
3.1.2 Results and discussion	76
3.1.3 Conclusion	85
3.1.4 Acknowledgement	86
3.1.5 Bibliography	86
3.2 Supporting Information: Towards the Nanosheet-Based Photonic Nose: Vapor Recognition and Trace Water Sensing with Antimony Phosphate Thin Film Devices	88
3.2.1 Methods	88
3.2.2 Characterization	89
3.2.3 Additional data	92
3.2.4 Bibliography	106
4 Revealing the influences of the interlayer cation on the sensing characteristics of photonic nanosheet-based sensors	107
4.1 Toward Tunable Photonic Nanosheet Sensors: Strong Influence of the Interlayer Cation on the Sensing Characteristics	107
4.1.1 Introduction	108
4.1.2 Results and discussion	110
4.1.3 Conclusion	118
4.1.4 Acknowledgement	119

4.1.5 Bibliography	119
4.2 Supporting Information: Toward Tunable Photonic Nanosheet Sensors: Strong Influence of the Interlayer Cation on the Sensing Characteristics	122
4.2.1 Methods	122
4.2.2 Characterization	123
4.2.3 Additional data	125
4.2.4 Bibliography	140
5 Controlling the interlayer cations in calcium niobate nanosheets thin films for sensing and μm scale patterning	141
5.1 Photocatalytic Nanosheet Lithography: Photolithography based on Organically Modified Photoactive 2D Nanosheets	141
5.1.1 Introduction	142
5.1.2 Results and discussion	143
5.1.3 Conclusion	147
5.1.4 Acknowledgement	147
5.1.5 Bibliography	147
5.2 Supporting Information: Photocatalytic Nanosheet Lithography: Photolithography based on Organically Modified Photoactive 2D Nanosheets	149
5.2.1 Methods	149
5.2.2 Additional data	150
5.2.3 Bibliography	153
6 Vapor-phase alkylamine intercalation: A smart, versatile and colorful way for sensor modification	154
6.1 Vapor-Phase Amine Intercalation for the Rational Design of Photonic Nanosheet Sensors	154
6.1.1 Introduction	155
6.1.2 Results and discussion	157
6.1.3 Conclusion	164
6.1.4 Acknowledgement	165
6.1.5 Bibliography	165

6.2 Supporting Information: Vapor-Phase Amine Intercalation for the Rational Design of Photonic Nanosheet Sensors	169
6.2.1 Methods	169
6.2.2 Characterization	171
6.2.3 Additional data	172
6.2.4 Bibliography	184
7 The silver exfoliation route	185
7.1 A New Fabrication Method for Single-Layer Nanosheets by Silver-Assisted Exfoliation	185
7.1.1 Introduction	187
7.1.2 Results and discussion	188
7.1.3 Outlook	191
7.1.4 Acknowledgement	192
7.1.5 Bibliography	192
7.2 Supporting Information: A New Fabrication Method for Single-Layer Nanosheets by Silver-Assisted Exfoliation	194
7.2.1 Methods	194
7.2.2 Characterization	195
7.2.3 Additional data	196
7.2.4 Bibliography	199
8 Conclusion and outlook	200
8.1 Conclusion	200
8.2 Outlook	201
8.3 Bibliography	206
9 Appendix	208
9.1 Table of Abbreviations	208
9.2 List of Publications	210
9.3 Patents	212
9.4 Contribution to conferences	212

1 Introduction

1.1 From omnipresent layered materials to superior nanosheet-based devices

Being scientifically explored for almost 200 years,^[1-5] layered materials are omnipresent in our daily life due to their utilization in various applications and devices ranging from graphite in pencils^[6] and as anode material in lithium ion batteries,^[7-9] over MoS₂ as lubricants^[10] to clays applied as construction materials^[11,12] as well as in cat litters.^[12,13] Although having very diverse properties, layered materials have also a common characteristic defining them: the anisotropy in their bonding situation featuring strong intralayer and weak interlayer bonds.^[3,14-16]

As early as in the 1950s,^[3,14,17-22] researchers succeeded in overcoming these weak interlayer forces by several methods such as ion exchange,^[22] redox-mediated^[20] as well as mechanical exfoliation^[21] and successfully exfoliated the layered materials into, most likely, single and few layers of nanosheets. The formation of nanosheets was difficult to prove at that point of time due to the lack of advanced characterization techniques.^[14,23] Further investigations up to the 1990s mainly focused on exploring new nanosheets and to characterize them,^[14,24] followed later by the development of different assembling techniques.^[25-27] Ignited by the experimental discovery of graphene's exceptional electronic properties in 2004 by Geim and Novoselov, intense research interest was attracted to the properties and applications of graphene.^[28-33] Along with exceptional electronic properties, graphene features excellent mechanical, thermal and optical properties, which are significantly different from the parent layered bulk material due to the size confinement and large anisotropy in 2D materials.^[6,17,28,29,31,33]

However, despite graphene's unprecedented properties, graphene is limited by its chemical composition (carbon),^[16] structure and modification possibilities.^[34] Therefore, graphene covers an important but only a limited region in the property and application space.^[29,32,34-38] Hence, over the past decade the exfoliation of other layered materials ranging, for instance, from semiconducting to insulating,^[3,14,17,29,39-42] together with the study of the nanosheet properties, gained tremendous interest.^[3,14,32,34,35,37,43,44] The discoveries of new nanosheets such as MXene,^[41,45-48] Xenes^[5,38,49,50] and exfoliated Zintl phases^[38,51,52] constantly add uniqueness and hence new dimensions to the field of solid state and materials chemistry.^[17,43] This development is not only intriguing from a fundamental, but also from practical perspective, as it expands the diversity of available nanosheets building blocks for devices.^[17,29,34,53,54] For the utilization in devices relevant for industrial applications, it is crucial to develop scalable solvent-based exfoliation routes,^[16,23,55-61] to position nanosheets reproducibly at desired locations,^[15,17,23,29,37,62-64] and to tailor nanosheet properties (see Figure 1.1).^[30,34,54,59,65-71]

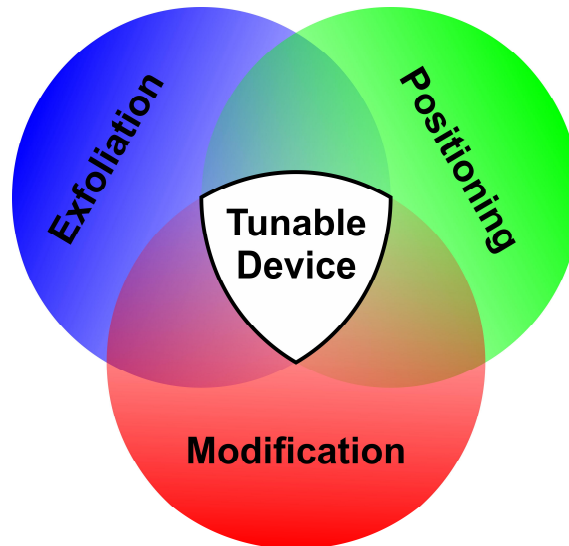


Figure 1.1. Toward nanosheet-based devices with tailor-made properties. A key requirement is the development of efficient, controllable, high throughput exfoliation routes (blue) providing large quantities of single layer nanosheets. Positioning methods should aim for reproducible and up-scalable deposition of nanosheets at specific locations with precise placement (lateral and vertical) in the sub nm range of the nanosheets (green). For industrial requirements, it is desirable to develop methods that tailor and tune the nanosheets' properties (red), as these provide access to application oriented optimization of the nanosheets' properties.

If all of these steps are successfully achieved, rationally designed devices at the molecular level with tailored properties at the industrial scale are within reach.^[15-17,29,37,42,71,72] The utilization of nanosheets in technical applications is of high interest as nanosheets exhibit several advantages compared to their bulk materials due to their ultrathin thickness, flexibility, good mechanical strength, higher surface area, distinct optical and electronic properties.^[17,32,41,73]

Due to the outstanding properties of the nanosheets, many potential and promising applications and devices have been developed in the laboratory, such as field effect transistors (FETs),^[63,74,75] diodes,^[76-79] capacitors,^[80,81] supercapacitors,^[73,82] sensors,^[83,84] thermoelectrics,^[85,86] membranes^[87-89] and catalysts.^[90,91] However, due to lack of synchronization of all three crucial points (scalable synthesis, highly reproducible assembly at the nanoscale, tunability), no nanosheet-based device has made large impact on the industrial markets yet.^[35,92] Therefore, these devices with improved performances are still mainly absent in our everyday life.^[44]

To overcome these challenges and to harvest the superior properties, in the last few years huge effort has been put into application oriented research (see Figure 1.2),^[23,29,32,48,63,73,74] especially into the three above mentioned points, exfoliation,^[3,39,41,55] positioning^[15,17,23,62-64,93] and tuning.^[66,71,87,88,94] With many research efforts and the enormous variety of structures and composition of nanosheets available,^[3,14,16,17,34] it is considered that impactful applications are achievable in the next couple of years.^[16,35,44,55,92]

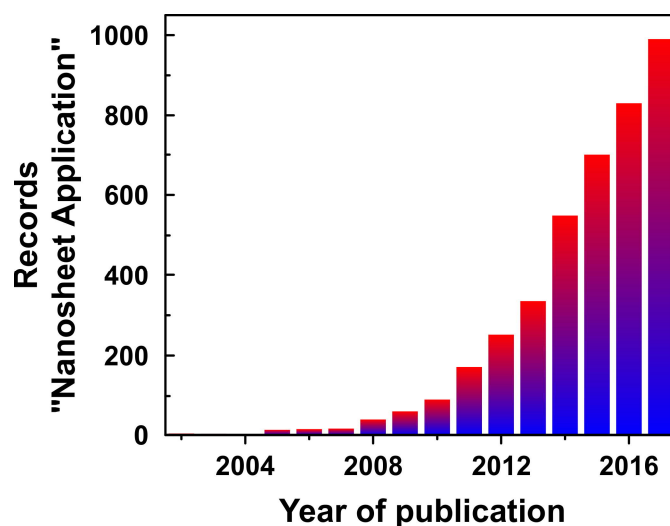


Figure 1.2. Number of publications per year based on the search topic “Nanosheet Application” in the Scifinder® database. Accessed: 23/02/2018. The plot shows almost an exponential increase from 2004, in which the exceptional electronic properties of graphene were experimentally discovered.^[95]

This thesis represents a little step toward the ultimate goal of achieving impactful applications with nanosheets, as it focuses around the development of novel exfoliation techniques (Chapter 7), the positioning (Chapter 5) and assembly of nanosheets (Chapter 2 and 3), tuning of their properties (Chapter 4-6), together with their utilization in vapor sensors (Chapter 2-6)).

In the following subchapters state of the art solvent-based exfoliation techniques, assembly methods, tailoring of nanosheets properties and relevant applications for the materials used in this thesis are described.

1.2 The many ways to nanosheets: solvent-based exfoliation methods

Nanosheets are defined as materials with monomolecular thickness and large 2D anisotropy.^[17] However, in current literature the term nanosheets is also applied for multilayer nanosheets consisting of up to 10 layers.^[3,17] Many ways exist to obtain nanosheets.^[3,14,16,17,33,41,57] These methods range from expensive vapor growth techniques,^[14] over the synthesis of artificial 2D materials^[96,97] to the exfoliation of layered materials.^[3,17,23,33,39,98] It is important to note that each method has its own set of advantages and disadvantages.^[3,16,23,33,41,57,58,99-101] Therefore, it is still important to develop new methods to obtain nanosheets and to improve existing ones.^[41,57,61,65,99,102-106] Solvent-based exfoliation techniques are considered to be among the most promising ones for applications because they are relatively inexpensive, scalable, and easily implementable within current technology. In contrast, vapor growth or scotch tape exfoliation techniques offer low amounts of higher quality nanosheets.^[3,6,16,23,30,57,58,61,102,107,108] The three most applied solvent-based exfoliation techniques (Figure 1.3), namely liquid-phase exfoliation,^[6,13,23,39,56,57,63,65] redox-mediated delamination,^[3,24,33,40,98-100,109-113] and ion exchange,^[3,16,17,114-117] are described in more detail.

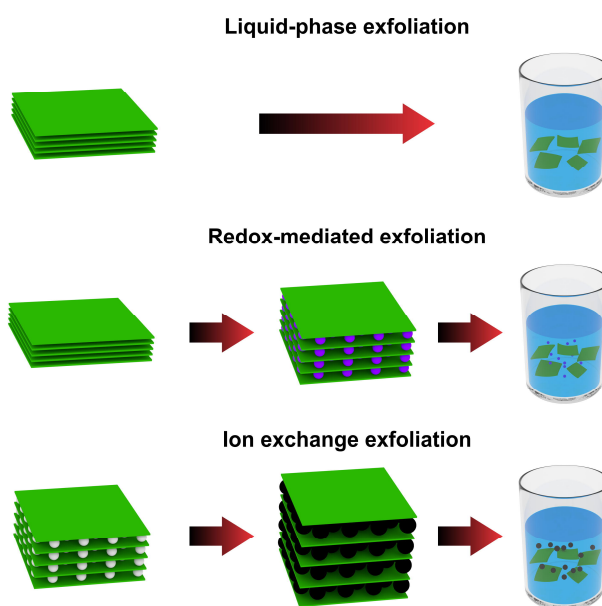


Figure 1.3. Schematic overview of the main solvent-based exfoliation methods. In the liquid-phase exfoliation (top) a layered material is immersed in a suitable solvent and a strong mechanical force is applied for exfoliation. Although the approach is straightforward, it leads to a broad size and especially thickness distribution of the nanosheets. In the redox-mediated exfoliation approach (middle), the layered material is treated with a reducing or oxidizing agent, leading to an altered oxidation state of the layered material. Due to the change in the oxidation state of the layered material, the properties of the interlayer gallery of the material are modified, which enables the delamination of the material. The redox-mediated approach yields mainly single layer nanosheets, however, it is limited by the rather delicate experimental procedure as well as the inability to recover completely the properties of the pristine nanosheets. In the ion exchange exfoliation route (bottom), the counterions in the layered charged material are replaced with other ions, which facilitate the exfoliation of the material. Typically, ion exchange results in weakened attractive forces between the layers and enhances the material's swelling properties. The ion exchange exfoliation route provides a high single layer yield, but it is rather a time-consuming procedure.

1.2.1 Liquid-phase exfoliation

Liquid-phase exfoliation had its great breakthrough by the work of Coleman and co-workers,^[39,56] who used it for the delamination of layered van der Waals materials starting from graphene, followed by transition metal dichalcogenides (TMDs) and charged nanosheets.^[3,39,56,57,102,118,119] In the liquid-phase exfoliation process a layered material is immersed into a suitable solvent, which can contain a surfactant or polymer, and then some mechanical force is applied to overcome the energy barrier for exfoliation by either ultrasonication, shear force, or ball milling.^[23,57] Subsequently, several centrifugation steps are applied to remove non-exfoliated materials and to select size and thickness.^[23,57,65] In the liquid-phase exfoliation it is crucial to reduce the net energy for exfoliation and to prevent reaggregation.^[23] Generally, Hansen solubility parameters or surface tension components of the solvents are matched with the corresponding parameters and components of the nanosheets to achieve good exfoliation.^[6,39,102,118] The optional addition of surfactants or polymers is mainly to prevent reaggregation either by charge or steric reasons.^[119] The advantages of liquid-phase exfoliation are the high throughput, versatility, and its inexpensiveness.^[3,39,57,65] However, liquid-phase exfoliation results in nanosheets with a broad thickness and size distribution. As the nanosheet properties can vary drastically with increasing thickness, several time-consuming centrifugation steps are required to narrow the size distribution.^[16,23,65,99]

1.2.2 Redox-mediated exfoliation

The redox-mediated exfoliation route is another important solvent-based exfoliation method for the delamination of layered van der Waals materials.^[16,24,33,98-100,110,111,113,120-122] Prominent examples include the exfoliation of graphite^[20,33,113] or TMDs,^[24,99-101] but also exotic ones such as binary halides.^[123] Usually, the exfoliation procedure is a two or three step process depending on whether the recovery of the initial oxidation state is desired.^[42,99,100,113,121,123] In the first step, the oxidation state of the layered material is modified by a reducing or oxidizing agent or electrochemically.^[24,33,99,100] This step involves either covalent modification of the host lattice or a redox intercalation step.^[99,113,123] In a second step, the layers with modified oxidation state are exfoliated, whereas the changed oxidation state or the introduced covalent modifications are the main driving force behind the process.^[99,113] For example, lithium intercalated reduced TMDs, and most likely binary halides as well, react with water under hydrogen production leading to a separation of the layers.^[24,99,123] On the other side, the oxidation of graphene to water swellable graphene oxide (GO) results in negatively charged covalently modified layers.^[33,113] In a third optional step, the oxidation state can be at least partially recovered, for instance by treatment with either reducing or oxidizing agents.^[33,123] This regeneration is usually of high interest because the exfoliated layers with changed oxidation state have significantly different properties than the single layers with the pristine oxidation state.^[23,33,42,113,121,123] For example, the recovery of the oxidation state results in higher electronic conductivity in reduced GO (rGO)^[113] or in RuCl₃ in the reappearance of magnetic ordering.^[123] The advantage of this method is the yield of a

large number of single layer nanosheets.^[16,99,119] However, the method requires sensitive experimental procedures and mostly ends up with an incomplete recovery of the oxidation state.^[23,33,113,119] Consequently, the exfoliated material has significantly modified properties compared to the nanosheets in their pristine oxidation state.^[23,33,113]

1.2.3 Ion exchange exfoliation

The ion exchange exfoliation routes are usually applied to charged (anionic or cationic) layered materials.^[3,16,17] Soft chemical methods are used to replace the interlayer ions by other ions, usually larger ones, which enable the material to undergo swelling in an appropriate solvent.^[16,17,114] Due to the swelling, the attractive, mainly electrostatic, forces between the layers are reduced and a small mechanical force, such as shaking or stirring is sufficient to delaminate the material into single nanosheets.^[16,17,116] For the delamination of cationic layered materials, mainly resulting in cationic hydroxide nanosheets, the reader is referred to recent review articles.^[16,17,114] For the delamination of anionic layered materials the main exfoliation route – the proton exchange route – used in this thesis is described in the following.^[16,17,116]

The proton-based ion exchange exfoliation route can be considered as a two-step process. In the first step the anionic layered material, which is obtained by solid state synthesis, is cation-proton exchanged by repetitive treatment with Brønsted acids, usually 1-8 M HCl or HNO₃.^[16,17] In the second step, an acid-base reaction takes place between the acidic (protonated) material and the basic alkylammonium solution (for instance, containing TBA⁺ OH⁻).^[16,17,117,124] To maintain charge neutrality, a large number of alkylammonium ions move between the layers from the external solution reservoir.^[16,17,117,124] This movement results in a high osmotic pressure leading to a huge and fast inflow of water molecules in between the layers, causing a high degree of swelling.^[115,117,124,125] Therefore, the overall swelling process is highly dependent on the alkylammonium concentration, but colligative in nature.^[16,117] The stability of the swollen phase is strongly influenced by the nature of the alkylammonium ions, *e.g.* bulky and less polar cations like TBA⁺ lead to faster exfoliation compared to TMA⁺ (tetramethylammonium) and DMAEH⁺ (protonated 2-(dimethylamino)ethanol).^[16,116,117] Moreover, the nanosheets size can be influenced by the exfoliation method and the applied alkylammonium ions (such as TBA⁺ or TMA⁺).^[16,116] Methods applying weaker forces result in larger nanosheets, whereas the harsher methods result in smaller sheets.^[16,116] The advantage of the ion exchange exfoliation route is the very high yield in single layer nanosheets.^[16] However, the time needed for exfoliation is longer compared to the liquid-phase exfoliation.^[23] Moreover, the applied alkylammonium salts during the exfoliation procedure can also alter the properties of the nanosheets in a desired or an undesired way.^[23]

Table 1. Comparison of the solvent-based nanosheet exfoliation techniques. All techniques have their own set of distinct advantages and disadvantages, and hence, are complementary in their current state.

	Liquid-phase exfoliation	Redox-mediated exfoliation	Ion exchange exfoliation
Applicability	very broad; layered van der Waals and ionic layered materials	broad; layered van der Waals materials	broad; layered ionic layered materials
Single layer nanosheet yield	moderate to low requires special techniques for significant enrichment	high yield	very high yield
Retention of the pristine properties of the nanosheet	high (if no surfactant is used)	moderate to low; requires post treatment to recover properties of the nanosheets; often only partial recovery of the properties	moderate; presence of counter ions influence the nanosheet properties in either a desired or an undesired way
Processing time / Experimental procedure	fast, from minutes to few days / scalable, simple in case one has an appropriate solvent	depends on method (from one day to several days) / delicate	moderate, depends on method (usually takes several days due to prior exchange steps) / simple to medium difficult
Lateral size of the nanosheet	medium to small (usually below: 1 μm x 1 μm)	depends on method: usually rather large (above: 500 nm x 500 nm)	large (usually above: 1 μm x 1 μm)
Scalability	very high	moderate to low	moderate

1.3 Assembly of nanosheets: resolving the contradiction of scalability and control

The nanosheets, which are obtained by several methods, can be assembled into more complex structures. Hereby, the ultimate goal of nanosheet assembly techniques is to place the nanosheets precisely and reproducibly in a scalable way at a desirable location to achieve specific functionalities.^[15,17,62,74,126] Current solvent-based nanosheet assembly methods range from drop-casting or flocculation, which are scalable, but have poor control over the positioning and alignment, to Langmuir-Blodgett (LB) and electrostatic layer-by-layer (eLbL) assembly methods, which allow a high degree of control, but are, in their current stage, limited in their scalability (see Figure 1.4 and 1.5).^[15-17,23,72,74,127,128]

The high degree of control of LB and eLbL is due to their single layer thickness increase per cycle, allowing precise control at the molecular level in the thickness and composition of the thin films.^[15,17,127] LB offers the higher level of control due to the monolayer compression step,^[15] whereas eLbL is the faster one of the two delicate processing techniques.^[62,129,130] Further methods, such as spin-coating and printing techniques, provide a high degree of scalability as they are compatible with current technology, while offering, in their current state, a moderate level of control.^[23,62,64,74]

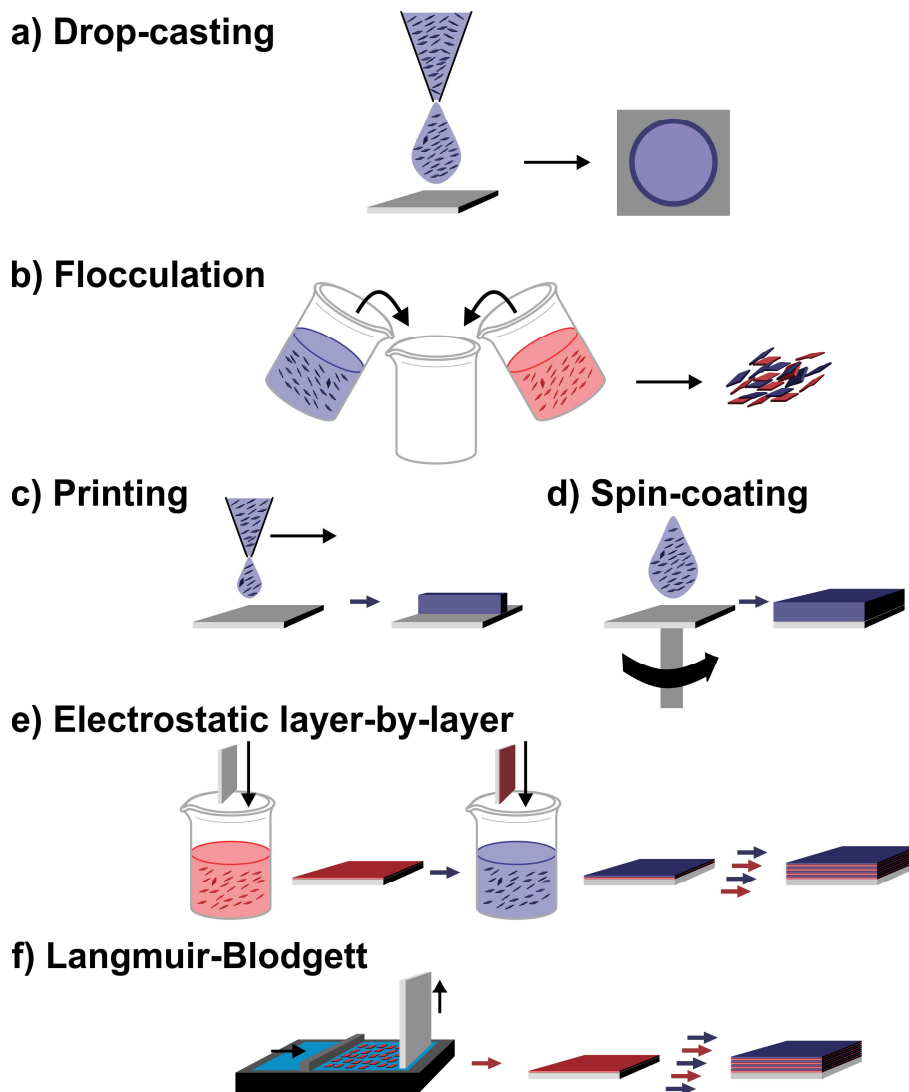


Figure 1.4. From low-control to high-control nanosheet assembly methods. a) Drop-casting of colloidal nanosheets on a substrate. This results in the fast formation of a film with limited homogeneity; especially at the edges a much thicker film is obtained due to the “coffee ring effect”.^[23,74] b) During the flocculation process charged nanosheets are either restacked with oppositely charged nanosheets, depicted here, or electrolytes.^[17,72,127] The rapid precipitation process results in a restacked compound, which has a poorly defined interlayer registry and disorganized microtexture.^[17,72,127] c) Printing of nanosheets with diverse methods is possible from ink jet printing to gravure printing. Crucial factors for the printing process include the viscosity, the surface tension and concentration of the nanosheet ink.^[23,74] d) In the spin-coating process a droplet of the colloidal nanosheet suspension is placed on a substrate, which is then accelerated to annular velocities.^[23,62,74] This results in the formation of rather homogenous thin film, but with a thickness usually in the range of several nanometers.^[17,23,62,74] e) The eLbL assembly method is carried out by sequential immersion of a substrate into oppositely charged nanosheet solutions, or in a nanosheet solution and a polyelectrolyte solution.^[15-17,72,127] After placing the substrate into one nanosheet dispersion it is intensively washed and sometimes also ultrasonicated to remove excess of nanosheets and to achieve a more homogenous alignment of the nanosheets.^[15,72,74] The eLbL method has the advantage of being a charge limiting process.^[72] f) In the LB assembly a monolayer of nanosheets is formed on the liquid-air interface in a Langmuir trough, compressed and subsequently transferred to a substrate by dip-coating.^[15-17,72,127] The advantage of the technique is the achieved high lateral packing density of the nanosheet layer.^[16,72,74] With repetition of the process even a multilayer of nanosheets with the same charge can be built up.^[15,72,127,131]

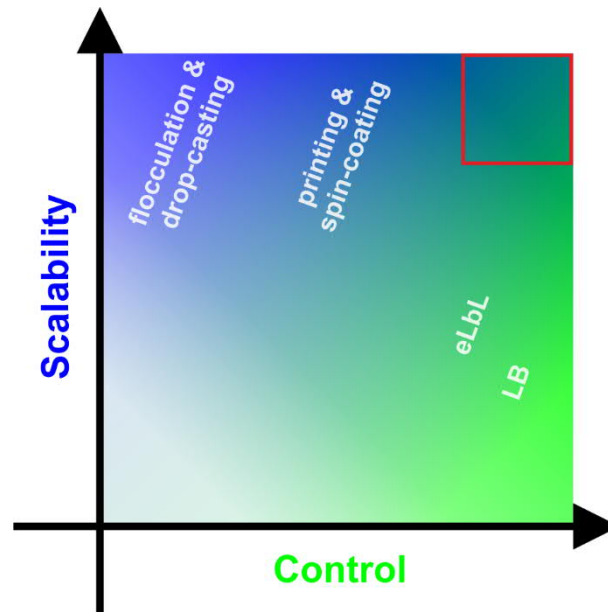


Figure 1.5. Schematic scalability against control diagram comparing different positioning techniques. While certain methods have better control, other methods exhibit better scalability. Framed with a red square is the ideal assembling area, in which both single nanosheet control and good scalability are achieved.

Figure 1.5 indicates that all the methods are limited when it comes to delivering both high precision (control) and high scalability in the deposition of liquid medium processed nanosheets.^[43] Therefore, current research efforts are directed to bridge this gap,^[126] for instance, by improving the control of the feature sizes and alignment with scalable printing techniques,^[23,64,65,93] the thickness control in spin-coating techniques,^[62,129,132] or by improving the speed of processing in LB derived thin films.^[133,134]

1.4 Tailoring of the nanosheets properties

Although nanosheets have, in their pristine form, many interesting and outstanding properties, it is highly desirable to tailor these properties in a rational manner, which enables the specific tailoring of their properties to certain applications.^[15-17,23,60,65,94] Currently, several methods are applied to tune the properties of nanosheets (see Figure 1.6). The most promising methods are covalent functionalization,^[34,38,67,68,135-143] intercalation and ion exchange,^[66,144-149] morphology (size control and thickness control) of the nanosheets,^[60,65,150-152] substitution^[15,17,153-158] and decoration (see Figure 1.6).^[159-162] It is important to note that each of these modification possibilities offers a further degree of freedom. Therefore, the modification possibilities can be even combined to achieve a higher degree of control. Current examples for the different modification possibilities are control of magnetic, dielectric and optical properties by substitution,^[155-158] ion conduction, catalytic and optoelectronic properties by morphology changes,^[60,65,150-152] as well as sensing and catalytic properties by decoration with NPs.^[159,160,162-166] For covalent modification and intercalation as well as ion exchange methods more detailed examples are given below.

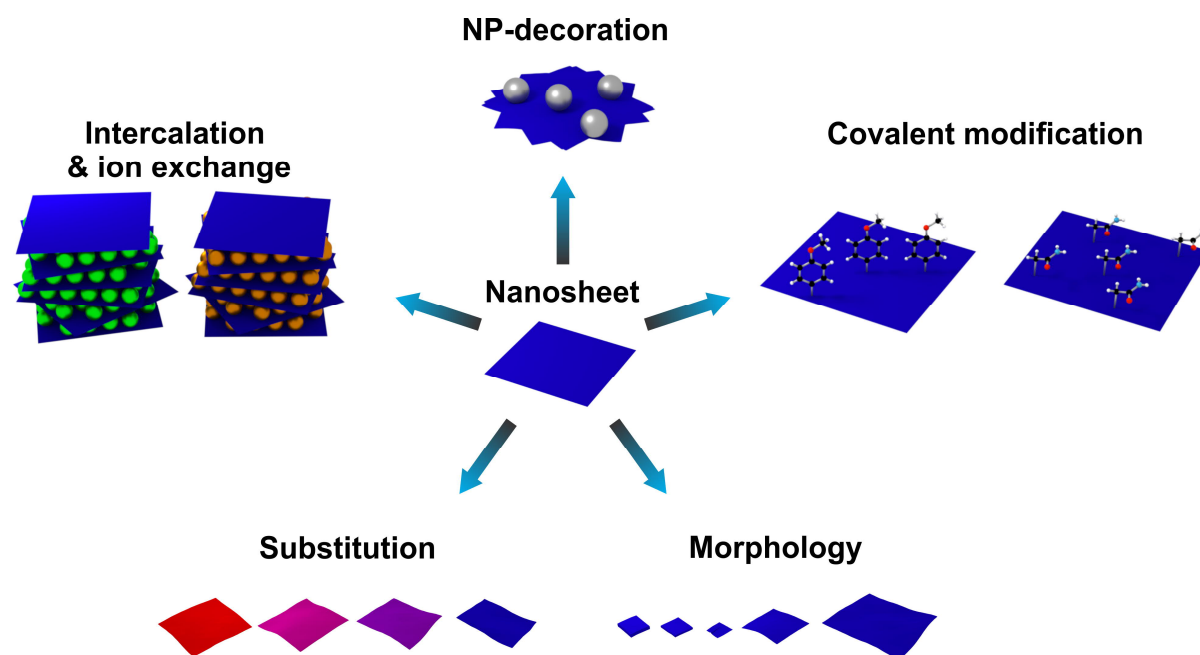


Figure 1.6. Tailoring of the nanosheet properties by various methods with a representative example given in brackets in italics. Starting from top and moving clockwise: NP decoration (*decoration of black phosphorus nanosheets with Pt NPs, utilized in sensors to increase the sensitivity toward H_2 and the stability*);^[159] covalent modification (*covalent modification of MoS_2 with methyl iodide, iodoacetamide and 4-methoxybenzenediazonium to tune the optoelectronic properties*);^[141] morphology thickness and size (*size selection to tune the photoluminescence properties of Ti_3C_2 sheets*);^[152] substitution (*substitution with Sr and Ta to tune the dielectric properties of $HfCa_2Nb_3O_{10}$ nanosheets*);^[155] and intercalation and ion exchange (*intercalation of a nanobattery setup with Li to tune the optical and electrical properties of MoS_2*).^[148] The orange and green spheres in the intercalation step can be ions as well as uncharged molecules.

1.4.1 Covalent modification

Covalent modification is among the most promising methods for tailoring nanosheet properties.^[34,38,68,94,138-141] Organic and inorganic chemical reactions provide the researcher with an almost unlimited toolbox to anchor desired molecules on the surface of nanosheets by covalent bond formation. By the judicious choice of the covalently linked molecule, size and functional groups, many properties such as electronic and optical properties, chemical stability and solubility can be rationally tuned.^[34,38,67,68,94,135,137-143,167] The rational and tunable control of these properties can be advantageous for several applications including transistors^[135,140-142] and sensors,^[67,137] or for the processing of nanosheets.^[67,68] A cutting-edge research field is the covalent functionalization of TMDs as well as Xenes. In these compounds modification possibilities range from the reactions with thiols,^[67,135,137] over electrophiles^[38,138-142] toward more exotic functionalization by coordination with metal salts.^[68,94] The reaction with thiols is thought to happen at S vacancies in transition metal disulfide nanosheets, resulting in the formation of covalently bonded molecules and hydrogen.^[67,168] This modification route was used to alter the electronic and sensing properties as well as the solubility.^[67,137] Along similar lines, the reaction of electrophiles, such as diazonium salts and alkyl iodides, with nucleophilic nanosheets, which are obtained for instance by redox-mediated exfoliation, was used to increase their chemical stability and to tailor their optical and electronic properties.^[38,138-142] Besides functionalization of TMDs and Xenes, covalent modification of oxide nanosheets is also possible and was realized for instance by Wada and co-workers.^[130,169] They used silane coupling agents such as trimethoxysilanes to introduce thiole and ene functional groups on the nanosheets.^[130,169] These functional groups can be utilized in a thiol-ene click reaction to covalently cross-link different oxide nanosheet layers to achieve an alternate stacking with a controlled stacking distance.^[130,169] Therefore, covalent modification cannot only be used for modification of nanosheet properties, but also for their targeted assembly.

1.4.2 Ion exchange and intercalation

Ion exchange and intercalation have proven to be highly efficient methods for tuning the properties of layered bulk materials.^[170,171] However, only in the last couple of years the tailoring of properties by intercalation or ion exchange in either restacked nanosheets or multilayer nanosheets gained substantial research interest.^[66] Recent work in the field focuses on tailoring the thermal,^[146] mechanical,^[172] optical,^[147,148,173] plasmonic,^[145] magnetic,^[123,174] electrochemical,^[82,149,175] electronic^[144,147,148,173,176] and superconducting^[144] properties by intercalating various species. In addition, the real-time *in situ* studies of these intercalation processes gained tremendous interest.^[144,146-148,176] Current strategies either are based on electrochemically driven intercalation,^[146-148,176] e.g. by using a nanobattery setup and reversible intercalation/deintercalation of alkali metals into multilayer nanosheets paired with *in situ* monitoring of the properties, or are based on the soft chemical ion exchange or liquid and vapor intercalation,^[145,149,172,173,175,177] which are often applied for the

modification of restacked nanosheets, or to multilayer nanosheets.^[66] Comparing the two intercalation techniques, chemical intercalation strategies provide a broad range of applicable host and guest species with limited level of intercalation control, whereas electrochemical methods provide a high level of intercalation control, but are limited to rather few guests and host materials.^[66] Both intercalation methods are highly suitable to tailor or even to impart novel properties to nanosheet-based structures.

1.5 The layered metal phosphates $A_nM_nP_2O_{5+3n}$ and the Dion-Jacobson phase $ACa_2Nb_3O_{10}$ with $M = Sb$ ($n = 1, 3$), Ta ($n = 1$) and $A = K$ and H

Having discussed in the previous subchapters general nanosheet-based aspects, now the material used in this thesis are described in more detail. Therefore, in the following a summary of the literature on the layered metal phosphates $A_nM_nP_2O_{5+3n}$ and the Dion-Jacobson (DJ) phase $ACa_2Nb_3O_{10}$ with $M = Sb$ ($n = 1, 3$), Ta ($n = 1$) and $A = K$ and H , as well as their nanosheets is presented.

1.5.1 The layered metal phosphates from past to present

Beginning with the discovery of the ion exchange properties of the metal phosphate salts in the 1950s a great amount of research was directed to understand the origin of these properties.^[178,179] In 1964 Clearfield and Stynes provided a layered structural model of α -zirconium phosphate (α -Zr(HPO₄)₂).^[180] This model gave a profound explanation for the ion exchange properties and chemical reactivity in these materials. By comparing with α -Zr(HPO₄)₂, the same connectivity was suggested for several other layered metal (V and IV) phosphates by Winkler and Thilo.^[181] Moreover, the same authors observed that these compounds are easily hydrated and ion exchanged. Further research on layered metal (V) phosphates unambiguously clarified their structure.^[182] The properties and applications of these phosphates were mainly investigated by Piffard and co-workers.^[182-193] The first exfoliation of α -Zr(HPO₄)₂ into individual layers was achieved by Alberti.^[194] Delamination of other metal phosphates like HSbP₂O₈ and H₃Sb₃P₂O₁₄ followed subsequently.^[195,196] Recent research interest in the field of layered phosphates includes their covalent modification, utilization of their ion mobility, ion exchange as well as conductivity, and the assembly of the nanosheets by various methods.

1.5.1.1 The phosphoantimonates and phosphotantalate $K_nM_nP_2O_{5+3n}$ with $M = Sb$ ($n = 1, 3$), Ta ($n = 1$)

The layered potassium phosphoantimonates ($KM_nP_2O_{5+3n}$) and tantalate ($KTaP_2O_8$) can be obtained by a solid state reaction of $NH_4H_2PO_4$, KNO_3 and Sb_2O_3 or Ta_2O_5 , respectively.^[182,184,191,193] $K_3Sb_3P_2O_{14} \cdot 1.3H_2O$, as $K_3Sb_3P_2O_{14}$ easily hydrates under ambient conditions, crystallizes in the space group $R\bar{3}m$ (166),^[193] $KSbP_2O_8$ in $R\bar{3}$ (148)^[182] and $KTaP_2O_8$ in $C2/m$ (12).^[191] Despite their different space groups, all of the structures consist of potassium ions located in the interlayer space of 2D layers of $Sb_3P_2O_{14}^{3-}$ or $MP_2O_8^-$ ($M = Ta, Sb$), which are composed of corner sharing MO_6 octahedra and PO_4 tetrahedra (see Figure 1.7).^[182,184,193]

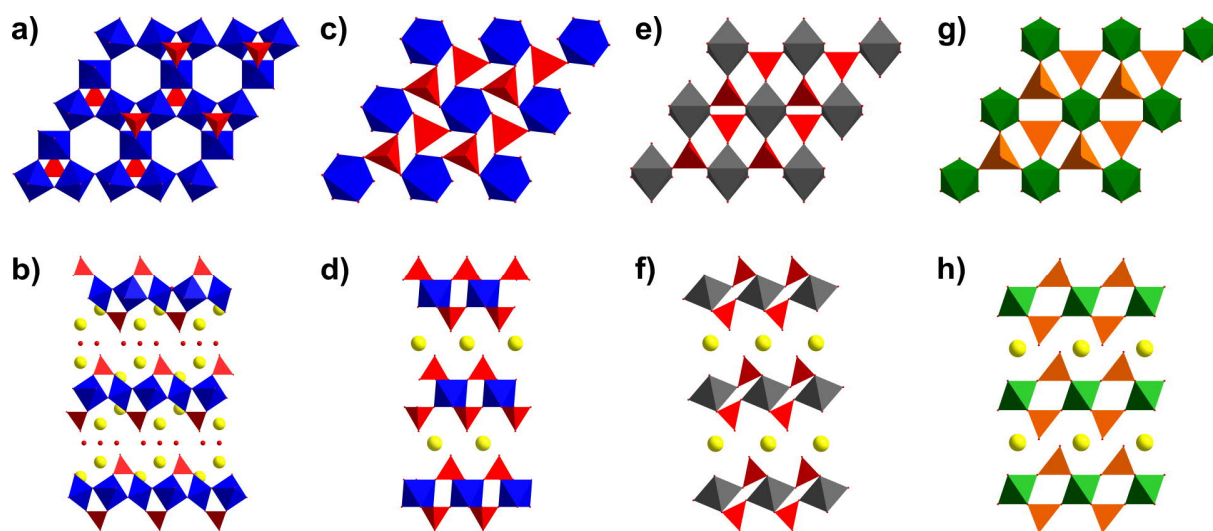


Figure 1.7. Structures of the potassium phosphatoantimonates ($K_nSb_nP_2O_{5+3n}$ ($n = 1, 3$)), potassium phosphatotantalate ($KTaP_2O_8$), as well as potassium aluminomolybdate ($KAl(MoO_4)_2$) for comparison. In the top row the structures are viewed along the c -axis and in the bottom row along the b -axis. For simplicity only one layer is depicted in the top row (view along c -axis) without any interlayer species. a), b) $K_3Sb_3P_2O_{14} \cdot 1.3 H_2O$, c), d) $KSbP_2O_8$, e), f) $KTaP_2O_8$ and g), h) $KAl(MoO_4)_2$. PO_4 tetrahedra in red, SbO_6 octahedra in blue, TaO_6 octahedra in dark grey, AlO_6 octahedra in green, MoO_4 tetrahedra in orange and the interlayer species K in yellow and O in red. For the interlayer water molecules in $K_3Sb_3P_2O_{14} \cdot 1.3H_2O$ only the oxygen position is shown (see b)).

However, the intralayer connectivities of the MO_6 octahedra and PO_4 tetrahedra in $Sb_3P_2O_{14}^{3-}$ and $MP_2O_8^-$ ($M = Sb, Ta$) layers are different (Figure 1.7a, c). In a $Sb_3P_2O_{14}^{3-}$ layer, each SbO_6 octahedron is corner-linked to four adjacent SbO_6 octahedra building up layers similar to those composed of WO_6 octahedra in microporous hexagonal tungsten bronze.^[184,197,198] In addition, the two remaining vertices of the SbO_6 octahedra are corner-linked to PO_4 tetrahedra in a way that a PO_4 tetrahedron is linked to three different SbO_6 octahedra and the unconnected corner of the tetrahedron is pointing toward the interlayer space (see Figure 1.7a).^[184,198] In contrast, the 2D layers of $MP_2O_8^-$ ($M = Ta$ and Sb) exhibit the same intralayer connectivity as in the well-known $ZrP_2O_8^{2-}$ layers in α - $Zr(HPO_4)_2$ (Figure 1.7c, e).^[182,191] In the $MP_2O_8^-$ layers every MO_6 octahedron is corner linked to six PO_4 tetrahedra and every PO_4 tetrahedron is connected to three MO_6 octahedra.^[191] The unconnected vertex of the PO_4 tetrahedron is pointing toward the interlayer space.^[182,191] Although the $TaP_2O_8^-$ and the $SbP_2O_8^-$ have similar intralayer connectivity, their crystal structures are distinct from each other due to distortions.^[191] Both distortions of the $MP_2O_8^-$ ($M = Sb, Ta$) layers can be described through a rotation of the PO_4 tetrahedra compared to the MoO_4 tetrahedra in the higher symmetric layers of $Al(MoO_4)_2^-$ in $KAl(MoO_4)_2$ ($P\bar{3}m1$, 164, Figure 1.7g, h).^[191] For $SbP_2O_8^-$ and $TaP_2O_8^-$ the PO_4 tetrahedra are rotated around an axis perpendicular or parallel to the layers, respectively (see Figure 1.7c-h). Besides X-ray analysis, other data such as nuclear magnetic resonance (NMR), infrared (IR), Raman spectroscopy are available for the phosphatoantimonates.^[185,199-201]

1.5.1.2 The phosphoantimonic and phosphotantallic acids $H_nM_nP_2O_{5+3n}$ with $M = Sb$ ($n = 1, 3$), Ta ($n = 1$)

As the potassium ions in the interlayer space of the phosphoantimonates and tantalates are quite mobile,^[202] they can readily be exchanged with protons by treatment with nitric acid.^[189,190,192] The resulting phosphoantimonic acids, $H_nSb_nP_2O_{5+3n}$, and tantallic acid, $HTaP_2O_8$ (also referred to as ‘antimony phosphates and tantalum phosphate’ in analogy to α -zirconium phosphate in the literature), which have the same intralayer connectivity compared to their potassium analogue, have been characterized by various methods, including NMR, TEM, IR, differential thermal analysis (DTA), thermogravimetric analysis (TGA) and Raman spectroscopy.^[189,190,192,203-205] All of the acids showed good ion exchange properties and a proton conductivity that depends on their hydration state.^[186,188-190,192,197,198,203,206,207] The humidity dependent swelling and proton conductivity of the phosphoantimonic acids were studied in detail by Piffard and co-workers.^[188] They realized that $H_3Sb_3P_2O_{14}$ is rather a ‘bulk ionic’ (lattice hydrate) conductor, whereas the ionic conductivity in $HSbP_2O_8$ is rather determined by the water sorbed between the grain boundaries (particle hydrate).^[188,208,209] Both of them are good proton conductors at high relative humidities (around 1 mS cm^{-1} and 20 mS cm^{-1} for $HSbP_2O_8$ and $H_3Sb_3P_2O_{14}$, respectively).^[188] Although further investigations have been carried out,^[205] the exact mechanism of the proton conduction in these phosphoantimonic acids is still elusive due to the complex situation, *e.g.* multiple proton species contributing to the conductivity, strongly anisotropic material, and due to the fact that the exact crystal structure of the various hydrates could not be determined due to disorder as well as the humidity dependent and temperature dependent interlayer spacing.

Nevertheless, due to their ion exchange properties and highly humidity dependent proton conductivities, some potential applications have been experimentally demonstrated with the phosphoantimonic acids. In these applications, they are applied as component in composite membranes for fuel cells,^[187,210-212] for the removal of radioactive ions (*e.g.* Cs, Am, Sr)^[186,197,198] or in electrochemical sensors working at elevated temperatures.^[213]

1.5.1.3 Delamination of the phosphoantimonic and phosphotantallic acids $H_nM_nP_2O_{5+3n}$ with $M = Sb$ ($n = 1, 3$), Ta ($n = 1$)

Initial observations by Piffard and co-workers indicated that the phosphoantimonic acids are able to swell and thereby, peptize in water.^[188,189] However, prove for the first delamination into single layers was provided later by Batail and co-workers by small angle X-ray scattering.^[195,196] They delaminated the phosphoantimonic acids by swelling them in a dialysis membrane for several days and investigated the liquid crystalline properties of the colloidal suspensions containing single layer nanosheets.^[195,196] They also found that addition of bulky organic surfactants like TBAOH increased the stability against flocculation of the nanosheets for a large pH-range,^[195] which subsequently led to TBAOH assisted exfoliation of $HSbP_2O_8$.^[214] It is to be noted that the exfoliation of a layered solid

acid in absence of any surfactant is a rare phenomenon. However, a more detailed characterization including TEM and AFM, of the single layer nanosheets was missing and was provided later in my master thesis for the first time.^[215] For HTaP₂O₈, the first exfoliation with TBAOH was reported in my master thesis as well.^[215] One of the primary objectives of this thesis was to investigate the delaminated phosphoantimonic and phosphotantallic acid nanosheets for practical applications.

1.5.2 From layered perovskite to the Dion-Jacobson phase KCa₂Nb₃O₁₀

In the last decades, low temperature topotactic reactions in layered perovskites for tuning their properties gained significant interest.^[216,217] The topotactic reactions applied to layered perovskites are enormous and range from grafting over intercalation and ion exchange to exfoliation.^[216,217] Among the most well-known families of layered perovskites are the DJ phases A'[A_{z-1}B_zO_{3z+1}], the Ruddlesden-Popper phases A'₂[A_{z-1}B_zO_{3z+1}] and the Aurivillius phases [Bi₂O₂][A_{z-1}B_zO_{3z+1}] with usually A' belonging to the group of alkali metals, A to alkaline earth metals, B to transition metals.^[216-218] Hereby, [A_{z-1}B_zO_{3z+1}] is the perovskite layer and z the number of corner-sharing BO₆ octahedra determining the thickness of the layers.^[218,219] In the 1980s, the latest addition to the family of layered perovskites were the DJ phases resulting from the pioneering work carried out by Dion and Jacobson.^[219-221] Dion and Tournoux were the first to synthesize KCa₂Nb₃O₁₀, which is among the most well-known examples of a DJ phase, if not the most.^[220] Soon after, ion exchange and intercalation studies as well as delamination of this compound followed.^[219,221-223] Due to their easy accessibility, handling, stability and remarkable properties calcium niobate nanosheets got into the focus of several studies carried out, amongst others, by the group of Sasaki,^[62,224-227] Mallouk^[228-231] and Osterloh.^[232-235]

1.5.2.1 The Dion-Jacobson phase KCa₂Nb₃O₁₀ and its diverse properties

KCa₂Nb₃O₁₀ can be obtained by a solid-state synthesis reaction of K₂CO₃, Nb₂O₅ and CaCO₃.^[219,236] The compound crystallizes in the space-group *P2₁/m* (11) as determined by neutron powder diffraction.^[236,237] KCa₂Nb₃O₁₀ consists of perovskite layers [A_{z-1}B_zO_{3z+1}]⁻ with A = Ca, B = Nb and z = 3 with A' = K⁺ sitting in the interlayer space (see also Figure 1.8).^[236] The cubic perovskite structure ABX₃ comprises corner sharing BX₆ octahedra, which form a three-dimensional (3D) structure similar to the structure of ReO₃ (Figure 1.8a, b).^[217] The remaining A-cation is located in the center of eight BX₆ octahedra, hence having a coordination number of twelve (cuboctahedron).^[217] An alternate description is that AX₃ forms a face centered cubic lattice and the B-cations are occupying one quarter of the octahedral voids.^[217] Usually X is oxygen, A is a large s-, d-, or f-block cation, and B is a small transition metal cation.^[216]

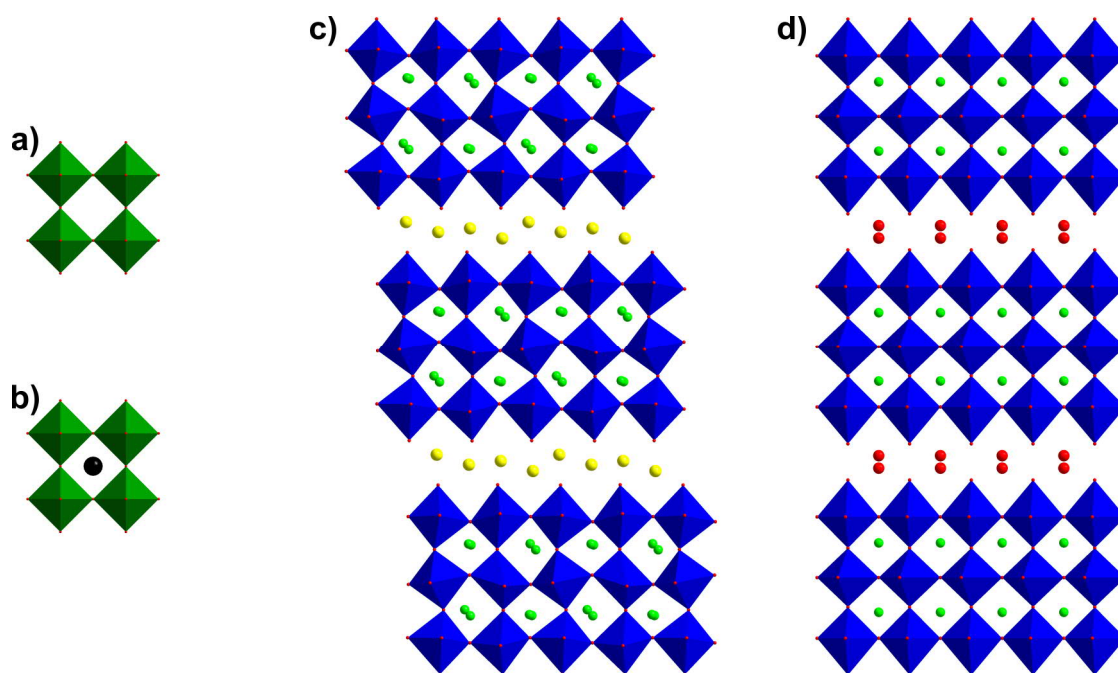


Figure 1.8. From the ReO_3 structure type to the layered perovskites $\text{KCa}_2\text{Nb}_3\text{O}_{10}$ and $\text{HCa}_2\text{Nb}_3\text{O}_{10}$. a) ReO_3 . b) Idealized cubic perovskite, ABX_3 . c) $\text{KCa}_2\text{Nb}_3\text{O}_{10}$ and d) $\text{HCa}_2\text{Nb}_3\text{O}_{10} \cdot 0.5 \text{H}_2\text{O}$; the O positions in the interlayer space are only occupied by one quarter. For a) ReO_6 octahedra in green, b) BX_6 octahedra in green and the twelve fold coordinated A in black, c) and d) NbO_6 octahedra in blue, Ca in light green, oxygen in red, K in yellow.

Similar to the cubic perovskites, layered perovskites are also often distorted by tilting BO_6 octahedra, which can have tremendous impact on the properties.^[238] For instance, tilting of the NbO_6 octahedra confers many interesting electronic and dielectric properties on $\text{KCa}_2\text{Nb}_3\text{O}_{10}$. The band gap (direct 3.1-3.2 eV) and electronic structure were investigated by EELS and DFT calculations.^[237] In other studies, doping Eu or La at the Ca site turned potassium calcium niobate luminescent.^[239] Interesting dielectric properties were also discovered in $\text{KCa}_2\text{Na}_{z-3}\text{Nb}_z\text{O}_{3z+1}$ ($z = 3-6$).^[240] It was observed that with increasing slab thickness (z) the polarizability increased, which led to improved dielectric constants. Moreover, it was found upon Li intercalation that the materials turned superconducting.^[241] $\text{KCa}_2\text{Nb}_3\text{O}_{10}$ also showed moderate performances as photocatalysts.^[242] Due to the manifold properties and, hence, possible applications, the material holds great potential for improvement upon ion exchange and subsequent delamination.

1.5.2.2 The proton exchanged $\text{HCa}_2\text{Nb}_3\text{O}_{10}$ - access to the interlayer space

$\text{KCa}_2\text{Nb}_3\text{O}_{10}$ can readily be ion exchanged with Brønsted acids yielding the solid acid $\text{HCa}_2\text{Nb}_3\text{O}_{10}$,^[219] which contains 1.5 H_2O under ambient conditions. From X-ray powder refinement it is reported that the dried compound $\text{HCa}_2\text{Nb}_3\text{O}_{10} \cdot 0.5 \text{H}_2\text{O}$ crystallizes in the space group $P4/mbm$ (127).^[243] The proton exchanged form exhibited a higher photocatalytic activity compared to its potassium analogue, which is attributed to the better accessible interlayer space.^[242] Moreover, the dielectric, ion exchange and intercalation properties as well as the ionic conductivity of the solid acid were investigated.^{[219,221-}

^{223,244,245]} Initial work focused on intercalation of primary alkylamines with various alkyl chain lengths and the back ion exchange with alkali metal ions.^[221,222] The knowledge about primary alkylamine intercalation was later on applied by Gopalakrishnan and co-workers to obtain information regarding the acidity and structure of substituted $\text{HCa}_2\text{Nb}_{3-x}\text{M}_x\text{O}_{10-x}$ ($\text{M} = \text{Al}, \text{Fe}$) and $\text{HCa}_{2-x}\text{La}_x\text{Nb}_{3-x}\text{Ti}_x\text{O}_{10}$ compounds.^[246,247] Note that tuning of the interlayer environment can have significant influence on various properties of the layered materials. For example, the primary alkylamine intercalation was found to have a profound influence on the ferroelectric properties of closely related $\text{HSr}_2\text{Nb}_3\text{O}_{10}$.^[248] Besides these modifications, other modification possibilities of the interlayer space in $\text{HCa}_2\text{Nb}_3\text{O}_{10}$ were also investigated. For instance, grafting of *n*-alcohols on the Nb-O vertices facing toward the interlayer space, resulting in the formation of alkoxides, was achieved at elevated temperatures in autoclaves.^[249] Moreover, delamination was accomplished by incorporating bulky surfactants, which contain a primary amine head group, and subsequently applying ultrasonication.^[223]

1.5.2.3 The $\text{Ca}_2\text{Nb}_3\text{O}_{10}^-$ nanosheets - a lego like building block with interesting properties

In 1990 starting from their first synthesis by Treacy *et al.*, calcium niobate nanosheets were developed due to their easy handling, stability and accessibility into a diverse building block with manifold possible applications.^[223] Currently, the by far most applied exfoliation route for $\text{HCa}_2\text{Nb}_3\text{O}_{10}$ belongs to the ion exchange exfoliation route using TBAOH as described in subchapter 1.2.3. To obtain a more profound knowledge of the nanosheets, initial and subsequent studies focused on characterizing the material in more detail.^[225,229,231,250,251] At the same time, due to their stability and easy handling, the calcium niobate nanosheets were also developed into a role model building block for the assembly of charged nanosheets into diverse structures.^[228,229,252-254] The applied assembly methods included, amongst others, mainly flocculation,^[224,230,243,252,255] spin-coating,^[62,256] LB^[80,81,131,154,155,226,227,257,258] or eLbL^[228,229,253,254] (see section 1.3). Hereby, some of the assembly methods were carried out due to fundamental interest or to improve the technique, while the others were applied to yield desired properties or geometries for certain applications. To provide an overview over the diversity, some examples are given. Flocculation was applied to obtain, under basic conditions, a nanotube morphology^[252] or to make intercalated materials with improved properties for catalysis.^[230] Assemblies with eLbL were carried out to provide proof of concepts experiments for novel artificial structures.^[228,254] Spin-coating with $\text{Ca}_2\text{Nb}_3\text{O}_{10}^-$ was used to improve the technique down to monolayer thicknesses,^[62] and LB to obtain densely packed mono- and multilayer heterostructures suitable for dielectric applications^[15] or as seed layers for oriented crystal growth.^[257] Notably, all of these assembly methods focused around the precise control of the thickness, whereas control of the lateral dimensions of the structures, apart from traditional lithography processes with photoresists, is still lacking. Currently the main research focus lies on the understanding and improvement of photocatalytic activities^[232-235,259-261] and in the application in nanoelectronics as a dielectric

component.^[15,218,262-264] Therefore, it would be favorable to develop scalable techniques for obtaining lateral structures made of the dielectric materials, *e.g.* by utilizing their photocatalytic activity.

1.6 Application and devices

The materials described in the previous section have promising properties, *e.g.* humidity dependent swelling and proton conductivity of layered bulk phosphates and the ultrahigh dielectric constants of $\text{HCa}_2\text{Nb}_3\text{O}_{10}$ nanosheets. Therefore, it is of high interest to utilize these properties in applications. Currently, considering also this work, the most promising applications of these compounds are in the field of vapor sensing and in electrical devices requiring high-*k* materials such as capacitors or transistors. Therefore, more detailed theoretical background information is given on vapor sensors and high-*k* dielectrics, with a larger focus on sensors as this is the application investigated in this thesis.

1.6.1 Chemical sensors

Chemical sensors are devices that convert an input signal caused by a chemical stimulus into a useful and readable output signal.^[265-267] Therefore, sensors fulfill two main functions, namely stimuli recognition and signal conversion (transduction).^[266,267] The component fulfilling the first function is called receptor,^[266,267] *e.g.* a compound that offers binding sites for molecules, and the second function is called the transducer, which is able to convert the change introduced in the receptor into a readable output signal.^[267] An example is the presence of a fluorescent molecule in close proximity to the receptor component. Sometimes there is no clear differentiation between a receptor and transducer component, *e.g.* a fluorescent molecule offering binding sites to molecules can fulfill both functions at once. The same applies for a compound, which changes its conductivity upon analyte sorption.^[267] Sensors are commonly classified by their method of transduction,^[265,266] which also determines their readout method. The main classes of chemical sensors are electrical & electrochemical, thermometric and optical & photonic sensors.^[265] Besides the method of transduction the sensors can also be grouped by the function they fulfill, *e.g.* liquid sensors, or vapors sensors.

1.6.1.1 Types of sensors investigated in this thesis and their sensing mechanism

Among the group of chemical sensors, vapor sensors are of particular interest due to their relevance in several important applications in various fields, including medical diagnostics, environmental monitoring, food control and industrial production.^[70,268-270] Nanosheets are ideal building blocks for vapor sensing devices due to their small size, high surface area, modification possibility and swelling capability.^[70,268-270] The two types of vapor sensors investigated in this thesis are interference-based Fabry-Pérot thin film sensors belonging to the group of photonic sensors, and impedance-based sensors belonging to the group of electrochemical sensors. In the following, a description of the two types of sensor and their working principles are given.

Besides achieving coloration through an inherently colorful material, for instance a pigment, coloration can also be obtained from assemblies of inherently colorless materials through reflection and/or diffraction of light.^[271-275] As the coloration arises from the arrangement of the materials, this phenomenon is referred to as “structural color”.^[271,272,274,276] Structures achieving structural coloration range from Fabry-Pérot thin film devices, to 1D, 2D and 3D periodic assemblies of dielectric materials, termed PCs.^[271-273] For Fabry-Pérot thin film devices and 1D PCs, 1D periodic multilayer arrangements also called Bragg stacks, the condition for constructive interference is illustrated in Figure 1.9.^[271,274] If this condition is fulfilled for wavelengths λ in the visible or close to the visible range, color arises.

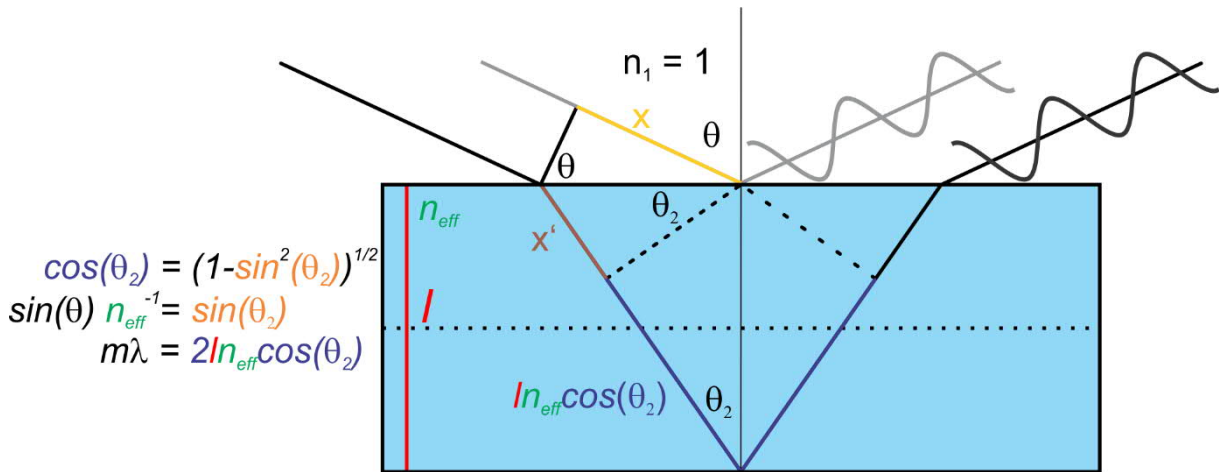


Figure 1.9. Illustrating the condition for a constructive interference in a thin film or in a simplified bilayer of a BS (bilayer separation indicated by dotted line). On the left some additional considerations for deriving the condition for constructive interference based on the dependence on the incident angle θ are depicted. By combining the three conditions on the left and noticing that the optical thickness of X and X' are equal due to Snell's law, one can obtain the Equation 1.1 for constructive interference depending on the illumination angle (θ).

As seen from Figure 1.9, constructive interference is given by a combination of Bragg's and Snell's law:^[271,274,277]

$$m\lambda = 2l \sqrt{n_{eff}^2 - \sin^2(\theta)} \quad (\text{Equation 1.1})$$

Hereby m is the spectral order (integer value), λ are the wavelengths for which constructive interference occurs, n_{eff} is the effective RI of the layer (Fabry-Pérot thin film) or bilayer (BS), l is the thickness of the layer (Fabry-Pérot thin film) or bilayer (BS), respectively, and θ is the illumination angle. Under normal incidence this equation transforms for the two cases to:

$$m\lambda = 2n_{eff}l \quad (\text{Equation 1.2})$$

for a thin film,^[278-280] and

$$m\lambda = 2(n_1l_1 + n_2l_2) \quad (\text{Equation 1.3})$$

for a BS.^[275,276]

For the latter, l_1 and l_2 are the layer thicknesses and n_1 and n_2 are the refractive indices of the individual layers contributing to the bilayer. From Equation 1.1-3 it can be seen that a change in the optical thickness (the product of RI times layer thickness; nl) of a layer results in a change of the condition of constructive interference and hence color (see Figure 1.10).^[275,276] Therefore, external stimuli causing a modulation in the RI, or thickness of the layers, or both, can be optically sensed (Figure 1.10).^[271,276,281] The materials undergoing the change act as a receptor and the thin film or 1D PC structure as a transducer of the photonic sensor. Photonic liquid and vapor sensors operating on RI changes are mainly based on filling the textural pores of NP layers with the analyte vapor while keeping the thickness of the layers constant.^[275,276,281] In contrary, sensors operating on layer thickness changes are mainly based on swelling of the layers by the incorporation of the analyte molecules.^[271,274,276] In the case of swelling, the RI of the analyte and of the thin film are usually not matching and therefore slight changes in the RI are also observed during the swelling process.^[274] The slight changes of the RI during swelling can for instance be observed in a turbostratically disordered nanosheet-based thin film. If the nanosheets are preferentially oriented parallel to the substrate, intercalation of the analyte in the interlayer space is one of the main causes for the swelling and hence in the color change (Figure 1.10 c).^[276,282]

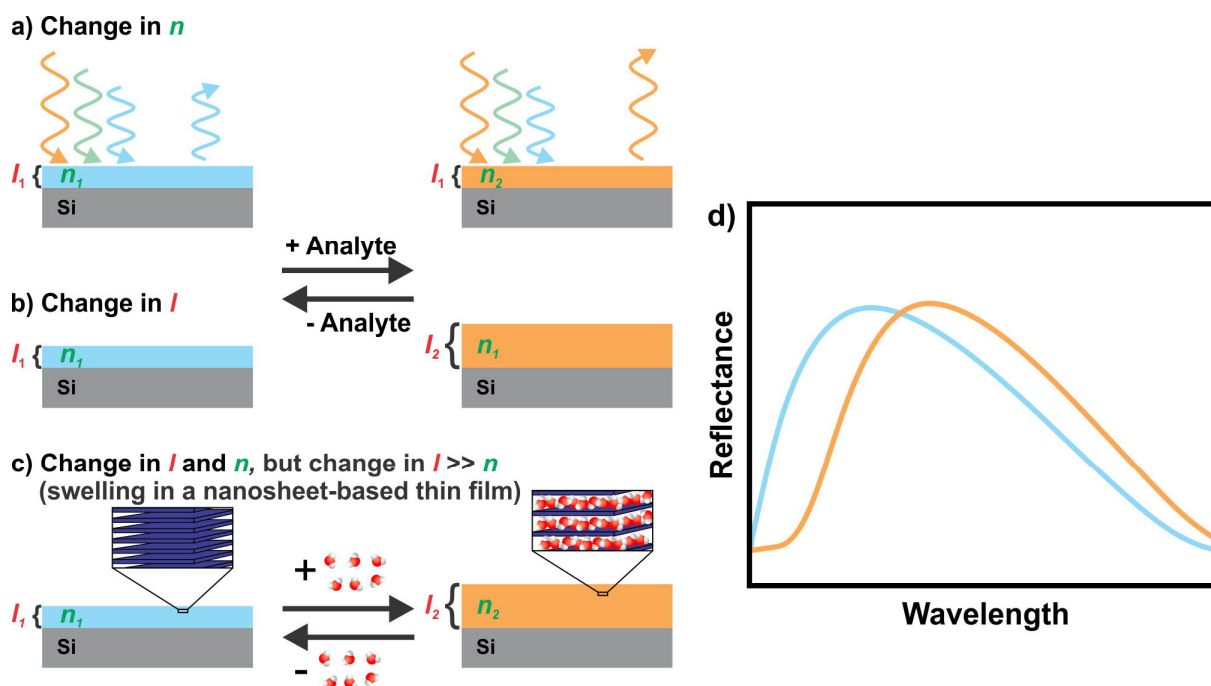


Figure 1.10. Schematic sensing with a photonic thin film illustrating the influence of analyte exposure on the optical thickness and hence, on the observed color. In the case the analyte uptake changes a) the RI of the thin film, e.g. an idealized pore filling scenario, b) the thickness of the thin film, for instance, an idealized swelling process with an analyte of the same RI as the thin film, and c) both, however, the layer change is much more dominant. Here, this is shown for the example of a nanosheet-based thin film, which is the main type of sensors investigated in this thesis. d) Schematic reflectance spectra of the thin film before and during analyte exposure, which can be obtained with an optical spectrometer.

Photonic sensors based on inorganic nanosheet swelling have rarely been studied until recently,^[282-287] whereas photonic sensors based on pore filling in nanostructures^[271-276] or swelling of organic materials^[288-295] have been studied extensively.

The other type of chemical vapor sensors, investigated in the thesis are electrochemical nanosheet-based humidity sensors relying on a change in proton conductivity. In general, the main mechanisms of proton conductivity are the Grotthuss and the vehicle mechanism.^[296-298] In the Grotthuss mechanism protons are transferred through a hydrogen bond network relying on the interplay of several rather stationary “binding sites” and their reorientation.^[296-298] In contrast, in the vehicle mechanism, the protons are bound to a vehicle such as H₂O and NH₃, which is able to diffuse through the structure.^[296-298]

In the electrochemical vapor sensors relying on a change of proton conductivity, the material can fulfill both sensor functions, namely signal recognition and transduction, which is in contrast to the photonic sensor discussed above.^[299,300] An increase in RH leads to a take up of water molecules in between the layers as well as grain boundaries of the sensing material (signal recognition). This water uptake leads to altered hydrogen bonding and diffusion as well as proton conduction pathways in the sample, which ultimately leads to a change in proton conductivity of the sample (transduction). The proton conductivity and its change can be measured by means of impedance spectroscopy. In

impedance spectroscopy the response (current) of the sample to an applied alternating voltage in a certain frequency range is measured. The impedance Z is thereby given by:^[301]

$$Z = \frac{V(t)}{I(t)} = \frac{V_A e^{j\omega t}}{I_A e^{j\omega t - j\varphi}} = Z_A (\cos \varphi + j \sin \varphi) = Z_{real} + jZ_{im} \quad (\text{Equation 1.4})$$

Hereby, V_A and I_A are the voltage and current amplitudes, ω the radial frequency of the applied voltage signal, Z_{real} (resistive parts) and Z_{im} (reactive parts) the real and imaginary part of the impedance, and φ the phase shift. The obtained frequency dependent impedance data can be plotted in a Nyquist ($-Z_{im}$ against Z_{real}) or Bode plot (Z_A and φ against frequency) and modelled with an equivalent circuit to obtain the proton conductivity.^[301,302]

1.6.1.2 Performance parameters of sensors

The performance of the different types of chemical sensors can be assessed by comparing the sensor parameters mainly represented by the important “4S”,^[70,83] which are sensitivity, selectivity, speed and stability (see Figure 1.11).

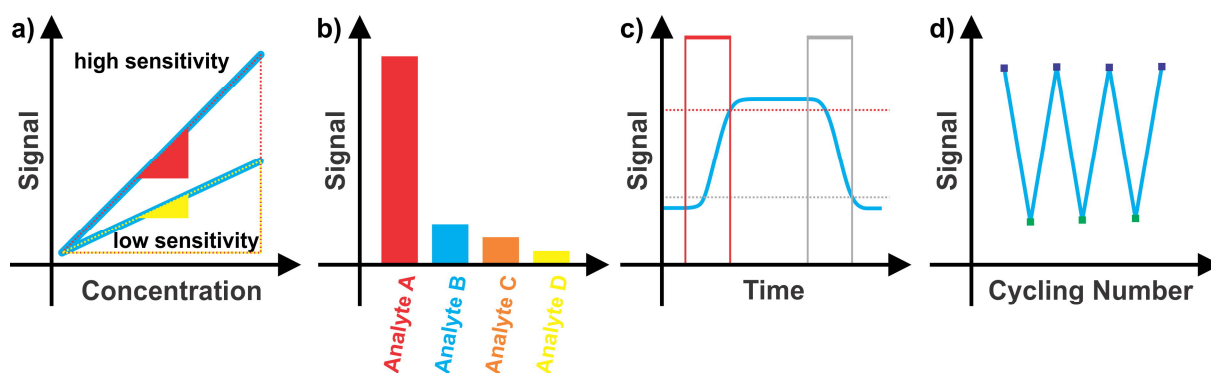


Figure 1.11. Illustration of the sensor performance parameters. a) Sensitivity according to the slope definition and the maximum sensitivity, which is shown by the dotted lines, for a sensor with a high (red) and low (yellow) sensitivity. b) Distinguishing capability of the sensor toward different sorts of stimuli (here analytes), which provides information on the sensor selectivity. c) Response (red) and recovery (grey) time, which are the times needed to achieve 90% of the signal change (dotted lines at 90% and 10% signal change for determination of the response and recovery time, respectively). d) Signal stability with cycling number providing information on the sensor stability. A cycle consists of one value of high (dark blue) and low (dark green) analyte concentration.

As the usage of some of these parameters is not consistent in the present literature, despite International Union of Pure and Applied Chemistry (IUPAC) guidelines from the 1990s and early 2000s,^[303-305] it is indispensable to provide a definition for the parameters used in this thesis.

The sensitivity describes the amount of signal change per concentration unit of the analyte (slope definition).^[267,303] Maximum sensitivity is also referred to as the total signal change in the whole dynamic range, which is the measurement range of analyte concentration. Sensitivity should not be

confused with (lower) the limit of detection, which is also a useful quantity, but describes a separate sensor characteristic, *i.e.* the lowest amount of analyte detectable, usually given in ppm or ppb.^[267,303]

The selectivity is the distinguishing capability of the system between analytes or groups of analytes. Note that the former is a simplified definition compared to the definition given by IUPAC, which states “*Selectivity refers to the extent to which the method can be used to determine particular analytes in mixtures or matrices without interference from other components*”.^[305] The more complex IUPAC definition would also take into account, for instance, non-additive dependence effects on the concentration of the interfering compound. Note that the term specificity is not equivalent to selectivity as specificity is regarded as being ultimately selective (absolute term, cannot be graded).^[305] Therefore, it is not recommended to use the term specificity with respect to sensors at all, as there is almost no sensor that is responding only toward one single analyte.^[305]

The speed of the sensor is given by the response time and recovery time.^[70] The response and recovery times for an analyser are defined as the time to achieve 90% of the signal change caused by a sudden change (stepwise change) in the quantity to be measured.^[303,304] Note that IUPAC provides also a second definition for response and recovery time for a detector, which does not explicitly specify the percentage of signal change,^[306] and in the literature even more definitions are used.^[300,307]

Sensor stability includes several important characteristics, including long term stability, chemical stability and cyclability.^[267,308] Hence, the stability, in principle, provides information on how long, how many times (cycles) and under which conditions a sensor maintains its performance.^[267]

Other important parameters not covered by the “4S” include hysteresis of the sensor, the detection limit, cost, and the size of the sensor, whereby the latter two are mainly important with regard to practical applications.

1.6.1.3 Comparison of current state of nanosheet-based vapors sensors

The most studied nanosheet-based vapor sensors in the present literature are by far chemiresistors and FETs, and to a much lesser extent impedance-based sensors as well as photonic sensors.^[70,136,268-270,283,286,299,300,309] Nanosheets used in chemiresistors and FETs are usually based on van der Waals materials and work on charge transfer processes of the analyte to the sensing material. They offer high sensitivities in the ppm to ppb region and, hence, also a low limit of detection,^[310-316] but they suffer from limited response and recovery times in the seconds to minutes range, as well as limited selectivity and lifetime.^[161,268-270,311,313-315] Although the limited selectivity can be partially overcome by covalent modification,^[137] metal NP decoration^[159,160,162] or utilizing new 2D materials,^[313] the relatively slow response and recovery times typically remain disadvantages. In contrast, impedance-based nanosheet sensors, which, for example, work on changes in the proton conductivity and are mainly GO-based, can offer fast response and recovery times. However, so far only little data is available regarding their selectivity and limit of detection.^[299,300] In comparison to the sensors discussed before, photonic nanosheet-based vapor sensors widen the scope of utilizable stimuli

responsive nanosheets as they operate on film thickness changes and hence, also non-conducting materials can be utilized.^[283,286] In addition, they offer the advantage of working without a power supply as well as providing, in principle, a fast response and recovery time.^[283,286] However, almost nothing is known regarding the sensitivity and selectivity toward other vapor analytes than humidity. All these approaches in their current state are lacking a widely tunable selectivity. In addition, only a few examples of impedance and photonic nanosheet-based sensors are known. Therefore, objectives of this thesis are to gain more fundamental knowledge about nanosheet-based impedance and photonic sensors, as well as to develop highly tunable photonic nanosheet sensors.

1.6.2 Transition metal oxide nanosheets: promising high- k dielectrics

Besides being good candidates for sensors some of the nanosheets investigated in this thesis are also good dielectrics. A dielectric material is a polarizable insulator.^[317,318] One of the most important parameter describing a dielectric material is its dielectric constant, also referred to as relative permittivity (denoted either ϵ_r , κ or k).^[317-319] The dielectric constant is a macroscopic measure of the response, a polarization, of a material to an applied stimulus, an electric field.^[317,318] Therefore, the dielectric constant can be described as the factor by how much an effective electric field is decreased due to polarization of the dielectric material.^[319]

$$\epsilon_r = \frac{E_0}{E} \quad (\text{Equation 1.5})$$

Hereby, E_0 is the electric field without a dielectric material and E with a dielectric material.

A material with a dielectric constant greater than that of silicon dioxide ($\epsilon_r = 3.9$) is called a high- k dielectric.^[15] In order to achieve a high dielectric constant the material needs to have a good polarizability.^[317,318] The total polarizability of a material consists of several contributions, such as electronic, ionic, orientational and space charge polarizability, but also defects can contribute.^[317] For homogenous isotropic materials (cubic or amorphous) with only electronic and ionic contributions to the polarizability, the polarizability can be directly related to the dielectric constant by the Clausius-Mossotti equation.^[317,319] In other cases, it is more complicated, but nevertheless the dielectric constant can be thought to consist of similar contributions as the polarizability.^[317] Note that these contributions are frequency dependent and hence, if a varying electric field is applied, the dielectric constant is best described by a complex number $\epsilon_r = \epsilon_r' - i \epsilon_r''$.^[317,318] The ratio between ϵ_r''/ϵ_r' is defined as the loss tangent δ , which is another important characteristic of a dielectric material, and is a measure of the energy loss, e.g. energy that gets transferred into heat.^[317,318]

Dielectric materials are omnipresent in our daily life due to their utilization in diverse electronic components.^[15,218] One of the main utilization of dielectric materials is in capacitors.^[15] A parallel plate capacitor consists of two conducting parallel plates and a dielectric material between them (Figure 1.12 a).^[317,319] The dielectric material has the effect of not only separating the plates at close distances and of increasing the breakdown voltage, but also to increase the capacitance (q/U), which is the amount of stored charges (q) per volt (U), by the factor ϵ_r .^[319] It can be either understood in case of a disconnected power supply, for example, a battery, where it lowers the electric field, thereby decreasing the voltage between the plates, or in the case of a connected power supply, where it pumps additional charges on the plates to maintain the voltage.^[319] The capacitance is given by:^[317,319]

$$C = \frac{q}{U} = \epsilon_0 \epsilon_r \frac{A}{d} \quad (\text{Equation 1.6})$$

where ϵ_0 is the vacuum permittivity, A the area of the plates, d the distance, and ϵ_r the dielectric constant of the material between the plates. Hence, in order to achieve a high capacitance, the dielectric constant ϵ_r and the area A need to be large, while the distance d should be small.

Another important application of a dielectric material is as a gate dielectric in a FET (Figure 12b).^[15,74] A high capacitance of the dielectric layer allows the FET to be operated at lower biases according to:^[74]

$$I_d = \mu_{lin} \frac{W}{L} C_i (V_g - V_t) V_d \text{ with } V_d \ll V_g - V_t \quad (\text{Equation 1.7})$$

Hereby, I_d is the source-drain current, μ_{lin} the linear mobility, W/L channel-width-to-length ratio, C_i the areal capacitance of the gate dielectric, V_g the gate voltage V_t the threshold voltage and V_d the source drain voltage. Moreover, achieving a higher C_i might allow for further downsizing, as the same capacitance can be achieved in a smaller area.^[15,262]

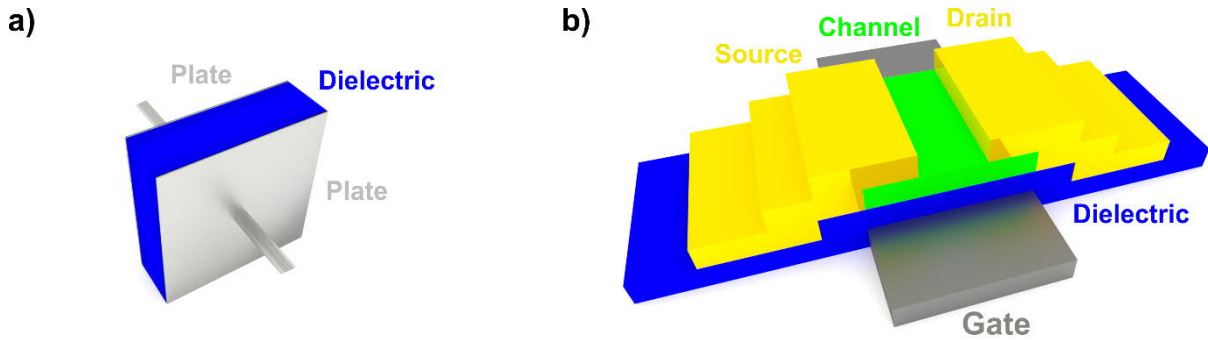


Figure 1.12. Application of dielectric materials in capacitors and in FETs. a) Schematic drawing of a parallel plate capacitor including a dielectric material between the two conductive plates. b) Schematic drawing of a FET. In the FET the dielectric material separates and insulates the gate electrode from the semiconducting channel material.

TMO nanosheets are very promising candidates for high- k dielectric materials as they inherently have a small thickness and are mainly insulating due to their d^0 configuration.^[15,74,262,320] More importantly, they can exhibit high dielectric constants ($\epsilon_r > 150$) owing to their highly polarizable components such as NbO_6 or TaO_6 octahedra.^[15,218] Moreover, nanosheets derived from layered perovskites, e.g. $\text{Ca}_2\text{Nb}_3\text{O}_{10}^-$, have shown low dielectric losses ($\tan \delta < 4\%$), leakage currents ($I_{\text{leak}} < 10^{-7} \text{ A cm}^{-2}$) and high break down voltages (dielectric strength 3-4 MVcm^{-1}).^[218,264,321] More importantly, in contrast to other currently investigated high- k materials like BaTiO_3 they have a very small temperature coefficient τ and show no “size effect”.^[226,227,264,321] The “size effect” is the decrease of ϵ_r with decreasing dielectric thickness,^[154,155] which is commonly attributed to “dead layer” issues.^[15,81,155,218] They are beneficial features for their utilization in miniaturized capacitors as well as high temperature applications.^[15,226,227] In addition, there exist several ways to optimize the dielectric performance of these perovskite-based nanosheets. One possibility is site engineering, like substitution of A or B site with Sr or Ta in $\text{Ca}_{2-x}\text{Sr}_x\text{Nb}_{3-y}\text{Ta}_y\text{O}_{10}^-$,^[155] which can lead to higher dielectric constants or lower leakage currents. Another option is tuning the structural nanosheet thickness, for instance the thickness of the

NbO_6 blocks z in $\text{Ca}_2\text{Na}_{z-3}\text{Nb}_z\text{O}_{3z+1}$, which can result in dielectric constants as high as 470 in ultrathin films (<10 nm), leading to a very good areal capacitance of $203 \mu\text{F cm}^{-2}$.^[80]

In summary, oxide nanosheets exhibit excellent dielectric performances. However, they have not yet been utilized in industrial applications due to the lack of re-producing identical nanostructures with reasonable lateral sizes at larger scales.^[15,264] Therefore, the development and improvement of processing, structuring and assembly techniques of these oxide nanosheets is of high interest. In Chapter 5 we are trying to close this gap with the development of a photolithographic structuring technique suitable for photocatalytically active nanosheets, *e.g.* $\text{Ca}_2\text{Nb}_3\text{O}_{10}$.

1.7 Objectives

Despite the extraordinary and outstanding properties of nanosheets, nanosheet-based devices are mainly absent in our everyday life. The main reason for their absence is the inability to synchronize the large-scale production of single layer nanosheets with the ability to reproducibly position them in a scalable fashion with high control, as well as to modify, and hence, tailor their properties according to industrial needs (see Chapter 1.1). To harvest the nanosheets' superior properties in impactful applications, it is hence indispensable to overcome this key-challenge.

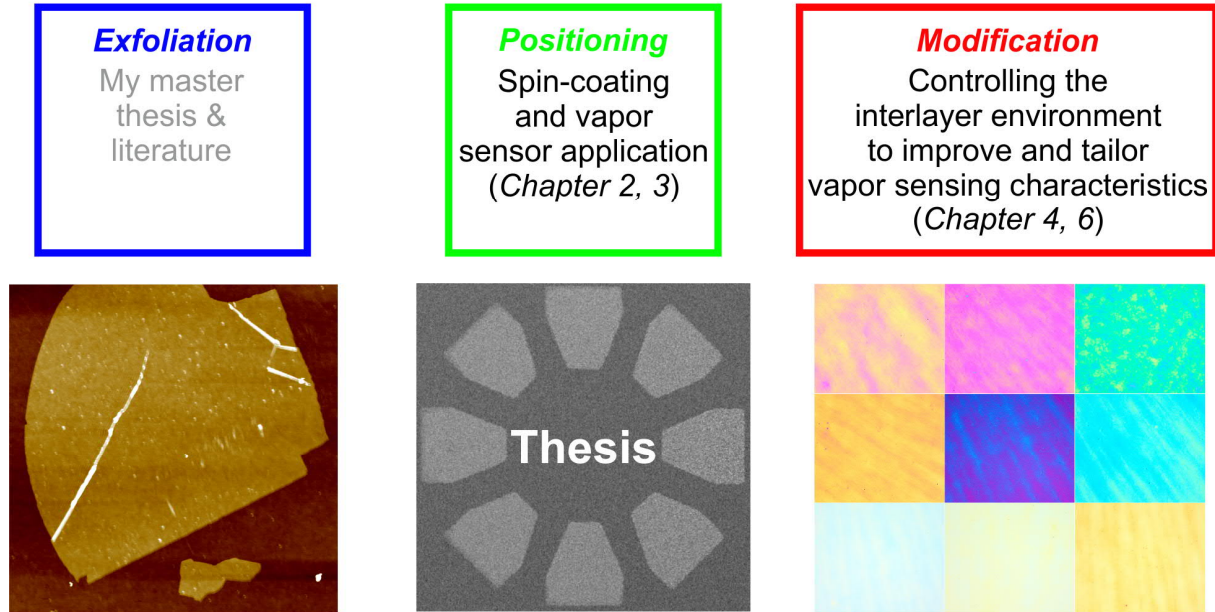
Therefore, the ultimate objective of this thesis was to overcome this key challenge for phosphate and oxide nanosheets. As outlined, this goal can be achieved by improving or developing new delamination, positioning and tuning methods for oxide and phosphate nanosheets. Therefore, achieving progress in these three research areas were coupled or linked subordinate objectives of this dissertation.

As for phosphoantimonate nanosheets a high single-layer yield and straightforward exfoliation procedure was reported before in my master thesis and by others, the two pivotal goals were to find a scalable assembly method as well as to identify promising areas of applications. As they were achieved in Chapter 2 and 3, the next objective was to demonstrate the tuneability of the nanosheet-based devices (Chapter 4 and 6).

For the other class of material, TMO nanosheets, several impressive properties combined with proof of concept applications have been demonstrated (see Chapter 1.6.2). However, efficient methods for controlling the lateral size of the nanosheet-based structures were lacking, thus hindering their out-of-lab application. A further bottleneck for their real life application is the lack of very efficient exfoliation strategies. Therefore, the additional objectives of this thesis were to develop alternative exfoliation strategies (Chapter 7) as well as to improve their positioning and patterning (Chapter 5).

A concise schematic overview of the conducted work is given in the following (s. Figure 1.13).

Phosphate nanosheets (*Sensors*)



Oxide nanosheets (*Sensors, dielectrics*)

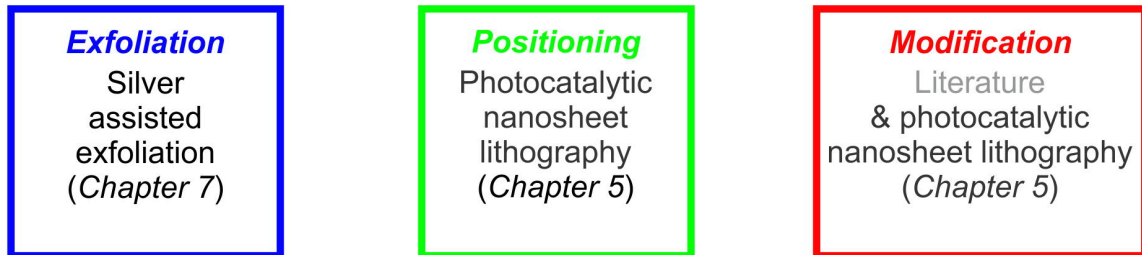


Figure 1.13. Schematic and concise overview of the work contributing to the current thesis. The nanosheets investigated in this thesis were mainly phosphate and oxide nanosheets. Their respective relevant applications are given in italics in the brackets. For achieving a tunable device, which is suitable for industrial applications, it is necessary to carry out research in the areas of exfoliation (blue, left column), positioning (green, middle column) and modification (red, right column) (see also Figure 1.1). The images shown in the central row belong to Chapter 7 (left; AFM image of exfoliated Ch-LaNb₂O₇ nanosheets; exfoliation), Chapter 5 (middle; SEM image of (NH₄)_xH_{1-x}Ca₂Nb₃O₁₀ nanosheet structures obtained by PNL; positioning) and Chapter 6 (right; optical microscope images of H₃Sb₃P₂O₁₄ thin films intercalated with primary alkylamines; modification) and are representative examples of the results obtained in the current thesis in these areas. The words highlighted in grey refer to topics already carried out before in the literature, which are hence not part of the thesis.

1.8 Bibliography

- [1] T. H. Webb, *Am. J. Sci. Arts* **1824**, 7, 55.
- [2] B. C. Brodie, *Philos. Trans. R. Soc. London* **1859**, 149, 249-259.
- [3] V. Nicolosi, M. Chhowalla, M. G. Kanatzidis, M. S. Strano, J. N. Coleman, *Science* **2013**, 340, 1226419.
- [4] G. R. Bhimanapati, Z. Lin, V. Meunier, Y. Jung, J. Cha, S. Das, D. Xiao, Y. Son, M. S. Strano, V. R. Cooper, L. Liang, S. G. Louie, E. Ringe, W. Zhou, S. S. Kim, R. R. Naik, B. G. Sumpter, H. Terrones, F. Xia, Y. Wang, J. Zhu, D. Akinwande, N. Alem, J. A. Schuller, R. E. Schaak, M. Terrones, J. A. Robinson, *ACS Nano* **2015**, 9, 11509-11539.
- [5] M. Pumera, Z. Sofer, *Adv. Mater.* **2017**, 29, 1605299.
- [6] J. N. Coleman, *Acc. Chem. Res.* **2013**, 46, 14-22.
- [7] N. Nitta, F. Wu, J. T. Lee, G. Yushin, *Mater. Today* **2015**, 18, 252-264.
- [8] M. F. El-Kady, Y. Shao, R. B. Kaner, *Nat. Rev. Mater.* **2016**, 1, 16033.
- [9] D. W. Olson, in *Mineral commodity summaries 2018: U.S. Geological Survey*, U.S. Geological Survey, Reston, **2018**, pp. 72-73.
- [10] N. M. Renevier, J. Hampshire, V. C. Fox, J. Witts, T. Allen, D. G. Teer, *Surf. Coat. Technol.* **2001**, 142-144, 67-77.
- [11] R. A. Kühnel, *Appl. Clay Sci.* **1990**, 5, 135-143.
- [12] D. N. West, in *Mineral commodity summaries 2018: U.S. Geological Survey*, U.S. Geological Survey, Reston, **2018**, pp. 48-49.
- [13] H. Andrew, B. B. John, G. Ian, G. K. Adam, M. S. Beata, M. Ghulam, T. Andrew, J. L. David, O. B. Paul, N. C. Jonathan, *2D Mater.* **2017**, 4, 025054.
- [14] S. Z. Butler, S. M. Hollen, L. Cao, Y. Cui, J. A. Gupta, H. R. Gutierrez, T. F. Heinz, S. S. Hong, J. Huang, A. F. Ismach, E. Johnston-Halperin, M. Kuno, V. V. Plashnitsa, R. D. Robinson, R. S. Ruoff, S. Salahuddin, J. Shan, L. Shi, M. G. Spencer, M. Terrones, W. Windl, J. E. Goldberger, *ACS Nano* **2013**, 7, 2898-2926.
- [15] M. Osada, T. Sasaki, *Adv. Mater.* **2012**, 24, 210-228.
- [16] R. Ma, T. Sasaki, *Acc. Chem. Res.* **2015**, 48, 136-143.
- [17] R. Ma, T. Sasaki, *Adv. Mater.* **2010**, 22, 5082-5104.
- [18] G. F. Walker, *Nature* **1960**, 187, 312-313.
- [19] R. F. Frindt, *J. Phys. Chem. Solids* **1963**, 24, 1107-1108.
- [20] H. P. Boehm, A. Clauss, G. O. Fischer, U. Hofmann, *Z. Naturforsch., B* **1962**, 17, 150.
- [21] R. F. Frindt, *J. Appl. Phys.* **1966**, 37, 1928-1929.
- [22] G. F. Walker, W. G. Garrett, *Science* **1967**, 156, 385-387.
- [23] F. Bonaccorso, A. Bartolotta, J. N. Coleman, C. Backes, *Adv. Mater.* **2016**, 28, 6136-6166.
- [24] P. Joensen, R. F. Frindt, S. R. Morrison, *Mater. Res. Bull.* **1986**, 21, 457-461.
- [25] S. W. Keller, H.-N. Kim, T. E. Mallouk, *J. Am. Chem. Soc.* **1994**, 116, 8817-8818.
- [26] E. R. Kleinfield, G. S. Ferguson, *Science* **1994**, 265, 370-373.
- [27] H. Lee, L. J. Kepley, H. G. Hong, T. E. Mallouk, *J. Am. Chem. Soc.* **1988**, 110, 618-620.
- [28] A. K. Geim, K. S. Novoselov, *Nat. Mater.* **2007**, 6, 183-191.
- [29] A. K. Geim, I. V. Grigorieva, *Nature* **2013**, 499, 419-425.
- [30] R. Ruoff, *Nat. Nanotechnol.* **2008**, 3, 10-11.
- [31] K. S. Novoselov, V. I. Falko, L. Colombo, P. R. Gellert, M. G. Schwab, K. Kim, *Nature* **2012**, 490, 192-200.
- [32] A. Kis, *npj 2D Materials and Applications* **2017**, 1, 1.
- [33] S. Park, R. S. Ruoff, *Nat. Nanotechnol.* **2009**, 4, 217-224.
- [34] K. J. Koski, Y. Cui, *ACS Nano* **2013**, 7, 3739-3743.
- [35] E. Gibney, *Nature* **2015**, 522, 274-276.
- [36] M. Xu, T. Liang, M. Shi, H. Chen, *Chem. Rev.* **2013**, 113, 3766-3798.
- [37] Y. Liu, N. O. Weiss, X. Duan, H.-C. Cheng, Y. Huang, X. Duan, *Nat. Rev. Mater.* **2016**, 1, 16042.

- [38] S. Jiang, M. Q. Arguilla, N. D. Cultrara, J. E. Goldberger, *Acc. Chem. Res.* **2015**, *48*, 144-151.
- [39] J. N. Coleman, M. Lotya, A. O'Neill, S. D. Bergin, P. J. King, U. Khan, K. Young, A. Gaucher, S. De, R. J. Smith, I. V. Shvets, S. K. Arora, G. Stanton, H.-Y. Kim, K. Lee, G. T. Kim, G. S. Duesberg, T. Hallam, J. J. Boland, J. J. Wang, J. F. Donegan, J. C. Grunlan, G. Moriarty, A. Shmeliov, R. J. Nicholls, J. M. Perkins, E. M. Grieveson, K. Theuwissen, D. W. McComb, P. D. Nellist, V. Nicolosi, *Science* **2011**, *331*, 568-571.
- [40] C. N. R. Rao, H. S. S. Ramakrishna Matte, U. Maitra, *Angew. Chem., Int. Ed.* **2013**, *52*, 13162-13185.
- [41] M. Alhabeab, K. Maleski, B. Anasori, P. Lelyukh, L. Clark, S. Sin, Y. Gogotsi, *Chem. Mater.* **2017**.
- [42] T. Nakato, J. Kawamata, S. Takagi, in *Inorganic Nanosheets and Nanosheet-Based Materials: Fundamentals and Applications of Two-Dimensional Systems* (Eds.: T. Nakato, J. Kawamata, S. Takagi), Springer Japan, Tokyo, **2017**, pp. 3-31.
- [43] Editorial, *Nat. Mater.* **2017**, *16*, 155-155.
- [44] Editorial, *Nat. Rev. Mater.* **2016**, *1*, 16089.
- [45] M. Naguib, M. Kurtoglu, V. Presser, J. Lu, J. Niu, M. Heon, L. Hultman, Y. Gogotsi, M. W. Barsoum, *Adv. Mater.* **2011**, *23*, 4248-4253.
- [46] O. Mashtalir, M. Naguib, V. N. Mochalin, Y. Dall'Agnese, M. Heon, M. W. Barsoum, Y. Gogotsi, *Nat. Commun.* **2013**, *4*, 1716.
- [47] M. Naguib, V. N. Mochalin, M. W. Barsoum, Y. Gogotsi, *Adv. Mater.* **2014**, *26*, 992-1005.
- [48] B. Anasori, M. R. Lukatskaya, Y. Gogotsi, *Nat. Rev. Mater.* **2017**, *2*, 16098.
- [49] S. Balendhran, S. Walia, H. Nili, S. Sriram, M. Bhaskaran, *Small* **2015**, *11*, 640-652.
- [50] A. Molle, J. Goldberger, M. Houssa, Y. Xu, S.-C. Zhang, D. Akinwande, *Nat. Mater.* **2017**, *16*, 163-169.
- [51] M. Q. Arguilla, J. Katoch, K. Krymowski, N. D. Cultrara, J. Xu, X. Xi, A. Hanks, S. Jiang, R. D. Ross, R. J. Koch, S. Ulstrup, A. Bostwick, C. Jozwiak, D. W. McComb, E. Rotenberg, J. Shan, W. Windl, R. K. Kawakami, J. E. Goldberger, *ACS Nano* **2016**, *10*, 9500-9508.
- [52] M. Q. Arguilla, N. D. Cultrara, Z. J. Baum, S. Jiang, R. D. Ross, J. E. Goldberger, *Inorg. Chem. Front.* **2017**, *4*, 378-386.
- [53] T. Sasaki, *J. Ceram. Soc. Jpn.* **2007**, *115*, 9-16.
- [54] J. Pan, S. Lany, Y. Qi, *ACS Nano* **2017**, *11*, 7560-7564.
- [55] K. R. Paton, E. Varrla, C. Backes, R. J. Smith, U. Khan, A. O'Neill, C. Boland, M. Lotya, O. M. Istrate, P. King, T. Higgins, S. Barwich, P. May, P. Puczarski, I. Ahmed, M. Moebius, H. Pettersson, E. Long, J. Coelho, S. E. O'Brien, E. K. McGuire, B. M. Sanchez, G. S. Duesberg, N. McEvoy, T. J. Pennycook, C. Downing, A. Crossley, V. Nicolosi, J. N. Coleman, *Nat. Mater.* **2014**, *13*, 624-630.
- [56] Y. Hernandez, V. Nicolosi, M. Lotya, F. M. Blighe, Z. Sun, S. De, I. T. McGovern, B. Holland, M. Byrne, Y. K. Gun'Ko, J. J. Boland, P. Niraj, G. Duesberg, S. Krishnamurthy, R. Goodhue, J. Hutchison, V. Scardaci, A. C. Ferrari, J. N. Coleman, *Nat. Nanotechnol.* **2008**, *3*, 563-568.
- [57] C. Backes, T. M. Higgins, A. Kelly, C. Boland, A. Harvey, D. Hanlon, J. N. Coleman, *Chem. Mater.* **2017**, *29*, 243-255.
- [58] H. Yuan, D. Dubbink, R. Besselink, J. E. ten Elshof, *Angew. Chem., Int. Ed.* **2015**, *54*, 9239-9243.
- [59] F. Bonaccorso, L. Colombo, G. Yu, M. Stoller, V. Tozzini, A. C. Ferrari, R. S. Ruoff, V. Pellegrini, *Science* **2015**, *347*.
- [60] E. Varrla, C. Backes, K. R. Paton, A. Harvey, Z. Gholamvand, J. McCauley, J. N. Coleman, *Chem. Mater.* **2015**, *27*, 1129-1139.
- [61] M. Matsumoto, Y. Saito, C. Park, T. Fukushima, T. Aida, *Nat. Chem.* **2015**, *7*, 730-736.
- [62] K. Matsuba, C. Wang, K. Saruwatari, Y. Uesusuki, K. Akatsuka, M. Osada, Y. Ebina, R. Ma, T. Sasaki, *Sci. Adv.* **2017**, *3*, e1700414.
- [63] A. G. Kelly, T. Hallam, C. Backes, A. Harvey, A. S. Esmaily, I. Godwin, J. Coelho, V. Nicolosi, J. Lauth, A. Kulkarni, S. Kinge, L. D. A. Siebbeles, G. S. Duesberg, J. N. Coleman, *Science* **2017**, *356*, 69-73.

- [64] D. McManus, S. Vranic, F. Withers, V. Sanchez-Romaguera, M. Macucci, H. Yang, R. Sorrentino, K. Parvez, S.-K. Son, G. Iannaccone, K. Kostarelos, G. Fiori, C. Casiraghi, *Nat. Nanotechnol.* **2017**, *12*, 343-350.
- [65] C. Backes, B. M. Szydłowska, A. Harvey, S. Yuan, V. Vega-Mayoral, B. R. Davies, P.-I. Zhao, D. Hanlon, E. J. G. Santos, M. I. Katsnelson, W. J. Blau, C. Gadermaier, J. N. Coleman, *ACS Nano* **2016**, *10*, 1589-1601.
- [66] J. Wan, S. D. Lacey, J. Dai, W. Bao, M. S. Fuhrer, L. Hu, *Chem. Soc. Rev.* **2016**, *45*, 6742-6765.
- [67] S. S. Chou, M. De, J. Kim, S. Byun, C. Dykstra, J. Yu, J. Huang, V. P. Dravid, *J. Am. Chem. Soc.* **2013**, *135*, 4584-4587.
- [68] C. Backes, N. C. Berner, X. Chen, P. Lafargue, P. LaPlace, M. Freeley, G. S. Duesberg, J. N. Coleman, A. R. McDonald, *Angew. Chem., Int. Ed.* **2015**, *54*, 2638-2642.
- [69] Y. Guo, K. Xu, C. Wu, J. Zhao, Y. Xie, *Chem. Soc. Rev.* **2015**, *44*, 637-646.
- [70] J. Zhang, X. Liu, G. Neri, N. Pinna, *Adv. Mater.* **2016**, *28*, 795-831.
- [71] Y. Zhu, L. Peng, Z. Fang, C. Yan, X. Zhang, G. Yu, *Adv. Mater.* **2018**, *30*, 1706347.
- [72] B. V. Lotsch, *Annu. Rev. Mater. Res.* **2015**, *45*, 85-109.
- [73] B. Mendoza-Sánchez, Y. Gogotsi, *Adv. Mater.* **2016**, *28*, 6104-6135.
- [74] J. Zhu, M. C. Hersam, *Adv. Mater.* **2017**, *29*, 1603895.
- [75] T. Georgiou, R. Jalil, B. D. Belle, L. Britnell, R. V. Gorbachev, S. V. Morozov, Y.-J. Kim, A. Gholinia, S. J. Haigh, O. Makarovskiy, L. Eaves, L. A. Ponomarenko, A. K. Geim, K. S. Novoselov, A. Mishchenko, *Nat. Nanotechnol.* **2012**, *8*, 100.
- [76] B. W. H. Baugher, H. O. H. Churchill, Y. Yang, P. Jarillo-Herrero, *Nat. Nanotechnol.* **2014**, *9*, 262.
- [77] J. S. Ross, P. Klement, A. M. Jones, N. J. Ghimire, J. Yan, D. G. Mandrus, T. Taniguchi, K. Watanabe, K. Kitamura, W. Yao, D. H. Cobden, X. Xu, *Nat. Nanotechnol.* **2014**, *9*, 268.
- [78] A. Pospischil, M. M. Furchi, T. Mueller, *Nat. Nanotechnol.* **2014**, *9*, 257.
- [79] F. Withers, O. Del Pozo-Zamudio, A. Mishchenko, A. P. Rooney, A. Gholinia, K. Watanabe, T. Taniguchi, S. J. Haigh, A. K. Geim, A. I. Tartakovskii, K. S. Novoselov, *Nat. Mater.* **2015**, *14*, 301.
- [80] B.-W. Li, M. Osada, Y.-H. Kim, Y. Ebina, K. Akatsuka, T. Sasaki, *J. Am. Chem. Soc.* **2017**, *139*, 10868-10874.
- [81] C. Wang, M. Osada, Y. Ebina, B.-W. Li, K. Akatsuka, K. Fukuda, W. Sugimoto, R. Ma, T. Sasaki, *ACS Nano* **2014**, *8*, 2658-2666.
- [82] M. R. Lukatskaya, O. Mashtalir, C. E. Ren, Y. Dall'Agnesse, P. Rozier, P. L. Taberna, M. Naguib, P. Simon, M. W. Barsoum, Y. Gogotsi, *Science* **2013**, *341*, 1502-1505.
- [83] X. Liu, T. Ma, N. Pinna, J. Zhang, *Adv. Funct. Mater.* **2017**, 1702168.
- [84] C. S. Boland, U. Khan, G. Ryan, S. Barwich, R. Charifou, A. Harvey, C. Backes, Z. Li, M. S. Ferreira, M. E. Möbius, R. J. Young, J. N. Coleman, *Science* **2016**, *354*, 1257-1260.
- [85] M.-J. Lee, J.-H. Ahn, J. H. Sung, H. Heo, S. G. Jeon, W. Lee, J. Y. Song, K.-H. Hong, B. Choi, S.-H. Lee, M.-H. Jo, *Nat. Commun.* **2016**, *7*, 12011.
- [86] J. Y. Oh, J. H. Lee, S. W. Han, S. S. Chae, E. J. Bae, Y. H. Kang, W. J. Choi, S. Y. Cho, J.-O. Lee, H. K. Baik, T. I. Lee, *Energy Environ. Sci.* **2016**, *9*, 1696-1705.
- [87] L. Chen, G. Shi, J. Shen, B. Peng, B. Zhang, Y. Wang, F. Bian, J. Wang, D. Li, Z. Qian, G. Xu, G. Liu, J. Zeng, L. Zhang, Y. Yang, G. Zhou, M. Wu, W. Jin, J. Li, H. Fang, *Nature* **2017**, *550*, 380.
- [88] W. Hirunpinyopas, E. Prestat, S. D. Worrall, S. J. Haigh, R. A. W. Dryfe, M. A. Bissett, *ACS Nano* **2017**, *11*, 11082-11090.
- [89] Q. Yang, Y. Su, C. Chi, C. T. Cherian, K. Huang, V. G. Kravets, F. C. Wang, J. C. Zhang, A. Pratt, A. N. Grigorenko, F. Guinea, A. K. Geim, R. R. Nair, *Nat. Mater.* **2017**, *16*, 1198.
- [90] D. Voiry, J. Yang, M. Chhowalla, *Adv. Mater.* **2016**, *28*, 6197-6206.
- [91] D. Voiry, H. Yamaguchi, J. Li, R. Silva, D. C. B. Alves, T. Fujita, M. Chen, T. Asefa, V. B. Shenoy, G. Eda, M. Chhowalla, *Nat. Mater.* **2013**, *12*, 850.
- [92] S. Park, *Nat. Rev. Mater.* **2016**, *1*, 16085.

- [93] D. J. Finn, M. Lotya, G. Cunningham, R. J. Smith, D. McCloskey, J. F. Donegan, J. N. Coleman, *J. Mater. Chem. C* **2014**, *2*, 925-932.
- [94] X. Chen, A. R. McDonald, *Adv. Mater.* **2016**, *28*, 5738-5746.
- [95] K. S. Novoselov, A. K. Geim, S. V. Morozov, D. Jiang, Y. Zhang, S. V. Dubonos, I. V. Grigorieva, A. A. Firsov, *Science* **2004**, *306*, 666-669.
- [96] C. Tan, H. Zhang, *Nat. Commun.* **2015**, *6*, 7873.
- [97] Z. Sun, T. Liao, Y. Dou, S. M. Hwang, M.-S. Park, L. Jiang, J. H. Kim, S. X. Dou, *Nat. Commun.* **2014**, *5*, 3813.
- [98] Q. H. Wang, K. Kalantar-Zadeh, A. Kis, J. N. Coleman, M. S. Strano, *Nat. Nanotechnol.* **2012**, *7*, 699-712.
- [99] Z. Zeng, Z. Yin, X. Huang, H. Li, Q. He, G. Lu, F. Boey, H. Zhang, *Angew. Chem., Int. Ed.* **2011**, *50*, 11093-11097.
- [100] H. S. S. Ramakrishna Matte, A. Gomathi, A. K. Manna, D. J. Late, R. Datta, S. K. Pati, C. N. R. Rao, *Angew. Chem., Int. Ed.* **2010**, *49*, 4059-4062.
- [101] J. Zheng, H. Zhang, S. Dong, Y. Liu, C. Tai Nai, H. Suk Shin, H. Young Jeong, B. Liu, K. Ping Loh, *Nat. Commun.* **2014**, *5*, 2995.
- [102] J. Shen, Y. He, J. Wu, C. Gao, K. Keyshar, X. Zhang, Y. Yang, M. Ye, R. Vajtai, J. Lou, P. M. Ajayan, *Nano Lett.* **2015**, *15*, 5449-5454.
- [103] P. L. Cullen, K. M. Cox, M. K. Bin Subhan, L. Picco, O. D. Payton, D. J. Buckley, T. S. Miller, S. A. Hodge, N. T. Skipper, V. Tileli, C. A. Howard, *Nat. Chem.* **2017**, *9*, 244-249.
- [104] G. Bepete, E. Anglaret, L. Ortolani, V. Morandi, K. Huang, A. Pénicaud, C. Drummond, *Nat. Chem.* **2017**, *9*, 347-352.
- [105] M. Honda, Y. Oaki, H. Imai, *Chem. Mater.* **2014**, *26*, 3579-3585.
- [106] N. I. Kovtyukhova, Y. Wang, A. Berkdemir, R. Cruz-Silva, M. Terrones, V. H. Crespi, T. E. Mallouk, *Nat. Chem.* **2014**, *6*, 957-963.
- [107] O. Bubnova, *Nat. Nanotechnol.* **2017**, doi:10.1038/nnano.2017.1172.
- [108] X. Zhang, Z. Lai, C. Tan, H. Zhang, *Angew. Chem., Int. Ed.* **2016**, *55*, 8816-8838.
- [109] M. Chhowalla, H. S. Shin, G. Eda, L.-J. Li, K. P. Loh, H. Zhang, *Nat. Chem.* **2013**, *5*, 263-275.
- [110] S. Manzeli, D. Ovchinnikov, D. Pasquier, O. V. Yazyev, A. Kis, *Nat. Rev. Mater.* **2017**, *2*, 17033.
- [111] X. Huang, Z. Zeng, H. Zhang, *Chem. Soc. Rev.* **2013**, *42*, 1934-1946.
- [112] Z. Zeng, T. Sun, J. Zhu, X. Huang, Z. Yin, G. Lu, Z. Fan, Q. Yan, H. H. Hng, H. Zhang, *Angew. Chem., Int. Ed.* **2012**, *51*, 9052-9056.
- [113] G. Eda, M. Chhowalla, *Adv. Mater.* **2010**, *22*, 2392-2415.
- [114] R. Ma, Z. Liu, L. Li, N. Iyi, T. Sasaki, *J. Mater. Chem.* **2006**, *16*, 3809-3813.
- [115] T. Sasaki, M. Watanabe, *J. Am. Chem. Soc.* **1998**, *120*, 4682-4689.
- [116] T. Maluangnont, K. Matsuba, F. Geng, R. Ma, Y. Yamauchi, T. Sasaki, *Chem. Mater.* **2013**, *25*, 3137-3146.
- [117] F. Geng, R. Ma, Y. Ebina, Y. Yamauchi, N. Miyamoto, T. Sasaki, *J. Am. Chem. Soc.* **2014**, *136*, 5491-5500.
- [118] G. Cunningham, M. Lotya, C. S. Cucinotta, S. Sanvito, S. D. Bergin, R. Menzel, M. S. P. Shaffer, J. N. Coleman, *ACS Nano* **2012**, *6*, 3468-3480.
- [119] R. J. Smith, P. J. King, M. Lotya, C. Wirtz, U. Khan, S. De, A. O'Neill, G. S. Duesberg, J. C. Grunlan, G. Moriarty, J. Chen, J. Wang, A. I. Minett, V. Nicolosi, J. N. Coleman, *Adv. Mater.* **2011**, *23*, 3944-3948.
- [120] A. Jawaid, J. Che, L. F. Drummy, J. Bultman, A. Waite, M.-S. Hsiao, R. A. Vaia, *ACS Nano* **2017**, *11*, 635-646.
- [121] G. Eda, H. Yamaguchi, D. Voiry, T. Fujita, M. Chen, M. Chhowalla, *Nano Lett.* **2011**, *11*, 5111-5116.
- [122] G. Eda, T. Fujita, H. Yamaguchi, D. Voiry, M. Chen, M. Chhowalla, *ACS Nano* **2012**, *6*, 7311-7317.
- [123] D. Weber, L. M. Schoop, V. Duppel, J. M. Lippmann, J. Nuss, B. V. Lotsch, *Nano Lett.* **2016**, *16*, 3578-3584.
- [124] F. Geng, R. Ma, A. Nakamura, K. Akatsuka, Y. Ebina, Y. Yamauchi, N. Miyamoto, Y. Tateyama, T. Sasaki, *Nat. Commun.* **2013**, *4*, 1632.

- [125] Y. Song, N. Iyi, T. Hoshide, T. C. Ozawa, Y. Ebina, R. Ma, N. Miyamoto, T. Sasaki, *Chem. Commun.* **2015**, 51, 17068-17071.
- [126] J. J. Richardson, M. Björnmalm, F. Caruso, *Science* **2015**, 348.
- [127] R. Ma, T. Sasaki, *Annu. Rev. Mater. Res.* **2015**, 45, 111-127.
- [128] R. A. Schoonheydt, Y. Umemura, in *Inorganic Nanosheets and Nanosheet-Based Materials: Fundamentals and Applications of Two-Dimensional Systems* (Eds.: T. Nakato, J. Kawamata, S. Takagi), Springer Japan, Tokyo, **2017**, pp. 33-53.
- [129] J. W. Kim, D. Kang, T. H. Kim, S. G. Lee, N. Byun, D. W. Lee, B. H. Seo, R. S. Ruoff, H. S. Shin, *ACS Nano* **2013**, 7, 8082-8088.
- [130] D. Mochizuki, K. Kumagai, M. M. Maitani, Y. Wada, *Angew. Chem., Int. Ed.* **2012**, 51, 5452-5455.
- [131] B.-W. Li, M. Osada, T. C. Ozawa, Y. Ebina, K. Akatsuka, R. Ma, H. Funakubo, T. Sasaki, *ACS Nano* **2010**, 4, 6673-6680.
- [132] H. Yamaguchi, G. Eda, C. Mattevi, H. Kim, M. Chhowalla, *ACS Nano* **2010**, 4, 524-528.
- [133] M. S. Kim, L. Ma, S. Choudhury, L. A. Archer, *Adv. Mater. Interfaces* **2016**, 3, 1600450.
- [134] M. S. Kim, L. Ma, S. Choudhury, S. S. Moganty, S. Wei, L. A. Archer, *J. Mater. Chem. A* **2016**, 4, 14709-14719.
- [135] D. M. Sim, M. Kim, S. Yim, M.-J. Choi, J. Choi, S. Yoo, Y. S. Jung, *ACS Nano* **2015**, 9, 12115-12123.
- [136] G. Jiang, M. Golezdinowski, F. J. E. Comeau, H. Zarrin, G. Lui, J. Lenos, A. Veileux, G. Liu, J. Zhang, S. Hemmati, J. Qiao, Z. Chen, *Adv. Funct. Mater.* **2016**, 26, 1729-1736.
- [137] J.-S. Kim, H.-W. Yoo, H. O. Choi, H.-T. Jung, *Nano Lett.* **2014**, 14, 5941-5947.
- [138] S. Jiang, S. Butler, E. Bianco, O. D. Restrepo, W. Windl, J. E. Goldberger, *Nat. Commun.* **2014**, 5, 3389.
- [139] S. Jiang, K. Krymowski, T. Asel, M. Q. Arguilla, N. D. Cultrara, E. Yanchenko, X. Yang, L. J. Brillson, W. Windl, J. E. Goldberger, *Chem. Mater.* **2016**, 28, 8071-8077.
- [140] C. R. Ryder, J. D. Wood, S. A. Wells, Y. Yang, D. Jariwala, T. J. Marks, G. C. Schatz, M. C. Hersam, *Nat. Chem.* **2016**, 8, 597-602.
- [141] D. Voiry, A. Goswami, R. Koppera, C. de Carvalho Castro e Silva, D. Kaplan, T. Fujita, M. Chen, T. Asefa, M. Chhowalla, *Nat. Chem.* **2015**, 7, 45-49.
- [142] K. C. Knirsch, N. C. Berner, H. C. Nerl, C. S. Cucinotta, Z. Gholamvand, N. McEvoy, Z. Wang, I. Abramovic, P. Vecera, M. Halik, S. Sanvito, G. S. Duesberg, V. Nicolosi, F. Hauke, A. Hirsch, J. N. Coleman, C. Backes, *ACS Nano* **2015**, 9, 6018-6030.
- [143] S. Presolski, M. Pumera, *Mater. Today* **2016**, 19, 140-145.
- [144] Y. Yu, F. Yang, X. F. Lu, Y. J. Yan, H. ChoYong, L. Ma, X. Niu, S. Kim, Y.-W. Son, D. Feng, S. Li, S.-W. Cheong, X. H. Chen, Y. Zhang, *Nat. Nanotechnol.* **2015**, 10, 270-276.
- [145] J. J. Cha, K. J. Koski, K. C. Y. Huang, K. X. Wang, W. Luo, D. Kong, Z. Yu, S. Fan, M. L. Brongersma, Y. Cui, *Nano Lett.* **2013**, 13, 5913-5918.
- [146] J. S. Kang, M. Ke, Y. Hu, *Nano Lett.* **2017**, 17, 1431-1438.
- [147] W. Bao, J. Wan, X. Han, X. Cai, H. Zhu, D. Kim, D. Ma, Y. Xu, J. N. Munday, H. D. Drew, M. S. Fuhrer, L. Hu, *Nat. Commun.* **2014**, 5, 4224.
- [148] F. Xiong, H. Wang, X. Liu, J. Sun, M. Brongersma, E. Pop, Y. Cui, *Nano Lett.* **2015**, 15, 6777-6784.
- [149] M. Boota, M. Pasini, F. Galeotti, W. Porzio, M.-Q. Zhao, J. Halim, Y. Gogotsi, *Chem. Mater.* **2017**, 29, 2731-2738.
- [150] C. Backes, R. J. Smith, N. McEvoy, N. C. Berner, D. McCloskey, H. C. Nerl, A. O'Neill, P. J. King, T. Higgins, D. Hanlon, N. Scheuschner, J. Maultzsch, L. Houben, G. S. Duesberg, J. F. Donegan, V. Nicolosi, J. N. Coleman, *Nat. Commun.* **2014**, 5, 4576.
- [151] P. Sun, R. Ma, X. Bai, K. Wang, H. Zhu, T. Sasaki, *Sci. Adv.* **2017**, 3, e1602629.
- [152] Z. Wang, J. Xuan, Z. Zhao, Q. Li, F. Geng, *ACS Nano* **2017**, 11, 11559-11565.
- [153] M. Osada, G. Takanaishi, B.-W. Li, K. Akatsuka, Y. Ebina, K. Ono, H. Funakubo, K. Takada, T. Sasaki, *Adv. Funct. Mater.* **2011**, 21, 3482-3487.

- [154] M. Osada, K. Akatsuka, Y. Ebina, H. Funakubo, K. Ono, K. Takada, T. Sasaki, *ACS Nano* **2010**, *4*, 5225-5232.
- [155] M. Osada, T. Sasaki, *Int. J. Appl. Ceram. Technol.* **2012**, *9*, 29-36.
- [156] M. Osada, Y. Ebina, K. Takada, T. Sasaki, *Adv. Mater.* **2006**, *18*, 295-299.
- [157] X. Dong, M. Osada, H. Ueda, Y. Ebina, Y. Kotani, K. Ono, S. Ueda, K. Kobayashi, K. Takada, T. Sasaki, *Chem. Mater.* **2009**, *21*, 4366-4373.
- [158] S. Ida, C. Ogata, M. Eguchi, W. J. Youngblood, T. E. Mallouk, Y. Matsumoto, *J. Am. Chem. Soc.* **2008**, *130*, 7052-7059.
- [159] S.-Y. Cho, H.-J. Koh, H.-W. Yoo, H.-T. Jung, *Chem. Mater.* **2017**, *29*, 7197-7205.
- [160] S.-Y. Cho, H.-J. Koh, H.-W. Yoo, J.-S. Kim, H.-T. Jung, *ACS Sensors* **2017**, *2*, 183-189.
- [161] K. Y. Ko, J.-G. Song, Y. Kim, T. Choi, S. Shin, C. W. Lee, K. Lee, J. Koo, H. Lee, J. Kim, T. Lee, J. Park, H. Kim, *ACS Nano* **2016**, *10*, 9287-9296.
- [162] D. Sarkar, X. Xie, J. Kang, H. Zhang, W. Liu, J. Navarrete, M. Moskovits, K. Banerjee, *Nano Lett.* **2015**, *15*, 2852-2862.
- [163] Z. Yin, B. Chen, M. Bosman, X. Cao, J. Chen, B. Zheng, H. Zhang, *Small* **2014**, *10*, 3537-3543.
- [164] Y. Kang, Y. Gong, Z. Hu, Z. Li, Z. Qiu, X. Zhu, P. M. Ajayan, Z. Fang, *Nanoscale* **2015**, *7*, 4482-4488.
- [165] X. Huang, Z. Zeng, S. Bao, M. Wang, X. Qi, Z. Fan, H. Zhang, *Nat. Commun.* **2013**, *4*, 1444.
- [166] J. R. Dunklin, P. Lafargue, T. M. Higgins, G. T. Forcherio, M. Benamara, N. McEvoy, D. K. Roper, J. N. Coleman, Y. Vaynzof, C. Backes, *npj 2D Materials and Applications* **2018**, *1*, 43.
- [167] J. I. Paredes, J. M. Munuera, S. Villar-Rodil, L. Guardia, M. Ayán-Varela, A. Pagán, S. D. Aznar-Cervantes, J. L. Cenis, A. Martínez-Alonso, J. M. D. Tascón, *ACS Appl. Mater. Interfaces* **2016**, *8*, 27974-27986.
- [168] A. Förster, S. Gemming, G. Seifert, D. Tománek, *ACS Nano* **2017**, *11*, 9989-9996.
- [169] F. Kishimoto, T. Ano, D. Mochizuki, T. Terauchi, M. M. Maitani, E. Suzuki, Y. Wada, *RSC Adv.* **2016**, *6*, 73830-73841.
- [170] W. Müller-Warmuth, R. Schöllhorn, *Progress in Intercalation Research*, Springer Science + Business Media, Dordrecht, **1994**.
- [171] M. S. Whittingham, A. J. Jacobson, *Intercalation Chemistry*, Academic Press, New York, **1982**.
- [172] S. Stankovich, D. A. Dikin, O. C. Compton, G. H. B. Dommett, R. S. Ruoff, S. T. Nguyen, *Chem. Mater.* **2010**, *22*, 4153-4157.
- [173] J. Yao, K. J. Koski, W. Luo, J. J. Cha, L. Hu, D. Kong, V. K. Narasimhan, K. Huo, Y. Cui, *Nat. Commun.* **2014**, *5*, 5670.
- [174] T. H. Bointon, I. Khrapach, R. Yakimova, A. V. Shytov, M. F. Craciun, S. Russo, *Nano Lett.* **2014**, *14*, 1751-1755.
- [175] K. Lu, Z. Hu, Z. Xiang, J. Ma, B. Song, J. Zhang, H. Ma, *Angew. Chem., Int. Ed.* **2016**, *55*, 10448-10452.
- [176] M. Kühne, F. Paolucci, J. Popovic, P. M. Ostrovsky, J. Maier, J. H. Smet, *Nat. Nanotechnol.* **2017**, *12*, 895-900.
- [177] W. M. R. Divigalpittya, R. F. Frindt, S. R. Morrison, *Science* **1989**, *246*, 369-371.
- [178] G. Alberti, M. Casciola, U. Costantino, R. Vivani, *Adv. Mater.* **1996**, *8*, 291-303.
- [179] G. Cao, H. G. Hong, T. E. Mallouk, *Acc. Chem. Res.* **1992**, *25*, 420-427.
- [180] A. Clearfield, J. A. Stynes, *J. Inorg. Nucl. Chem.* **1964**, *26*, 117-129.
- [181] A. Winkler, E. Thilo, *Z. Anorg. Allg. Chem.* **1966**, *346*, 92-112.
- [182] Y. Piffard, S. Oyetola, S. Courant, A. Lachgar, *J. Solid State Chem.* **1985**, *60*, 209-213.
- [183] Y. Piffard, A. Lachgar, M. Tournoux, *Rev. Chim. Miner.* **1985**, *22*, 101-106.
- [184] Y. Piffard, A. Lachgar, M. Tournoux, *J. Solid State Chem.* **1985**, *58*, 253-256.
- [185] E. Husson, A. Lachgar, Y. Piffard, *J. Solid State Chem.* **1988**, *74*, 138-146.
- [186] S. Zouad, J. Jeanjean, C. Loos-Neskovic, M. Fedoroff, Y. Piffard, *J. Radioanal. Nucl. Chem.* **1994**, *182*, 193-204.
- [187] B. Baradie, C. Poinsignon, J. Y. Sanchez, Y. Piffard, G. Vitter, N. Bestaoui, D. Foscallo, A. Denoyelle, D. Delabouglise, M. Vaujany, *J. Power Sources* **1998**, *74*, 8-16.
- [188] S. Deniard-Courant, Y. Piffard, P. Barboux, J. Livage, *Solid State Ionics* **1988**, *27*, 189-194.

- [189] Y. Piffard, A. Verbaere, A. Lachgar, S. Deniard-Courant, M. Tournoux, *Rev. Chim. Miner.* **1986**, *23*, 766-775.
- [190] Y. Piffard, A. Verbaere, S. Oyetola, S. Deniard-Courant, M. Tournoux, *Eur. J. Solid State Inorg. Chem.* **1989**, *26*, 113-127.
- [191] S. Oyetola, A. Verbaere, Y. Piffard, M. Tournoux, *Eur. J. Solid State Inorg. Chem.* **1988**, *25*, 259-278.
- [192] S. Oyetola, A. Verbaere, D. Guyomard, Y. Piffard, M. Tournoux, *Eur. J. Solid State Inorg. Chem.* **1989**, *26*, 175-191.
- [193] A. Lachgar, S. Deniard-Courant, Y. Piffard, *J. Solid State Chem.* **1988**, *73*, 572-576.
- [194] G. Alberti, M. Casciola, U. Costantino, *J. Colloid Interface Sci.* **1985**, *107*, 256-263.
- [195] J.-C. P. Gabriel, F. Camerel, B. J. Lemalre, H. Desvaux, P. Davidson, P. Batail, *Nature* **2001**, *413*, 504-508.
- [196] F. Camerel, J. C. P. Gabriel, P. Batail, P. Panine, P. Davidson, *Langmuir* **2003**, *19*, 10028-10035.
- [197] J. G. Decaillon, Y. Andres, J. C. Abbe, M. Tournoux, *Solid State Ionics* **1998**, *112*, 143-152.
- [198] C. S. Griffith, V. Luca, J. Cochrane, J. V. Hanna, *Microporous Mesoporous Mater.* **2008**, *111*, 387-403.
- [199] E. Husson, Y. Repelin, Y. Piffard, A. Verbaere, *Eur. J. Solid State Inorg. Chem.* **1995**, *32*, 1077-1088.
- [200] F. Taulelle, C. Sanchez, J. Livage, A. Lachgar, Y. Piffard, *J. Phys. Chem. Solids* **1988**, *49*, 299-305.
- [201] E. Husson, F. Genet, A. Lachgar, Y. Piffard, *J. Solid State Chem.* **1988**, *75*, 305-312.
- [202] E. Wang, M. Greenblatt, *Chem. Mater.* **1991**, *3*, 542-546.
- [203] A. B. Yaroslavtsev, A. E. Nikolaev, *Mendeleev Commun.* **1995**, 136-137.
- [204] A. B. Yaroslavtsev, V. F. Chuvaev, R. Sonntag, *Solid State Ionics* **1997**, *97*, 277-280.
- [205] E. Husson, F. M. Durand-Le, C. Doremieux-Morin, S. Deniard, Y. Piffard, *Solid State Ionics* **1989**, *35*, 133-142.
- [206] V. A. Tarnopol'skii, A. B. Yaroslavtsev, *Zh. Neorg. Khim.* **2005**, *50*, 1221-1224.
- [207] A. B. Yaroslavtsev, V. A. Tarnopol'skii, *Zh. Neorg. Khim.* **1997**, *42*, 548-552.
- [208] W. A. England, M. G. Cross, A. Hamnett, P. J. Wiseman, J. B. Goodenough, *Solid State Ionics* **1980**, *1*, 231-249.
- [209] P. Barboux, R. Morineau, J. Livage, *Solid State Ionics* **1988**, *27*, 221-225.
- [210] P. Krishnan, J.-S. Park, C.-S. Kim, *Eur. Polym. J.* **2007**, *43*, 4019-4027.
- [211] H. B. Attia, C. Iojoiu, J. C. Leprêtre, J. Guindet, N. Bellakhal, J. Y. Sanchez, *Energy Procedia* **2012**, *14*, 1717-1722.
- [212] P. Genova-Dimitrova, B. Baradie, D. Foscallo, C. Poinignon, J. Y. Sanchez, *J. Membr. Sci.* **2001**, *185*, 59-71.
- [213] N. Miura, H. Mizuno, N. Yamazoe, *Jpn. J. Appl. Phys., Part 2* **1988**, *27*, 931-933.
- [214] G. K. Prasad, N. Kumada, J. Yamanaka, Y. Yonesaki, T. Takei, N. Kinomura, *J. Colloid Interface Sci.* **2006**, *297*, 654-659.
- [215] P. Ganter, Master thesis, University of Munich (LMU), **2014**.
- [216] R. E. Schaak, T. E. Mallouk, *Chem. Mater.* **2002**, *14*, 1455-1471.
- [217] K. G. Sanjaya Ranmohotti, E. Josepha, J. Choi, J. Zhang, J. B. Wiley, *Adv. Mater.* **2011**, *23*, 442-460.
- [218] M. Osada, T. Sasaki, *Dalton Trans.* **2018**.
- [219] A. J. Jacobson, J. W. Johnson, J. T. Lewandowski, *Inorg. Chem.* **1985**, *24*, 3727-3729.
- [220] M. Dion, M. Ganne, M. Tournoux, *Mater. Res. Bull.* **1981**, *16*, 1429-1435.
- [221] A. J. Jacobson, J. W. Johnson, J. T. Lewandowski, *Mater. Res. Bull.* **1987**, *22*, 45-51.
- [222] A. J. Jacobson, J. T. Lewandowski, J. W. Johnson, *Mater. Res. Bull.* **1990**, *25*, 679-686.
- [223] M. M. J. Treacy, S. B. Rice, A. J. Jacobson, J. T. Lewandowski, *Chem. Mater.* **1990**, *2*, 279-286.
- [224] Y. Ebina, T. Sasaki, M. Harada, M. Watanabe, *Chem. Mater.* **2002**, *14*, 4390-4395.
- [225] Y. Ebina, T. Sasaki, M. Watanabe, *Solid State Ionics* **2002**, *151*, 177-182.
- [226] Y.-H. Kim, H.-J. Kim, M. Osada, B.-W. Li, Y. Ebina, T. Sasaki, *ACS Appl. Mater. Interfaces* **2014**, *6*, 19510-19514.
- [227] B.-W. Li, M. Osada, Y. Ebina, K. Akatsuka, K. Fukuda, T. Sasaki, *ACS Nano* **2014**, *8*, 5449-5461.
- [228] M. Fang, C. H. Kim, G. B. Saupe, H.-N. Kim, C. C. Waraksa, T. Miwa, A. Fujishima, T. E. Mallouk, *Chem. Mater.* **1999**, *11*, 1526-1532.

- [229] R. E. Schaak, T. E. Mallouk, *Chem. Mater.* **2000**, *12*, 2513-2516.
- [230] H. Hata, Y. Kobayashi, V. Bojan, W. J. Youngblood, T. E. Mallouk, *Nano Lett.* **2008**, *8*, 794-799.
- [231] P. Xu, T. J. Milstein, T. E. Mallouk, *ACS Appl. Mater. Interfaces* **2016**, *8*, 11539-11547.
- [232] O. C. Compton, E. C. Carroll, J. Y. Kim, D. S. Larsen, F. E. Osterloh, *J. Phys. Chem. C* **2007**, *111*, 14589-14592.
- [233] O. C. Compton, F. E. Osterloh, *J. Phys. Chem. C* **2009**, *113*, 479-485.
- [234] E. M. Sabio, M. Chi, N. D. Browning, F. E. Osterloh, *Langmuir* **2010**, *26*, 7254-7261.
- [235] E. M. Sabio, R. L. Chamousis, N. D. Browning, F. E. Osterloh, *J. Phys. Chem. C* **2012**, *116*, 3161-3170.
- [236] T. Tokumitsu, K. Toda, T. Aoyagi, D. Sakuraba, K. Uematsu, M. Sato, *J. Ceram. Soc. Jpn.* **2006**, *114*, 795-797.
- [237] K. S. Virdi, Y. Kauffmann, C. Ziegler, P. Ganter, B. V. Lotsch, W. D. Kaplan, P. Blaha, C. Scheu, *Phys. Rev. B* **2013**, *87*, 115108.
- [238] N. A. Benedek, *Inorg. Chem.* **2014**, *53*, 3769-3777.
- [239] M. A. Bizeto, V. R. L. Constantino, H. F. Brito, *J. Alloys Compd.* **2000**, *311*, 159-168.
- [240] B.-W. Li, M. Osada, Y. Ebina, T. C. Ozawa, R. Ma, T. Sasaki, *Appl. Phys. Lett.* **2010**, *96*, 182903.
- [241] F. Hiroshi, I. Toshiyuki, Y. Shoji, *Chem. Lett.* **1997**, *26*, 703-704.
- [242] K. Domen, J. Yoshimura, T. Sekine, A. Tanaka, T. Onishi, *Catal. Lett.* **1990**, *4*, 339-343.
- [243] Y. Chen, X. Zhao, H. Ma, S. Ma, G. Huang, Y. Makita, X. Bai, X. Yang, *J. Solid State Chem.* **2008**, *181*, 1684-1694.
- [244] H. Yim, S.-Y. Yoo, S. Nahm, S.-J. Hwang, S.-J. Yoon, J.-W. Choi, *Ceram. Int.* **2013**, *39*, 611-.
- [245] T. I. Draskovic, T. Wang, C. N. Henderson, T. E. Mallouk, *Int. J. Hydrogen Energy* **2014**, *39*, 4576-4580.
- [246] J. Gopalakrishnan, S. Uma, V. Bhat, *Chem. Mater.* **1993**, *5*, 132-136.
- [247] S. Uma, J. Gopalakrishnan, *Chem. Mater.* **1994**, *6*, 907-912.
- [248] Z. Zhong, W. Ding, W. Hou, Y. Chen, X. Chen, Y. Zhu, N. Min, *Chem. Mater.* **2001**, *13*, 538-542.
- [249] S. Tahara, Y. Sugahara, *Langmuir* **2003**, *19*, 9473-9478.
- [250] K. Akatsuka, G. Takanashi, Y. Ebina, M.-a. Haga, T. Sasaki, *J. Phys. Chem. C* **2012**, *116*, 12426-12433.
- [251] K. S. Virdi, Y. Kauffmann, C. Ziegler, P. Ganter, P. Blaha, B. V. Lotsch, W. D. Kaplan, C. Scheu, *J. Phys. Chem. C* **2016**, *120*, 11170-11179.
- [252] R. Ma, Y. Bando, T. Sasaki, *J. Phys. Chem. B* **2004**, *108*, 2115-2119.
- [253] C. Ziegler, S. Werner, M. Bugnet, M. Wörsching, V. Duppel, G. A. Botton, C. Scheu, B. V. Lotsch, *Chem. Mater.* **2013**, *25*, 4892-4900.
- [254] L. Li, R. Ma, Y. Ebina, K. Fukuda, K. Takada, T. Sasaki, *J. Am. Chem. Soc.* **2007**, *129*, 8000-8007.
- [255] L. Gao, Q. Gao, Q. Wang, S. Peng, J. Shi, *Biomaterials* **2005**, *26*, 5267-5275.
- [256] L. Chang, M. A. Holmes, M. Waller, F. E. Osterloh, A. J. Moule, *J. Mater. Chem.* **2012**, *22*, 20443-20450.
- [257] T. Shibata, K. Fukuda, Y. Ebina, T. Kogure, T. Sasaki, *Adv. Mater.* **2008**, *20*, 231-235.
- [258] B.-W. Li, M. Osada, Y. Ebina, S. Ueda, T. Sasaki, *J. Am. Chem. Soc.* **2016**, *138*, 7621-7625.
- [259] C. Ziegler, T. Dennenwaldt, D. Weber, V. Duppel, C. Kamella, F. Podjaski, B. Tuffey, I. Moudrakovski, C. Scheu, B. V. Lotsch, *Z. Anorg. Allg. Chem.* **2017**, *643*, 1668-1680.
- [260] Y. Okamoto, S. Ida, J. Hyodo, H. Hagiwara, T. Ishihara, *J. Am. Chem. Soc.* **2011**, *133*, 18034-18037.
- [261] S. Ida, Y. Okamoto, S. Koga, H. Hagiwara, T. Ishihara, *RSC Adv.* **2013**, *3*, 11521-11524.
- [262] M. Osada, in *Inorganic Nanosheets and Nanosheet-Based Materials: Fundamentals and Applications of Two-Dimensional Systems* (Eds.: T. Nakato, J. Kawamata, S. Takagi), Springer Japan, Tokyo, **2017**, pp. 347-356.
- [263] M. Osada, T. Sasaki, *J. Mater. Chem.* **2009**, *19*, 2503-2511.
- [264] K. Hyung-Jun, O. Minoru, S. Takayoshi, *Jpn. J. Appl. Phys.* **2016**, *55*, 1102A31-1102A36.
- [265] J. R. Askim, M. Mahmoudi, K. S. Suslick, *Chem. Soc. Rev.* **2013**, *42*, 8649-8682.
- [266] A. Hulanicki, S. Glab, F. Ingman, *Pure Appl. Chem.* **1991**, *63*, 1247.
- [267] P. Gründler, *Chemical Sensors An Introduction for Scientists and Engineers*, Springer Berlin Heidelberg, Berlin, Heidelberg, **2007**.

- [268] W. Yang, L. Gan, H. Li, T. Zhai, *Inorg. Chem. Front.* **2016**, *3*, 433-451.
- [269] S. Yang, C. Jiang, S.-h. Wei, *Appl. Phys. Rev.* **2017**, *4*, 021304.
- [270] P. K. Kannan, D. J. Late, H. Morgan, C. S. Rout, *Nanoscale* **2015**, *7*, 13293-13312.
- [271] C. Fenzl, T. Hirsch, O. S. Wolfbeis, *Angew. Chem., Int. Ed.* **2014**, *53*, 3318-3335.
- [272] I. Pavlichenko, Dissertation, University of Munich (LMU), **2014**.
- [273] A. Ranft, Dissertation, University of Munich (LMU), **2015**.
- [274] Y. Zhao, Z. Xie, H. Gu, C. Zhu, Z. Gu, *Chem. Soc. Rev.* **2012**, *41*, 3297-3317.
- [275] L. D. Bonifacio, B. V. Lotsch, D. P. Puzzo, F. Scotognella, G. A. Ozin, *Adv. Mater.* **2009**, *21*, 1641-1646.
- [276] M. E. Calvo, S. Colodrero, N. Hidalgo, G. Lozano, C. Lopez-Lopez, O. Sanchez-Sobrado, H. Miguez, *Energy Environ. Sci.* **2011**, *4*, 4800-4812.
- [277] O. Stenzel, in *The Physics of Thin Film Optical Spectra: An Introduction*, Springer International Publishing, Cham, **2016**, pp. 131-161.
- [278] G. Lu, J. T. Hupp, *J. Am. Chem. Soc.* **2010**, *132*, 7832-7833.
- [279] J. Gao, T. Gao, Y. Y. Li, M. J. Sailor, *Langmuir* **2002**, *18*, 2229-2233.
- [280] T. Gao, J. Gao, M. J. Sailor, *Langmuir* **2002**, *18*, 9953-9957.
- [281] H. Xu, P. Wu, C. Zhu, A. Elbaz, Z. Z. Gu, *J. Mater. Chem. C* **2013**, *1*, 6087-6098.
- [282] B. V. Lotsch, G. A. Ozin, *ACS Nano* **2008**, *2*, 2065-2074.
- [283] E. R. Kleinfield, G. S. Ferguson, *Chem. Mater.* **1995**, *7*, 2327-2331.
- [284] B. V. Lotsch, G. A. Ozin, *J. Am. Chem. Soc.* **2008**, *130*, 15252-15253.
- [285] B. V. Lotsch, G. A. Ozin, *Adv. Mater.* **2008**, *20*, 4079-4084.
- [286] H. Chi, Y. J. Liu, F. Wang, C. He, *ACS Appl. Mater. Interfaces* **2015**, *7*, 19882-19886.
- [287] E. Colusso, G. Perotto, Y. Wang, M. Sturaro, F. Omenetto, A. Martucci, *J. Mater. Chem. C* **2017**, *5*, 3924-3931.
- [288] Y. Kang, J. J. Walsh, T. Gorishnyy, E. L. Thomas, *Nat. Mater.* **2007**, *6*, 957.
- [289] H. S. Kang, J. Lee, S. M. Cho, T. H. Park, M. J. Kim, C. Park, S. W. Lee, K. L. Kim, D. Y. Ryu, J. Huh, E. L. Thomas, C. Park, *Adv. Mater.* **2017**, *29*, 1700084.
- [290] A. Noro, Y. Tomita, Y. Shinohara, Y. Sageshima, J. J. Walsh, Y. Matsushita, E. L. Thomas, *Macromolecules* **2014**, *47*, 4103-4109.
- [291] T. J. Park, S. K. Hwang, S. Park, S. H. Cho, T. H. Park, B. Jeong, H. S. Kang, D. Y. Ryu, J. Huh, E. L. Thomas, C. Park, *ACS Nano* **2015**, *9*, 12158-12167.
- [292] E. P. Chan, J. J. Walsh, A. M. Urbas, E. L. Thomas, *Adv. Mater.* **2013**, *25*, 3934-3947.
- [293] Y. Fan, S. Tang, E. L. Thomas, B. D. Olsen, *ACS Nano* **2014**, *8*, 11467-11473.
- [294] H. S. Lim, J.-H. Lee, J. J. Walsh, E. L. Thomas, *ACS Nano* **2012**, *6*, 8933-8939.
- [295] Z. Wang, J. Zhang, J. Xie, C. Li, Y. Li, S. Liang, Z. Tian, T. Wang, H. Zhang, H. Li, W. Xu, B. Yang, *Adv. Funct. Mater.* **2010**, *20*, 3784-3790.
- [296] K.-D. Kreuer, A. Rabenau, W. Weppner, *Angew. Chem., Int. Ed.* **1982**, *21*, 208-209.
- [297] T. Norby, *Solid State Ionics* **1999**, *125*, 1-11.
- [298] K.-D. Kreuer, *Chem. Mater.* **1996**, *8*, 610-641.
- [299] B.-H. Wee, W.-H. Khoh, A. K. Sarker, C.-H. Lee, J.-D. Hong, *Nanoscale* **2015**, *7*, 17805-17811.
- [300] S. Borini, R. White, D. Wei, M. Astley, S. Haque, E. Spigone, N. Harris, J. Kivioja, T. Ryhänen, *ACS Nano* **2013**, *7*, 11166-11173.
- [301] V. F. Lvovich, in *Impedance Spectroscopy*, John Wiley & Sons, Inc., **2012**, pp. 1-21.
- [302] K.-D. Kreuer, in *Proton Conductors: Solids, Membranes and Gels - Materials and Devices* (Ed.: P. Colomban), Cambridge University Press, Cambridge, **1992**, pp. 409-417.
- [303] J. G. Calvert, *Pure Appl. Chem.* **1990**, *62*, 2167.
- [304] D. R. Thevenot, K. Tóth, R. A. Durst, G. S. Wilson, *Pure Appl. Chem.* **1999**, *71*, 2333.

- [305] J. Vessman, I. Stefan Raluca, F. van Staden Jacobus, K. Danzer, W. Lindner, T. Burns Duncan, A. Fajgelj, H. Müller, *Pure Appl. Chem.* **2001**, 73, 1381.
- [306] K. Laqua, B. Schrader, G. G. Hoffmann, D. S. Moore, T. Vo-Dinh, *Pure Appl. Chem.* **1995**, 67, 1745.
- [307] Q. Y., Y. S., *Adv. Funct. Mater.* **2007**, 17, 1345-1352.
- [308] N. Yamazoe, Y. Shimizu, *Sens. Actuators* **1986**, 10, 379-398.
- [309] Y. Yao, X. Chen, J. Zhu, B. Zeng, Z. Wu, X. Li, *Nanoscale Res. Lett.* **2012**, 7, 363.
- [310] F. Schedin, A. K. Geim, S. V. Morozov, E. W. Hill, P. Blake, M. I. Katsnelson, K. S. Novoselov, *Nat. Mater.* **2007**, 6, 652.
- [311] K. Lee, R. Gatensby, N. McEvoy, T. Hallam, G. S. Duesberg, *Adv. Mater.* **2013**, 25, 6699-6702.
- [312] J. T. Robinson, F. K. Perkins, E. S. Snow, Z. Wei, P. E. Sheehan, *Nano Lett.* **2008**, 8, 3137-3140.
- [313] S.-Y. Cho, Y. Lee, H.-J. Koh, H. Jung, J.-S. Kim, H.-W. Yoo, J. Kim, H.-T. Jung, *Adv. Mater.* **2016**, 28, 7020-7028.
- [314] S.-Y. Cho, S. J. Kim, Y. Lee, J.-S. Kim, W.-B. Jung, H.-W. Yoo, J. Kim, H.-T. Jung, *ACS Nano* **2015**, 9, 9314-9321.
- [315] F. K. Perkins, A. L. Friedman, E. Cobas, P. M. Campbell, G. G. Jernigan, B. T. Jonker, *Nano Lett.* **2013**, 13, 668-673.
- [316] S. J. Kim, H.-J. Koh, C. E. Ren, O. Kwon, K. Maleski, S.-Y. Cho, B. Anasori, C.-K. Kim, Y.-K. Choi, J. Kim, Y. Gogotsi, H.-T. Jung, *ACS Nano* **2018**, 12, 986-993.
- [317] R. J. D. Tilley, in *Understanding Solids*, John Wiley & Sons, Ltd, **2005**, pp. 337-362.
- [318] R. J. D. Tilley, in *Perovskites*, John Wiley & Sons, Ltd, **2016**, pp. 176-216.
- [319] P. A. Tipler, G. Mosca, in *Physik: für Wissenschaftler und Ingenieure* (Eds.: P. A. Tipler, G. Mosca, J. Wagner), Springer Berlin Heidelberg, Berlin, Heidelberg, **2015**, pp. 761-797.
- [320] K. Akatsuka, M.-a. Haga, Y. Ebina, M. Osada, K. Fukuda, T. Sasaki, *ACS Nano* **2009**, 3, 1097-1106.
- [321] K. Muhammad Shuaib, K. Hyung-Jun, T. Takaaki, E. Yasuo, S. Takayoshi, O. Minoru, *Appl. Phys. Express* **2017**, 10, 091501.

2 Implementation of $H_3Sb_3P_2O_{14}$ nanosheets in touchless positioning interfaces

2.1 Touchless Optical Finger Motion Tracking Based on 2D Nanosheets with Giant Moisture Responsiveness

Katalin Szendrei, Pirmin Ganter,* Olalla Sánchez-Sobrado, Roland Eger, Alexander Kuhn, and Bettina V. Lotsch*

published: *Adv. Mater.* **2015**, 27, 6341-6348.

DOI: 10.1002/adma.201503463

<http://onlinelibrary.wiley.com/doi/10.1002/adma.201503463/abstract>

*equally contributed

Copyright © 2015 WILEY-VCH Verlag GmbH & Co. KGaA, Weinheim. Reproduced with the permission of WILEY-VCH.

Contribution of P.G.:

P.G. carried out the nanosheet synthesis, characterization and contributed to the experimental optimization of the spin-coating process of the nanosheets. P.G. also carried out the impedance measurements for the humidity sensing experiments of the thin films under supervision of A.K.. P.G. wrote the nanosheet synthesis, characterization and electrochemical humidity sensor and axial touchless positioning interface part and contributed to the abstract, introduction, results and discussion as well as the conclusion section. In addition, P.G. contributed to the preparation of the graphical material and literature screening.

Abstract

The exponential growth of digital technology has triggered the need for input devices with high spatio-temporal fidelity. Next-generation user interfaces relying on touchless operating principles may be realized by sensors with a high local sensitivity to a relevant external stimulus. Herein, we present a novel optical concept for touchless positioning interfaces operating as ultrasensitive humidity sensors based on 2D phosphoantimonate nanosheets. First, by utilizing the remarkable moisture-induced swelling capacity of the nanosheets, a resistive thin film device with a dynamic ionic conductance range covering five orders of magnitude over the complete humidity range was realized, corresponding to a 170-fold signal increase triggered by the humidity sheath of a finger. This giant moisture response was implemented in a photonic sensing platform based on porous 1D PCs with a

high selectivity for water vapor. The unprecedented sensitivity toward humidity is demonstrated by an ultrafast stop band shift of the BP by 517 nm, thus translating into a full spectrum color-change under touchless conditions. Moreover, we demonstrate reversible, complete transparency switching through RI matching. The observed ultra-sensitive, spatially confined color-change near the fingertip provides a unique tool enabling touchless tracking of finger movements based on a simple optical read-out.

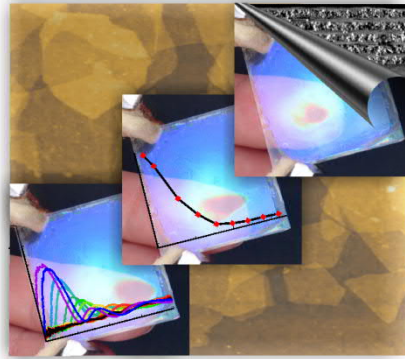


Table of Content: A new optical touchless positioning interface-based on ultrasensitive humidity responsive 1D PCs utilizing the giant moisture dependent swelling capacity of 2D phosphatoantimonate nanosheets is presented. The spatially confined, full spectral color change combined with reversible transparency switching induced by the humidity sheath of a human finger allows for real time, true color lateral finger motion tracking under touchless conditions.

2.1.1 Introduction

One of the key challenges in the development of next-generation electronic devices such as laptops, smartphones, or tablets is the design of powerful hardware control systems. In this context, humidity sensors exhibiting high spatial sensitivity to the degree of environmental moisture are promising candidates for smart TPI, which operate based on local variations in the humid atmosphere around a pointing object, such as the human finger.^[1]

Here, we introduce a novel optical TPI concept for next-generation interactive user interfaces based on a PC humidity sensing platform, which enables contact-less tracking of finger motion with direct optical feedback in a stand-alone fashion.

1D PCs, referred to as BSs, are periodic multilayer systems comprising two materials with different refractive indices (RI),^[2] which are capable of translating environmental stimuli into an optical read-out, induced by a shift in their stop band position.^[3-5] Besides, these periodic structures are capable of tuning the displayed color while keeping their transparency, thus opening up the possibility to fabricate smart windows with tunable color as a function of the environmental conditions.

Although porous BSs have been extensively used to detect organic vapors and humidity through RI changes induced by infiltration with analytes,^[6-12] the observed shifts in the BP are rarely larger than a few tens of nanometers, and typically well below 100 nm,^[9-11,13] which limits the resolution in terms of humidity sensing.^[14] An alternative mechanism to trigger changes in the structural color of a BS is to

modify the layer thicknesses,^[3,4,6,15-18] which is particularly powerful when integrating dimensionally flexible polymer layers into a BS.^[3,16,17] The demonstrated panchromatic BP shift in such systems induced by liquid water however comes at the expense of low thermal and chemical stability, as well as slow response times of the active organic layers to organic solvent vapors or humidity. The largest shift for photonic humidity sensors was reported by Tian *et al.* using a photonic hydrogel with a stop band shift of around 300 nm and a response time in the range of 100 s.^[19] Xuan *et al.* reported a Fe_2O_3 NP-polymer hybrid sensor with a stop band shift of around 150-230 nm, depending on the polymer cross-linking degree. Here again, due to the characteristic polymer swelling, the response time was in the range of hours.^[20] A similar sensor performance was reported by Kim *et al.*, who observed a stop band shift of 137 nm in a polymer-based 3D opal structure with high cycling stability of thousands of cycles.^[21] In addition, several humidity sensors were reported with smaller stopband shifts in the range of tens of nanometers and response times on the order of a few seconds.^[22,23] Recently, Steele *et al.*^[24] and Hawkeye and Brett^[25] presented mesoporous TiO_2 gratings used for humidity applications, which show an ultrafast response time in the subsecond range, but rather small stop band shifts (and therefore resolution) on the order of 30 nm.

Here, we replace the dimensionally flexible organic component in BS by phosphatoantimonic acid $H_3Sb_3P_2O_{14}$ nanosheets^[26,27] with giant moisture responsiveness. The protonic bulk material, which has long been known for its remarkable swelling characteristics driven by moisture and the resulting humidity-dependent proton conductivity,^[28,29] can be readily delaminated into 2D nanosheets, giving rise to stable liquid crystalline suspensions with anisotropic optical properties.^[26,27]

The integration of other 2D nanosheets into resistive sensing devices has already led to a superior sensing performance as compared to the corresponding bulk materials, exemplified by a VS_2 nanosheet-based TPI featuring moisture-sensitive electric, rather than ionic conductance.^[1] While flexible in their design, these resistive VS_2 nanosheet sensors have certain drawbacks such as low chemical stability under ambient conditions and rather poor sensitivity. Further examples of nanosheet-based humidity sensors include NbS_2 ,^[30] GO ,^[31,32] MoS_2 ,^[33] and ZnO .^[34] Nearly all of these nanosheet sensors have either slow response times (*e.g.*, 600 s for ZnO),^[34] or low sensitivity^[30,32,33] (*e.g.*, factor 5 increase in resistance for a change from 6% RH to 74% RH for NbS_2).^[30] Therefore, it still remains a major challenge to design nanosheet-based humidity sensors for real-time interaction devices with sufficient sensitivity.

In this work, we fashion thin films of phosphatoantimonic acid nanosheets into chemically stable, transparent, and low-cost humidity sensing devices operating either with resistive or optical read out, both of which can be applied as TPI based on spatially resolved humidity tracking. Drawing on the smoother (*i.e.*, less stepwise) RH-dependent swelling behavior of the nanosheets compared to the bulk material^[28] and the fabrication of mechanically stable, yet flexible thin films, we detect a significantly enhanced response to a humid pointer as compared to existing devices. The novel optical TPI introduced in this work is capable of contactless finger movement tracking through a combination of

unique features such as ultra large stop band shift (>500 nm), along with reversible transparency switching and a fast response time.

2.1.2 Results and discussion

The layered phosphatoantimonate $K_3Sb_3P_2O_{14}$ and the proton exchanged phosphatoantimonic acid $H_3Sb_3P_2O_{14}$ (Figure S2.1, Supporting Information) were synthesized by a conventional solid-state reaction followed by ion exchange with 8M HNO_3 (Figures S2.2, S2.3, Table S2.1).^[28,35] The protonation and exfoliation process in pure water is schematically shown in Figure 2.1a. The schlieren texture and the Tyndall effect of the resulting aqueous suspension indicate successful delamination and the anisotropic nature of the nanosheets (Figure S2.4), while drop-casting the suspension gives rise to randomly overlapping, *c*-oriented nanosheets (Figure 2.1b, c; Figures S2.5, S2.6). The thickness of the $Sb_3P_2O_{14}^{3-}$ nanosheets as determined by AFM amounts to 1.3 ± 0.1 nm on average (Figure 2.1b), which agrees well with the crystallographic thickness of 1.10 nm for a single $Sb_3P_2O_{14}^{3-}$ layer.^[26,35] TEM-EDX analysis and SEM-EDX analysis confirm the expected elemental composition (Tables S2.2 and S2.3) and the *d* values of the SAD pattern agree well with those of the nanosheet pellet by PXRD (Table S2.4). The XRD pattern of a turbostratically disordered nanosheet pellet obtained by centrifugation at 18000 rpm can be indexed on the basis of a trigonal layer group (Figure S2.7) and exhibits Warren like peak profiles of the (*hk*) reflections typical of 2D materials.^[36,37]

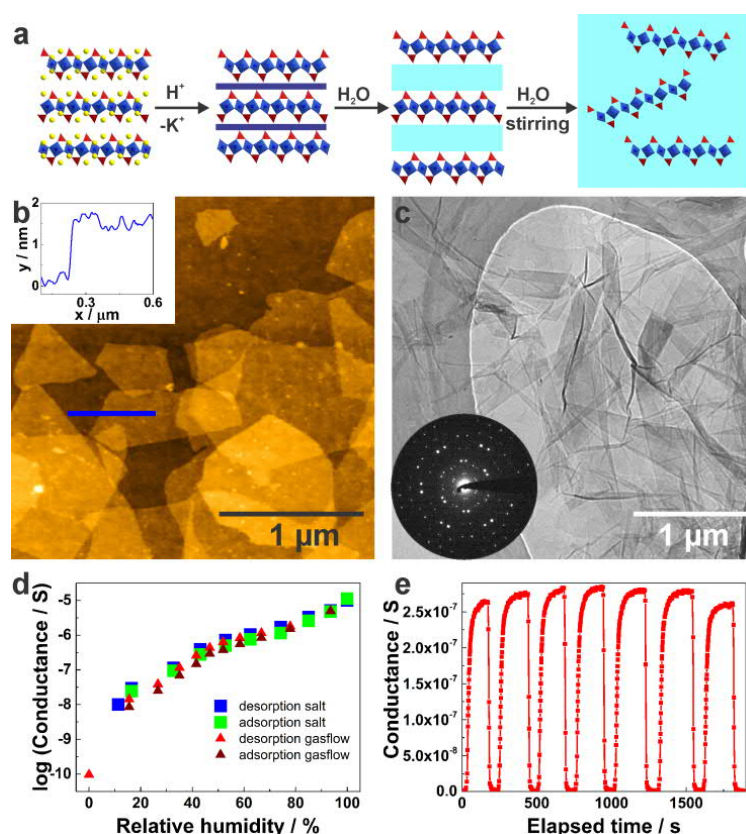


Figure 2.1. Exfoliation scheme, nanosheet characterization, and conductance-based humidity sensing. a) Schematic process of ion exchange and exfoliation for $K_3Sb_3P_2O_{14}$, assuming that swelling takes place first, followed by exfoliation. b) AFM image of randomly oriented $Sb_3P_2O_{14}^{3-}$ nanosheets with a corresponding height profile of a single nanosheet labeled by the blue line. c) TEM image of overlapping exfoliated $Sb_3P_2O_{14}^{3-}$ nanosheets with a representative SAD pattern of the sample, which here is the pattern resulting from two nanosheets rotated against each other. d) Ionic conductance as a function of RH obtained from measurements above saturated salt solutions (salt adsorption and desorption) and with an argon flow setup (gasflow desorption and adsorption) for a film device with a thickness of 112 nm. e) Cycling behavior of the same film device between 0% and 47% RH, measured in a chamber with an approximate volume of 100 mL.^[38]

Nanosheet thin films with thicknesses around 100 nm can directly be used as resistive humidity sensors. The transparent thin film device is displayed in Figure S2.8 along with two SEM cross-section images from different areas, which illustrate the ultrathin nature of the device. Drawing on the well-known moisture-dependent proton conductivity of phosphoantimonic acid,^[28] we first measured the RH-dependent ionic conductance between 0% and 100% RH using two methods, a gas flow setup and saturated salt solutions (for details see Figure 2.1d; Figures S2.8, S2.9, S2.10). Remarkably, we observed an increase in conductance of the sample with increasing RH by five orders of magnitude over the complete humidity range, with only a small hysteresis loop (Figure 2.1d), which is at least three orders of magnitude larger than that observed for VS_2 nanosheet devices. To the best of our knowledge, this level of sensitivity is the highest observed for any nanosheet-based conductance or resistance humidity sensor reported to date.^[1,30-34] The cycling behavior of the thin film device between 0% and 47% RH shows good reversibility (Figure 2.1e).^[38] Notably, the RH dependence of the proton conductance of our thin film device is quite different from that of phosphoantimonic acid

bulk material reported in the literature.^[28] While the bulk material shows distinct step like behavior, this is not the case for the nanosheet film device. We attribute the smoother increase in conductance to the smaller particle size, leading to an increased amount of grain boundary adsorption, and to the non-uniform interlayer space resulting in less well-defined water adsorption sites between the randomly oriented nanosheets. Such textural effects likely change the water uptake mechanism from that of a lattice hydrate (bulk material) to that of a particle hydrate (nanosheets), which accommodates a large amount of water molecules on the internal and external surfaces of the nanosheets.

To further explore the sensing capabilities of the phosphoantimonate nanosheets, thin films with tunable thicknesses in the range of 50-150 nm were prepared by spin-coating the colloidal suspension of exfoliated nanosheets at different spinning speeds. Upon increasing the RH from 0-100%, the nanosheet film swells to the double of its thickness (*e.g.*, Figure S2.11: from 72 to 128 nm). Hereby, a particularly pronounced change is observed in the high humidity range above 90% RH (112-128 nm) as determined by spectroscopic ellipsometry. This effect is accompanied by a RI decrease (from 1.62 to 1.52), again with a pronounced drop in the RH range above 90%, corresponding to the water uptake and the resulting thickness change. The continuous RI decrease in the higher RH range then is the result of mixing the refractive indices of water (1.33) and the nanosheets. The RI increase and the nearly unchanged layer thickness in the low humidity range up to 10% RH are rationalized by the structural pore filling of the randomly restacked nanosheets (Figure S2.11). While the bulk material shows distinct step like swelling behavior,^[28] this is not the case for the nanosheet film device. We attribute the smoother increase to the same morphology reasons as discussed for the conductance changes.

Inspired by the unprecedentedly large swelling properties of the nanosheet films, BSs were assembled from $H_3Sb_3P_2O_{14}$ nanosheets as the humidity-sensitive component and either TiO_2 or SiO_2 NP layers providing the required RI contrast. At ambient air (30% RH), the nanosheet film shows a RI of 1.56 as determined by spectroscopic ellipsometry (Figure S2.11b). While TiO_2 NPs exhibit a higher RI (1.85), SiO_2 NP layers show a lower RI (1.35) Figure S2.12. The particle nature of the TiO_2 and SiO_2 layers acts as a gate, ensuring the access of the water molecules to the moisture-sensitive nanosheet layers through textural porosity.^[10] Figure 2.2a, b show cross sectional SEM images of two BSs containing 12 and 11 alternating layers of $H_3Sb_3P_2O_{14}$ nanosheets and SiO_2 and TiO_2 NPs, respectively, evidencing long range stacking order and lateral layer uniformity across at least several microns. The spectral position of the first-order BP maximum and, hence, the structural color at normal incidence is given by Equation 2.1:^[39]

$$\lambda_B = 2(n_1d_1 + n_2d_2) \quad (\text{Equation 2.1})$$

where n_1 and n_2 are the RIs of the different layers and d_1 and d_2 their respective thicknesses.

The BSs depicted in Figure 2.2c ($H_3Sb_3P_2O_{14}/SiO_2$) and d ($H_3Sb_3P_2O_{14}/TiO_2$) show pronounced structural colors, which can be judiciously adjusted and gradually fine-tuned during the fabrication procedure across the visible spectrum.

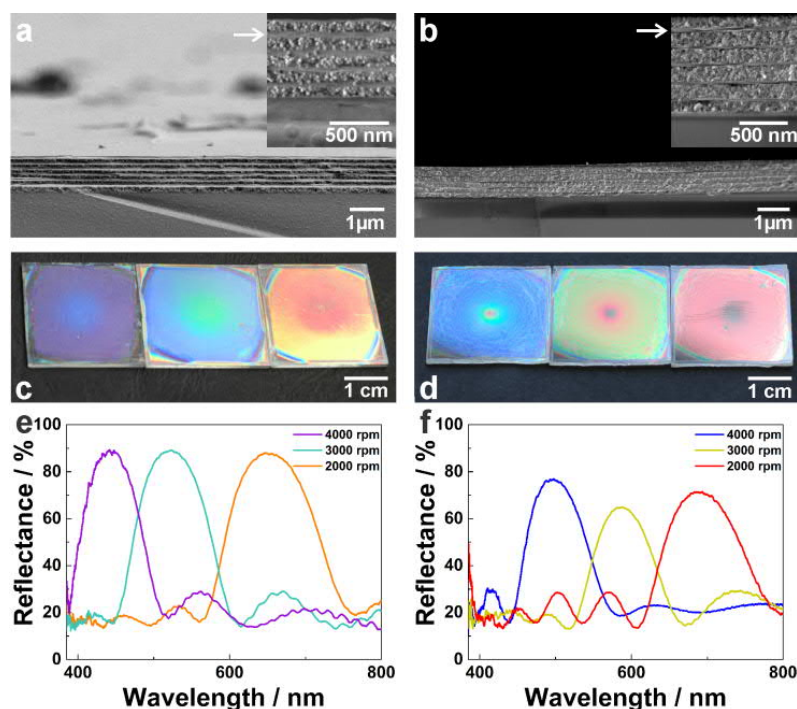


Figure 2.2. Optical and structural characterization of the $SiO_2/H_3Sb_3P_2O_{14}$ and $TiO_2/H_3Sb_3P_2O_{14}$ nanosheet-based BSs. a) SEM cross-section images of the $SiO_2/H_3Sb_3P_2O_{14}$ BS fabricated by 4000 rpm spin coating speed. The lower magnification image was taken with the SE detector and the higher magnification inset with the in lens detector. The white arrows indicate the nanosheet layers. b) SEM cross-section images of the $TiO_2/H_3Sb_3P_2O_{14}$ BS fabricated at 4000 rpm spin coating speed. Both images were taken with the in lens detector. c) Photographs of the $SiO_2/H_3Sb_3P_2O_{14}$ BSs fabricated at different spin coating speeds, from left to right: 2000, 3000, 4000 rpm, respectively. d) Photographs of the $TiO_2/H_3Sb_3P_2O_{14}$ BSs fabricated at different spin-coating speeds, from left to right: 2000, 3000, 4000 rpm, respectively. e) Optical spectra of the corresponding $SiO_2/H_3Sb_3P_2O_{14}$ BSs shown in the photographs (c) in the corresponding order. f) Optical spectra of the corresponding $TiO_2/H_3Sb_3P_2O_{14}$ BSs shown in the photographs (d) in the corresponding order.

In order to study the key features of our optical humidity sensors, the two BSs were introduced into a closed chamber with a transparent upper window, and the position of the BP was measured for different RH values controlled by saturated salt solutions at 25 °C.^[40,41] The supposed sensing mechanism of the BSs is schematically depicted in Figure 2.3a. Here, the thickness of the particle layers is assumed invariable, so three main processes affect the humidity-dependent optical response of the BS: i) The RI changes of the TiO_2 and SiO_2 NP layers with the adsorption/desorption of water into their textural pores (i.e., interparticle voids, Figure S2.12), ii) the change of the RI of the nanosheet layers through uptake/loss of water (Figure S2.11b), iii) the humidity-dependent thickness of the nanosheet layers (Figure S2.11a). While for SiO_2 and TiO_2 the effective RI of the layers increases with increasing water content due to the pore filling process, it decreases for the nanosheet layers as the effective RI approaches that of pure water with increasing degree of hydration. The latter

phenomenon is driven by the massive swelling of the nanosheet layers in contrast to the more compact NP layers. These features can be extracted from the humidity-dependent reflectance spectrum and the overall optical changes can also be monitored as color changes with the naked eye. The two BSs qualitatively behave differently: In the $H_3Sb_3P_2O_{14}/SiO_2$ BS, the photonic stop band red-shifts by 100 nm in the lower RH range (up to 90%) as plotted in Figure 2.3 b (solid lines). The set of microscope images shown below corresponds to the color displayed by the BS for three different RH values (32%, 93%, 100%). For increasing values of the RH, the BP redshifts, while its reflectance intensity gradually decreases and finally vanishes (Figure 2.3b, black spectrum). The color displayed by the sensor (Figure 2.3c) follows this behavior and for the highest value of humidity, the 1D PC switches off, i.e., becomes completely transparent (Figure S2.13). This effect finds its explanation in the elimination of the optical contrast between the layers forming the BS with increasing RH. While the RI of the particle layer increases and its thickness roughly remains constant, the RI of the nanosheet layer decreases while the layer thickness increases, leading to an overall redshift of the BP. Since the RIs of the nanosheet and NP layers follow opposite trends, both values ultimately become nearly equal at above 95% RH, leading to the disappearance of the optical contrast. As the BP is canceled out, the optical sensor turns completely transparent and light is transmitted by the structure throughout the visible range (Figure S2.13). Complete transparency switching through reversible RI matching has previously been realized by rational porosity and RI tuning of the constituent layers.^[42,43] These hydrochromic multilayers however are only capable of detecting liquid water, rather than humidity sensors.

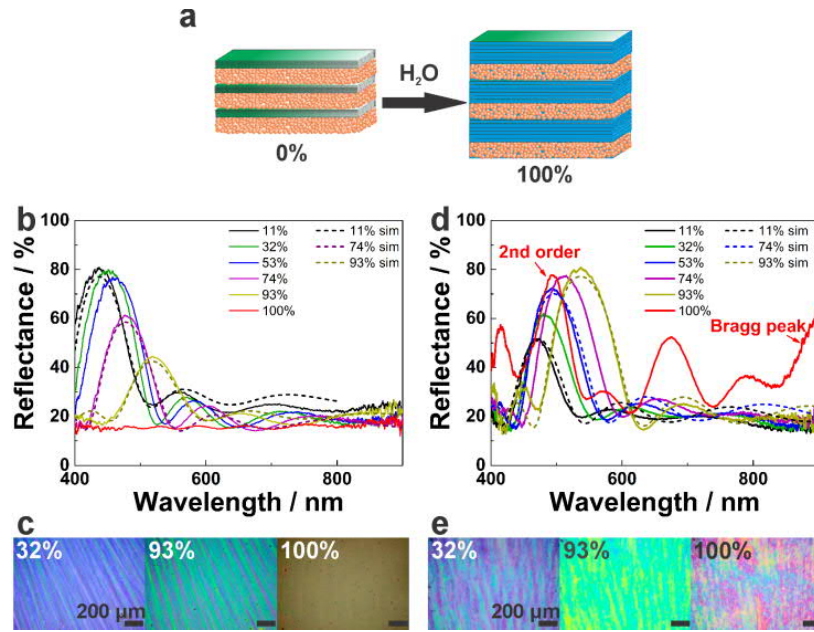


Figure 2.3. Optical humidity sensing features of the $\text{SiO}_2/\text{H}_3\text{Sb}_3\text{P}_2\text{O}_{14}$ and $\text{TiO}_2/\text{H}_3\text{Sb}_3\text{P}_2\text{O}_{14}$ BSs. a) Scheme of the suggested humidity sensing mechanism. b) Experimental (solid spectra) and simulated (dashed spectra) reflectance spectra of the $\text{SiO}_2/\text{H}_3\text{Sb}_3\text{P}_2\text{O}_{14}$ BS at different RH values. c) Microscope images of the $\text{SiO}_2/\text{H}_3\text{Sb}_3\text{P}_2\text{O}_{14}$ BS surface at RH values of 32%, 93%, and 100%, respectively. d) Experimental (solid spectra) and simulated (dashed spectra) reflectance spectra of the $\text{TiO}_2/\text{H}_3\text{Sb}_3\text{P}_2\text{O}_{14}$ BS at different RH values. e) Microscope images of the $\text{TiO}_2/\text{H}_3\text{Sb}_3\text{P}_2\text{O}_{14}$ BS surface at RH values of 32%, 93%, and 100%, respectively.

The specular reflectance spectra taken for the $\text{TiO}_2/\text{H}_3\text{Sb}_3\text{P}_2\text{O}_{14}$ BS are plotted in Figure 2.3d (solid lines), along with the corresponding surfaces of the BS for different RH values (Figure 2.3e). The BP redshifts by 100 nm in the RH range of 0-90%. Contrary to the SiO_2 containing BS, the reflectance rises with increasing RH and the stop band broadens, which can be rationalized by the increase in optical contrast of the layers with increasing RH. We observe a total redshift of more than 517 nm, shifting the BP out of the visible range into the IR, while the second-order BP is observed at 495 nm (red curve of Figure 2.3d). The observed red shift at high RH is the largest ever observed for a BS for moisture sensing applications. Note that besides these unique color changes, the fast response time, high reproducibility, and cyclability of the BS device (Figures S2.14, S2.15) are unprecedented. Although there have been a few systems reported in the literature, which show stop band shifts larger than 100 nm, these systems invariably exhibit slow response times due to diffusion limitations in the swelling of the integrated polymers.^[19-21] The porous nature of the NP layers in our BS sensor and the fast equilibration time of the nanosheet layers ensure easy access of the water molecules into the device and a fast response time throughout the entire device. Simulations of the optical spectra were carried out with a Matlab code^[9] to confirm the optical properties observed for our BSs (Figure 2.3b, d, dashed lines; for the input parameters used, see Figures S2.11, S2.12, Tables S2.5, S2.6). The excellent agreement between the values obtained in both cases proves the validity of the proposed sensing mechanism (Figure 2.3a).

Both, the conductance of the nanosheet thin film and the optical properties of the BSs show a reproducible, fast, and selective response to changes in RH, which are important performance parameters for position-sensitive user control interfaces. Since the fingertip is surrounded by a distance dependent humidity atmosphere, the read-out schemes developed above present intriguing candidates for the development of 3D (i.e., lateral and height-sensitive) non-contact interactive interfaces. To probe the touchless sensing capability of our nanosheet thin films and the BS, first, the nanosheet film on a quartz substrate was studied. Hereby, an increase of the conductance by more than a factor of 170 was observed when the distance of the finger from the sensor surface was reduced from 1.6 to 0.1 cm at 30% ambient RH (Figure 2.4a). This is notably higher than the values recently reported for VS_2 or GO thin film devices with a reported 3- or 0.35-fold signal increase.^[1,32] Note also that the fast full response (<2 s) and recovery times (3 s) toward “tapping” finger motion even allow to resolve subsecond events as shown in Figure S2.16. The observed response times are rather fast compared to other nanostructured humidity sensing devices with typical response times on the order of tens to hundreds of seconds,^[34,44-47] and even faster than those of state-of-the-art resistive sensors based on GO or VS_2 ,^[1,32] or commercially available sensors.^[48-50] The finger-tip induced conductance changes monitored in a dynamic measurement (Video S2.1) also demonstrate that the thin film device indeed has a very fast and reversible response to finger distance changes.

With the highly sensitive photonic read-out scheme presented above, the tools are at hand to go one step further and develop a novel optical TPI based on the lateral tracking of a humid pointer with an optical read-out visible by the naked eye. For such optical devices, no integration with an electronic assembly is necessary to visualize the lateral finger position above a photonic surface. Our experiments, which demonstrate the feasibility of this touchless optical sensing principle, are summarized in Figure 2.4 and visualized by Videos S2.2, S2.3, S2.4, and S2.5. Positioning the finger in a vertical distance of 1 mm from both presented BS surfaces leads to a color gradient along a distance between 1.0 and 1.8 mm from the finger tip, as shown in the microscope pictures corresponding to the two configurations proposed for $TiO_2/H_3Sb_3P_2O_{14}$ and $SiO_2/H_3Sb_3P_2O_{14}$ BSs, respectively (Figure 2.4d, e). This is in perfect agreement with the conductance behavior, as in the small distance range the sensing signal drops similarly fast (Figure 2.4 a) due to the spatially dependent humidity gradient around the finger. Looking at the structural colors of the gradient, the color at 1.0 mm real distance corresponds to the 100% RH sensing signal (where the optical contrast and reflectance are lost) in the case of the $SiO_2/H_3Sb_3P_2O_{14}$ BS. In both cases, the structural color for a distance of 1.5 mm corresponds to a RH of around 90% (see Figure 2.3). In Figure S2.17, we show that the BS can be operated as a TPI also at longer distances up to ≈ 12 mm. The stop band shift is observed immediately (Figure 2.4f, g), and the captured reflectance spectra for the $SiO_2/H_3Sb_3P_2O_{14}$ BS show a response time of 3 s (defined as the time it takes for 90% of the stopband shift before the structural color vanishes). Further cycling experiments (Figures S2.18, S2.19, and S2.20) demonstrate that a $SiO_2/H_3Sb_3P_2O_{14}$ BS responds instantaneously to fast “tapping” finger motion, resulting in a

subsecond time resolution (note that the “tapping” motion was also carried out under touchless conditions). The fast response is also obvious from lateral movement of the finger across the BS (Figure 2.4h-l, Video S2.5). An instantaneous color response precisely following the finger movement was observed, which is equivalent to a high-accuracy tracking of the finger movement (see Figure 2.4 h-l, Video S2.5). The BS response occurs exclusively due to the local water vapor atmosphere surrounding the finger, rather than a temperature effect, as: i) the response in the finger-on state (Video S2.2) is completely analogous to the measurement at very high RH carried out at RT, and ii) no color change is observed if the finger is protected by a nitrile glove (Figure 2.4c), while a fast and pronounced color change is directly seen by approaching the naked finger (Figure 2.4b, Figure 2.4h-l). Notably, the humidity response is fully reversible during cycling (Figure 2.4g inset, Figures S2.18, S2.20) and the BS can be cycled for more than 1000 times without observing any signs of degradation (Figures S2.19, S2.20) or changes in its response behavior. Finally, the BSs show long term stability without any loss of functionality after repeated usage and storing them in air for more than 8 months (see Figure S2.21).

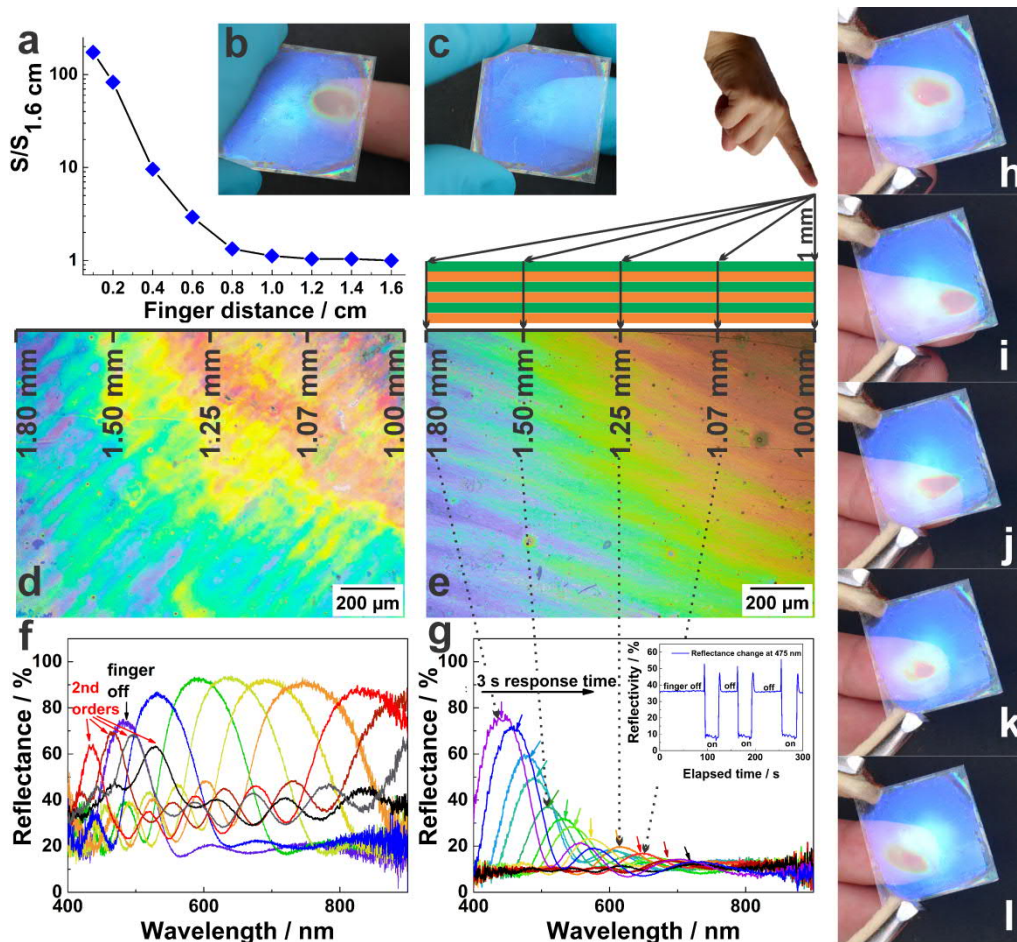


Figure 2.4. $H_3Sb_3P_2O_{14}$ nanosheet-based devices acting as a TPI. a) Sensing response characteristics as a function of the finger distance of a thin film device obtained by spin-coating at 3000 rpm. The measurement was performed at around 30% RH. b) Photograph of the $SiO_2/H_3Sb_3P_2O_{14}$ BS with an approaching finger. Note that the finger is not in direct contact with the BS. c) Photograph of the $SiO_2/H_3Sb_3P_2O_{14}$ BS with an approaching finger covered with a nitrile glove. No response is observed in this case. d) Real color microscope image of the $TiO_2/H_3Sb_3P_2O_{14}$ BS, showing the lateral color gradient around the finger position. The finger was positioned at the top right corner, in a vertical distance of 1 mm from the BS surface. Real distances from the finger to the corresponding image positions are indicated. e) Real color microscope image of the $SiO_2/H_3Sb_3P_2O_{14}$ BS showing the lateral color gradient around the finger position. The scheme shows the position of the finger in the top right image corner in a vertical distance of 1 mm. The real distances from the finger at the corresponding image positions (calculated by the Pythagorean theorem) are indicated. f) Evolution of the reflectance spectra of the $TiO_2/H_3Sb_3P_2O_{14}$ BS upon keeping the finger at 1 mm vertical distance to the BS surface. The different colors correspond to the different magnitudes of the response. g) Evolution of the reflectance spectra of the $SiO_2/H_3Sb_3P_2O_{14}$ BS taken after 3 s optical response time upon keeping the finger at 1 mm vertical distance to the BS surface. Inset: Intensity changes of the $SiO_2/H_3Sb_3P_2O_{14}$ BS while cycling between the finger-on and finger-off states. h - l) Photographs showing the finger movement tracking capability of the photonic TPI. The pictures are video frames from a similar video as Video S2.5 taken at 1, 2, 3, 4, and 5 s, while the finger was continuously moved laterally along the $SiO_2/H_3Sb_3P_2O_{14}$ BS without direct contact with the photonic TPI surface.

2.1.3 Conclusion

In summary, we have demonstrated the potential of phosphoantimonic acid nanosheet-based resistive and photonic humidity sensors as TPI, which represents a novel concept complementary to the contact-based technology. Transparent nanosheet thin films can be applied as a resistive RH sensor, since the ionic conductance of the film strongly depends on the surrounding RH, featuring high sensitivity with a response of five orders of magnitude, good cyclability, and ultrafast response characteristics in the subsecond range. We have demonstrated that due to these properties, the nanosheet thin film device can be applied as a touchless axial positioning interface with a change of ionic conductance between the finger on and finger off state by a factor of 170. Further, “smart” 1D PCs were developed as versatile humidity sensors with a simple optical read out. The ultrahigh stop band shift of 517 nm of the TiO_2 -based BSs and the switchable transparency through optical contrast loss of the SiO_2 -based BSs are unique features of the proposed sensing platform. This second property, the gradual loss of reflectance accompanied by a color change, makes these multilayers potential candidates for privacy windows or smart window applications. Due to the straightforward optical tunability, the extremely high sensitivity, reproducibility, ultrafast response and recovery times, a new concept of a position-sensitive optical TPI was demonstrated for the first time. As the humidity-responsive photonic device gives the user direct optical feedback about successful interaction, no additional soft- and hardware, which is implemented for contact visualization in current state of the art capacitive touch screens, is needed. Using the contactless optical read out proposed in this work, the disadvantages of conventional touch screens such as scratches or fingerprints could be eliminated, while touchless tracking of finger motion is achieved in a simple fashion without complex electronic circuitry.

2.1.4 Acknowledgement

Financial support was granted by the Max Planck Society, the University of Munich (LMU), the Center for NanoScience (CeNS), and the Deutsche Forschungsgemeinschaft (DFG) through the Cluster of Excellence “Nanosystems Initiative Munich” (NIM). B.V.L. gratefully acknowledges financial support by the Fonds der Chemischen Industrie. The authors thank Viola Duppel for TEM and SEM as well as Claudia Kamella for the SEM-EDX measurements as well as Willi Hölle for his technical support with the self built flow setup. The authors thank Daniel Selmeczi and the team of Semilab Sopra for their support with the ellipsometry measurements.

2.1.5 Bibliography

- [1] J. Feng, L. Peng, C. Wu, X. Sun, S. Hu, C. Lin, J. Dai, J. Yang, Y. Xie, *Adv. Mater.* **2012**, *24*, 1969.
- [2] J. D. Joannopoulos, P. R. Villeneuve, S. Fan, *Nature* **1997**, *386*, 143.
- [3] A. C. Arsenault, T. J. Clark, G. von Freymann, L. Cademartiri, R. Sapienza, J. Bertolotti, E. Vekris, S. Wong, V. Kitaev, I. Manners, R. Z. Wang, S. John, D. Wiersma, G. A. Ozin, *Nat. Mater.* **2006**, *5*, 179.
- [4] Z. Wang, J. Zhang, J. Xie, C. Li, Y. Li, S. Liang, Z. Tian, T. Wang, H. Zhang, H. Li, W. Xu, B. Yang, *Adv. Funct. Mater.* **2010**, *20*, 3784.

- [5] J. H. Holtz, S. A. Asher, *Nature* **1997**, 389, 829.
- [6] B. V. Lotsch, G. A. Ozin, *Adv. Mater.* **2008**, 20, 4079.
- [7] L. D. Bonifacio, D. P. Puzzo, S. Breslav, B. M. Willey, A. McGeer, G. A. Ozin, *Adv. Mater.* **2010**, 22, 1351.
- [8] D. Lee, D. Omolade, R. E. Cohen, M. F. Rubner, *Chem. Mater.* **2007**, 19, 1427.
- [9] M. C. Fuertes, S. Colodrero, G. Lozano, A. R. González-Elipe, D. Grosso, C. Boissière, C. Sánchez, G. J. de A. A. Soler-Illia, H. Míguez, *J. Phys. Chem. C* **2008**, 112, 3157.
- [10] S. Colodrero, M. Ocaña, H. Míguez, *Langmuir* **2008**, 24, 4430.
- [11] N. Hidalgo, M. E. Calvo, H. Míguez, *Small* **2009**, 5, 2309.
- [12] J. Kobler, B. V. Lotsch, G. A. Ozin, T. Bein, *ACS Nano* **2009**, 3, 1669.
- [13] F. M. Hinterholzinger, A. Ranft, J. M. Feckl, B. Rühle, T. Bein, B. V. Lotsch, *J. Mater. Chem.* **2012**, 22, 10356.
- [14] a) C. Fenzl, T. Hirsch, O. S. Wolfbeis, *Angew. Chem. Int. Ed.* **2014**, 53, 3318; b) C. Fenzl, T. Hirsch, O. S. Wolfbeis, *Angew. Chem.* **2014**, 126, 3384.
- [15] B. V. Lotsch, G. A. Ozin, *ACS Nano* **2008**, 2, 2065.
- [16] Y. Kang, J. J. Walsh, T. Gorishnyy, E. L. Thomas, *Nat. Mater.* **2007**, 6, 957.
- [17] A. C. Arsenault, D. P. Puzzo, I. Manners, G. A. Ozin, *Nat. Photonics* **2007**, 1, 468.
- [18] F. Castles, S. M. Morris, J. M. C. Hung, M. M. Qasim, A. D. Wright, S. Nosheen, S. S. Choi, B. I. Outram, S. J. Elston, C. Burgess, L. Hill, T. D. Wilkinson, H. J. Coles, *Nat. Mater.* **2014**, 13, 817.
- [19] E. Tian, J. Wang, Y. Zheng, Y. Song, L. Jiang, D. Zhu, *J. Mater. Chem.* **2008**, 18, 1116.
- [20] R. Xuan, Q. Wu, Y. Yin, J. Ge, *J. Mater. Chem.* **2011**, 21, 3672.
- [21] S. Kim, J. Lee, H. Jeon, H. J. Kim, *Appl. Phys. Lett.* **2009**, 94, 133503.
- [22] J. Shi, V. K. S. Hsiao, T. R. Walker, T. J. Huang, *Sens. Actuators, B* **2008**, 129, 391.
- [23] R. A. Barry, P. Wiltzius, *Langmuir* **2006**, 22, 1369.
- [24] J. J. Steele, A. C. van Popta, M. M. Hawkeye, J. C. Sit, M. J. Brett, *Sens. Actuators, B* **2006**, 120, 213.
- [25] M. M. Hawkeye, M. J. Brett, *Adv. Funct. Mater.* **2011**, 21, 3652.
- [26] J.-C. P. Gabriel F. Camerel, B. J. Lemalre, H. Desvaux, P. Davidson, P. Batail, *Nature* **2001**, 413, 504.
- [27] F. Camerel, J. C. P. Gabriel, P. Batail, P. Panine, P. Davidson, *Langmuir* **2003**, 19, 10028.
- [28] S. Deniard-Courant, Y. Piffard, P. Barboux, J. Livage, *Solid State Ionics* **1988**, 27, 189.
- [29] Y. Piffard, A. Verbaere, A. Lachgar, S. Deniard-Courant, M. Tournoux, *Rev. Chim. Miner.* **1986**, 23, 766.
- [30] W. M. R. Divigalpitaya, R. F. Frindt, S. R. Morrison, *J. Phys. D: Appl. Phys.* **1990**, 23, 966.
- [31] S. Borini, R. White, D. Wei, M. Astley, S. Haque, E. Spigone, N. Harris, J. Kivioja, T. Ryhänen, *ACS Nano* **2013**, 7, 11166.
- [32] X. Wang, Z. Xiong, Z. Liu, T. Zhang, *Adv. Mater.* **2015**, 27, 1370.
- [33] S.-L. Zhang, H.-H. Choi, H.-Y. Yue, W.-C. Yang, *Curr. Appl. Phys.* **2014**, 14, 264.
- [34] F.-S. Tsai, S.-J. Wang, *Sens. Actuators, B* **2014**, 193, 280.
- [35] Y. Piffard, A. Lachgar, M. Tournoux, *J. Solid State Chem.* **1985**, 58, 253.
- [36] D. Yang, R. F. Frindt, *J. Appl. Phys.* **1996**, 79, 2376.
- [37] A. Kuhn, T. Holzmann, J. Nuss, B. V. Lotsch, *J. Mater. Chem. A* **2014**, 2, 6100.
- [38] For further details on the determination of the response time and measurement of the response characteristics, see Figure S2.16a-c.
- [39] J. D. Joannopoulos, S. G. Johnson, J. N. Winn, R. D. Meade, *Photonic Crystals: Molding the Flow of Light*, Princeton University Press, Princeton, NJ **2008**.
- [40] P. W. Winston, D. H. Bates, *Ecology* **1960**, 41, 232.
- [41] L. Greenspan, *J. Res. Natl. Bur. Stand.* **1977**, 81A, 89.
- [42] M. N. Ghazzal, O. Deparis, J. De Coninck, E. M. Gaigneaux, *J. Mater. Chem. C* **2013**, 1, 6202.
- [43] K. E. Shopsowitz, H. Qi, W. Y. Hamad, M. J. MacLachlan, *Nature* **2010**, 468, 422.
- [44] H. Jamil, S. S. Batool, Z. Imran, M. Usman, M. A. Rafiq, M. Willander, M. M. Hassan, *Ceram. Int.* **2012**, 38, 2437.

- [45] J. Wang, M.-Y. Su, J.-Q. Qi, L.-Q. Chang, *Sens. Actuators, B* **2009**, 139, 418.
- [46] Q. Kuang, C. Lao, Z. L. Wang, Z. Xie, L. Zheng, *J. Am. Chem. Soc.* **2007**, 129, 6070.
- [47] Y. Zhang, W. Fu, H. Yang, Q. Qi, Y. Zeng, T. Zhang, R. Ge, G. Zou, *Appl. Surf. Sci.* **2008**, 254, 5545.
- [48] AG Sensirion, commercially available humidity sensors, <http://www.sensirion.com/en/products/humidity-temperature> (accessed: May **2015**).
- [49] E+E ELEKTRONIK Gesellschaft m.b.H., commercially available humidity sensors, <http://www.epluse.com/en/products/humidityinstruments/humidity-sensor> (accessed: May **2015**).
- [50] Vaisala, commercially available humidity sensors, <http://www.vaisala.com/en/products/humidity/Pages/default.aspx> (accessed: May **2015**).

2.2 Supporting Information: Touchless Optical Finger Motion Tracking Based on 2D Nanosheets with Giant Moisture Responsiveness

2.2.1 Methods

Solid state synthesis, protonation and exfoliation of nanosheets

For the synthesis of $K_3Sb_3P_2O_{14}$ the precursors (KNO_3 (99 %, Merck), Sb_2O_3 (99.6 %, Alfa Aesar), $NH_4H_2PO_4$ (98 %+, Acros Organics)) were thoroughly ground in a stoichiometric ratio and heated up as described elsewhere.^[1] For the proton exchange reaction, 2 g of $K_3Sb_3P_2O_{14}$ were treated with 250 mL of 8 M nitric acid (diluted 65 wt%, Merck) overnight, filtrated, washed with ethanol and dried at room temperature. This treatment was repeated one more time to complete the exchange reaction.^[2] The success was monitored by XRD. Exfoliation was carried out by stirring the $H_3Sb_3P_2O_{14}$ vigorously overnight in pure water with a concentration of bulk protons of 7.3 mmol L^{-1} . The obtained colloidal suspensions were centrifuged at 3000 rpm for 30 min to remove non-exfoliated bulk material. The supernatant is a suspension of mainly single layer nanosheets. To obtain the nanosheet pellet, an additional centrifugation step was applied at 18000 rpm for 30 min. The supernatant was discarded and the gel like colorless wet aggregate was dried at $100 \text{ }^\circ\text{C}$.

Synthesis of NPs

TiO_2 nanoparticulate sols were synthesized using a procedure described elsewhere.^[3] The colloidal suspension of titania NPs used for spin coating was obtained by collection of the particles by repeated centrifugation at 24000 rpm and redispersion in methanol.

SiO_2 nanocolloids were purchased from Dupont (LUDOX TMA, Aldrich, 30 nm particle size, 34 wt%).

Preparation of colloidal suspensions

The dried colorless precipitate of the water exfoliated $H_3Sb_3P_2O_{14}$ nanosheets was redispersed with a concentration of 42 mmol L^{-1} in a water/ethanol mixture (60 vol% ethanol) and sonicated for 2 h. The TiO_2 suspensions had a concentration of 2.5 wt% in methanol. The commercial colloids of SiO_2 were redispersed at 3 wt% in methanol.

Fabrication of thin films and BSs

All films were made by means of spin-coating using a spin-coater (WS-650S-NPP-Lite, Laurell Technologies Corporation) and concentrations given above. Different film thicknesses were accessed by varying the spin-coating speed, which allowed the fine-tuning of the optical properties.^[4] On plasma cleaned microscope glass slides with the dimensions of $2.5 \text{ cm} \times 2.5 \text{ cm}$, $400 \text{ }\mu\text{l}$ of the colloidal suspensions were spin coated alternatingly for 1 min with a defined speed, and heated to $80 \text{ }^\circ\text{C}$ for 15 min after each layer deposition. 2000 rpm, 3000 rpm and 4000 rpm spin coating speeds

were applied (the same speed for each layer within a BS) to tune the optical properties, while other parameters such as colloidal concentration, spin coating time and acceleration rate (10000 rpm/s) were kept constant. For conductance measurements, this redispersed $Sb_3P_2O_{14}^{3-}$ nanosheet colloid was spin-coated at 3000 rpm or 2000 rpm for 1 min with a 10000 rpm s^{-1} acceleration ramp on a 1.5 cm x 1.5 cm plasma-cleaned quartz substrate. Gold contacts were sputter-coated (108auto, Cressington) with 180 s sputtering time.

2.2.2 Characterization

Structural characterization

TEM images and SAED patterns were obtained with a Phillips CM30 ST TEM (300 kV, LaB_6 cathode) equipped with a Gatan CCD camera. TEM EDX analysis was performed with a Si/Li detector (Thermo Fisher, Noran System Seven). SEM images of the nanosheet pellet were collected with a Vega TS 5130 MM (Tescan) equipped with Si/Li detector (Oxford). SEM cross-sectional images of the BSs were taken with a Zeiss Merlin FE SEM. AFM measurements were done on a Veeco CP II system in non-contact mode. XRD patterns were collected on a powder X-ray diffractometer (Stadi P, STOE) working with Ge(111) monochromated $Mo-K_{\alpha 1}$ radiation ($\lambda = 70.926$ pm) or $Cu-K_{\alpha 1}$ radiation ($\lambda = 154.051$ pm) in Debye Scherrer or transmission geometry with an image plate detector or a point detector. Well ground samples were either put between two Mylar® foils or filled in a glass capillary. Indexing was performed with the software DiffracPlus TOPAS v4.2 (Bruker AXS). The images of the BS surfaces were obtained with an optical microscope (Olympus BX51), operating in reflection mode with a 4x objective.

Conductance measurements

To obtain the conductance measurements, two different methodologies were used. In the first one, the films were kept over saturated salt solutions,^[5,6] at around 25 °C in a closed atmosphere at least 15 min before the conductance measurements. In the second one, we used an argon flow set up (Figure S2.10). A dry Ar flow and a water vapor saturated Ar stream were mixed in different ratios to define the humidity between 0-93.5%. The setup was calibrated using the conductance values previously measured at the RH defined by the salt solutions. The cycling experiments were performed with either the Ar flow setup, Figure S2.10, or by a tapping motion of a human finger. The change in conductance was monitored by impedance spectroscopy (in plane geometry, two point measurement) with an impedance bridge (Princeton Applied Research, VersaSTAT MC) applying an AC voltage of 500 mV and a frequency range of 1 Hz to 1 MHz. Cycling measurements were performed with a fixed frequency of 300 Hz.

Optical measurements

Porosimetry measurements were carried out by the porosimetry tool of Sopra PS-1000 SAM, whereby the sample was equilibrated at all water vapor relative pressure values for 15 min. The measurement results were fitted with the software Sopra SAE using the model combination Cauchy and Lorentz. The thickness of the NP layers was considered as constant and only the RI was fitted over the relative pressure range. For the nanosheet thin films both values, the layer thickness and also the RI were fitted. Before all measurements, the NP samples were heated for at least 30 min at 200 °C and the nanosheet thin films for 30 min at 60 °C in vacuum to make sure that the pores are empty. To obtain the optical isotherms, all fitted measurement results were plotted against the analyte relative pressure. All optical spectra were measured with a fiber optic spectrometer (USB2000+, Ocean Optics) attached to a microscope (DM2500, Leica) with normal incidence and the optical spectra were always taken at the same spot ($1 \times 1 \text{ mm}^2$ in area). To obtain the optical changes with RH change, the BSs were kept in a stainless steel chamber with a transparent glass window and a total volume of 5 mL, placed above 0.7 mL of the saturated salt solutions at around 25 °C^[5,6] as described above (see conductance measurements). At each step, 20 min atmosphere equilibration time was needed. To illustrate the reversibility, a dynamic method using a nitrogen flow setup (see below) was applied. Hereby, the reflectance intensity changes of the BP were observed at a certain wavelength placed at the red stop band edge. While the BP shifts in response to the analyte exposure, the reflectance intensity changes at the observed wavelength. In these dynamic measurements, the BSs were placed into a closed chamber with the dimensions of $2.5 \times 2.5 \times 0.5 \text{ cm}^3$, where well-defined RH values were realized by connecting the inserted pipette tip with a liquid gas flow controller (Bronkhorst) and a vaporizer (CEM) with a massflow controlled carrier gas flow. To observe a specific RH, the carrier gas nitrogen (200 mL min^{-1}) and the liquid water were dosed into the CEM (controlled evaporation and mixing, W101A 130 K, Bronkhorst High Tech),^[7] where the thermal evaporation of water took place. The CEM was heated to temperatures above the boiling point (120 °C for water). The relative vapor pressures were calculated via the software FLUIDAT (CEM calculation), which considers the actual atmospheric pressure, the temperature and the properties of the analyte (vapor pressure, heat capacity).^[8] The spectra were measured in the visible range with an OCEAN OPTICS QP400-2-UV-BX optical fiber interfaced with a LEICA DM 2500 M microscope. The obtained data were analyzed with the SPECTRA SUITE (2008) software.

Touchless positioning interface measurements

Conductance measurements were carried out by impedance spectroscopy (see above) by placing a finger in different distances to the film surface (between 0.1 and 1.6 cm) without touching the thin film device. For determination of the response and recovery time, a human finger was approached (ca. 1 mm distance) to the surface and removed subsequently. The response and recovery times were

determined as the time to observe 90% of the conductance change (see Figure S2.16). The real time conductance manipulation video was recorded using a smartphone camera.

Optical measurements were carried out similarly; a finger was approached to the BS in 1 mm distance. Hereby, lateral optical changes were detected by the optical microscope (Olympus BX51) coupled to a CMOS camera and an Ocean Optics USB4000-XR1-ES spectrometer. A finger cycling was carried out by approaching and distancing the finger in regular intervals of ca. 30 s. This measurement was used to determine the response time of the BS, which was defined as the time it takes for 90% of the stopband shift before the structural color vanishes. To detect the stopband changes, the intensity changes at the wavelength 475 nm were followed. The optical tracking of the finger movements close to the BS surface were recorded by a conventional smartphone camera.

2.2.3 Additional data

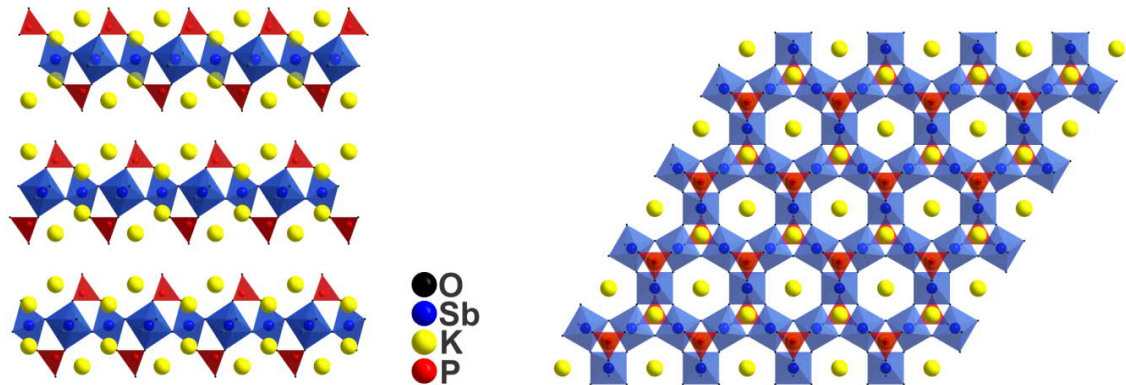
 $K_3Sb_3P_2O_{14}$ and $H_3Sb_3P_2O_{14}$ bulk materials synthesis and characterization

Figure S2.1. From left to right: Structure of $K_3Sb_3P_2O_{14} \cdot 1.3 H_2O$ viewed along [010] (left) and [001] (right). For a better overview, only one layer is shown along [001] and for $K_3Sb_3P_2O_{14} \cdot 1.3 H_2O$ the O positions between the layers were left out.

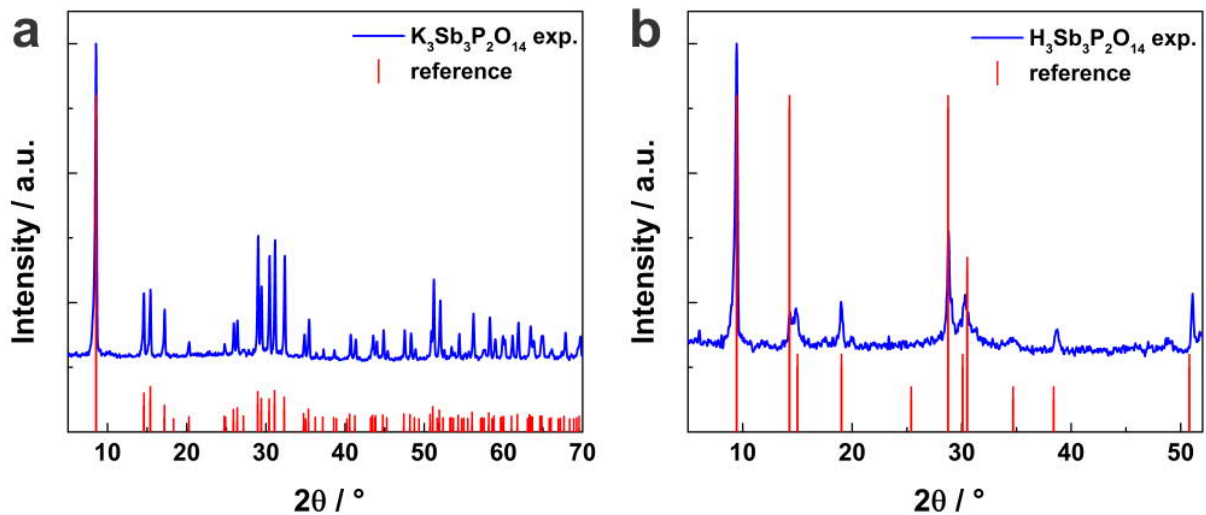
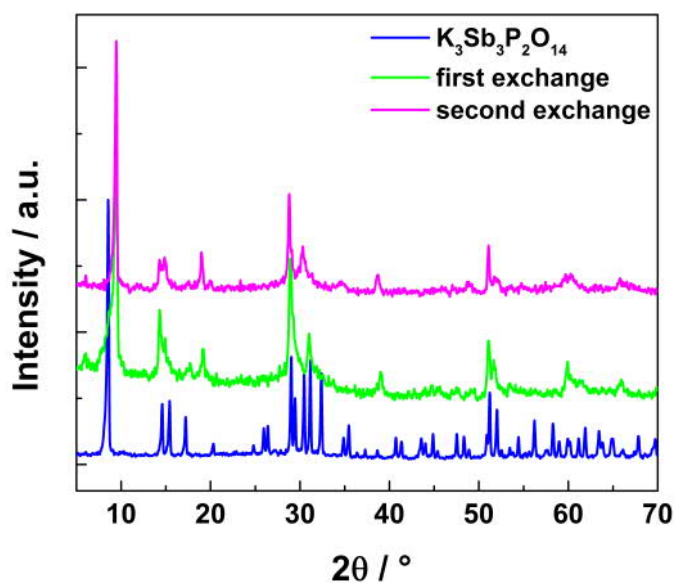


Figure S2.2. Experimental XRD patterns of a) $K_3Sb_3P_2O_{14}$ and b) $H_3Sb_3P_2O_{14}$ (in blue) and reference XRDs from the literature (red) for (a) $K_3Sb_3P_2O_{14} \cdot 5 H_2O$ and (b) for $H_3Sb_3P_2O_{14} \cdot 5 H_2O$, respectively. Experimental XRD patterns were recorded with $Cu-K_{\alpha 1}$ radiation.

Table S2.1. EDX data for $K_3Sb_3P_2O_{14}$ (measured over five points) and for $H_3Sb_3P_2O_{14}$ (measured over four points). Standard deviations are given in the brackets.

Sample	K Atom%	Sb Atom%	P Atom%	O Atom%	Calc. Formula
Theoretical values	11.1	11.1	7.4	70.4	$K_3Sb_3P_2O_{14} \cdot 5 H_2O$
Exper.	11 (2)	11 (2)	7.2 (6)	71 (5)	$K_{3.05}Sb_{3.08}P_2O_{19.86}$
Theoretical values	-	15.8	10.5	73.6	$H_3Sb_3P_2O_{14}$
Exper.	-	15 (2)	9.1(7)	76 (3)	$H_3Sb_{3.28}P_2O_{16.72}$

**Figure S2.3.** Details of the evolution of the cation - proton exchange for $K_3Sb_3P_2O_{14}$ (two exchange steps required). Experimental XRD patterns recorded with $Cu-K\alpha_1$ radiation.

Characterization of the nanosheets

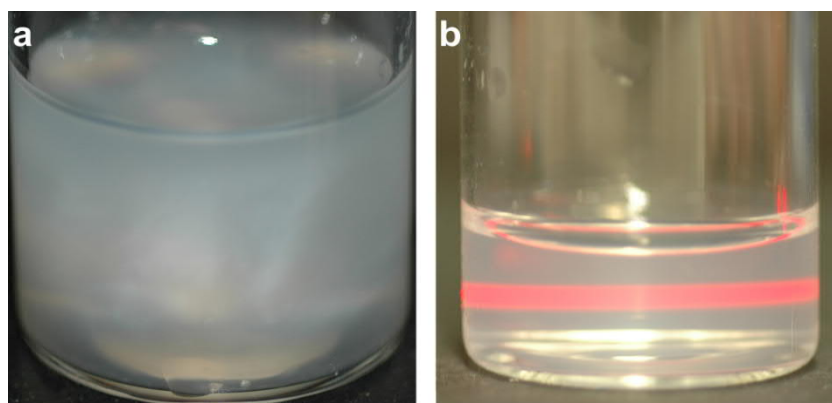
**Figure S2.4.** Schlieren texture a) and Tyndall effect b) of $Sb_3P_2O_{14}^{3-}$ nanosheet suspensions in water.

Table S2.2. TEM-EDX data for the different samples of exfoliated $Sb_3P_2O_{14}^{3-}$ nanosheets.

Sample	Sb Atom%	P Atom%	O Atom%	Calc. Formula
Theoretical values	15.8	10.5	73.6	$Sb_3P_2O_{14}^{3-}$
Exper. (I)	15.23	9.38	75.40	$Sb_{3.25}P_2O_{16.08}$
Exper. (II)	15.23	10.25	74.52	$Sb_{2.97}P_2O_{14.54}$

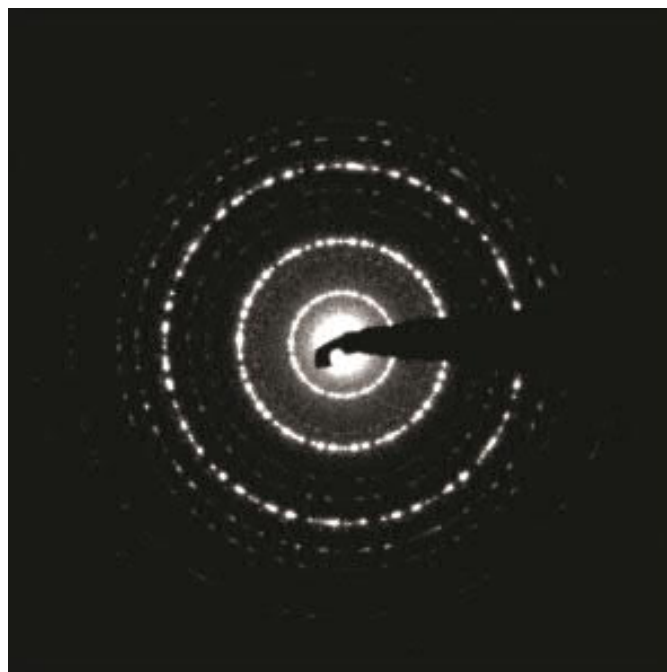
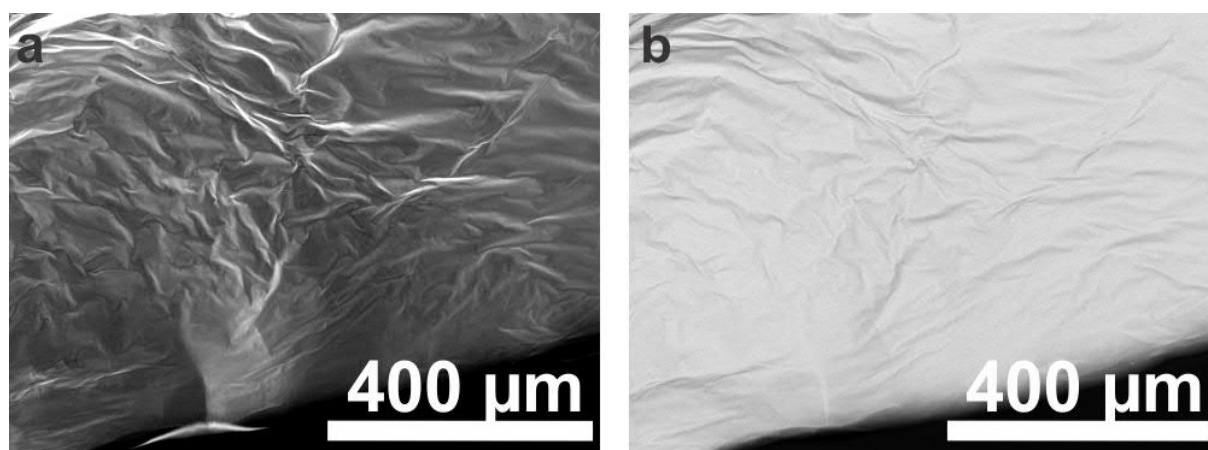
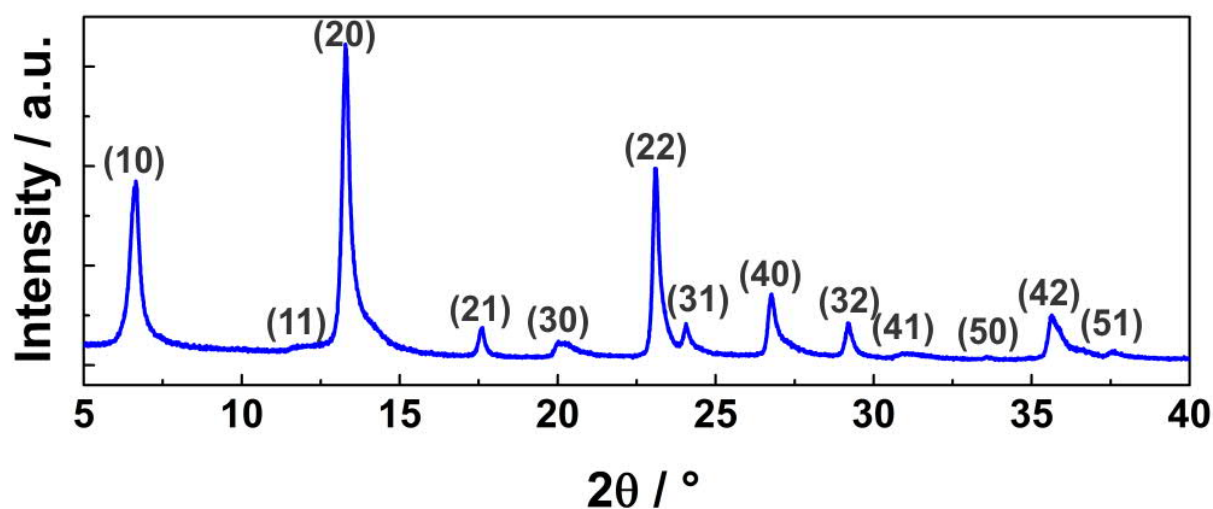
**Figure S2.5.** SAD pattern of $Sb_3P_2O_{14}^{3-}$ nanosheets. The concentric circular shaped pattern indicates the turbostratic disorder along the c -axis, which indicates exfoliation and random restacking.**Figure S2.6.** a) SE image and b) BSE image of a $Sb_3P_2O_{14}^{3-}$ nanosheet pellet obtained from centrifugation at 18000 rpm of the sample exfoliated in water.

Table S2.3. SEM-EDX analysis of a $Sb_3P_2O_{14}^{3-}$ nanosheet pellet obtained from three sample points.

Sample	Sb Atom%	P Atom%	O Atom%	Calc. Formula
Theoretical values	15.8	10.5	73.6	$Sb_3P_2O_{14}^{3-}$
Exper.	13.0 (5)	8.4 (2)	78.6 (7)	$Sb_{3.10}P_2O_{18.71}$

Table S2.4. Comparison and indexing of d -values of SAD and XRD pattern (Figure S2.7). The value marked with an asterisk cannot clearly be determined because of a broad maximum only slightly above the noise level in the XRD pattern.

$Sb_3P_2O_{14}^{3-}$		
Miller indices	d -value SAD [Å]	d value XRD [Å]
(10)	6.02	6.12
(11)	3.55	3.41*
(20)	3.04	3.06
(21)	2.34	2.32
(30)	2.04	2.04
(22)	1.77	1.77
(40)	1.53	1.53
(23)	1.41	1.41

**Figure S2.7.** Experimental XRD pattern of $Sb_3P_2O_{14}^{3-}$ nanosheet pellet recorded with Mo- $K_{\alpha 1}$ radiation and indexing based on a trigonal layer group ($\bar{p}3m1$ No. 72) with $a = 7.0914(3)$ Å. Note the Warren-type peak profile of the (hk) reflections.

Resistive RH sensing

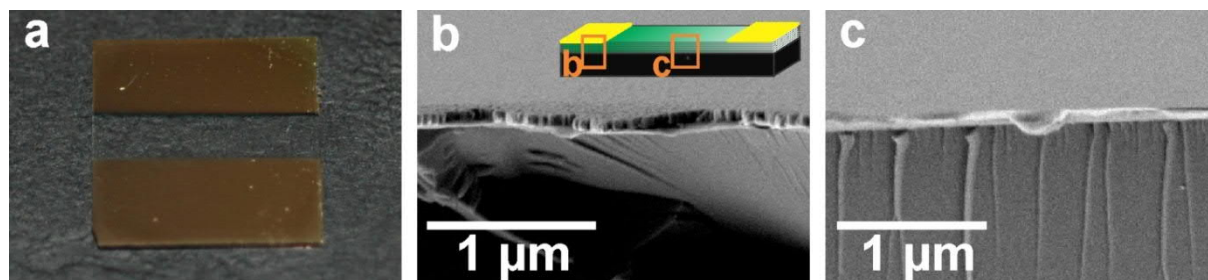


Figure S2.8. a) Thin transparent nanosheet film device with quartz substrate, spin-coated thin film and sputtered gold contacts on the top. b) SEM cross-section of the region with gold contacts on the top (bottom to top: quartz substrate, thin layer of the nanosheets, Au contacts and vacuum). Inset: scheme of the resistive thin film substrate indicating the glass substrate (black), $H_3Sb_3P_2O_{14}$ nanosheet thin film (green) and the gold contacts (yellow). The orange rectangles indicate the cross section areas corresponding to the SEM images b and c. c) Cross-section of the thin film region without the gold contacts. The nanosheet film (light grey) appears thicker due to charging effects in c.

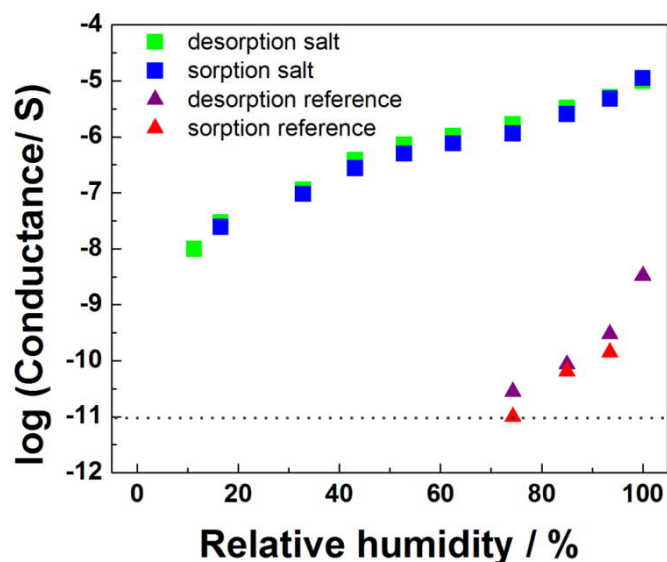


Figure S2.9. Conductance plotted against RH for the nanosheet sample (salt) and empty quartz substrate with only gold electrodes (reference). The dashed line indicates the detection threshold of our impedance device.

It should be noted that the change in the measured conductance for the nanosheet thin film is substrate-dependent. However, by measuring the conductance increase of an empty quartz substrate as a reference substrate with increasing RH, it can be shown that the increase in conductance is due to the film and film-substrate interactions, rather than due to the empty substrate itself (Figure S2.9).

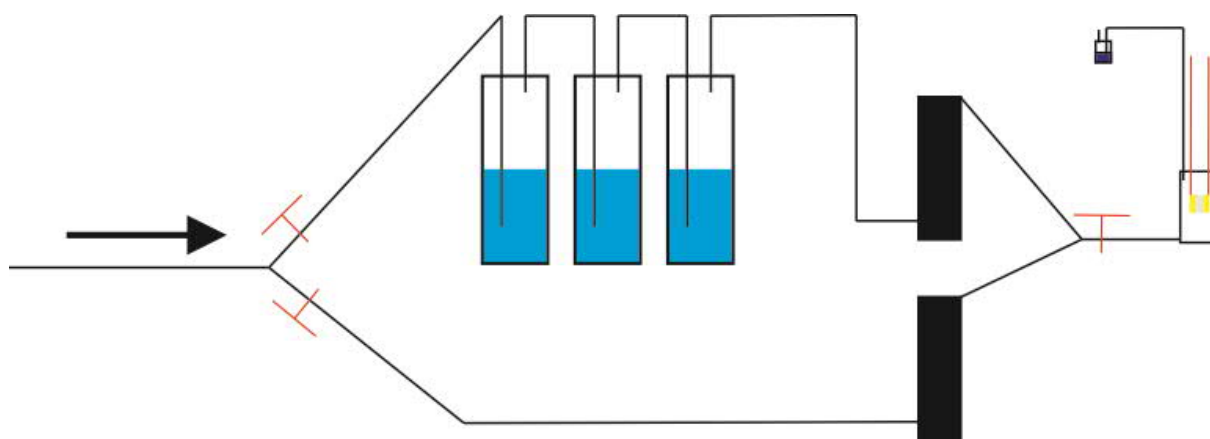


Figure S2.10. Ar-stream setup for cycling and RH-dependent conductance measurements. The Ar stream splits up into 2 streams, where one is saturated with H_2O by bubbling through three washing bottles. The rotameters for the stream adjustment are shown in black, and the chamber with the film and the gas outlet is shown on the right hand side. In red, the three valves for additional control are depicted.

Thin films characterizations

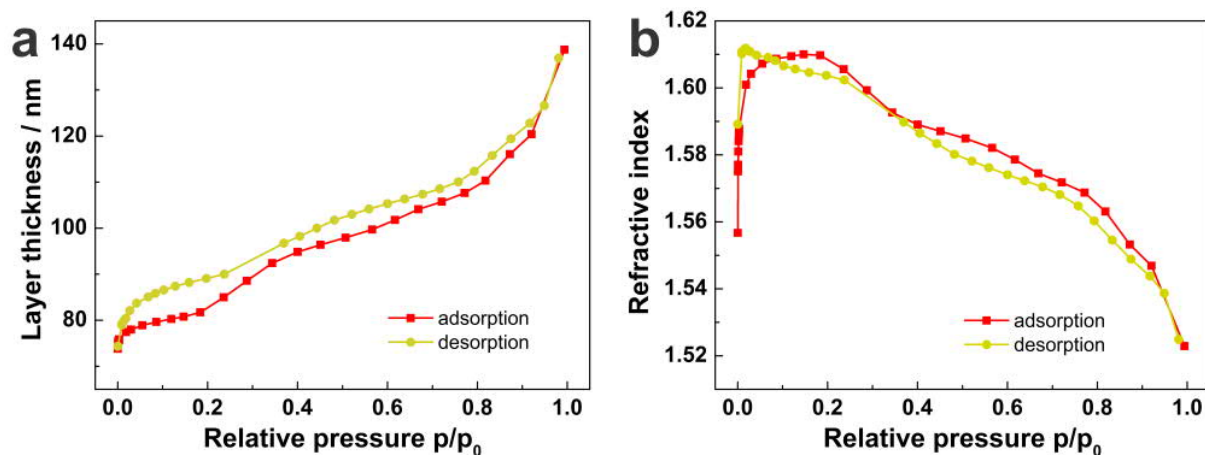


Figure S2.11. Optical isotherms of a thin film containing $H_3Sb_3P_2O_{14}$ nanosheets. a) Layer thickness and b) RI change of a $H_3Sb_3P_2O_{14}$ nanosheet thin film measured at different relative pressures of water vapor.

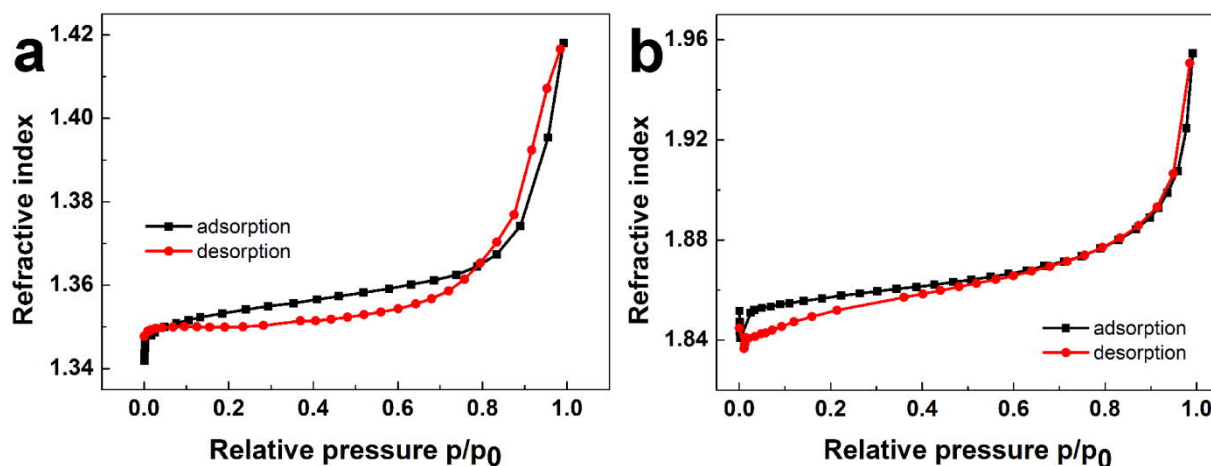


Figure S2.12. Optical isotherm of the a) SiO_2 NP monolayer and b) TiO_2 NP monolayer monitoring the RI changes upon increasing the relative pressure of water vapor.

Optical humidity sensing and TPI

Table S2.5. Refractive indices and monolayer thicknesses for the $SiO_2/H_3Sb_3P_2O_{14}$ BS used for the Matlab simulations at different RH values. The layer thickness changes for the BS at different RH values were calculated from the ellipsometry measurements (Figure S2.11a) for the actual thicknesses of the BS.

Monolayer property	11% RH	74% RH	93% RH
$n(H_3Sb_3P_2O_{14})$	1.6090	1.5708	1.5449
$n(SiO_2 \text{ NP})$	1.3500	1.3624	1.3980
$d(H_3Sb_3P_2O_{14})$	52.5 nm	70.0 nm	85.0 nm
$d(SiO_2 \text{ NP})$	90.0 nm	90.0 nm	90.0 nm

Table S2.6. Refractive indices and monolayer thicknesses for the $TiO_2/H_3Sb_3P_2O_{14}$ BS used for the Matlab simulations at different RH values. The layer thickness changes for the BS at different RH values were calculated from the ellipsometry measurements (Figure S2.11a) for the actual thicknesses of the BS.

Monolayer property	11% RH	74% RH	93% RH
$n(H_3Sb_3P_2O_{14})$	1.6090	1.5729	1.5449
$n(TiO_2 \text{ NP})$	1.8400	1.8733	1.8900
$d(H_3Sb_3P_2O_{14})$	53.0 nm	69.0 nm	85.0 nm
$d(TiO_2 \text{ NP})$	78.0 nm	78.0 nm	78.0 nm

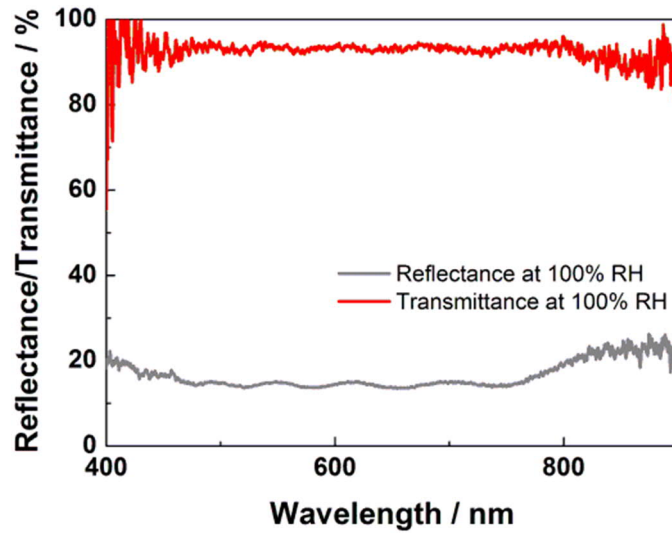


Figure S2.13. Transmittance (red curve) and reflectance (grey curve) spectrum of the $SiO_2/H_3Sb_3P_2O_{14}$ BS at 100% RH. The spectra show the total transmittance and the loss of reflectance, resulting in complete transparency of the RI matching multilayer across the whole visible range.

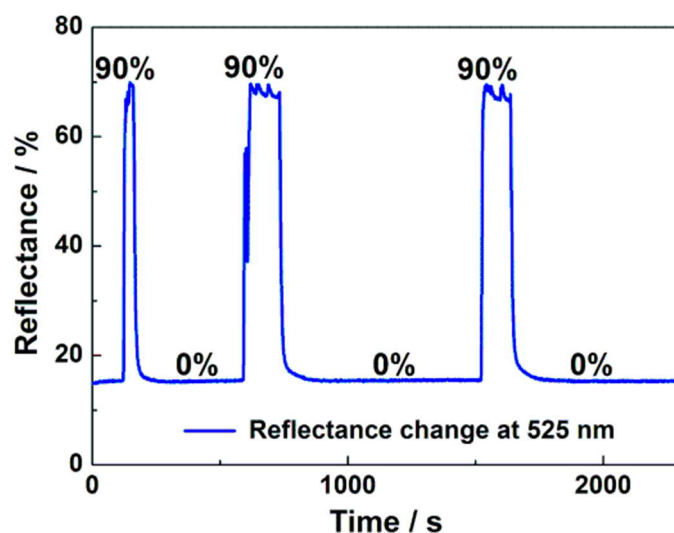


Figure S2.14. Cycling behavior of the $TiO_2/H_3Sb_3P_2O_{14}$ BS with time. The cycling was performed using the nitrogen setup and applying 0% and 93% relative pressures of water vapor. The spectral changes were detected by recording the reflectance intensity at 525 nm in the original spectrum. This wavelength was carefully chosen to be at the red edge of the stop band at 0% humidity. The slight reflectance intensity changes were caused by the oscillation character of the vapor dosing system.

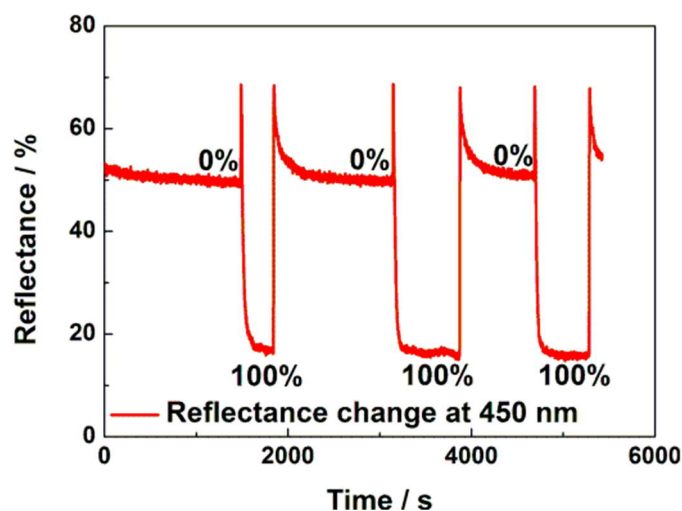


Figure S2.15. Cycling behavior of the $SiO_2/H_3Sb_3P_2O_{14}$ BS with time. The cycling was performed using the nitrogen setup and applying 0% and 100% relative pressures of water vapor. The spectral changes were detected by recording the reflectance intensity at 450 nm in the original spectrum. This wavelength was carefully chosen to be at the red edge of the stop band at 0% humidity. This chosen wavelength of 450 nm is redshifted compared to the original BP position (around 430 nm). The sudden intensity drops during the adsorption and also the desorption are observed because the BP shifts pass the observed wavelength of 450 nm, causing a reflectance maximum at the observed point. The reflectance intensity at 100% RH is lower than at 0% because of the RI contrast cancelling upon water vapor adsorption.

Note that the response time cannot be extracted from the cycling behavior shown in Fig. 2.1e since the chamber used for this measurement reaches saturation slower than the sensor itself. The response time can be measured by excluding the dead volume, which has been done by applying a humidity stimulus given by a finger, as demonstrated in Figure S2.16 below. The same method was used for the optical sensor, and the response time was determined with a finger stimulus (Figure 2.4g inset, Figure S2.18).

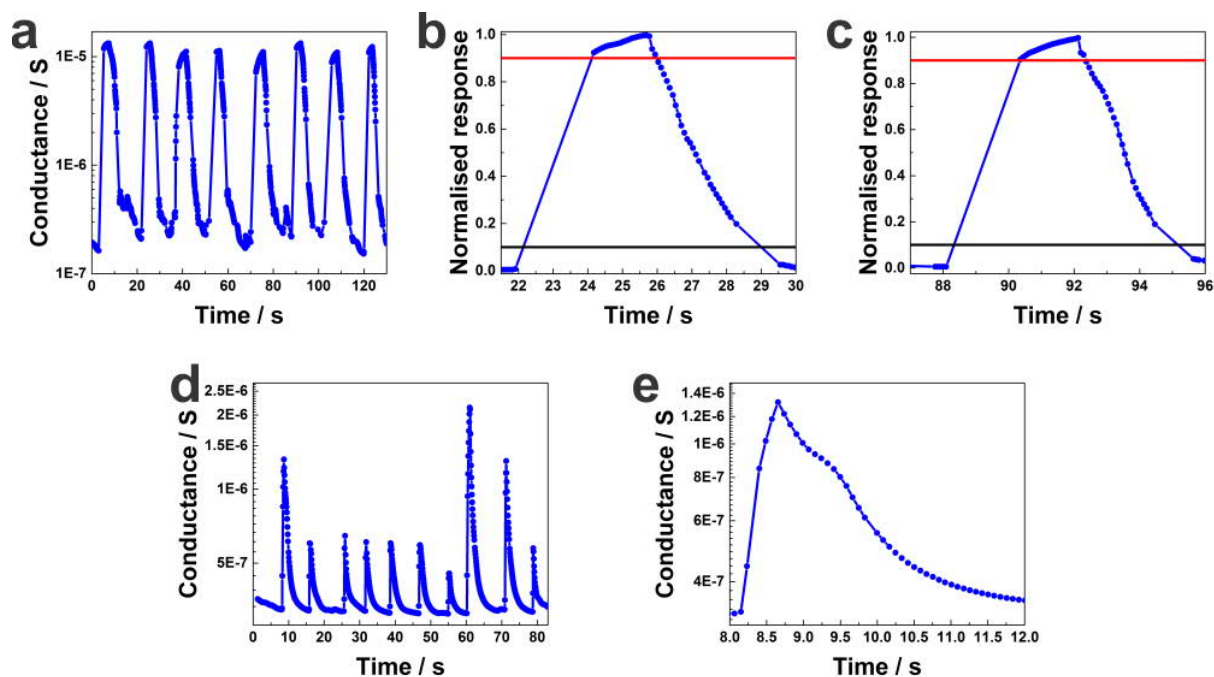


Figure S2.16. Conductance response of a nanosheet thin film to a finger stimulus under touchless conditions. a) Response toward a “finger-on” state under touchless conditions, with a response time of about 2 s (note that signal saturation is reached within this time). b) and c) normalized magnifications of a) used for determination of the response and recovery time of the sensor (defined as reaching 90% of the total signal change; response time, red line, and recovery time, black line). The response time is around 2 s and the recovery time around 3 s for cycling between ambient conditions and close to 100% RH (finger proximity). d) Conductance response of a nanosheet thin film toward a fast tapping motion (occurring on a timescale of $\ll 0.5$ s) and e) magnification of the region of d) between 8 and 12 s. The data show that subsecond events can be resolved as demonstrated by the finger motion trapping detection (the signal triples in less than 0.5 s). Therefore, due to the fast response, the thin film can be used for real-time interactions (note that measurement a) was carried out under slightly different ambient RH values as compared to d), as indicated by the conductance values).

To prove the long-term stability of the optical sensor, the measurements shown in Figure S2.17-21 were carried out with an 8-months-old BS.

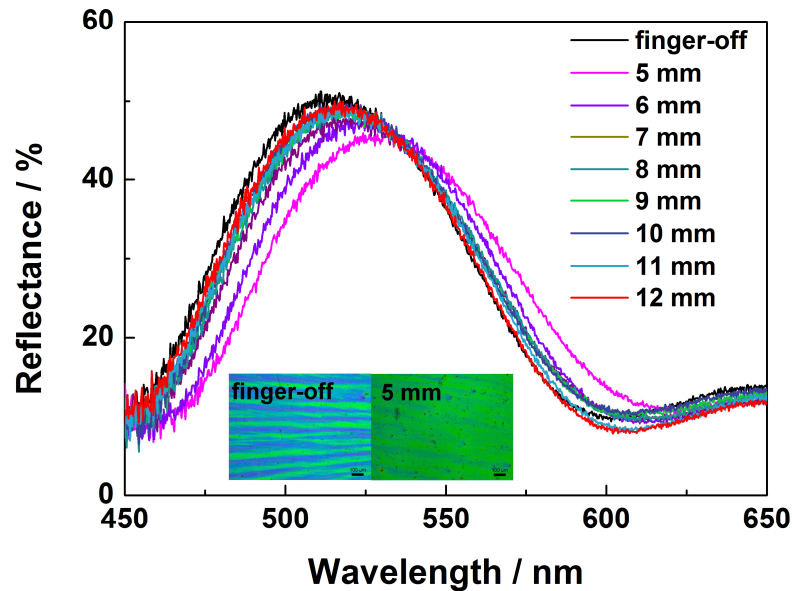


Figure S2.17. Distance-dependent optical response of the $SiO_2/H_3Sb_3P_2O_{14}$ BS to a finger stimulus. Inset: Microscope images of the BS surface at 5 mm finger distance and a finger-off state.

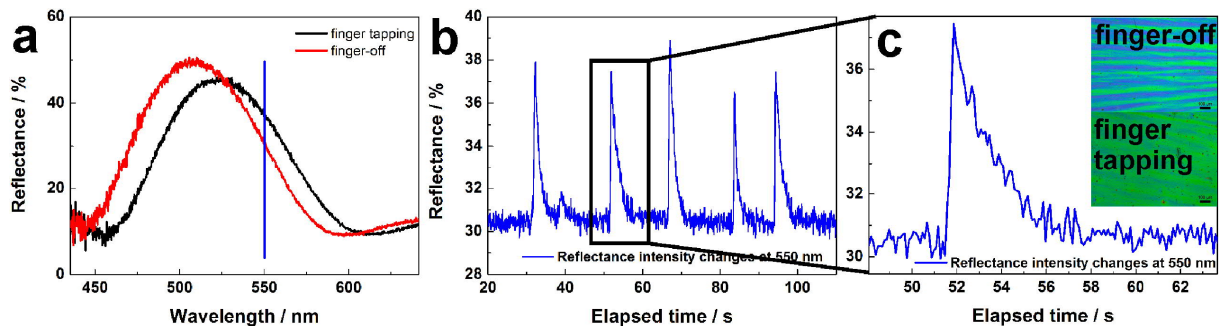


Figure S2.18. a) Optical response of a $SiO_2/H_3Sb_3P_2O_{14}$ BS to a fast tapping finger motion as a function of time. Measurements were carried out in a similar way as described in Figure S2.15, however for detection of the reflection a wavelength of 550 nm was chosen and a finger was used as the humid pointer. a) For the tapping experiments we have chosen a threshold value of 20 nm stop band shift, which is detectable by the naked eye (inset of c)). b) Time-resolved response of a BS toward a fast finger tapping motion. Even subsecond events can clearly be resolved, *e.g.* a reflectance change from 30% to 37%, which corresponds to 20 nm shift and is detectable with the naked eye, is observed within less than 0.5 s. c) Close-up of the region between 50-62 s, shown in b), inset: microscope images of the finger-off and tapping structural color, indicating that the 20 nm stop band shift is detectable by the naked eye.

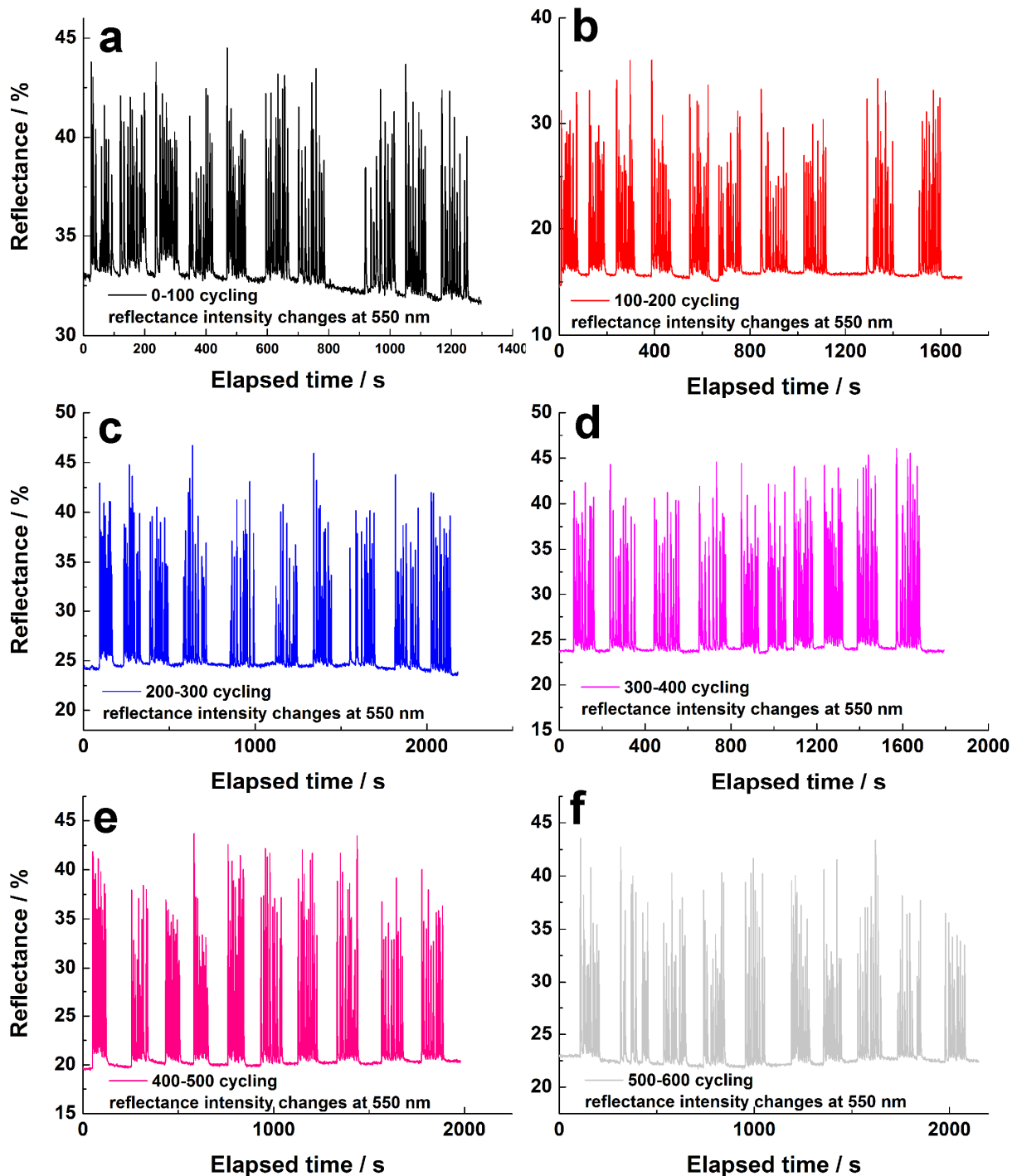


Figure S2.19: The first part of the 1000 times cycling procedure. a-f) In each diagram 10 x 10 cycles are plotted. For time and simplicity reasons, one cycle corresponds to a finger “tapping” experiment. The human finger was approached for a short time to the BS surface, thereby only a smaller stop band shift was induced and not the whole stop band shift was reached. This experiment was repeated 10 times in a short time range - this is one “signal package”. This 10-cycle-experiment was repeated 10 times to reach 100 cycles in one plot. This was repeated 10 times to reach 1000 cycles. 1-600 cycles are shown in this figure.

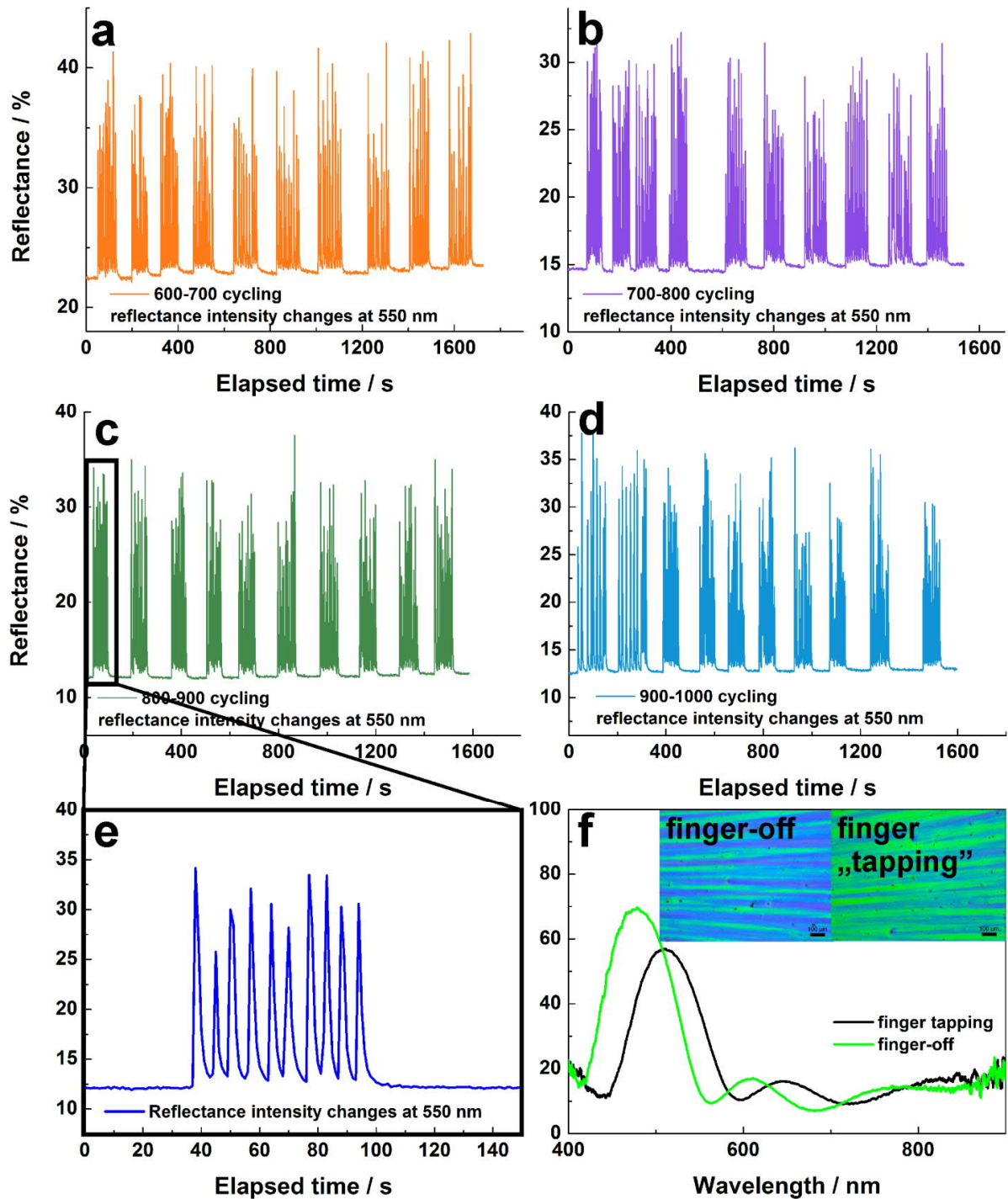


Figure S2.20. The second part of the 1000 times cycling procedure. a-d) 601-1000 cycles are shown in the diagrams. Similar to Figure S2.19, 10 x 10 cycles are shown in one diagram. e) Magnification of one "signal package" of 10 cyclings. For one cycle, a finger "tapping" experiment was used in which a human finger was only shortly approached to the BS surface without touching it. In such a "tapping experiment", a reflectance intensity change of 10-20% is observed. f) Reflectance spectra of the finger-off and finger "tapping" scenarios. A finger "tapping" corresponds to a signal change of around 20-30 nm. Inset: the corresponding microscope images indicating the structural color change upon a finger approaching.

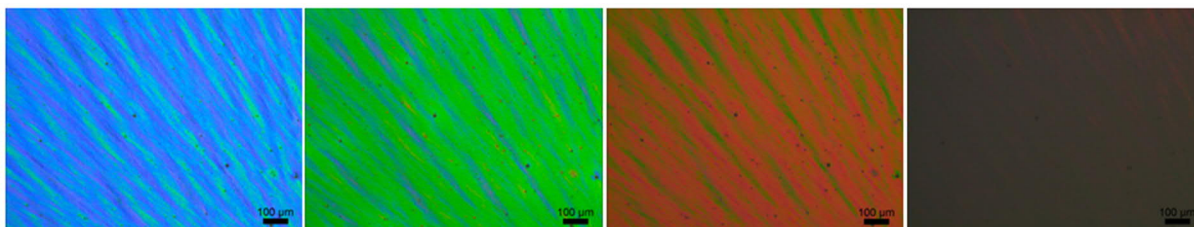
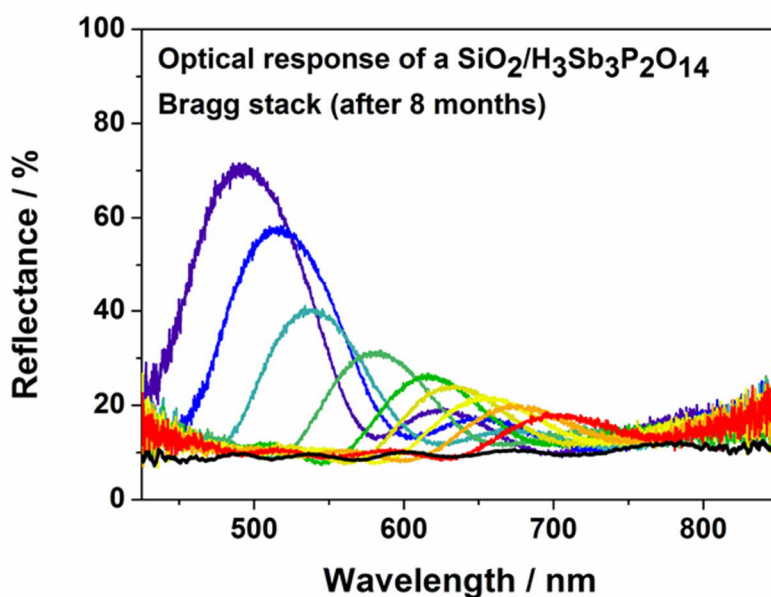


Figure S2.21. Optical response of a 8-months-old $SiO_2/H_3Sb_3P_2O_{14}$ BS to an approaching finger. The reflectance spectra show an unchanged optical response after 8 months. Also the microscope images indicate the structural color change with changing RH. Finally, at high relative humidities the BP completely vanishes and optical transparency is observed (indicated by the black color of the right microscope image).

Note

For real-time manipulations see also: Video S2.1, S2.2, S2.3, S2.4 and S2.5 available at:
<http://onlinelibrary.wiley.com/doi/10.1002/adma.201503463/full#footer-support-info>

2.2.4 Bibliography

- [1] Y. Piffard, A. Lachgar, M. Tournoux, *J. Solid State Chem.* **1985**, *58*, 253-256.
- [2] J.-C. P. Gabriel, F. Camerel, B. J. Lemalre, H. Desvaux, P. Davidson, P. Batail, *Nature* **2001**, *413*, 504-508.
- [3] B. V. Lotsch, F. Scotognella, K. Moeller, T. Bein, G. A. Ozin, **2010**, 7713V.
- [4] M. E. Calvo, O. Sánchez-Sobrado, S. Colodrero, H. Míguez, *Langmuir* **2009**, *25*, 2443-2448.
- [5] P. W. Winston, D. H. Bates, *Ecology* **1960**, *41*, 232-237.
- [6] L. Greenspan, *J. Res. Nat. Bur. Stand.* **1977**, *81A*, 89-96.
- [7] A. T. Exner, I. Pavlichenko, D. Baierl, M. Schmidt, G. Derondeau, B. V. Lotsch, P. Lugli, G. Scarpa, *Laser & Photonics Reviews* **2014**, *5*, 726-733.
- [8] Bronkhorst High-Tech, www.fluidat.com, accessed: 06-12/2014

3 Utilization of HSbP₂O₈ nanosheets in trace water sensing and vapor distinction

3.1 Towards the Nanosheet-Based Photonic Nose: Vapor Recognition and Trace Water Sensing with Antimony Phosphate Thin Film Devices

Pirmin Ganter, Katalin Szendrei,* and Bettina V. Lotsch*

published: *Adv. Mater.* **2016**, 28, 7436-7442.

DOI: 10.1002/adma.201601992

<http://onlinelibrary.wiley.com/doi/10.1002/adma.201601992/abstract>

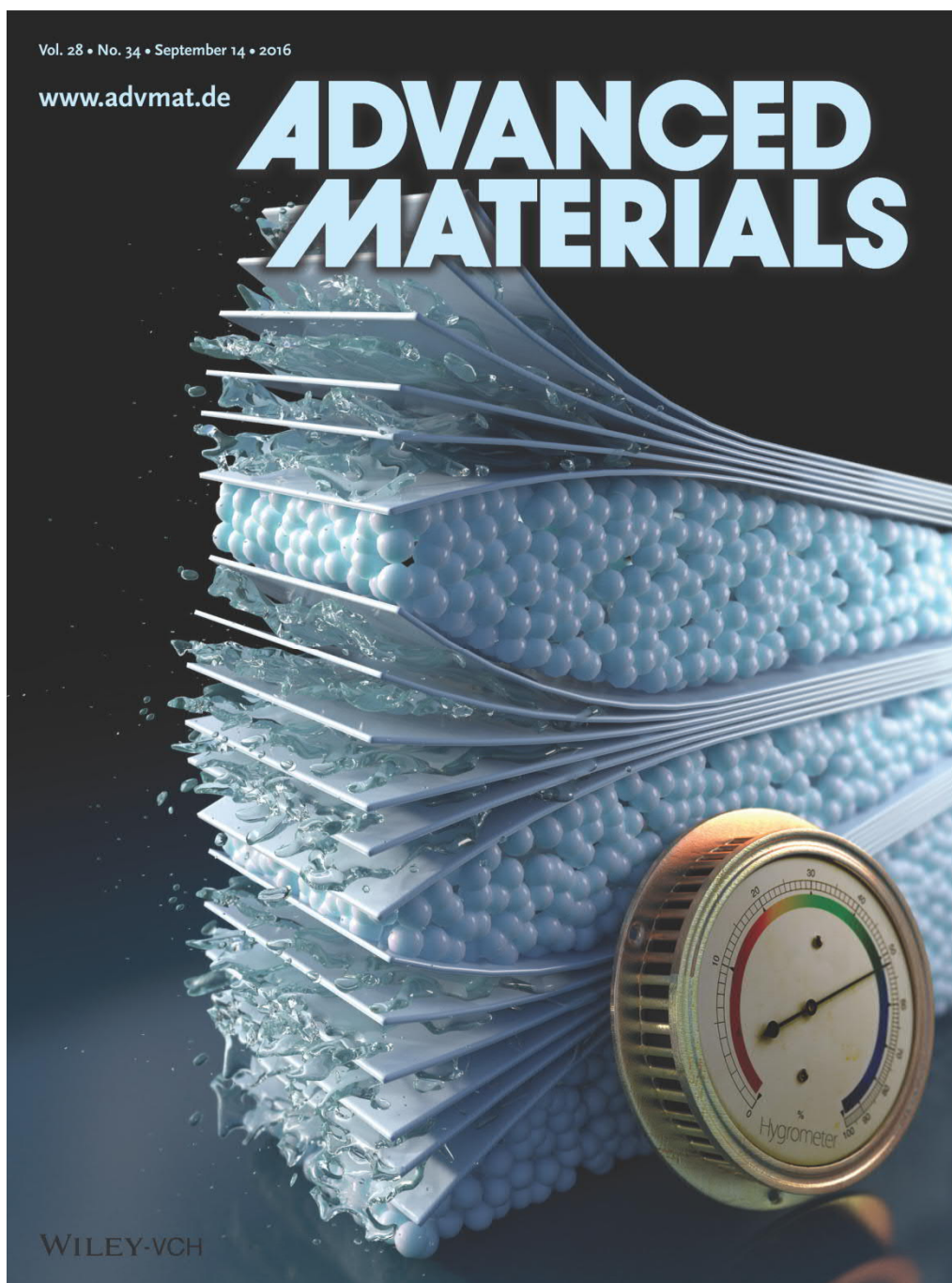
*equally contributed

Copyright © 2016 WILEY-VCH Verlag GmbH & Co. KGaA, Weinheim. Reproduced with the permission of WILEY-VCH.

Contribution of P.G.: *P.G. contributed the nanosheet synthesis & characterization as well as the measurements of the resistive humidity sensor and trace amounts of water detection. P.G. wrote the corresponding parts in the manuscript as well as major parts of the abstract, introduction and conclusion section. In addition, P.G. designed the TOC image, carried out major part of the literature research and prepared the graphical material.*

Abstract

Artificial noses, i.e. sensors with high sensitivity and selectivity for humidity as well as volatile organic compounds, are of increasing interest in medical diagnostics, pharmaceuticals and food or beverage control. However, the optical recognition of organic vapors by photonic noses still requires sophisticated sensor design or complex data processing. Herein, we address this issue by realizing a single-component sensing platform based on swellable 2D antimony phosphate (HSbP₂O₈) nanosheets, which can be operated with a resistive or an optical readout. While the resistive humidity sensor can be utilized for tracking trace amounts of water in alcohol water mixtures, 1D PCs based on HSbP₂O₈ nanosheets have been developed as colorimetric sensors with superior vapor recognition capability. This new type of photonic nose can distinguish between water vapor, non-protic and protic solvent vapors with high fidelity based on the saturation time and structural color shift as two independent descriptors. Chemically similar solvent vapors and even isomers, which interact with the nanosheet layers through an intercalative sensing mechanism, can be reliably distinguished based on their diffusion characteristics and analyte-specific host-guest interactions.



Inside Front Cover: On page 7436, B. V. Lotsch and co-workers report the fabrication of antimony phosphate nanosheet-based thin-film devices. While a resistive thin-film device can detect trace amounts of water, a photonic $\text{HSbP}_2\text{O}_8/\text{TiO}_2$ multilayer structure is effective at optically distinguishing between chemically similar solvent vapors through an intercalative sensing mechanism based on analyte-specific host-guest interactions. Cover Image by Christoph Hohmann, Nanosystems Initiative Munich (NIM).



Table of Content: A 2D nanosheet-based photonic nose for vapor identification is presented. A HSbP_2O_8 nanosheet thin-film sensor with resistive readout is developed for the tracking of trace amounts of water, and a photonic $\text{HSbP}_2\text{O}_8/\text{TiO}_2$ multilayer structure is effective at optically distinguishing between chemically similar solvent vapors through analyte-specific host-guest interactions.

3.1.1 Introduction

Artificial noses, mimicking the animal olfactory system, are of increasing interest in various technologically relevant fields such as medical diagnostics, pharmaceuticals, food and beverage control, ambient monitoring, and homeland security.^[1-3] Currently, the optical discrimination and classification of organic vapors by photonic noses still requires complicated experimental procedures or sophisticated data processing methods.^[1-4]

State of the art photonic noses can be divided into three main groups: single-element sensors,^[5-10] sensing arrays,^[1-3,11] and complex sensing structures, *e.g.*, topologically complex architectures or biological systems which are challenging to emulate in the lab.^[4,12] While each system can be adapted to specific environments, the following drawbacks remain: Current single sensor photonic noses, which are easy to fabricate, suffer from low resolution in terms of analyte recognition and classification into solvent vapors with different polarity.^[5,7-10] Sensing arrays rely on multiple sensors for good analyte resolution, requiring a complex mixture of materials or functionalization strategies. In addition, they necessitate complicated data processing algorithms for pattern recognition and discrimination.^[1,3,11] Complex sensor nanostructures, such as multiple stacked, porous Si PCs,^[4] or the Morpho butterfly wing - a naturally occurring photonic nose - can show good analyte identification, but invariably need sophisticated sample preparation or are not applicable on the large scale.^[12] Due to these reasons, there is a strong need for a smart but easy to fabricate single sensor photonic nose, which is able to distinguish and classify different types of analytes.

Recently, we have demonstrated the successful integration of 2D phosphoantimonate ($\text{H}_3\text{Sb}_3\text{P}_2\text{O}_{14}$) nanosheets into 1D PC.^[13] Their ultrahigh sensitivity to local humidity changes enables color-coded touchless finger motion tracking, thus illustrating the high potential of swellable 2D materials as active sensing components in photonic nanostructures. To demonstrate the generality of this approach and to highlight the potential of an intercalative sensing mechanism for analyte discrimination, we here

introduce a new type of stimuli-responsive 2D material, namely HSbP₂O₈ antimony phosphate nanosheets.

Similar to H₃Sb₃P₂O₁₄, HSbP₂O₈ as a bulk material has extraordinary swelling properties,^[14] which have been used to produce nematic liquid crystalline phases in water.^[15] In contrast to H₃Sb₃P₂O₁₄, HSbP₂O₈ loses water completely at zero humidity, hence making it a superior sensor candidate owing to its higher sensitivity in this humidity regime.^[14,16] The reason for the incomplete water loss of H₃Sb₃P₂O₁₄ can be rationalized by the presence of structural pores which can host water molecules, while the layers in HSbP₂O₈ are dense. The highly polar and acidic interlayer environment of HSbP₂O₈, its high sensitivity at low RH^[14,16] and the generally higher sensitivity of nanosheets compared to their bulk materials^[13,17,18] renders HSbP₂O₈ nanosheet-based thin film devices promising candidates for tracking trace amounts of water as well as for the discrimination of organic vapors.

Here, we report the first comprehensive characterization of HSbP₂O₈ 2D nanosheets and demonstrate their outstanding sensitivity to humidity - especially in the low humidity range. Based on these features, we develop resistive thin film sensors that are able to detect even trace amounts of water in alcohols. We then exploit the unique film forming capability of the 2D nanosheets to develop highly sensitive PC sensors which can identify various organic vapors with high accuracy, which is superior to all other single-component photonic vapor sensing structures reported to date.^[5-10]

3.1.2 Results and discussion

KSbP₂O₈ was synthesized by a solid-state reaction starting from KNO₃, Sb₂O₃, and NH₄H₂PO₄ and protonated with 8 M HNO₃ (Figures S3.1 and S3.2, and Table S3.1, Supporting Information).^[14,15,19,20] The antimony phosphate and its corresponding solid acid consist of anionic 2D SbP₂O₈⁻ sheets separated by charge compensating cations which occupy the interlayer space (Figure S3.3).^[19,20] The hexagonal crystal habit of HSbP₂O₈ is shown in Figure 3.1a. Upon exfoliation with pure water (Figure S3.4), the morphology becomes “silk-like” (Figure 3.1b, Figure S3.5), indicating successful delamination. Exfoliation into single layer nanosheets was further confirmed by various analytical techniques (see Figure 3.1, Figures S3.6, S3.7, and S3.8, and Tables S3.2 and S3.3). The thickness of a single nanosheet was determined to be 0.9 ± 0.1 nm by AFM (Figure 3.1d), which agrees well with the crystallographic single layer thickness of 0.66 nm.^[21] The high aspect ratio and film texture can be clearly seen by TEM (Figure 3.1e). The SAED pattern of an individual nanosheet (Figure 3.1e inset) exhibits *d*-values that are in excellent agreement with those obtained from PXRD measurements (see Table S3.2, and Figure 3.1c), illustrating the structural in-plane integrity. Rietveld refinement of the diffraction pattern of a precipitated nanosheet pellet, showing a characteristic Warren-type peak profile (Figure 3.1c) evidences the turbostratically disordered nanosheet arrangement.

Large area thin films were prepared by spin-coating nanosheets from the colloidal suspension and investigated by thin film XRD (Figure S3.9) and by ellipsometric porosimetry (Figure S3.10). Only the *00l* reflections were observed in the out-of-plane XRD pattern pointing toward a parallel

orientation of the nanosheets to the surface of the substrate. Upon exposure to moisture, the thin film swells to almost double its thickness. The swelling of the film is caused by intercalation of water molecules between the turbostratically disordered nanosheets and into the resulting grain boundaries. The RI n decreases from 1.57 to 1.50 with increasing humidity as the film becomes more “water-like” with increasing water uptake. Water uptake was also monitored by the Raman spectra of the bulk material as well as the nanosheet pellet (Figure S3.11). Slight changes are observed by the emergence of a band at 482 cm^{-1} (Sb-O \cdots P stretching vibration) and by narrowing of the terminal P-O stretching vibration at 1270 cm^{-1} . The latter band is sensitive to water uptake as the P-O bond points toward the interlayer space in which water is intercalated.

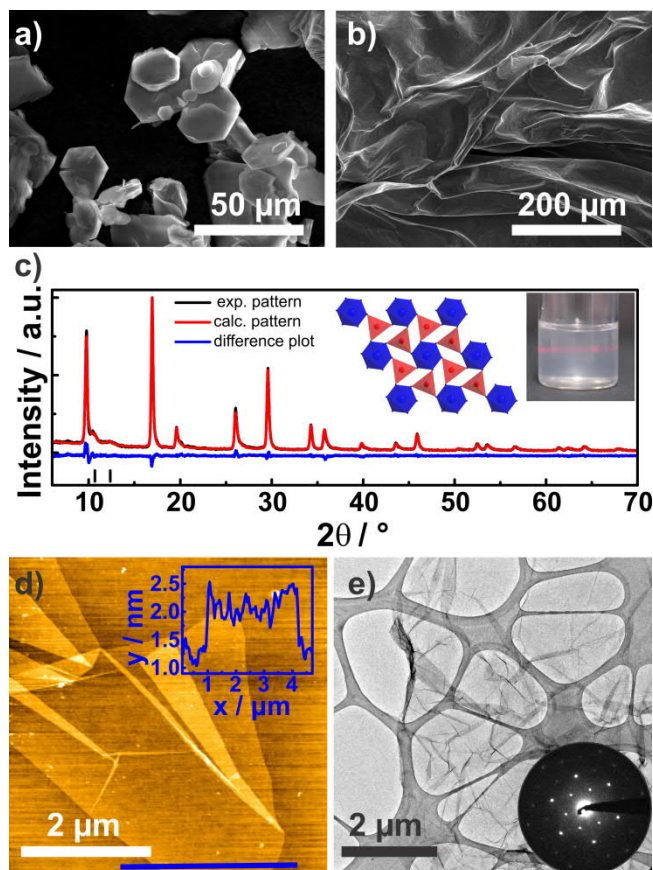


Figure 3.1. Characterization of HSbP_2O_8 nanosheets. a) SEM image of the HSbP_2O_8 crystallites featuring hexagonal shapes. b) SEM image of the exfoliated and randomly restacked nanosheet pellet, exhibiting a “silk-like” morphology. c) Rietveld refinement of the XRD pattern of a HSbP_2O_8 nanosheet pellet showing a Warren-type peak profile (experimental pattern in black, calculated pattern in red, and difference plot in blue) with the resulting structure ([001] viewing direction, PO_4 tetrahedra red, SbO_6 octahedra blue).^[32] The inset on the right in (c) shows the Tyndall effect of the nanosheet colloidal suspension. d) AFM image of overlapping HSbP_2O_8 monolayer nanosheets with the corresponding height profile of a single layer nanosheet. e) TEM image of randomly overlapping HSbP_2O_8 nanosheets with a representative SAD of a single nanosheet (inset).

Inspired by the swelling capability as well as the humidity dependent proton conductivity reported for the bulk material,^[14] we developed two ultrathin sensing devices based on HSbP_2O_8 nanosheets (Figure 3.2): first, we constructed a resistive thin film device by spin coating the nanosheet suspension on quartz substrates; the contacts were obtained by sputtering gold on top of the thin film (Figure 3.2a). Second, we combined the HSbP_2O_8 nanosheet films with TiO_2 NPs as high RI optical contrast material to fabricate a photonic multilayer structure known as 1D PC or BS (Figure 3.2). By combining these two robust inorganic materials in an alternating fashion, we observe the emergence of a pronounced photonic stop band (Figure 3.2b). The band gap and, hence, structural color can be adjusted and gradually fine-tuned across the visible spectrum (Figure 3.2b and c) by simply changing the layer thicknesses through varying the spin-coating speed in the fabrication steps. The position of the BP for normal incidence is given by the optical equivalent of the Bragg-equation^[22]

$$\lambda_B = 2(n_1 d_1 + n_2 d_2) \quad (\text{Equation 3.1})$$

where n_1 and n_2 are the RIs of the different layers and d_1 and d_2 their respective thicknesses.

Although BSs with up to eleven layers and good optical quality could be reproducibly made (Figure S3.12), an average number of seven layers deposited on a reflective silicon substrate turned out to be an optimal compromise in terms of optical quality (reflectance of 60%) and sensing performance, the latter resulting from fast analyte uptake and short diffusion pathways. The scanning electron microscope (SEM) cross-section images (Figure 3.2d) indicate stacking periodicity and excellent lateral layer uniformity across several micrometers, which is crucial for high optical quality multilayer films.

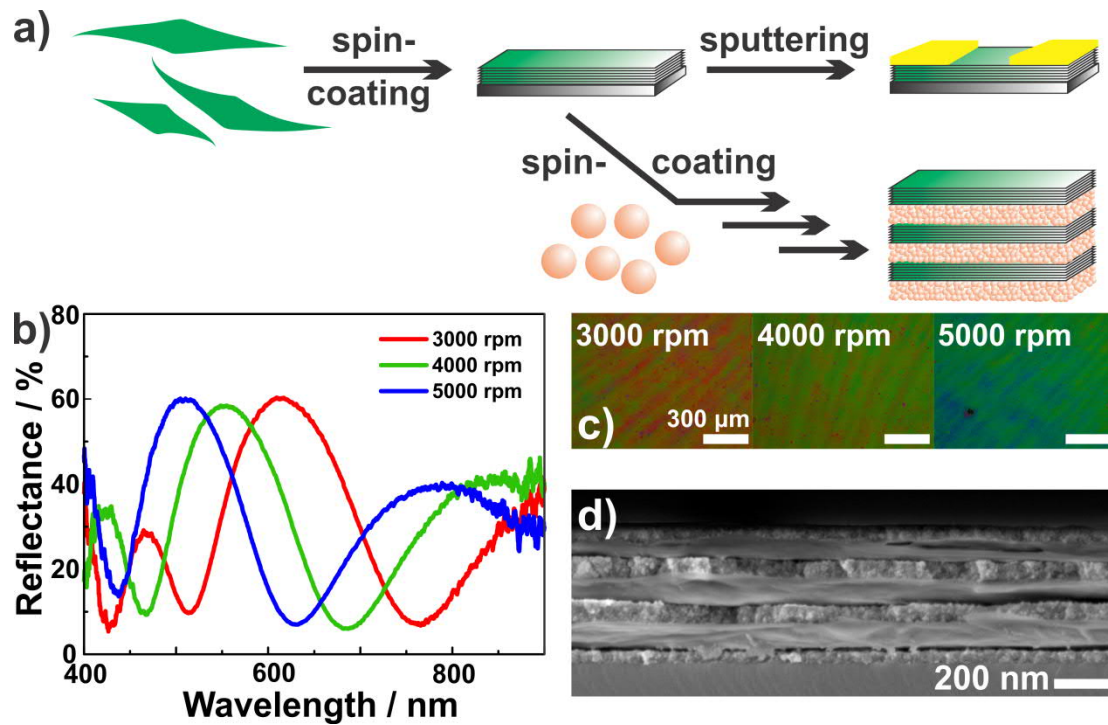


Figure 3.2. Fabrication and characterization of the nanosheets thin film devices: a) Schematic processing of HSbP_2O_8 nanosheets into thin film resistive devices (top) and 1D PC (bottom). b) Reflectance spectra of the HSbP_2O_8 nanosheet/ TiO_2 NP BS with seven layers, fabricated at 3000 rpm (150 nm bilayer thickness, red), 4000 rpm (135 nm bilayer thickness, green), and 5000 rpm rotational speeds (124 nm bilayer thickness, blue) and c) the corresponding microscope images, showing the different structural colors. d) In-lens SEM cross-section image of a HSbP_2O_8 nanosheet/ TiO_2 NP BS comprising seven layers.

Next, we studied the humidity sensing capabilities of the resistive nanosheet thin film and the BS (Figure 3.3a). We observe an increase in proton conductance of the thin film of five orders of magnitude upon humidity exposure from 0% to 100% RH (Figure 3.3b), which is larger than the change observed for the non-exfoliated bulk material^[14] and comparable to the best nanosheet thin film humidity sensing devices reported to date.^[13,17] Interestingly, in comparison to $\text{H}_3\text{Sb}_3\text{P}_2\text{O}_{14}$ nanosheet thin film sensors^[13] and the HSbP_2O_8 bulk material,^[14] the HSbP_2O_8 thin films show higher sensitivity

in the low humidity regime. Comparing to the bulk material, this can be explained by the fact that the thin film is able to desorb water molecules more easily due to its higher surface to volume ratio as well as the smaller domain size, most likely one nanosheet, compared to the bulk material, hence resulting in a greater water loss at low humidity values. The increased sensitivity of HSbP_2O_8 as compared to $\text{H}_3\text{Sb}_3\text{P}_2\text{O}_{14}$ can be understood by the complete water loss by HSbP_2O_8 due to the lack of structural adsorption sites for water. Moreover, the response of the thin film toward humidity is completely reversible as demonstrated by cycling experiments between 0% and 93.5% RH (Figure 3.3b inset). Inspired by this exceptional sensitivity to humidity, we tested the sensing performance of the photonic nanostructures. To this end, the BS was introduced into a closed chamber with a transparent glass window, whereby the humidity within the chamber was controlled by saturated binary salt solutions at around 25 °C.^[23,24] Simultaneously, reflectance spectra and microscope images were taken as shown in Figure 3.3c and Figure S3.13. The proposed sensing mechanism is depicted in Figure 3.3a. The sensor response is dominated by three effects: (i) the thickness of the nanosheet layers changes upon water adsorption/desorption, (ii) the effective RI of the nanosheet layers changes, and (iii) the effective RI of the NP layers changes upon water uptake/loss into/from the textural pores, while at the same time the thickness of the NP layers is constant over the entire humidity range as confirmed by spectroscopic ellipsometry. The combination of these effects gives rise to a pronounced optical response of the multilayer structure: with increasing humidity, a significant redshift of the stop band is observed, while the intensity of the BP increases. The main contribution to the stop band shift is caused by the massive swelling of the nanosheet layers during humidity uptake. As depicted in Figure S3.10, the nanosheet film swells from 85 to 132 nm between 0% and 100% RH. In the lower humidity range up to 93% RH, a nearly linear stop band shift of 150 nm is observed, while in the high humidity range (>93% RH) the stop band shifts dramatically by 400 nm, shifting the BP out of the visible spectral range (the second order of the BP is observed at 500 nm, see Figure S3.13, red curve). As shown in Figure S3.13, we simulated the reflectance spectra for different RH values using the layer thicknesses from the SEM cross-section image combined with the swelling behavior at higher RH values and the RIs from the porosimetry measurements (see Table S3.4).^[25] The excellent agreement with the measured spectra confirms the correctness of the proposed sensing mechanism and the water vapor distribution in the system. The observed shift is similar to that reported previously^[13] and thus larger than those observed for all vapor sensing devices.^[26-29] The microscope images displayed in Figure 3.3c convey the concomitant color changes which are easily detected by the naked eye. The second effect - the increase in reflectance intensity - is explained by the RI changes upon water uptake: while the RI of the NP layers increases (from 1.84 to 1.96) by filling the textural pores (Figure S3.14), the RI of the nanosheet layer decreases (from 1.56 to 1.50) by water intercalation. These opposite trends induce an increase in the RI contrast and, hence, in the reflectivity of the multilayer system at increasing humidity levels (Figure S3.13).

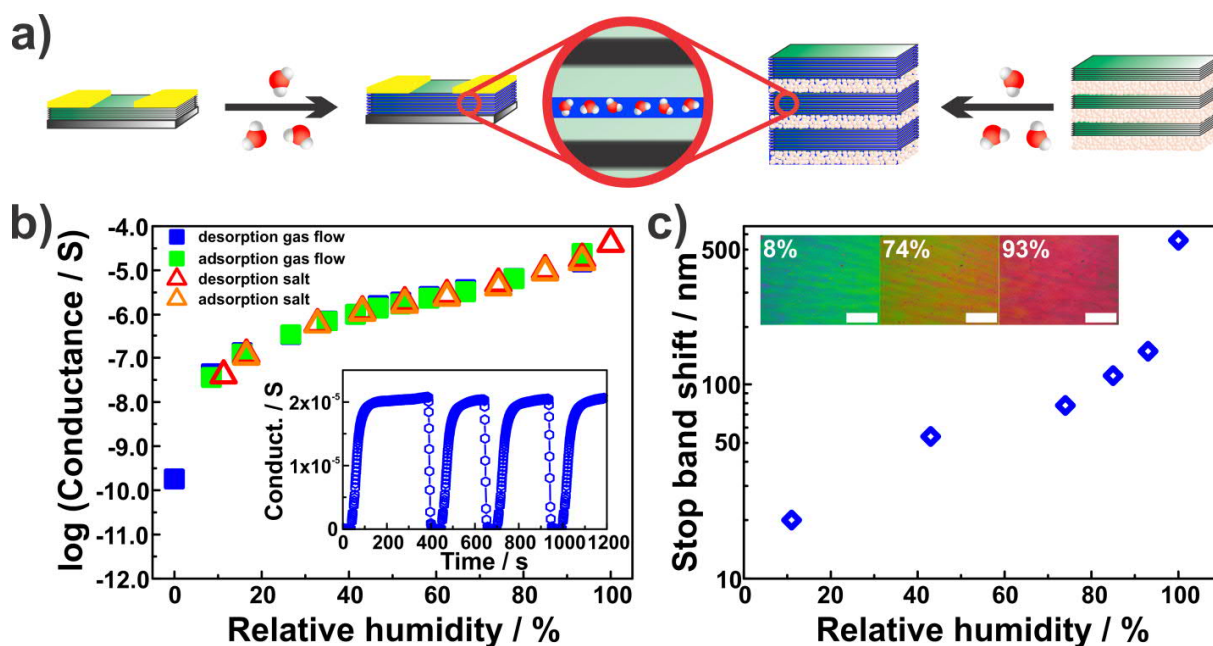


Figure 3.3. Humidity sensing of the HSbP_2O_8 nanosheet thin film and the $\text{HSbP}_2\text{O}_8/\text{TiO}_2$ BS sensor. a) Schematic of the analyte (water)-sensor interaction, shown for the resistive thin film sensor (left) and for the $\text{HSbP}_2\text{O}_8/\text{TiO}_2$ BS (right). The middle depicts a close-up of the swollen nanosheet layer. b) Humidity-dependent conductance behavior of the resistive thin film sensor with a film thickness of ≈ 120 nm, shown for two different methods (saturated salt solutions and Ar gas flow), and reversible cycling behavior between 0% and 93.5% RH (inset). c) Influence of humidity on the BP positions for the $\text{HSbP}_2\text{O}_8/\text{TiO}_2$ BS, and microscope images of the $\text{HSbP}_2\text{O}_8/\text{TiO}_2$ BS taken at different RH values (inset).

Besides sensitivity, another important performance parameter for sensors is the response time, defined as the time which is needed to reach 90% of the stop band shift between 0% and 100% RH. The fast response time of 23 s (Figure S3.15), which is superior to most existing humidity sensing devices with a large signal resolution based on a swelling mechanism,^[26-29] again underlines the applicability of these platforms for practical humidity sensing. It is important to note in this context that the time response of the reflectance intensity change represented by its time derivative (Figure S3.15) is instantaneous and so is the associated optical response: humidity changes cause an immediate stop band shift, which translates into an ultrafast increase or decrease in reflectance intensity at the observed wavelength within seconds (see inset of Figure S3.15). Other important sensor properties such as longterm stability and cycling stability were tested by applying a 2-month-old sample in a multiple cycling experiment (shown in Figure S3.15). As a result, the sensing performance (stop band shift and response time) was found unchanged as compared to the freshly prepared samples.

The high sensitivity in the low humidity regime renders the resistive thin film device an intriguing candidate for trace water sensing. Thus, we tested its selectivity toward water by analyzing alcohol-water mixtures. The large changes in conductance in response to water enabled us to detect amounts of water as low as 2000 ppm (Figure 3.4a), which are typical concentrations of trace water in polar solvents. Moreover, an exponential relationship between the measured conductance (Figure 3.4a, b inset) and the water content in the range between 2000 and 20000 ppm is observed, which is highly desirable for sensing applications. Moreover, the results for trace water detection are reproducible as

shown by the insets which report data averaged over three different samples. The antimony phosphate nanosheet sensor hence provides an attractive alternative to the more time consuming traditional methods for water determination such as the Karl-Fischer titration in the high ppm regime, thus pointing toward a new field of application of nanosheet thin film sensors in low-cost and high-throughput trace water analysis.

Besides achieving high sensitivity and selectivity toward one particular analyte (such as water), it is of major interest to optically distinguish between several different analytes. Here, we use a single 1D PC platform as a solution to both requirements - sensitivity and vapor discrimination capability - as demonstrated in Figure 3.4c, d. To this end, we plot the sensitivity - i.e., the magnitude of the stop band shifts - and saturation times of the sensor for different solvent vapors. To render the data for the different analytes comparable, the saturation times were calculated as the full time which is needed for the stop band to shift from 0% to 100% relative solvent vapor pressure. Similar to the water response described above, the onset of the optical shift is significantly faster than the saturation times implies but still differs for different solvents. As demonstrated in Figure 3.4c, the responses of the investigated solvents differ significantly and, besides water, can be grouped into two types of analytes: non-protic vapors (non-polar and polar) and protic vapors.

For water vapor, the sensor shows the largest stop band shift as well as the fastest saturation time, as expected. Non-polar analytes (*n*-heptane and toluene) and the polar, non-protic analyte acetonitrile show similar behavior; their saturation times are rather fast and the stop band shifts small. A qualitatively different response is seen if the BS is exposed to polar and protic analytes, namely alcohols: long response times are accompanied by larger stop band shifts (Table S3.5). According to the distinct optical responses (Figures S3.16 and S3.17) as probed by spectroscopy, we derive an interaction mechanism between analyte and sensor (Figure 3.4d), which is corroborated by optical simulations (Figures S3.16 and S3.17, dashed lines). The selectivity is defined by the interplay of several effects such as interlayer hydration and protonation, which determine the chemical environment as well as the molecular size of the analyte and its chemical and dielectric properties.

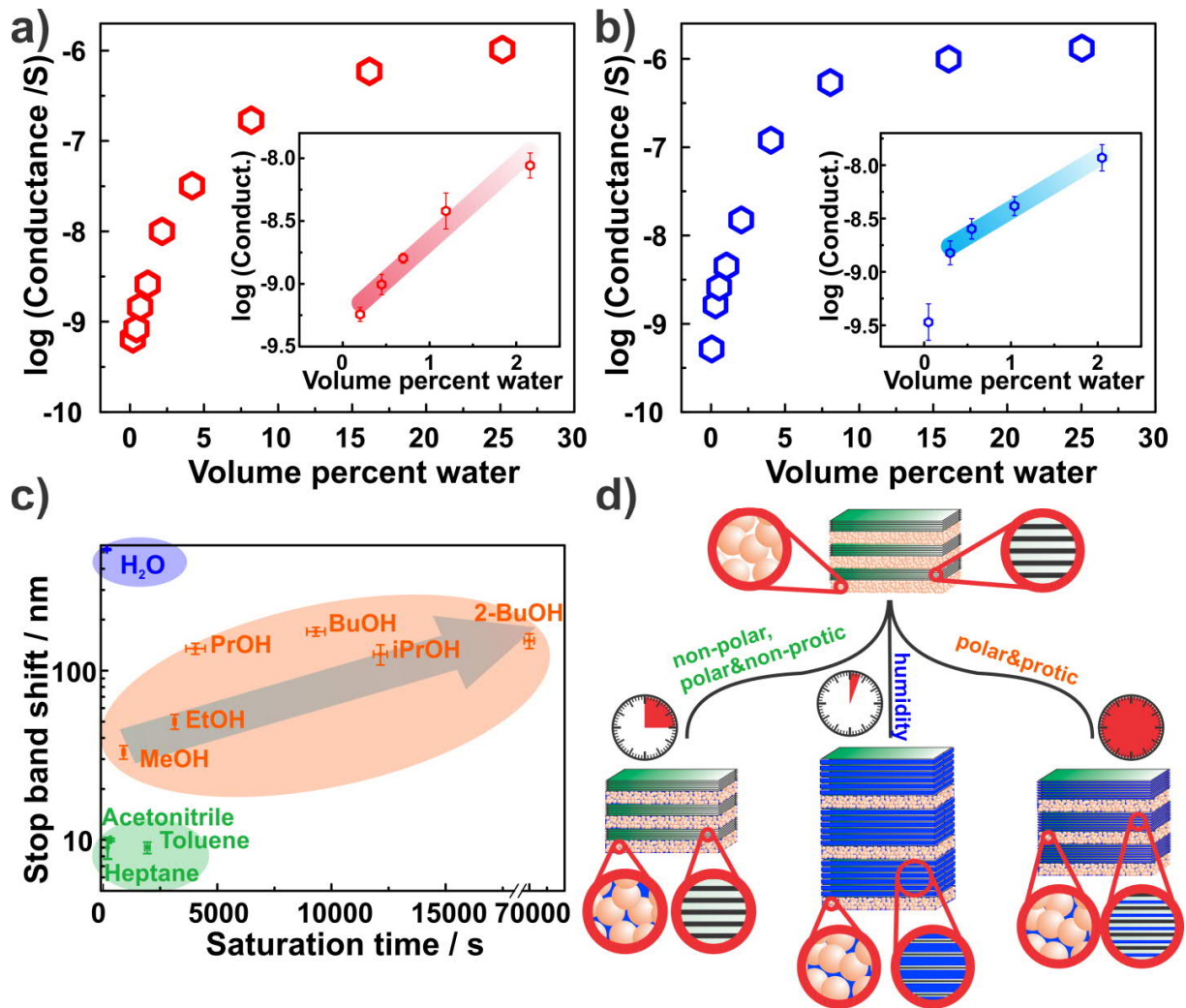


Figure 3.4. Sensitivity and selectivity features of the two devices. Representative trace water sensing of a thin film (120 nm) for a) ethanol and b) isopropanol. In both insets, a close-up of the region 0 and 2.5 volume percent of water is displayed with standard deviations resulting from averaging over three thin films. c) Logarithmic stop band shifts plotted against the response times for the different solvent vapors (BS fabricated at 5000 rpm). d) Schematic showing the interactions of the HSBP₂O₈ nanosheet/TiO₂ NP BS with the different types of solvent vapors, which serve as a fingerprint for analyte identification.

The non-polar analytes and aprotic acetonitrile show small stop band shifts (9, 9, and 10 nm for heptanes, toluene, and acetonitrile, respectively) combined with relatively fast saturation times (317, 1936, and 201 s for *n*-heptane, toluene, and acetonitrile, respectively). These vapors do not wet the polar and protic interlayer space of the nanosheets but only fill the textural pores of the NP layers, as corroborated by optical simulations. As a consequence, the stop band is broadened and its reflectance increases, while the blue edge of the stop band remains constant (Figure S3.16). This behavior is due to the increase in RI contrast,^[30] caused by the NP layer filling, while the RI and the thickness of the nanosheet layer remains nearly constant, as confirmed by the good agreement between the measured and simulated reflectance spectra (Figure S3.16, dashed line, and Table S3.6). As the stop band shifts are nearly the same for all these analytes, we assume that the dielectric properties only play a minor role regarding the extent of the stop band shift. The saturation time is determined by the interplay of

several analyte specific parameters, such as the kinetic diameter and the dipole moment. Although these effects are molecule specific and interrelated, we found the saturation time for the non-polar and polar, non-protic analytes to correlate most clearly with the kinetic diameter of the molecules (Figures S3.18 and S3.19): increasing saturation times correlate with the increasing molecular sizes and the resulting delayed diffusion of toluene (1936 s, 6.1 Å) compared to *n*-heptane (317 s, 4.3 Å) and acetonitrile (201 s, 3.4 Å).

In contrast, the optical response of the BS to protic solvent vapors - alcohols - significantly differs from that seen for aprotic analytes. Here, rather large stop band shifts were detected across the series methanol (33 nm) < ethanol (58 nm) < 2-propanol (120 nm) < 1-propanol (132 nm) < 2-butanol (150 nm) < 1-butanol (170 nm), with slow response times increasing in the following order: methanol (897 s) < ethanol (3130 s) < 1-propanol (4043 s) < 1-butanol (9320 s) < 2-propanol (12140 s) < 2-butanol (≈ 70000 s). In all cases, larger stop band shifts are observed compared to the stop band broadening for non-protic vapors (non-polar vapors and acetonitrile). Contrary to the non-protic analytes, however, the color shift is dominated by changes in the nanosheet layer thickness upon analyte infiltration, as evidenced by ellipsometric porosimetry and as exemplarily shown for ethanol (Figure S3.20): the protic character of the analytes allows for stronger interactions with the protic interlayer space and causes layer swelling upon intercalation. Further, we analyzed the time-dependent stop band changes and could distinguish two different phases during vapor sorption (Figure S3.21). Within the first ≈ 6 s, we observe a fast response expressed by a broadening of the stop band, accompanied by an increase in reflectance, similar to the overall response observed for the non-protic analytes. We attribute this initial behavior to the filling of the more easily accessible porous NP layers. In a second stage, a slower, analyte-specific response is observed, corresponding to a distinct stop band shift and giving rise to the analyte-specific saturation time, which is due to the intercalation of the analyte into the nanosheet layer. According to this time-dependent behavior, we clearly see that the rate-limiting step is associated with the intercalation of the analytes between the nanosheet layers, while the infiltration of the NP layers is rather fast, as shown also for the non-protic solvents as well as for water vapor. This interpretation is in line with rather weak interactions of the NP layer and the analytes, which is expected since no surface functionalization was carried out and the diffusion through a mesoporous layer is generally rather fast.^[31] To understand the sensing mechanism, which for the alcohols is dominated by the nanosheet layer-analyte interaction, we investigate the influence of several parameters on the stop band shift, such as the analyte's kinetic diameter, dipole moment, dielectric constant, and the RI. These parameters give rise to the analyte's dielectric, optical, and physicochemical properties such as its polarity and ability to form hydrogen bonds. The stop band shift and the saturation times most obviously correlate with the analyte's kinetic diameter, whereby we could confirm by optical simulations that the layer thickness swelling is increasing with increasing molecular sizes (Table S3.6). However, empirical correlations can be found as well for the dielectric constant and the RI of the analytes (Figures S3.18 and S3.19). In summary, although the above

parameters are interrelated and most likely their complex interplay determines the stop band shift, it is this interplay that is distinct for each individual analyte, hence giving rise to an analyte-specific response.

It is of note that even constitutional isomers, *e.g.*, those of propanol and butanol, can be distinguished by our nanosheet-based photonic nose. The saturation time is increased for 2-propanol compared to 1-propanol by a factor of 3 (12140 s vs 4043 s), and for 2-butanol compared to 1-butanol by a factor > 7 (≈ 70000 s vs 9320 s), whereby the stop band shifts are comparable for both isomers (132 nm vs 120 nm and 170 nm vs 150 nm). Although the kinetic diameters for both isomers are similar, subtle differences in the molecular shape and polarity may have a significant effect on the analyte's interaction with the nanosheet layers and, hence, its diffusivity, which is reflected in the significantly different saturation times. Overall, while the degree of swelling caused by the two isomers is similar, a differentiation of both constitutional isomers is clearly possible through the saturation times. Note that the reproducibility of the sensor response was verified by measuring each solvent vapor three times. The error bars in Figure 3.4c are testament to the high reproducibility and the ability of our system to reliably discriminate between different solvent vapors.

In addition, we studied the sensor performance for analyzing multiple component mixtures. For water-ethanol mixtures (Figure S3.22) we find that with increasing water amount in the mixture the stop band shifts also increase. With this, the relative amount of water in a water-ethanol mixture can be reliably determined by evaluating the stop band shift, which is as large as 80 nm for water contents between 0% and 90% (Figure S3.22b-e).

3.1.3 Conclusion

In summary, we have introduced a new type of HSBP₂O₈ nanosheet-based humidity sensor which can operate in two different modes, *i.e.*, with a resistive and an optical readout. The resistive humidity sensor shows superior sensitivity for water in the low humidity regime, which we utilize for tracking trace amounts of water in alcohol-water mixtures. The photonic humidity sensor, while exhibiting high sensitivity for humidity, shows also an exceptionally high selectivity toward water vapor. Further, this new type of photonic nose, based on swellable nanosheets embedded in a BS, presents a single-component sensor, which can clearly distinguish between water vapor, non-protic (non-polar and polar), and protic solvent vapors (alcohols) based on the saturation time and color shift as two independent descriptors. In particular, we find that even chemically similar solvent vapors, such as homologous alcohols, or even isomers, which interact with both the nanosheet and NP layers, can be reliably distinguished based on their sorption and diffusion characteristics. This single-component sensor adds to a new generation of nanosheet sensing devices which operate based on an interaction-driven, intercalative sensing mechanism that uniquely exploits both thermodynamic and kinetic properties of the host-guest system, namely dispersive analyte-nanosheet interactions and the diffusion properties of the analyte within the nanosheet layers. The rapidly increasing library of accessible and

chemically distinct nanosheet systems bodes well for the development of highly analyte-specific colorimetric artificial noses, which opens up new possibilities in environmental monitoring, trace water analysis, and biosensing.

3.1.4 Acknowledgement

Financial support was granted by the Max Planck Society, the University of Munich (LMU), the Center for NanoScience (CeNS), and the Deutsche Forschungsgemeinschaft (DFG) through the Cluster of Excellence Nanosystems Initiative Munich (NIM). The authors thank Alexander Kuhn and Roland Eger for prior investigations on the antimony phosphate system, Viola Duppel for TEM and SEM measurements, Claudia Kamella for the EDX-SEM measurements, Willi Hölle for his technical support with the home-built argon flow setup, Armin Schulz for Raman measurements, Frank Adams for thin film XRD, and Bernhard Illes for contributing to the BS fabrication. Further, the authors thank Daniel Selmeczi and the team of Semilab Sopra for their support with the ellipsometry measurements.

3.1.5 Bibliography

- [1] L. D. Bonifacio, D. P. Puzzo, S. Breslav, B. M. Willey, A. McGeer, G. A. Ozin, *Adv. Mater.* **2010**, *22*, 1351.
- [2] L. D. Bonifacio, G. A. Ozin, A. C. Arsenault, *Small* **2011**, *7*, 3153.
- [3] Z. Xie, K. Cao, Y. Zhao, L. Bai, H. Gu, H. Xu, Z.-Z. Gu, *Adv. Mater.* **2014**, *26*, 2413.
- [4] T. L. Kelly, A. G. Sega, M. J. Sailor, *Nano Lett.* **2011**, *11*, 3169.
- [5] Y. Wu, F. Li, W. Zhu, J. Cui, C. Tao, C. Lin, P. M. Hannam, G. Li, *Angew. Chem., Int. Ed.* **2011**, *50*, 12518.
- [6] F. M. Hinterholzinger, A. Ranft, J. M. Feckl, B. Ruhle, T. Bein, B. V. Lotsch, *J. Mater. Chem.* **2012**, *22*, 10356.
- [7] C. Cui, Y. Liu, H. Xu, S. Li, W. Zhang, P. Cui, F. Huo, *Small* **2014**, *10*, 3672.
- [8] L. Li, X. Jiao, D. Chen, B. V. Lotsch, C. Li, *Chem. Mater.* **2015**, *27*, 7601.
- [9] Y. Wu, F. Li, Y. Xu, W. Zhu, C. Tao, J. Cui, G. Li, *Chem. Commun.* **2011**, *47*, 10094.
- [10] Z. Hu, C. Tao, F. Wang, X. Zou, J. Wang, *J. Mater. Chem. C* **2015**, *3*, 211.
- [11] A. Ranft, F. Niekietel, I. Pavlichenko, N. Stock, B. V. Lotsch, *Chem. Mater.* **2015**, *27*, 1961.
- [12] R. A. Potyrailo, H. Ghiradella, A. Vertiatchikh, K. Dovidenko, J. R. Cournoyer, E. Olson, *Nat. Photonics* **2007**, *1*, 123.
- [13] K. Szendrei, P. Ganter, O. Sánchez-Sobrado, R. Eger, A. Kuhn, B. V. Lotsch, *Adv. Mater.* **2015**, *27*, 6341.
- [14] S. Deniard-Courant, Y. Piffard, P. Barboux, J. Livage, *Solid State Ionics* **1988**, *27*, 189.
- [15] F. Camerel, J. C. P. Gabriel, P. Batail, P. Panine, P. Davidson, *Langmuir* **2003**, *19*, 10028.
- [16] N. Miura, H. Mizuno, N. Yamazoe, *Jpn. J. Appl. Phys., Part 2* **1988**, *27*, L931.
- [17] S. Borini, R. White, D. Wei, M. Astley, S. Haque, E. Spigone, N. Harris, J. Kivioja, T. Ryhänen, *ACS Nano* **2013**, *7*, 11166.
- [18] J. Feng, L. Peng, C. Wu, X. Sun, S. Hu, C. Lin, J. Dai, J. Yang, Y. Xie, *Adv. Mater.* **2012**, *24*, 1969.
- [19] Y. Piffard, S. Oyetola, S. Courant, A. Lachgar, *J. Solid State Chem.* **1985**, *60*, 209.
- [20] Y. Piffard, A. Verbaere, S. Oyetola, S. Deniard-Courant, M. Tournoux, *Eur. J. Solid State Inorg. Chem.* **1989**, *26*, 113.
- [21] G. K. Prasad, N. Kumada, J. Yamanaka, Y. Yonesaki, T. Takei, N. Kinomura, *J. Colloid Interface Sci.* **2006**, *297*, 654.
- [22] J. D. Joannopoulos, S. G. Johnson, J. N. Winn, R. D. Meade, *Photonic Crystals: Molding the Flow of Light*, Princeton University Press, Princeton, NJ, USA **2008**.
- [23] P. W. Winston, D. H. Bates, *Ecology* **1960**, *41*, 232.

- [24] L. Greenspan, *J. Res. Natl. Bur. Stand.* **1977**, *81A*, 89.
- [25] M. C. Fuertes, S. Colodrero, G. Lozano, A. R. González-Elipé, D. Grosso, C. Boissière, C. Sánchez, G. J. d. A. A. Soler-Illia, H. Míguez, *J. Phys. Chem. C* **2008**, *112*, 3157.
- [26] E. Tian, J. Wang, Y. Zheng, Y. Song, L. Jiang, D. Zhu, *J. Mater. Chem.* **2008**, *18*, 1116.
- [27] J. H. Kim, J. H. Moon, S.-Y. Lee, J. Park, *Appl. Phys. Lett.* **2010**, *97*, 103701.
- [28] Z. Wang, J. Zhang, J. Xie, C. Li, Y. Li, S. Liang, Z. Tian, T. Wang, H. Zhang, H. Li, W. Xu, B. Yang, *Adv. Funct. Mater.* **2010**, *20*, 3784.
- [29] R. Xuan, Q. Wu, Y. Yin, J. Ge, *J. Mater. Chem.* **2011**, *21*, 3672.
- [30] L. D. Bonifacio, B. V. Lotsch, D. P. Puzzo, F. Scotognella, G. A. Ozin, *Adv. Mater.* **2009**, *21*, 1641.
- [31] I. Pavlichenko, E. Broda, Y. Fukuda, K. Szendrei, A. K. Hatz, G. Scarpa, P. Lugli, C. Brauchle, B. V. Lotsch, *Mater. Horiz.* **2015**, *2*, 299.
- [32] The two weak reflections marked with vertical scatters (Figure 3.1c) are stacking reflections and result from noncomplete preferred sample orientation. These peaks were fitted with a single peak phase function.

3.2 Supporting Information: Towards the Nanosheet-Based Photonic Nose: Vapor Recognition and Trace Water Sensing with Antimony Phosphate Thin Film Devices

3.2.1 Methods

Synthesis of the bulk, protonation and exfoliation

KNO₃ (99%, Merck), Sb₂O₃ (99.6%, Alfa Aesar) and NH₄H₂PO₄ (98%+, Acros Organics) were ground in a stoichiometric ratio and heated up in a corundum crucible as previously described to yield KSbP₂O₈.^[1] To obtain HSbP₂O₈, KSbP₂O₈ was treated with 8 M HNO₃ (250 mL, diluted 65 wt%, Merck) overnight, filtrated, washed with ethanol and dried at room temperature. This treatment was repeated at least two more times to complete the ion exchange reaction. The exchange reaction was followed by XRD (Figure S3.2). For exfoliation HSbP₂O₈ was vigorously stirred overnight in water (7.3 mmol L⁻¹). The resulting colloidal suspension was then centrifuged at 3000 rpm for 30 min to remove non-exfoliated bulk material. The supernatant, consisting mainly of single layer nanosheets, was collected and centrifuged at 18000 rpm for 30 min to yield a nanosheet pellet. The gel-like colorless wet aggregate was dried at 100 °C.

Preparation of colloidal suspensions

The dried HSbP₂O₈ nanosheets were suspended in a mixture of water : ethanol (60 : 40 wt%) with a concentration of 41 mmol L⁻¹. To avoid agglomerates, the suspension was sonicated for 2 h. This suspension was directly used for thin film formation without any further treatment. TiO₂ nanoparticulate sols were synthesized using a procedure described elsewhere.^[2] Briefly, 12.4 mL Ti(OEt)₄ (Sigma Aldrich) was added dropwise under vigorous stirring to 75 mL 0.1 M HNO₃. This mixture was heated to 80 °C for 8 h. After collection of the particles by repeated centrifugation at 20000 rpm and redispersion in methanol, the suspension with 3wt% was directly used in the BS fabrication.

Fabrication of thin films and BSs

All thin films and BSs were fabricated by means of spin-coating using a spin coater (WS-650S-NPP-Lite, Laurell Technologies Corporation) and colloidal suspensions of the nanosheets and NPs, respectively, with the colloidal concentrations given above, in the previous section.

For conductance measurements, the redispersed nanosheet colloid was spin-coated at 3000 rpm or 2000 rpm for 1 min with a 10000 rpm s⁻¹ acceleration ramp on a 1.5 cm x 1.5 cm plasma-cleaned quartz glass substrate. To achieve a sufficient film thickness (around 100 nm) for the conductance measurements, this deposition step was repeated once. Gold contacts were sputter-coated (108auto, Cressington) with 180 s sputtering time.

For the BS fabrication, different film thicknesses were accessed by varying the spin coating speed, which allowed for fine-tuning of the optical properties.^[3] On plasma cleaned silicon substrates (1.5 cm

x 1.5 cm) 150 μ l of the colloidal suspensions were spin coated alternately for 1 min with a defined speed and heated to 80 °C for 15 min after each layer deposition. 3000 rpm, 4000 rpm and 5000 rpm spin coating speeds were applied (the same speed for each layer within a BS) to tune the optical properties. To create a single nanosheet layer within the BS, two deposition steps were applied, both with the same speed, as given above, and further an acceleration rate of 500 rpm s⁻¹ was used. After both deposition steps, the sample was heated to 80 °C for 20 min before the deposition of the next layer. For the TiO₂ NPs, an acceleration rate of 5000 rpm s⁻¹ was applied. The starting and also the last layers are composed of the high RI NPs (TiO₂), in order to ensure the adhesion to the substrate and to increase the RI contrast with the surrounding air.

3.2.2 Characterization

Structural characterization

SEM images of the HSbP₂O₈ crystals and the nanosheet pellet were acquired with a Vega TS 5130 MM (Tescan) equipped with Si/Li detector (Oxford). Cross-section images of the BSs were taken with a Zeiss Merlin FE SEM. TEM images and SAED patterns were obtained with a Phillips CM30 ST TEM (300 kV, LaB₆ cathode) equipped with a Gatan CCD camera. TEM-EDX analysis was performed with a Si/Li detector (Thermo Fisher, Noran System Seven). XRD patterns were recorded on a powder X-ray diffractometer (Stadi P, STOE) working with Ge(111) monochromated Mo-K _{α} 1 radiation ($\lambda = 70.926$ pm) or Cu-K _{α} 1 radiation ($\lambda = 154.051$ pm). Rietveld refinement of the nanosheet pellet measured in transmission geometry was performed with the software DiffracPlus TOPAS v4.2 (Bruker AXS). A quasi single layer approach similar to the one described in the literature was used to approximate the turbostratic disorder.^[4,5] The sample showed preferred orientation effects such that almost exclusively the *hk0* reflections were observed, which allows us to use a simplified model compared to the models as described in the literature, which in addition include modeling of the *00l* reflections. AFM images were acquired on a Veeco CP II system in non-contact mode. The images of the surfaces of the BS were obtained with an optical microscope (Olympus BX51), operating in reflection mode with a 4x objective.

Conductance measurements

To obtain the conductance measurements for RH, two different methodologies were used. In the first one, the films were kept over saturated salt solutions at around 25 °C^[6,7] in a closed atmosphere at least 20 min before the conductance measurements. In the second one we used an argon flow set up. A dry Ar flow and a water vapor saturated Ar stream were mixed in different ratios to define the humidity between 0-93.5%. The setup was calibrated using the conductance values previously measured at the RH defined by the salt solutions. The cycling experiments were performed with the Ar flow setup. For sensing trace amounts of water in alcohol (ethanol 99.8%, water \leq 0.2%, Roth; 2-propanol 99.8%, water \leq 0.05%, Merck) water mixtures, an Ar stream at a constant rate of 8.4 L min⁻¹

was passed through 100 mL of solution. By passing an Ar stream through the solution the stream takes up certain amounts of moisture and ethanol, which leads to a change in the conductance of the thin film sensor.

The change in conductance was monitored by impedance spectroscopy (in-plane geometry, two point measurement) with an impedance bridge (Princeton Applied Research, VersaSTAT MC) applying an AC voltage of 500 mV and a frequency range of 1 Hz to 1 MHz. Cycling measurements were performed with a fixed frequency of 300 Hz.

Optical characterization

Porosimetry measurements were carried out by the porosimetry tool of Sopra PS-1000 SAM, whereby the sample was equilibrated at all water vapor relative pressure values for 15 min. The measurement results were fitted with the software Sopra SAE using the model combination Cauchy and Lorentz. The thickness of the NP layers was confirmed by ellipsometry to be constant with changing vapor relative pressure and only the RI was fitted. For the nanosheet thin films, both the layer thickness and the RI were fitted over the relative pressure range simultaneously. Prior to all measurements, the NP samples were heated for at least 30 min at 200 °C and the nanosheets thin films for 30 min at 60 °C in vacuum to make sure that the pores are empty. To obtain the optical isotherms, all fitted measurement results were plotted against the analyte relative pressure.

All optical spectra were measured with a fiber optic spectrometer (USB2000+, Ocean Optics) attached to a microscope (DM2500, Leica) with normal incidence and the optical spectra were always taken at the same spot ($1 \times 1 \text{ mm}^2$ in area).

To obtain the optical changes with changes in RH, the BSs were kept in a stainless steel chamber with a total volume of 5 mL and with a transparent glass window. In the chamber, 0.7 mL of saturated salt solutions^[6,7] were filled without touching the sample surface, and kept at around 25 °C to define the humidity in the closed atmosphere. At each step, 20 min equilibration time was needed.

To measure the response to solvent vapors and the saturation times for all analytes (including the cycling experiments), a mass flow controller with a controlled evaporation mixer (CEM) (see below) was applied. To measure the saturation time, the reflectance intensity changes of the BP were observed at a certain wavelength placed at the red stop band edge. While the BP shifts as a response to the analyte exposure, the reflectance intensity changes at the observed wavelength. The full response from 0% to 100% vapor relative pressure was taken defined as the saturation time. In these dynamic measurements, the BSs were placed into a closed chamber with the dimensions of $2.5 \times 2.5 \times 0.5 \text{ cm}^3$, where well-defined vapor relative pressure values were realized by connecting the inserted pipette tip with a liquid gas flow controller (Bronkhorst) and a vaporizer (CEM) with a massflow controlled carrier gas flow. To observe a specific solvent vapor relative pressure, the carrier gas nitrogen (200 mL min^{-1}) and the liquid solvent were dosed into the CEM (controlled evaporation and mixing, W101A 130 K, Bronkhorst High Tech), where the thermal evaporation of the solvent took place. The

CEM was heated to temperatures slightly above the boiling point. The relative vapor pressures were calculated via the software FLUIDAT (CEM calculation), which considers the actual atmospheric pressure, the temperature and the properties of the analyte (vapor pressure, heat capacity).^[8] The obtained data were analyzed with the SPECTRA SUITE (2008) software.

Simulations

Simulations of the reflectance spectra were carried out using a Matlab code based on a full vector calculation using the transfer matrix method.^[9] The layer thicknesses at 0% RH and 0% analyte relative pressure were taken from the SEM cross section images. The refractive indices were taken from the porosimetry measurements. For the simulations of the selectivity measurements, the layer thicknesses at 100% were fitted according to the measured reflectance spectra. The refractive indices in the optical isotherms are given at 623 nm.

3.2.3 Additional data

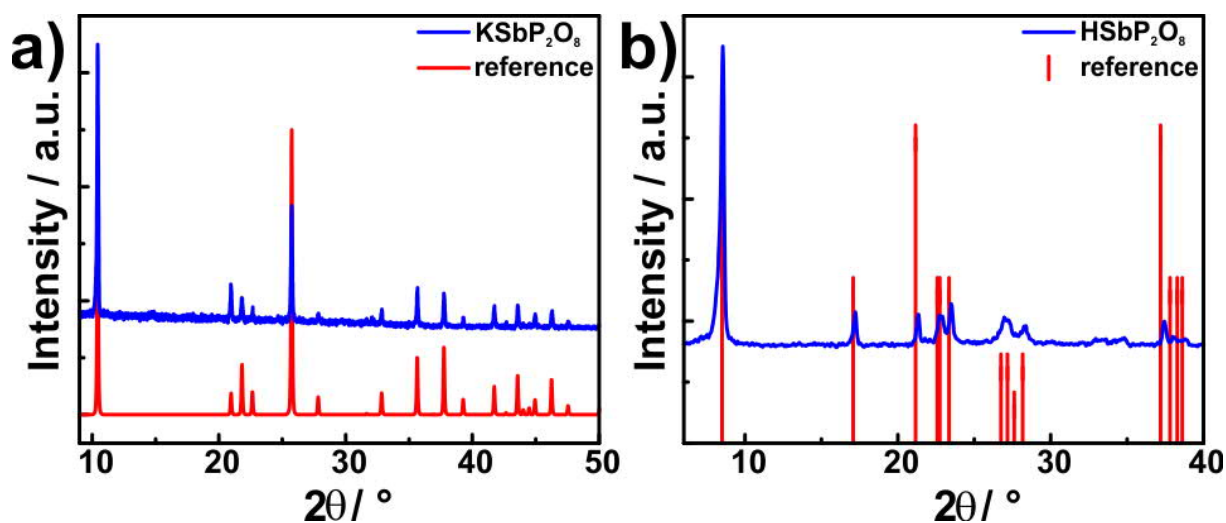


Figure S3.1. Experimental XRD patterns of a) KSbP_2O_8 b) HSbP_2O_8 (in blue) and reference XRD patterns (red) from the literature for (a) KSbP_2O_8 obtained from single crystal data and (b) for $\text{HSbP}_2\text{O}_8 \cdot 2 \text{H}_2\text{O}$. Both XRD patterns were recorded with $\text{Cu-K}\alpha_1$ radiation.

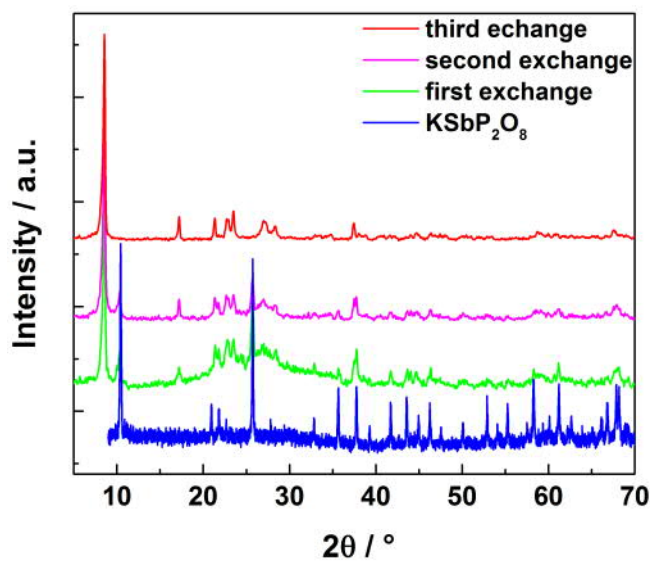


Figure S3.2. Cation-proton exchange for KSbP_2O_8 monitored by XRD. Three exchange steps are necessary for complete cation-proton exchange as illustrated. All XRD patterns were recorded with $\text{Cu-K}\alpha_1$ radiation.

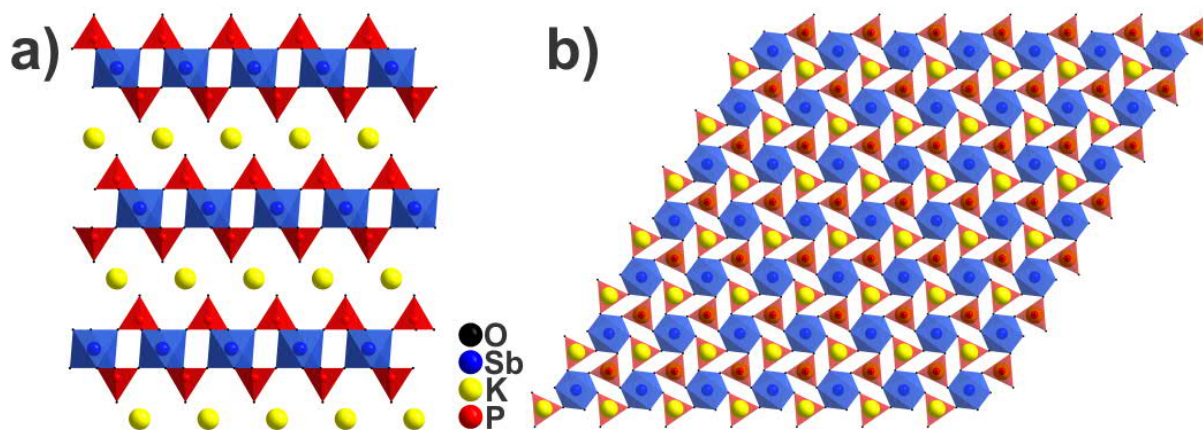


Figure S3.3. Structure of KSBP_2O_8 viewed along a) $[010]$ and b) $[001]$. K atoms in yellow, Sb atoms in blue, P atoms in red and O atoms in black. For a better overview only one layer is shown along $[001]$.

Table S3.1. EDX data of KSBP_2O_8 and $\text{HSbP}_2\text{O}_8 \cdot \text{H}_2\text{O}$. The given data are averaged over four points; standard deviation in brackets. The small amount of Al found is due to the synthesis in corundum crucibles.

	K Atom%	Sb Atom%	P Atom%	O Atom%	Al Atom%	Calc. Formula
Theo. values	8.3	8.3	16.6	66.6		KSBP_2O_8
Exp. values	8.4 (1.8)	8.4 (1.8)	15.5 (1.9)	66 (5)	0.6 (4)	$\text{KSb}_{1.01}\text{P}_{1.85}\text{O}_{7.95}$
Theo. values		8.3	16.7	75		$\text{HSbP}_2\text{O}_8 \cdot \text{H}_2\text{O}$
Exp. values		8.4 (1.4)	15.5 (1.1)	76 (2)		$\text{HSbP}_{1.83}\text{O}_{9.03}$

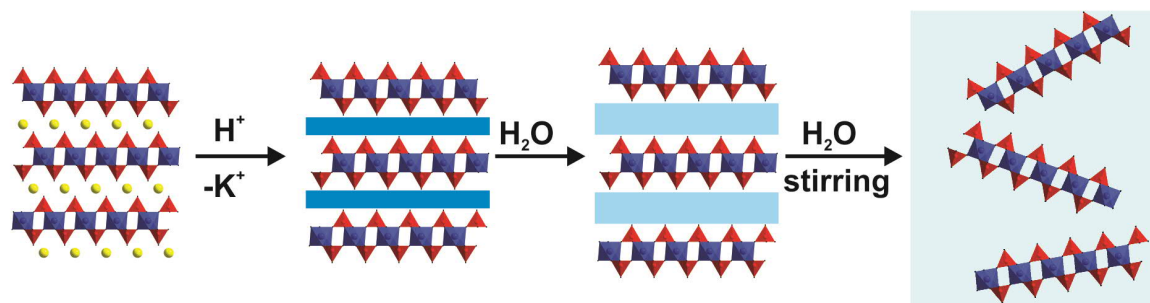


Figure S3.4. Schematic exfoliation of HSbP_2O_8 assuming that first swelling takes place, followed by exfoliation.

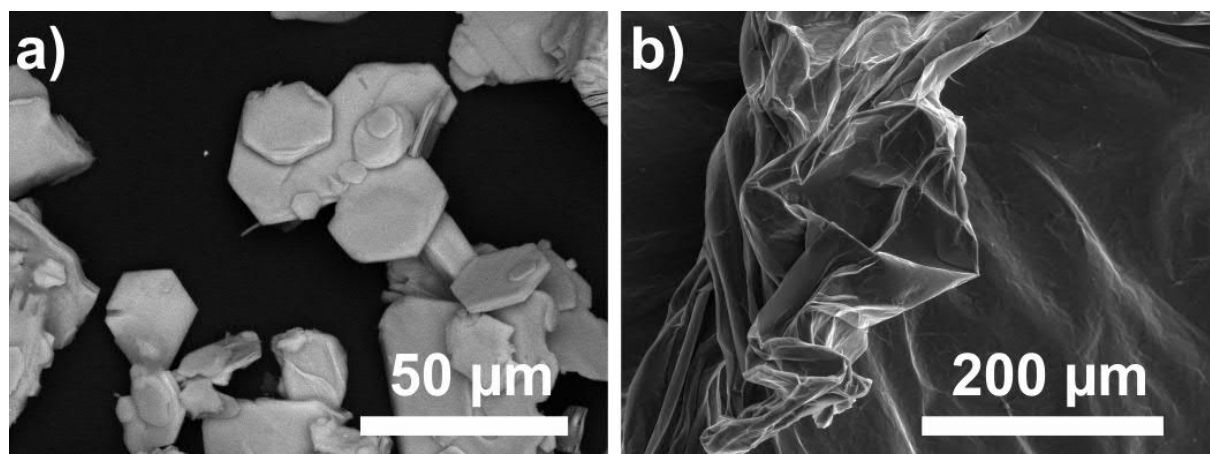


Figure S3.5. Additional SEM pictures. a) BSE image of HSbP_2O_8 bulk phase and b) SE image of a HSbP_2O_8 nanosheet pellet.

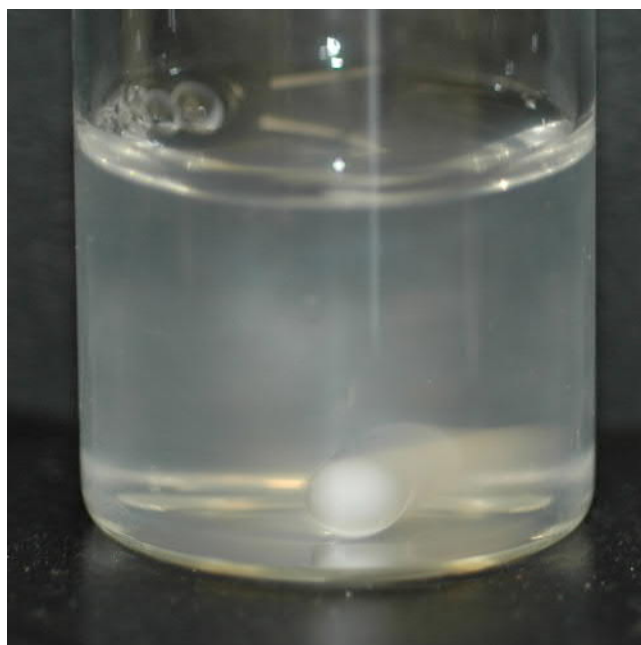


Figure S3.6. Schlieren texture of the exfoliated nanosheets in suspension.

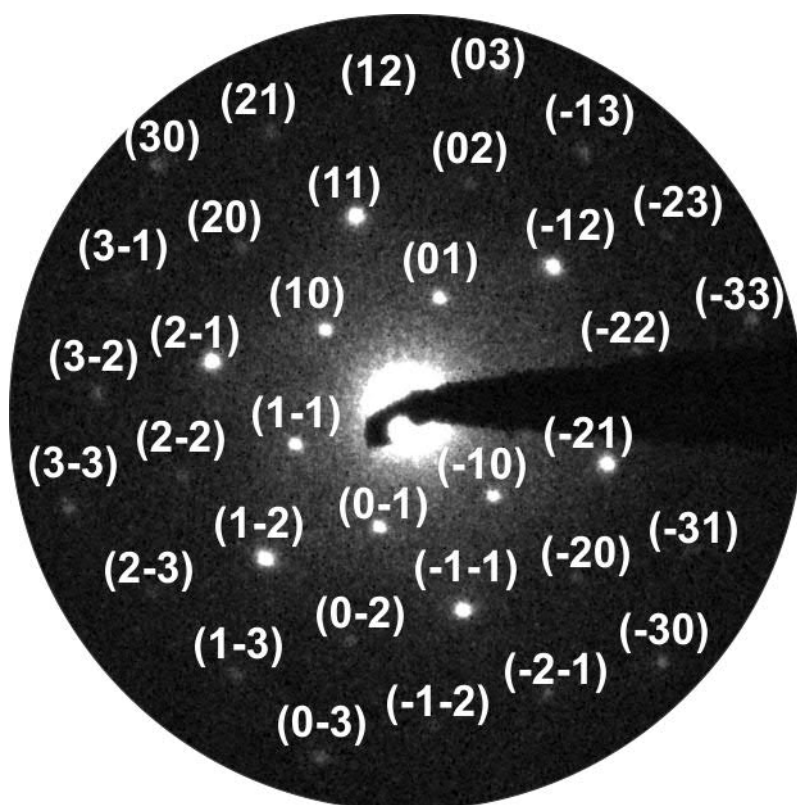


Figure S3.7. Indexed and magnified SAD pattern from Figure 3.1e).

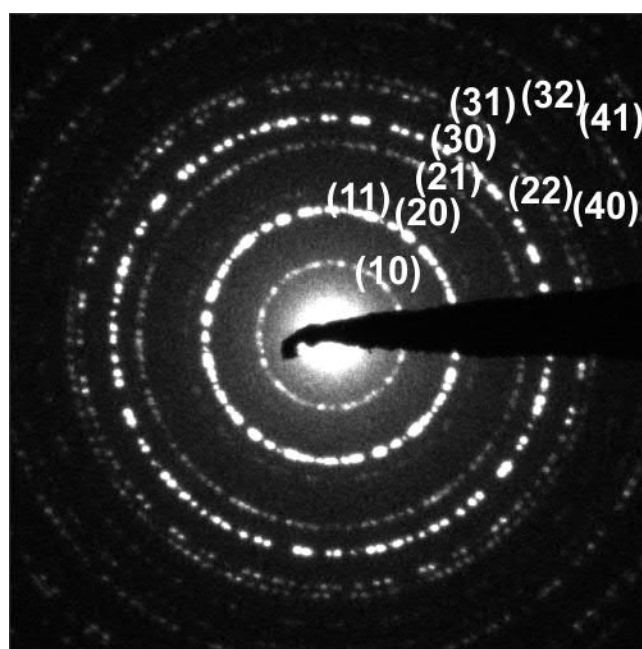


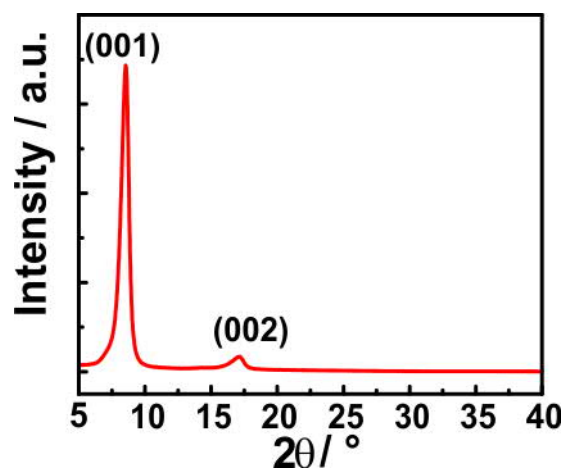
Figure S3.8. Indexed SAD pattern of HSbP_2O_8 nanosheets. The concentric rings are due to randomly overlapping (e.g. rotated along $[001]$) nanosheets.

Table S3.2. Comparison and indexing of d -values of SAD (Figure S3.7 and S3.8) and XRD patterns (Figure 3.1c). Note that as the nanosheet has a layer group ($p\bar{3}$ (66)) only (hk) indices are used for indexing.

HSbP_2O_8 nanosheets			
Miller indices	d value SAD [\AA] (Figure S3.7)	d value SAD [\AA] (Figure S3.8)	d value XRD [\AA]
(10)	4.24	4.16	4.17
(11)	2.46	2.43	2.41
(20)	2.11	2.09	2.08
(21)	1.59	1.58	1.57
(30)	1.41	1.40	1.39
(22)		1.21	1.20
(31)		1.16	1.16

Table S3.3. EDX data of the nanosheet pellet at two measured points.

	Sb Atom%	P Atom%	O Atom%	Calc. Formula
Theo. values	7.7	15.4	76.9	$\text{HSbP}_2\text{O}_8 \cdot 2 \text{H}_2\text{O}$
Exp. values (I)	7.7	15.1	77.3	$\text{HSbP}_{1.96}\text{O}_{10.04}$
Exp. values (II)	7.2	14.6	78.2	$\text{HSbP}_{2.02}\text{O}_{10.86}$

**Figure S3.9.** Out-of-plane XRD-pattern of a 120 nm thick HSbP_2O_8 nanosheet film deposited by spin-coating on a Si-substrate. Note that we only observe the (00 l) reflections while ($hk0$) reflections are absent, indicating a strongly preferred sample orientation (i.e. most of the sheets are lying parallel to the surface of the substrate).

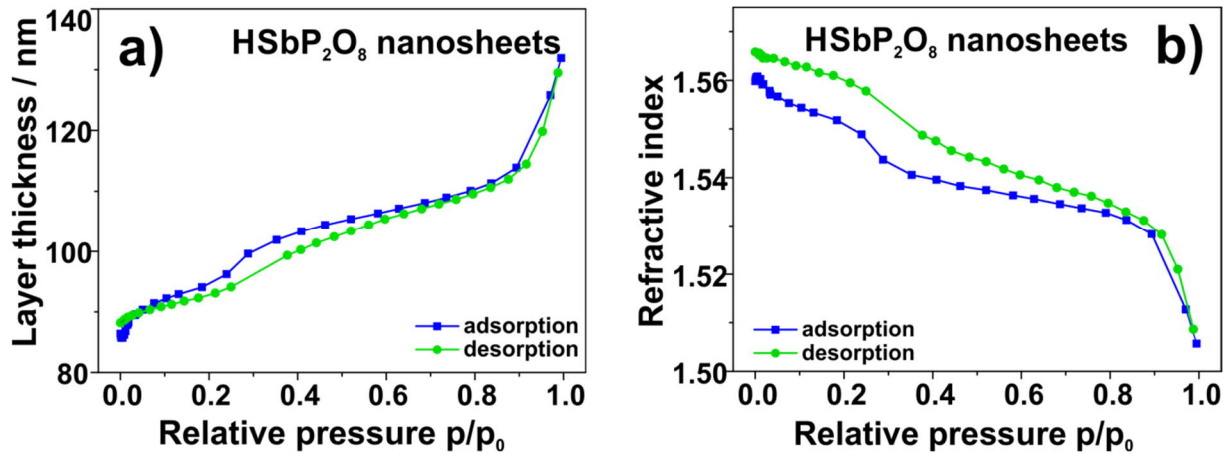


Figure S3.10. Optical isotherms of a thin film of HSbP_2O_8 nanosheets measured by ellipsometric porosimetry. a) Layer thickness and b) RI (at 623 nm) change of a HSbP_2O_8 nanosheet thin film measured at different relative pressures of water vapor.

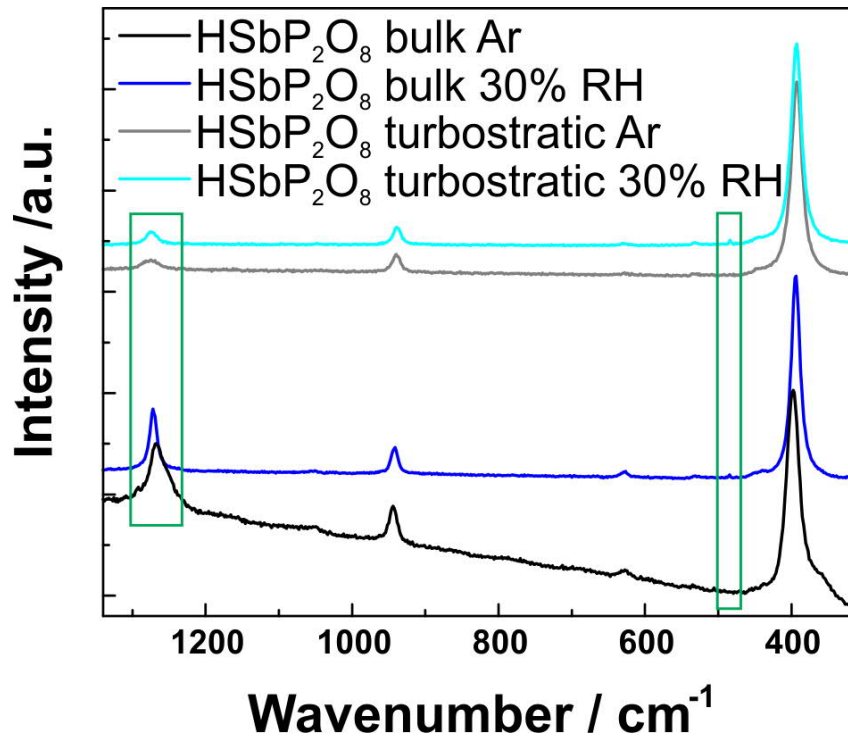


Figure S3.11. Raman spectra of the bulk material HSbP_2O_8 and the turbostratically disordered nanosheet pellet under ambient conditions (ca 30% RH) and Ar atmosphere, respectively. Note that due to luminescence we were unable to extract data for the region where the O-H stretching vibrations are expected (3600-2900 cm^{-1}). The spectra are in good agreement with the ones reported in the literature.^[10,11] A minor impurity band is present in bulk HSbP_2O_8 at around 1049 cm^{-1} , but can be removed by the exfoliation - centrifugation procedure to obtain the nanosheet pellet. The most significant changes are highlighted in green. One small band appears at 482 cm^{-1} for the samples measured under ambient conditions compared to the dried samples. This observation is consistent with the literature, in which a similar band is reported for $\text{HSbP}_2\text{O}_8 \cdot 2\text{H}_2\text{O}$ in contrast to KSbP_2O_8 , which does not have any crystal water. The band is most likely assigned to the Sb-O \cdots P stretching vibrations.^[10] Another difference is observed at 1270 cm^{-1} : The band broadens when the sample is dried and becomes sharper under humid conditions. The band is assigned to the P-O terminal stretching vibration, which is largely influenced by the interlayer environment and, thus, hydration state.^[10,11] Note, that all these change are reproducible and reversible.

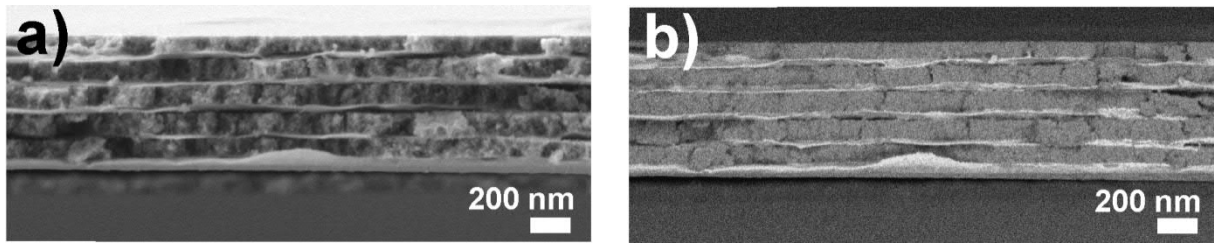


Figure S3.12. a) In-lens and b) backscattered SEM cross-section images of a HSbP_2O_8 nanosheet/ TiO_2 NP BS comprised of 11 layers showing the two different materials and the different morphologies.

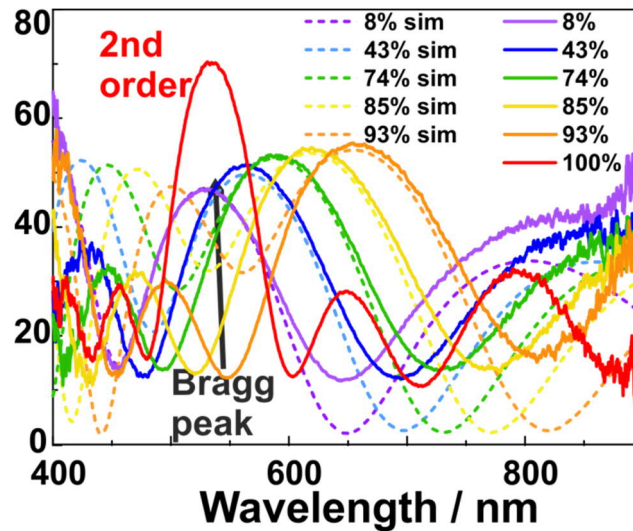


Figure S3.13. Reflectance spectra and simulated spectra (dashed lines) of the HSbP_2O_8 nanosheet/ TiO_2 NP BS taken at different RH values.

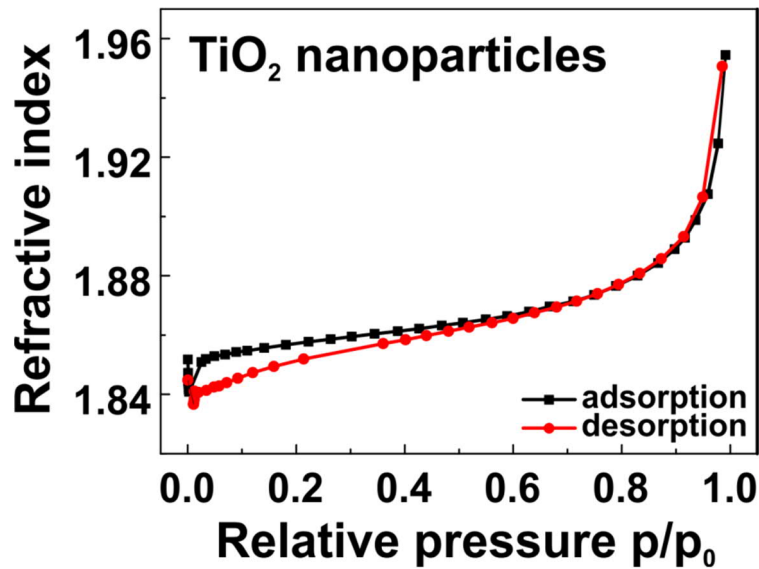


Figure S3.14. Optical isotherm of the TiO_2 NP monolayer monitoring the RI changes (at 623 nm) upon increasing the relative pressure of water vapor measured by ellipsometric porosimetry.

Table S3.4. Refractive indices and monolayer thicknesses for the $\text{TiO}_2/\text{HSbP}_2\text{O}_8$ BS used for the Matlab simulations at different RH values. The layer thickness changes for the BS at different RH values were calculated from the ellipsometry measurements (Figure S3.10a) for the actual thicknesses of the BS.

RH	TiO_2		HSbP_2O_8	
	Layer thickness	RI	Layer thickness	RI
8%	58 nm	1.840	78 nm	1.560
43%	58 nm	1.870	91 nm	1.539
74%	58 nm	1.93	97 nm	1.533
85%	60 nm	1.934	103 nm	1.525
93%	61 nm	1.940	115 nm	1.520

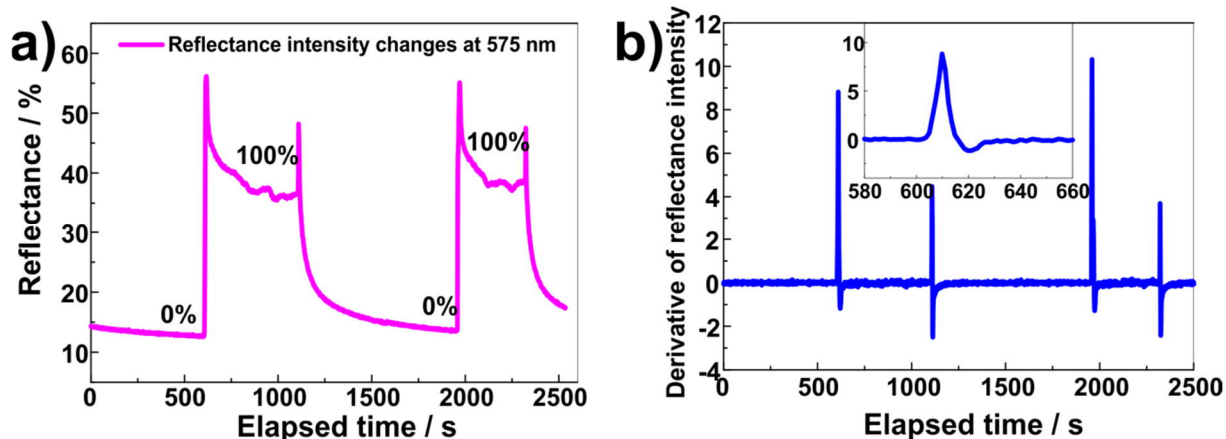


Figure S3.15. Time-dependent optical response of the HSbP_2O_8 nanosheet/ TiO_2 NP BS showing a) the reflectance intensity changes at 575 nm and b) the derivative of the reflectance intensity changes. Note that the oscillations after analyte exposure are due to oscillations of the vapor dosing setup. Inset: Magnification of the derivative curve of the time-dependent reflectance intensity changes between 580 and 660 s.

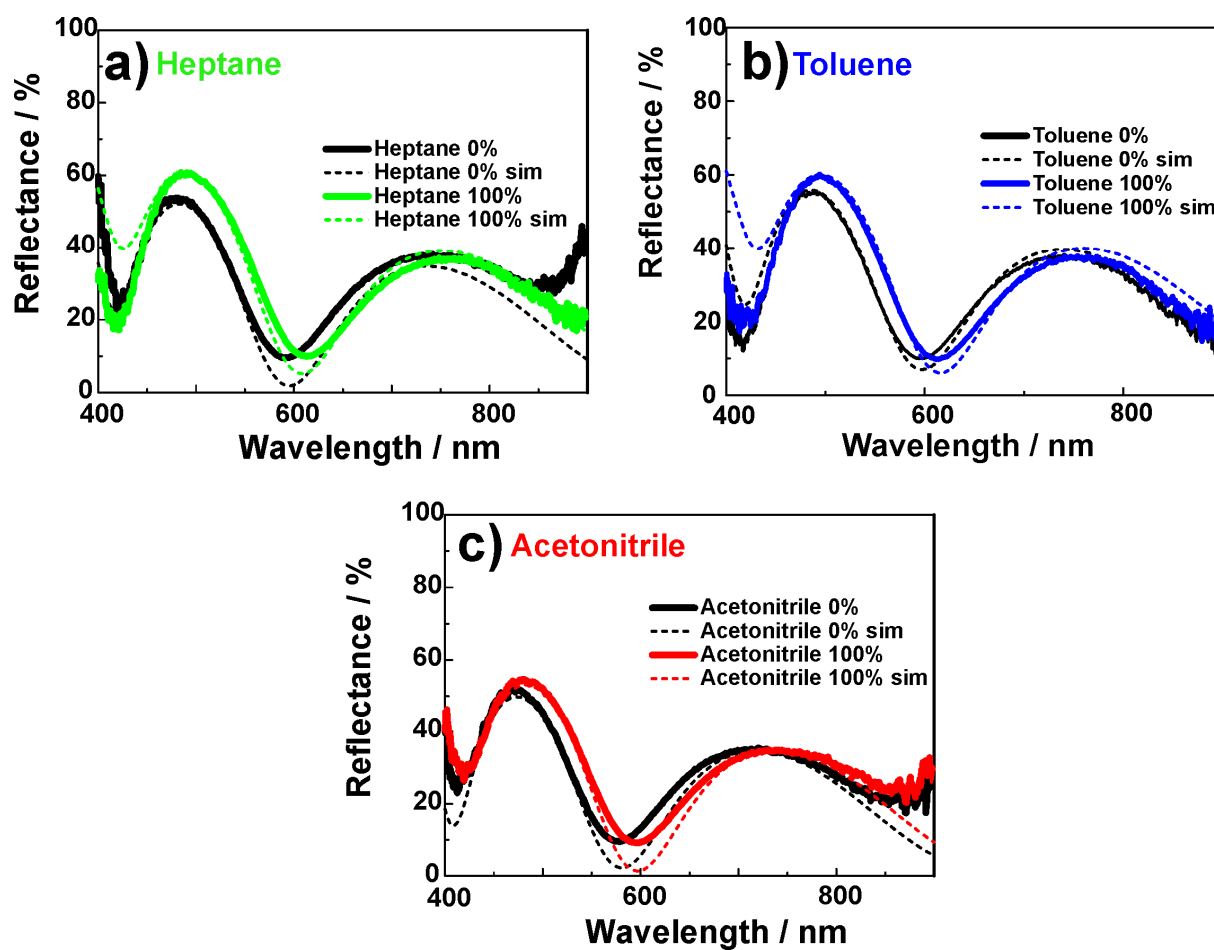


Figure S3.16. Reflectance spectra and simulated spectra (dashed lines) of the HSbP_2O_8 nanosheet/ TiO_2 NP BS containing 7 layers, demonstrating the stop band shifts upon adsorption of the non-polar and polar, non-protic solvent vapors: a) heptane, b) toluene, c) acetonitrile.

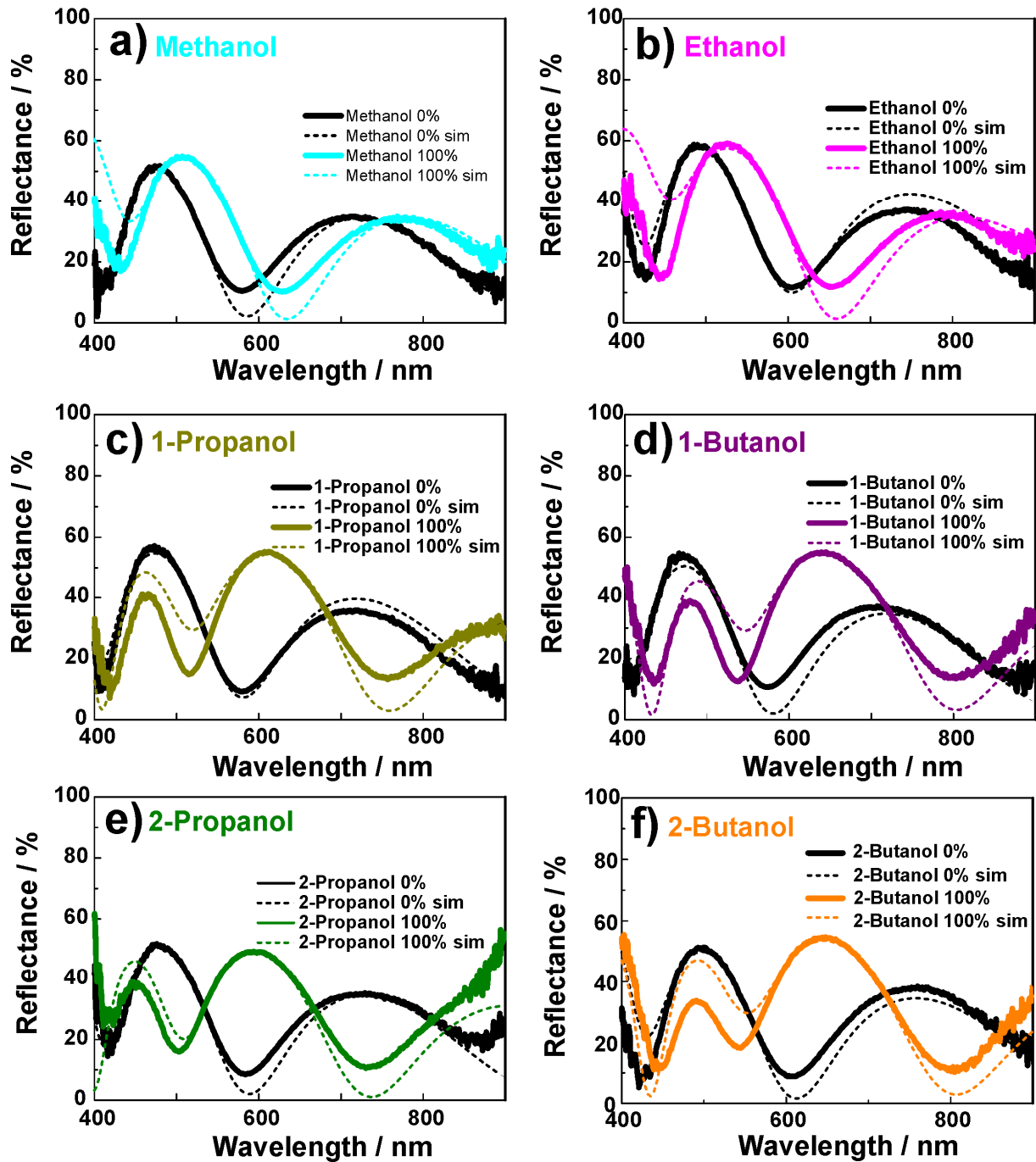


Figure S3.17. Reflectance spectra and simulated spectra (dashed lines) of the HSbP_2O_8 nanosheet/ TiO_2 NP BS containing 7 layers, demonstrating the stop band shifts upon adsorption of the polar solvent vapors: a) methanol, b) ethanol, c) 1-propanol, d) 1-butanol, e) 2-propanol, f) 2-butanol.

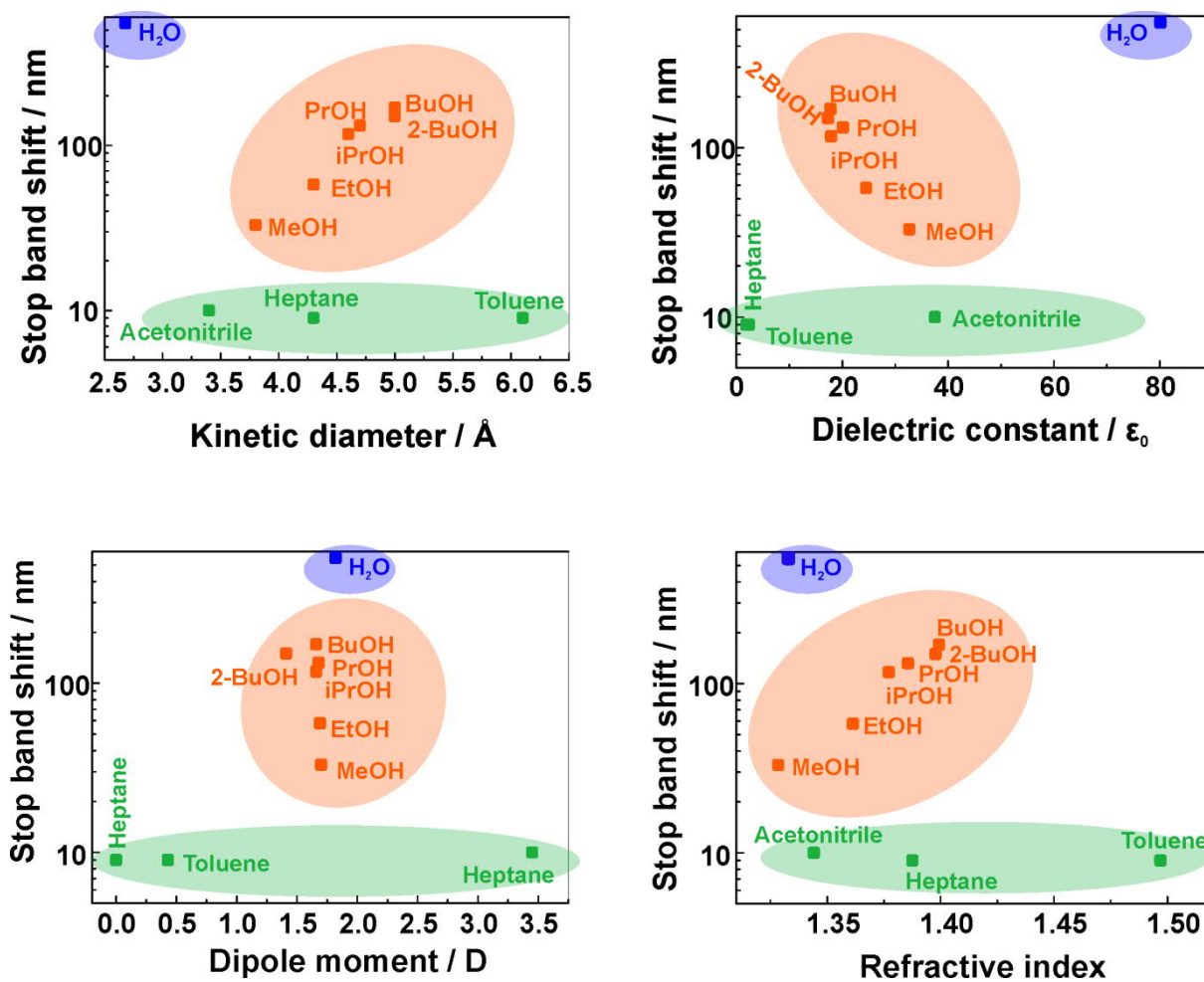


Figure S3.18. Kinetic diameter, dielectric constant, dipole moment and RI of the analyte molecules plotted against the stop band shift.

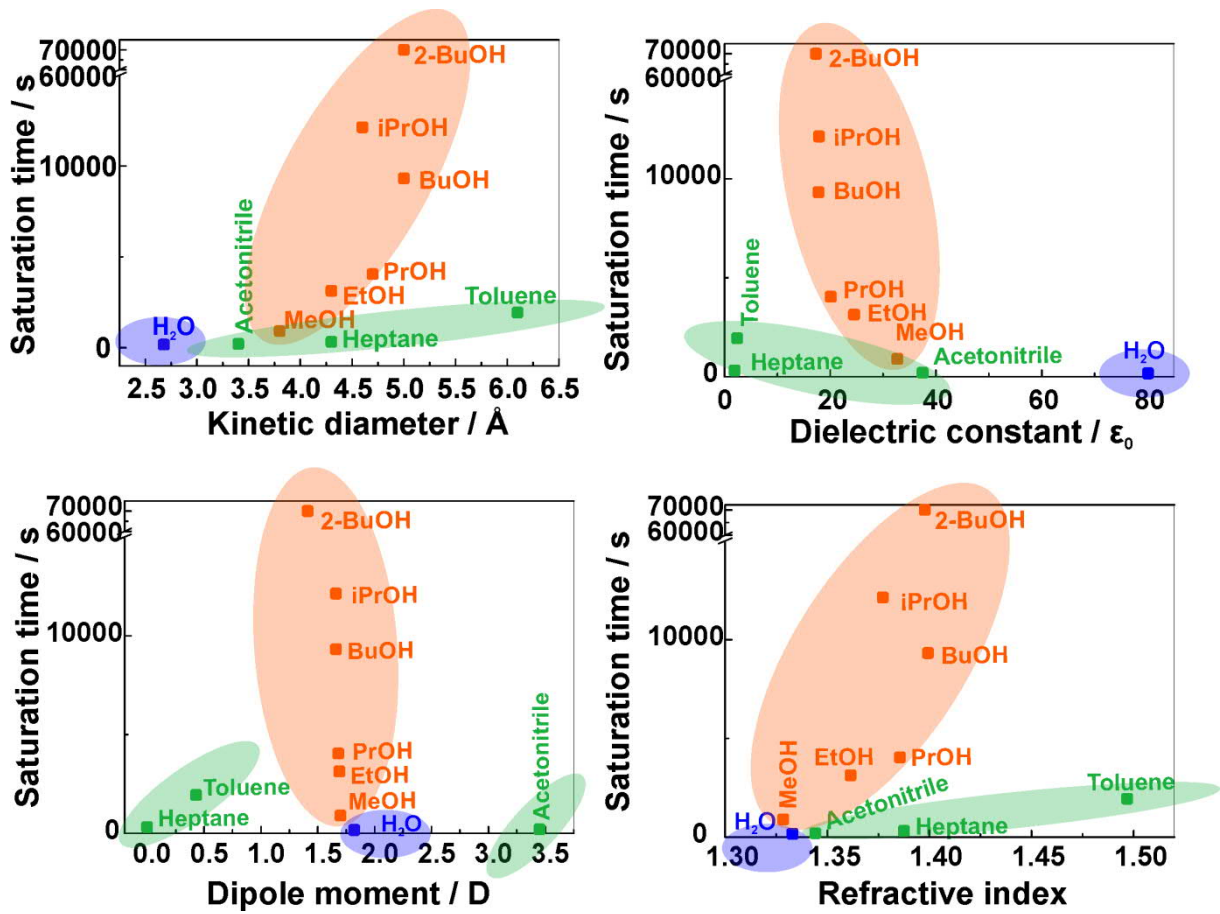


Figure S3.19. Kinetic diameter, dielectric constant, dipole moment and RI of the analyte molecules plotted against the saturation time.

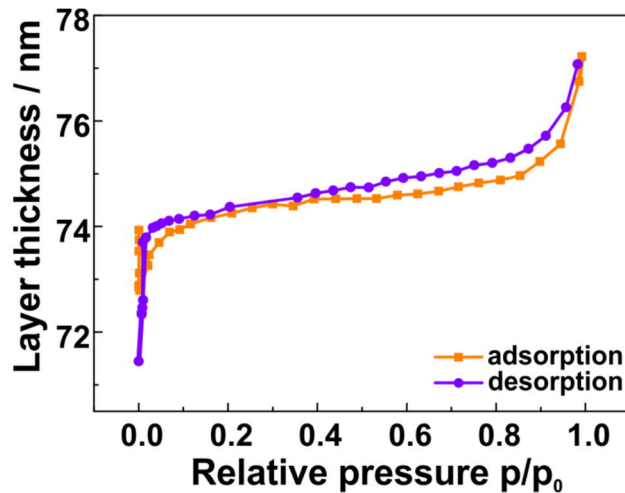


Figure S3.20. Layer thickness change of a HSbP_2O_8 nanosheet thin film measured at different relative pressures of ethanol vapor by ellipsometric porosimetry.

Table S5.5. Stop band shifts and saturation times of the HSbP₂O₈ nanosheet/TiO₂ NP BS to different analytes.^[12-14]

Analyte	Stop band shift (nm)	Saturation time (s)	RI	Dielectric constant (ϵ_0)	Dipole moment (D)	Kinetic diameter (Å)
Water	550	166	1.3330	80.1	1.82	2.68
Acetonitrile	10	201	1.3441	37.5	3.45	3.4
Heptane	9	317	1.3876	1.92	0	4.3
Toluene	9	1937	1.4969	2.38	0.43	6.1
Methanol	33	897	1.3284	32.7	1.7	3.8
Ethanol	58	3130	1.3614	24.5	1.69	4.3
1-Propanol	132	4043	1.3856	20.1	1.68	4.7
2-Propanol	120	12140	1.3772	17.9	1.66	4.6
1-Butanol	170	9320	1.3993	17.8	1.66	5.0
2-Butanol	150	~70000	1.3978	17.3	1.41	5.0

Table S5.6. Refractive indices and monolayer thicknesses for the TiO₂/HSbP₂O₈ BS used for the Matlab simulations for different analytes. The layer thicknesses and refractive indices at 100% analyte relative pressures were fitted to the measured reflectance spectra. Note that for experimental reasons, a different sample was used for the 2-butanol measurements, which is the reason for slightly different TiO₂ NP layer thicknesses.

Analyte	Relative pressure	TiO ₂		HSbP ₂ O ₈	
		Layer thickness	RI	Layer thickness	RI
Acetonitrile	0%	55 nm	1.880	65 nm	1.540
	100%	55 nm	1.980	65 nm	1.540
Heptane	0%	55 nm	1.920	67 nm	1.537
	100%	55 nm	1.990	67 nm	1.537
Toluene	0%	56 nm	1.900	67 nm	1.537
	100%	56 nm	1.990	67 nm	1.537
Methanol	0%	56 nm	1.880	65 nm	1.540
	100%	56 nm	1.980	72 nm	1.530
Ethanol	0%	57 nm	1.880	67 nm	1.540
	100%	57 nm	1.980	78 nm	1.530
1-Propanol	0%	55 nm	1.880	65 nm	1.540
	100%	55 nm	1.980	108 nm	1.530
1-Butanol	0%	55 nm	1.900	64 nm	1.540
	100%	55 nm	1.960	119 nm	1.530
2-Propanol	0%	55 nm	1.900	66 nm	1.540
	100%	55 nm	1.970	104 nm	1.530
2-Butanol	0%	60 nm	1.900	65 nm	1.540
	100%	60 nm	1.960	114 nm	1.530

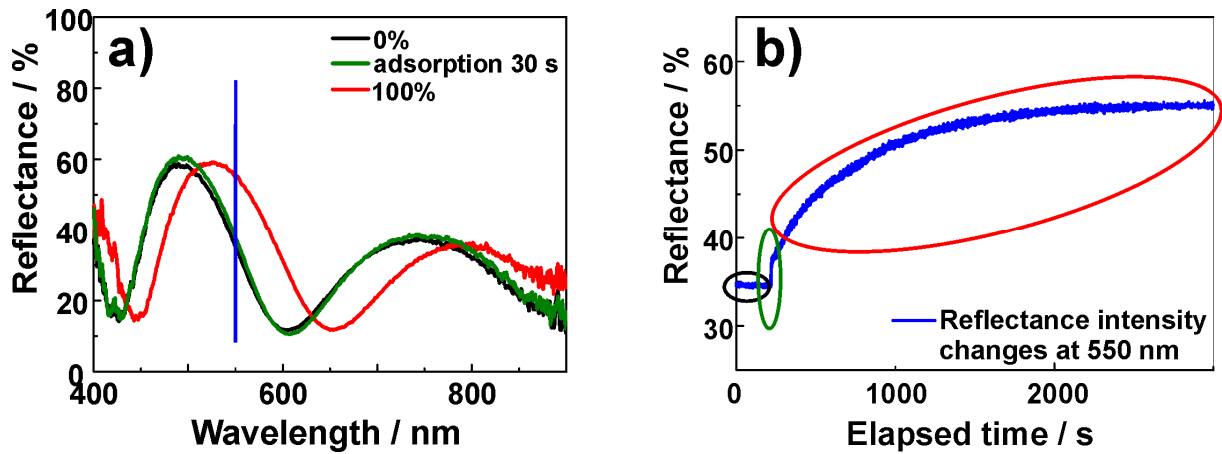


Figure S3.21. Time-dependent changes of the $\text{TiO}_2/\text{HSbP}_2\text{O}_8$ BS upon ethanol adsorption. a) Reflectance spectra at 0% ethanol vapor pressure (black), after 30 s adsorption (green), and at 100% ethanol relative pressure (red), the blue line indicates at which wavelength the intensity changes were reported in b. b) Time dependent reflectance intensity changes of the spectra from a) at 550 nm. Hereby the different ranges are marked with different colors. Black is the intensity at 0% ethanol relative vapor pressure, green is the evolution in the first 6 s of the adsorption. Here, we attribute this initial fast intensity increase to the pore filling of the TiO_2 NP layer. The area marked with red indicates the saturation time of the BS.

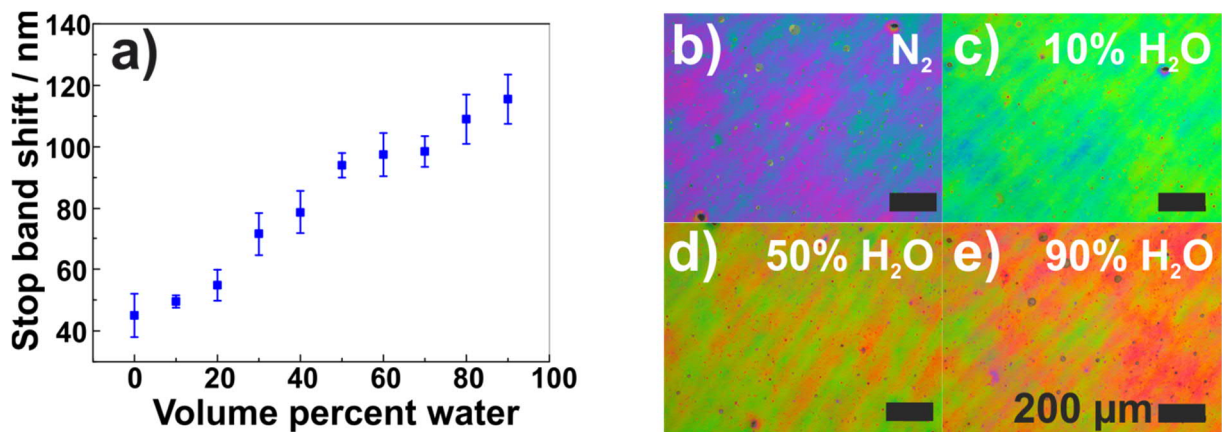


Figure S3.22. Optical response of the HSbP_2O_8 nanosheet / TiO_2 NP-based PC to water-ethanol vapor mixtures. a) The stop band shifts against the water amount in the investigated mixtures and the corresponding microscope images showing the structural color of the BSs in b) dry atmosphere with only N_2 c) at 10:90, d) 50:50 and e) 90:10 water : ethanol mixtures.

3.2.4 Bibliography

- [1] Y. Piffard, S. Oyetola, S. Courant, A. Lachgar, *J. Solid State Chem.* **1985**, *60*, 209-213.
- [2] B. V. Lotsch, F. Scotognella, K. Moeller, T. Bein, G. A. Ozin, 2010, 7713V.
- [3] Z. Hu, C.-a. Tao, F. Wang, X. Zou, J. Wang, *J. Mater. Chem. C* **2015**, *3*, 211-216.
- [4] K. Ufer, G. Roth, R. Kleeberg, H. Stanjek, R. Dohrmann, J. Bergmann, *Z. Kristallogr.* **2004**, *219*, 519-527.
- [5] X. Wang, J. Li, R. D. Hart, A. van Riessen, R. McDonald, *J. Appl. Crystallogr.* **2011**, *44*, 902-910.
- [6] P. W. Winston, D. H. Bates, *Ecology* **1960**, *41*, 232-237.
- [7] L. Greenspan, *J. Res. Nat. Bur. Stand.* **1977**, *81A*, 89-96.
- [8] Bronkhorst-High-Tech, www.fluidat.com, accessed: 08/2015.
- [9] M. C. Fuertes, S. Colodrero, G. Lozano, A. R. González-Elipe, D. Grosso, C. Boissière, C. Sánchez, G. J. d. A. A. Soler-Illia, H. Míguez, *J. Phys. Chem. C* **2008**, *112*, 3157-3163.
- [10] E. Husson, F. Genet, A. Lachgar, Y. Piffard, *J. Solid State Chem.* **1988**, *75*, 305-312.
- [11] E. Husson, M. Durand-Le Floch, C. Doremieux-Morin, S. Deniard, Y. Piffard, *Solid State Ionics* **1989**, *35*, 133-142.
- [12] H. Wu, Q. Gong, D. H. Olson, J. Li, *Chem. Rev.* **2012**, *112*, 836-868.
- [13] T. Borjigin, F. Sun, J. Zhang, K. Cai, H. Ren, G. Zhu, *Chem. Commun.* **2012**, *48*, 7613-7615.
- [14] W. M. Haynes, D. R. Lide, *CRC handbook of chemistry and physics : a ready-reference book of chemical and physical data*, 92 ed., CRC Press, Boca Raton, **2011**.

4 Revealing the influences of the interlayer cation on the sensing characteristics of photonic nanosheet-based sensors

4.1 Toward Tunable Photonic Nanosheet Sensors: Strong Influence of the Interlayer Cation on the Sensing Characteristics

Pirmin Ganter, Leslie M. Schoop and Bettina V. Lotsch

published: *Adv. Mater.* **2017**, 29, 1604884.

DOI: 10.1002/adma.201604884

<http://onlinelibrary.wiley.com/doi/10.1002/adma.201604884/abstract>

Copyright © 2016 WILEY-VCH Verlag GmbH & Co. KGaA, Weinheim. Reproduced with the permission of WILEY-VCH.

Contribution of P.G.: *P.G. carried out all the experiments and wrote the major part of the manuscript. P.G. also prepared all graphical material and performed the literature research.*

Abstract

Tailoring a sensor's sensitivity and capability to differentiate between different types of volatiles is still very challenging. Current approaches mainly rely on the search for new sensing materials or on the covalent modification of existing compounds. In this work, we present an alternative approach based on exploiting non-covalent host-guest interactions through cation exchange in nanosheet-based Fabry-Pérot devices. We find that the sensitivity of photonic thin film sensors toward volatile organic compounds (VOCs) is greatly enhanced if TBA cations are hosted in the interlayer space of phosphate nanosheets, enabling the colorimetric differentiation between polar, moderately polar and non-polar vapors. We find that even very similar vapors such as anisole and toluene can be distinguished by a color change visible with the naked-eye. In addition, we observe a significant decrease in response time, paired with an ultra-large optical shift for alcohols vapors by more than 1400 nm, thus enabling the tracking of subsecond vapors pulses. Our approach therefore enables the scalable design of cheap, yet highly solvent-selective colorimetric sensors without the use of luminescent host-guest systems or complex sensing arrays.



Table of Content: An approach toward intercalant tunable nanosheet-based Fabry-Pérot sensors is presented. The intercalant tetrabutylammonium significantly increases the sensitivity of the photonic nose sensor to volatile organic compounds with increasing polarity, enabling polarity-driven color-coded vapor differentiation. Paired with the improved millisecond response times for polar vapors, vapor imaging with spatio-temporal resolution is within reach.

4.1.1 Introduction

Enhancing certain functions of sensors, such as their sensitivity or capability to differentiate between vapors of various VOCs, is of high interest for numerous applications including medical diagnostics, industrial processing, and environmental monitoring.^[1-5] Current approaches rely mostly on the introduction of new materials or on their covalent modification.^[1-14] Approaches that introduce functionality through intercalants have received far less attention for applications in vapor sensing, despite showing very promising results in other sensing fields.^[15-17] For example, crystalline, layered polydiacetylene obtained from polymerization of 10,12-pentacosadiyonic acid can be cation exchanged, which enhances its performance for temperature sensing.^[17]

2D materials have recently been shown to provide a fruitful foundation as a new class of sensing materials due to their large surface area, small size, and good swelling capability, which are all properties that are inherent to or derived from being 2D.^[3,5,8,10,11,18-24] The diverse library of available 2D nanosheets is steadily growing^[25-30] and in combination with the progress made in processing nanosheets to make thin films, devices based on nanosheets are on the rise.^[5,10,11,21,23,31-34] Several nanosheet-based sensors for detecting and distinguishing vapors have recently been studied, showing very promising results.^[3,5,20,21,35] For example, we showed that by integrating swellable antimony phosphate nanosheets into 1D PCs, stimuli-responsive sensors can be built that are able to distinguish vapors of both chemically similar and dissimilar alcohols, and water and non-polar solvents optically.^[5] Additionally, Jung and co-workers demonstrated vapor differentiation with black phosphorous nanosheet-based chemiresistors.^[21]

Nanosheets can be covalently modified by various organic groups,^[3,36-40] a general concept which has recently been applied in MoS₂ nanosheet-based chemiresistive sensors for tuning their response to VOCs.^[3] Covalent modifications are also employed for other materials, such as silica NPs or etched porous silicon wafers, in order to tune their response to VOCs.^[1,2,41,42] The resulting sensors are

typically used in photonic sensing, a more well-studied field in terms of covalent modifications as compared to chemiresistive sensing.^[6,12,43] However, the impact of these modifications on the sensitivity and therefore, vapor discrimination capability is rather moderate, being intrinsically limited by the change of RI, whereas nanosheet-based photonic sensors which predominantly operate on changes of film thickness can show much larger responses due to nearly unrestricted swelling capability of the 2D materials.^[44-47]

In addition to introducing new materials or covalent modifications, another very interesting way to tune the response of a sensor is by exchanging intercalating species, such as counter ions that intercalate into nanosheet stacks to compensate the layer charge.^[15-17,48] This has been demonstrated for nanocellulose-based sensors to differentiate liquids^[15] and in bulk layered materials, mainly clays, with luminescent intercalants used to detect liquids or vapors.^[48] For developing such tunable optical sensors based on the choice of counter ions, nanosheet-based sensors are ideal candidates, as most nanosheet materials carry a layer charge, which is compensated by exchangeable counter ions. In addition, exfoliation of the layered bulk material is often surfactant assisted,^[25,31,44] resulting in surfactant-modified interlayer spaces upon re-stacking. Like PCs, nanosheet-based Fabry-Pérot devices are label-free sensors that utilize interference effects producing inherent structural color (Figure S4.1, Supporting Information). Hence, the need for specific luminescent guest molecules is eliminated, which significantly enlarges the number of possible intercalants. The first Fabry-Pérot device based on nanosheets was published by Kleinfeld and Ferguson.^[49] In this study, the authors demonstrated the application of Laponite thin films fabricated *via* layer-by-layer assembly as fast humidity sensors. (Laponite is a synthetic smectite clay and a trademark of the company BYK Additives Ltd.) This approach was extended by Lotsch and Ozin to Laponite-based Fabry-Pérot devices obtained by spincoating, which were deployed for sensing alkylammonium surfactants.^[50,51] While taking advantage of the cation exchange properties of clays, none of these studies investigated the role and impact of the interlayer cation on the sensing characteristics of the modified nanosheet thin films to other types of analytes. As new surfactants for exfoliating 2D materials are being explored, the role of the intercalant becomes pivotal in that it adds a new toolbox for tuning the sensor response.^[44,47]

In this work, we present the synthesis and characterization of novel tantalum phosphate nanosheets by exfoliating $\text{HTaP}_2\text{O}_8 \cdot 2\text{H}_2\text{O}$ with TBAOH and TBPOH. The nanosheets are spin-coated to create optically homogenous thin films containing the respective counter ions. The impact of the counter ion for distinguishing VOCs is then evaluated and compared to $\text{H}_3\text{Sb}_3\text{P}_2\text{O}_{14}$ and $\text{TBA}_x\text{H}_{3-x}\text{Sb}_3\text{P}_2\text{O}_{14}$ nanosheet thin film devices. We find a clear improvement on the sensitivity toward several solvent vapors with varying polarity, resulting in a better vapor differentiation capability if organic counter ions are present. Moreover, the presence of the counter ions significantly reduces the response and the recovery time for alcohol vapors.

4.1.2 Results and discussion

Synthesis of $\text{TBA}_x\text{H}_{1-x}\text{TaP}_2\text{O}_8$ and $\text{TBP}_x\text{H}_{1-x}\text{TaP}_2\text{O}_8$ nanosheets was performed in three steps (Figure 4.1a). First, KTaP_2O_8 was synthesized by mixing Ta_2O_5 , KNO_3 , and $\text{NH}_4\text{H}_2\text{PO}_4$ in a stoichiometric ratio and heating it to $850\text{ }^\circ\text{C}$ for 48 h.^[52,53] KTaP_2O_8 crystallizes in the $\text{KFe}(\text{SO}_4)_2$ structure type, which is closely related to that of KSbP_2O_8 . It has the same intralayer connectivity - MO_6 octahedra are corner-linked by PO_4 tetrahedra, with one P-O vertex pointing toward the interlayer space.^[52] KTaP_2O_8 can be proton exchanged with 8 M HNO_3 to yield $\text{HTaP}_2\text{O}_8 \cdot 2\text{H}_2\text{O}$ (Figure S4.2 and Table S4.1).^[53] Exfoliation of $\text{HTaP}_2\text{O}_8 \cdot 2\text{H}_2\text{O}$ was achieved by stirring the powder in an aqueous solution of TBAOH or TBPOH (1:1 molecular ratio) (Figure 4.1a); note that exfoliation of HTaP_2O_8 into nanosheets has not been reported as yet. The single layer height of $\text{TBA}_x\text{H}_{1-x}\text{TaP}_2\text{O}_8$ and $\text{TBP}_x\text{H}_{1-x}\text{TaP}_2\text{O}_8$ nanosheets was measured with AFM and amounts to $1.31 \pm 0.16\text{ nm}$ and $1.61 \pm 0.12\text{ nm}$, respectively (Figure 4.1b and Figure S4.3), and is consistent with the presence of TBA or TBP, which adds to the crystallographic layer thickness of the TaP_2O_8^- layers of 0.8 nm . Since TBP is larger than TBA the increased thickness of the TBP exfoliated nanosheets is not surprising. Exfoliation with TBP results in nanosheets with slightly smaller lateral sizes, as similarly seen before for TBP exfoliated nanosheets of $[\text{Ti}_{1.2}\text{Fe}_{0.8}]\text{O}_4^{0.8-}$.^[47] We also investigated the nanosheets by TEM, and SAED patterns were obtained from overlapping nanosheet regions (Figure 4.1b, Figure S4.3). The d -values for the intralayer (hk) reflections from SAD patterns are in good agreement with the ones from PXRD (Figure 4.1c, Table S4.2). No significant changes for the different cations were observed. In comparison to HSbP_2O_8 nanosheets, a slightly larger lattice parameter is observed for Ta-based compounds, in agreement with the parent bulk compounds.^[5,53,54] The composition of the nanosheet pellet was also verified by EDX spectroscopy (Table S4.3). The $\text{TBA}_x\text{H}_{1-x}\text{TaP}_2\text{O}_8$ and $\text{TBP}_x\text{H}_{1-x}\text{TaP}_2\text{O}_8$ nanosheets, both with $x = 0.6$ (Table S4.4), were spin-coated on silicon substrates to create thin films (Figure 4.1d, Figures S4.4 and S4.5). By altering the spin-coating speed, the film thickness and hence the structural color of the resulting Fabry-Pérot device can be tuned (Figure 4.1d, Figures S4.4 and S4.5) in line with the condition for constructive interference under normal incidence.^[7,41,55]

$$m\lambda = 2n_{eff}l \quad (\text{Equation 4.1})$$

where m is the spectral order (integer value), λ the wavelengths that allow constructive interference, n_{eff} the effective RI and l the layer thickness (Figure S4.1; note that a layer is composed of several unilamellar nanosheets). The product $n_{eff}l$ is also known as the optical thickness. By changing the optical thickness, either through material choice, film porosity or thickness, the condition for constructive interference changes (Equation 4.1), which also changes the displayed color. Besides such static ways to tune the color, the optical thickness can also be influenced dynamically through external stimuli, enabling optical sensing.

To illustrate the large lateral homogeneity of our Fabry-Pérot devices, images of the thin films are displayed in Figure 4.1d. SEM cross-section images (Figure 4.1e) show the uniformity of the thin films on the sub micrometer scale. Out-of-plane XRD patterns (Figure 4.1e) show a stacking distance of 17.98 Å for $\text{TBA}_x\text{H}_{1-x}\text{TaP}_2\text{O}_8$ and 19.25 Å for $\text{TBP}_x\text{H}_{1-x}\text{TaP}_2\text{O}_8$, which is consistent with the crystallographic thickness of 0.8 nm for a TaP_2O_8 layer and the height of ≈ 1 nm for a TBA monolayer^[45] and slightly larger for a TBP monolayer (see also Figure S4.6 for Le Bail fits).

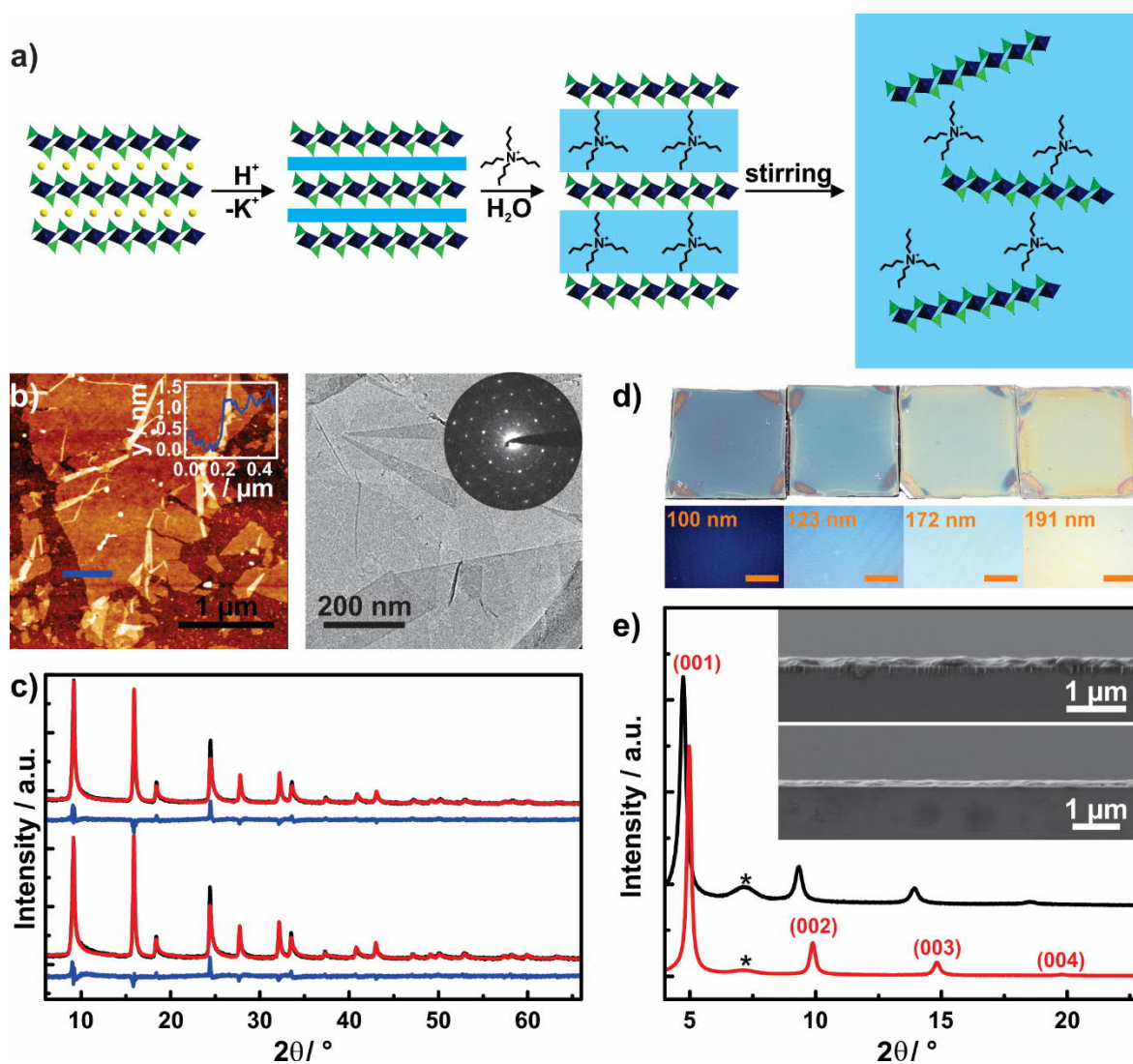


Figure 4.1. Schematic of the exfoliation and the characterization of $TBA_x/TBP_xH_{1-x}TaP_2O_8$ nanosheets and thin films. a) Schematic of the exfoliation starting from $KTaP_2O_8$ (TaO_6 octahedra dark blue, PO_4 tetrahedra green, potassium yellow). First, the material is ion exchanged by repeated treatment with 8 M HNO_3 leading to $HTaP_2O_8 \cdot 2H_2O$. This is followed by treating the protonic phase with either TBA or TBP hydroxide in an aqueous solution, leading to a highly swollen phase. Exfoliation into single layer nanosheets is achieved by applying a weak mechanical force such as stirring. b) AFM image with corresponding height profile (inset) of $TBA_xH_{1-x}TaP_2O_8$ nanosheets (left) and TEM image of $TBA_xH_{1-x}TaP_2O_8$ nanosheets with a representative SAD pattern (right). For AFM and TEM images of $TBP_xH_{1-x}TaP_2O_8$ see the Supporting Information. c) Powder diffraction patterns and Rietveld refinements of $TBA_xH_{1-x}TaP_2O_8$ (bottom) and $TBP_xH_{1-x}TaP_2O_8$ (top) nanosheets. Experimental patterns are shown in black, calculated patterns in red and difference curves in blue. d) Images of $TBA_xH_{1-x}TaP_2O_8$ thin films with different thicknesses that result in different interference colors (scale bar 400 μm ; for UV-Vis spectra see the Supporting Information). e) Out-of-plane XRD patterns of $TBP_xH_{1-x}TaP_2O_8$ (top, black) and $TBA_xH_{1-x}TaP_2O_8$ (bottom, red), and in the inset SEM cross-section images of $TBP_xH_{1-x}TaP_2O_8$ (top) and $TBA_xH_{1-x}TaP_2O_8$ (bottom) thin films. The broad reflection at around 7° marked with an asterisk stems from the sample chamber window material, inherent to the diffractometer.

Next, we investigated the optical response of the thin films toward different solvent vapors. To understand the effect of the intercalant, a protonated control sample without organic surfactant would be desirable. Since protonated tantalum phosphate nanosheets can only be exfoliated by means of ion

exchange with a bulky organic surfactant, $\text{H}_3\text{Sb}_3\text{P}_2\text{O}_{14}$ nanosheets, which can be exfoliated with and without surfactants,^[56,57] were used for this purpose. $\text{H}_3\text{Sb}_3\text{P}_2\text{O}_{14}$ thin films were obtained as described earlier;^[11] to obtain $\text{TBA}_x\text{H}_{3-x}\text{Sb}_3\text{P}_2\text{O}_{14}$ thin films with $x = 1.8$ (Table S4.4), TBA was added to the spin-coating solution (see the Supporting Information). Thin film out-of-plane XRD confirmed the presence of TBA in the interlayer space (Figure S4.7).

All TBA and TBP intercalated tantalum and antimony phosphate samples show an increase in sensitivity toward water vapor in the high humidity regime ($>80\%$ RH) in comparison to the regular $\text{H}_3\text{Sb}_3\text{P}_2\text{O}_{14}$ films (Figure 4.2 and Figure S4.8). As seen in Figure S4.8, upon exposure to moisture the first order Fabry-Pérot fringe shifts out of the visible regime and the second order Fabry-Pérot fringe appears in the region of the visible spectrum. This results in a significant color change for the TBA and TBP modified samples in contrast to the unexchanged $\text{H}_3\text{Sb}_3\text{P}_2\text{O}_{14}$ films, as visible in Figure 4.2. This is remarkable since $\text{H}_3\text{Sb}_3\text{P}_2\text{O}_{14}$ already is highly hydrophilic and ultrasensitive to moisture, which previously had been exploited for realizing TPI driven by the moist atmosphere around a humid pointer.^[11] The interlayer cation thus further enhances the intercalative swelling process, likely due to the pronounced hydration capability of the TBA and TBP cations. Compared to $\text{TBA}_x\text{H}_{1-x}\text{TaP}_2\text{O}_8$, the overall response to humidity is very similar in $\text{TBP}_x\text{H}_{1-x}\text{TaP}_2\text{O}_8$. Only in the very high humidity range the response is slightly weaker for the $\text{TBP}_x\text{H}_{1-x}\text{TaP}_2\text{O}_8$ sample (Figure 4.2), which is likely caused by the smaller polarity of the TBP ion. Optical isotherms for the TBA treated thin films in comparison to $\text{H}_3\text{Sb}_3\text{P}_2\text{O}_{14}$ thin films are shown in Figure S4.9 (data for pristine $\text{H}_3\text{Sb}_3\text{P}_2\text{O}_{14}$ are taken from ref. [11]). Distinct changes in the optical isotherms are visible: First, the effective RI is significantly lowered due to the contribution of TBA ($n_{\text{TBAOH } 40 \text{ wt\% in water}} = 1.405$). Second, no pore filling for the structural pores of $\text{H}_3\text{Sb}_3\text{P}_2\text{O}_{14}$ (Figure S4.10) is observed in the low partial pressure regime in the case of the $\text{TBA}_x\text{H}_{3-x}\text{Sb}_3\text{P}_2\text{O}_{14}$ thin film, as evidenced by the changes in RI. This is most likely caused by TBA occupying or blocking access of water molecules to this position (Figure S4.10). Finally, a higher degree of swelling is observed for both TBA containing samples in the high H_2O partial pressure regime (also visible in the UV-Vis spectra). Both TBA treated samples show very similar optical isotherms; therefore, we conclude that the response to moisture is dominated by the interlayer cation rather than the host material.

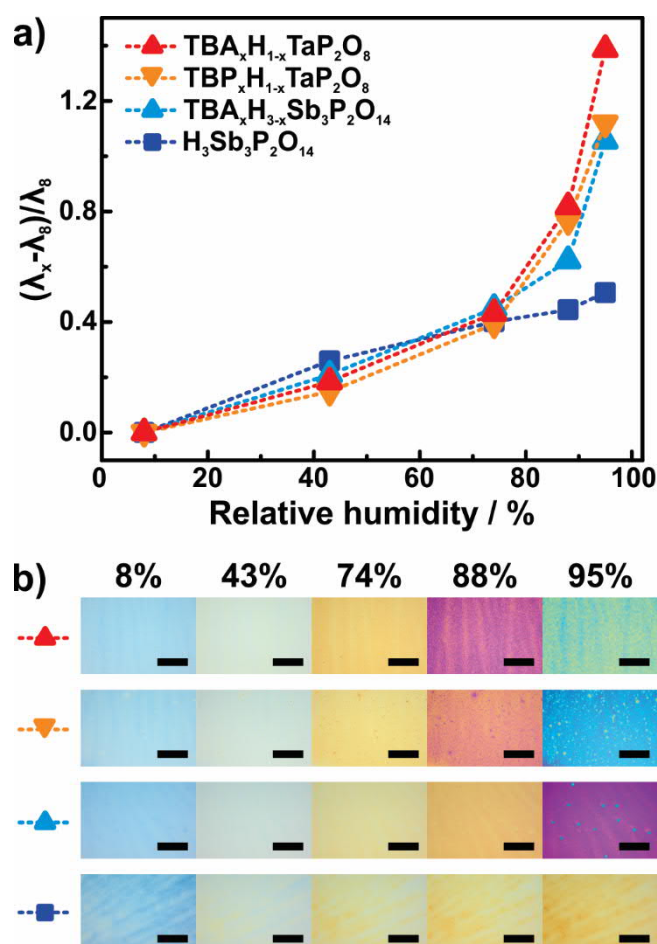


Figure 4.2. Humidity sensing with $\text{H}_3\text{Sb}_3\text{P}_2\text{O}_{14}$, $\text{TBA}_x\text{H}_{3-x}\text{Sb}_3\text{P}_2\text{O}_{14}$, $\text{TBP}_x\text{H}_{1-x}\text{TaP}_2\text{O}_8$, and $\text{TBA}_x\text{H}_{1-x}\text{TaP}_2\text{O}_8$ thin films. a) Normalized spectral response $(\lambda_x - \lambda_8)/\lambda_8$ of the films plotted against different RH values (8, 43, 74, 88 and 95%). For single UV-Vis spectra see Figure S4.8. b) Corresponding optical microscope images for $\text{H}_3\text{Sb}_3\text{P}_2\text{O}_{14}$, $\text{TBA}_x\text{H}_{3-x}\text{Sb}_3\text{P}_2\text{O}_{14}$, $\text{TBP}_x\text{H}_{1-x}\text{TaP}_2\text{O}_8$, and $\text{TBA}_x\text{H}_{1-x}\text{TaP}_2\text{O}_8$ thin films at 8, 43, 74, 88 and 95% RH. The scale bar is 300 μm for all images. Note that for 95% RH the first order Fabry-Pérot fringe shifts into the IR region for $\text{TBA}_x\text{H}_{3-x}\text{Sb}_3\text{P}_2\text{O}_{14}$, $\text{TBP}_x\text{H}_{1-x}\text{TaP}_2\text{O}_8$, and $\text{TBA}_x\text{H}_{1-x}\text{TaP}_2\text{O}_8$, and the second order peak appears in the visible spectral range.

To further investigate the impact of the intercalant on the sensing performance, we studied the response of $\text{TBA}_x\text{H}_{3-x}\text{Sb}_3\text{P}_2\text{O}_{14}$, $\text{TBA}_x\text{H}_{1-x}\text{TaP}_2\text{O}_8$, and $\text{H}_3\text{Sb}_3\text{P}_2\text{O}_{14}$ thin films to vapors with different polarity, in particular non-polar *n*-octane and cyclohexane, moderately polar toluene and anisole, and polar ethanol, and compared it to the response to 95% RH (Figure 4.3a,b and Figures S4.11 and S4.12). We focus on the TBA containing samples in the following. The TBA modified thin films show a significant difference in their optical response toward solvent vapors of varying polarity (Figure S4.12). Even within a group of non-polar or moderately polar solvents, the different solvent vapors are distinguishable with TBA containing sensors. For example, the color difference between films that have been exposed to toluene and anisole is visible with the naked eye (Figure 4.3b). In contrast, in the case of $\text{H}_3\text{Sb}_3\text{P}_2\text{O}_{14}$ thin films, no clear difference can be observed between non-polar and moderately polar vapors, hence solvents within one group of polarity (non-polar or moderately polar) remain indistinguishable (Figure 4.3b and Figure S4.11 for anisole vs toluene). Through the addition of TBA we are now able to distinguish between toluene and cyclohexane or *n*-octane vapors based on their

optical shift, in contrast to previous devices.^[5] In addition, the TBA containing samples show a much higher sensitivity compared to the unmodified system toward moderately polar and polar vapors such as anisole and ethanol, respectively. Compared to the optical shifts reported for RI-based sensing the shifts observed here are much larger for moderately polar and polar vapors as they are dominated by layer thickness changes that significantly outweigh the blueshift due to the decreasing effective RI, resulting in an overall large redshift (Figures S4.9 and S4.13).^[7] Therefore, the addition of TBA results in a better differentiation between several types of vapors across a broad range of polarities; this points to a general concept for the development of photonic nose applications based on intercalant-modified sensors. The observation that quaternary amines increase the affinity toward aromatic molecules and show a better discrimination capability for non-polar solvent vapors, thus resulting in a better overall vapor differentiation, is in line with previous publications.^[58-64] This can be explained by the interplay of different effects caused by TBA: First, the TBA ions widen the interlayer space, which allows larger vapor molecules to diffuse into that space, and secondly, they partially hydrophobize the interlayer environment, rendering the intercalation of less polar molecules more favorable as compared to the non-modified system. At the same time, TBA easily hydrates, thus enhancing the response to humidity as compared to the unmodified nanosheets, see above.

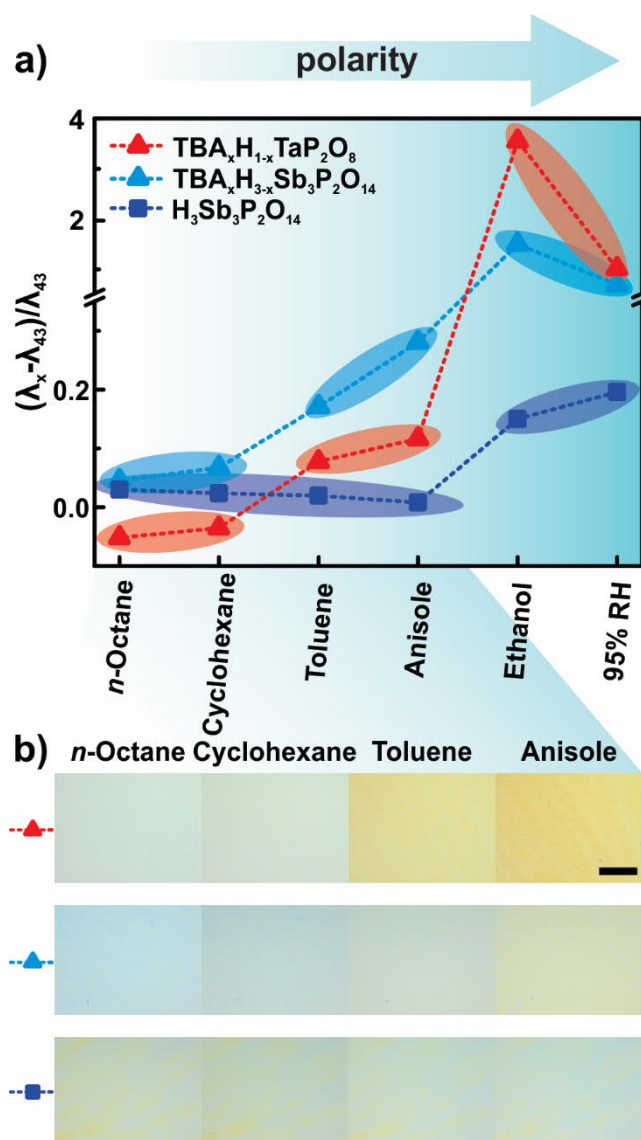


Figure 4.3. Influences of the interlayer cation TBA on the sensitivity. a) Response of TBA_xH_{1-x}TaP₂O₈, TBA_xH_{3-x}Sb₃P₂O₁₄, and H₃Sb₃P₂O₁₄ thin films toward vapors with different polarity given as $(\lambda_x - \lambda_{43})/\lambda_{43}$, where λ_x is the peak position of the first order peak in the UV-Vis reflectance spectra (Figure S11) under the saturated atmosphere of each solvent and λ_{43} is the first order peak at 43% RH. b) Corresponding optical microscope images (scale bar 200 μm) depicting the response of TBA_xH_{1-x}TaP₂O₈, TBA_xH_{3-x}Sb₃P₂O₁₄, and H₃Sb₃P₂O₁₄ nanosheet thin films toward different solvent vapors: *n*-octane, cyclohexane, toluene, anisole. For H₃Sb₃P₂O₁₄ almost no difference is observed, whereas for the samples intercalated with TBA a clear difference is observed between groups of different polarity (e.g., non-polar and moderately polar solvents) as well as within these groups.

To investigate the response time of TBA-based sensors toward different solvent vapors, we recorded time dependent UV-Vis spectra as well as videos showing the sensor's response to a vapor pulse (Figure 4.4, Figures S4.14-18, Videos S4.1-S4.4). For TBA_xH_{1-x}TaP₂O₈ films exposed to a short pulse of ethanol vapor, we observe a large optical shift of 1429 nm within only 322 ms (Figure 4.4a, Figure S4.14). To our knowledge, this is the largest optical shift toward ethanol vapor and among the fastest response and recovery times (276 and 219 ms, respectively, see Figure S4.15a) to ethanol vapor reported to date (for a typical measurement see Video S4.1 and Figure S4.16).^[65-71] We primarily

attribute the fast response time to the large surface area of the unilamellar nanosheets, augmented by their small size, their turbostratic disorder, and the fact that TBA⁺ widens the interlayer space, all of which create a large number of grain boundaries acting as conduits for the diffusion of small molecules. If we take into account that the average time for the human eye to detect a different frame is about 13 ms,^[72] this ultralarge and fast optical shift gains some perspective. In 13 ms our sensor shifts by ≈ 58 nm, which is equivalent to a shift from blue to green or from yellow to red (Calculation S4.1). In terms of film thickness, this means that within 13 ms the sensor increases its thickness by about 15%, assuming an average rate of change and fixed RI of 1.5 (Calculation S4.2). The response of TBA_xH_{3-x}Sb₃P₂O₁₄ and H₃Sb₃P₂O₁₄ thin films toward short ethanol pulses is also shown in Video S4.2 to visualize the stark effect of the TBA intercalant. For TBA_xH_{3-x}Sb₃P₂O₁₄, a distinct response is visible whereas for H₃Sb₃P₂O₁₄ no response is observed, owing to the slow response time of the latter. For both sensors, a few frames from this video are shown in Figure 4.4b; the complete frame series of one ethanol pulse for the TBA_xH_{3-x}Sb₃P₂O₁₄ sensor is shown in Figure S4.17. For ethanol, we also tested the minimum detectable concentration. Both the TBA_xH_{1-x}TaP₂O₈ as well as the TBA_xH_{3-x}Sb₃P₂O₁₄ sensors detect ethanol amounts as low as 200 ppm (Figure S4.19). This is competitive with other state-of-the-art photonic sensors where detection limits in the range of 100-900 ppm were reported.^[2,7,73] Note, however, that the detection limit to low amounts of ethanol is not improved compared to H₃Sb₃P₂O₁₄ without TBA (Figure S4.19c). Besides ethanol, other vapors such as isopropanol can also be tracked with similarly fast response and recovery times (296 and 427 ms, respectively, for isopropanol, see Figure S4.15b, c), and sensitivities (Figure 4.4c, Video S4.3 and Figure S4.18). The same fast response holds for water vapor (Video S4.4) as demonstrated with TBA_xH_{1-x}TaP₂O₈ thin films. The very fast response times bode well for the direct spatio-temporally resolved optical imaging of vapor streams (Videos S4.2-S4.4). Besides demonstrating fast and reversible switching (Videos S4.1-S4.4), we also measured the cycling stability of a TBA_xH_{3-x}Sb₃P₂O₁₄ thin film toward H₂O vapor over five cycles and found no signs of degradation (Figure S4.20).

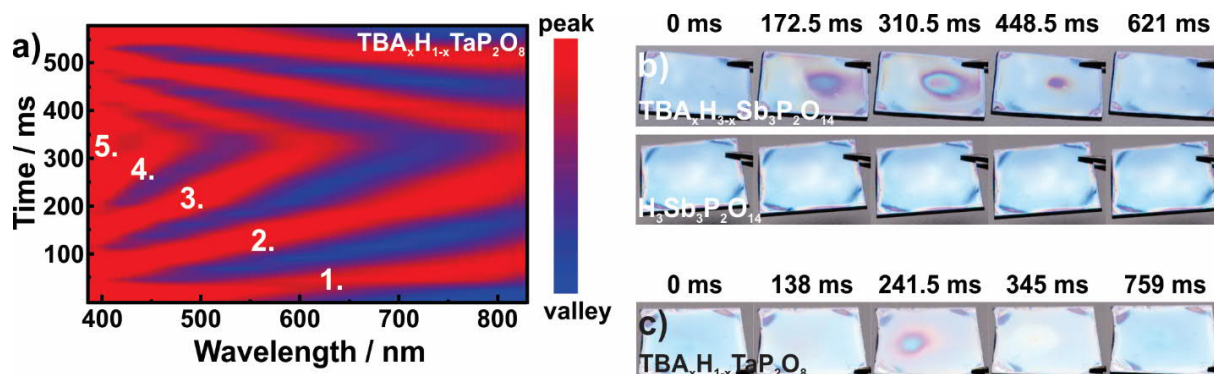


Figure 4.4. Influences of the interlayer cation TBA on the response and recovery time. a) Time resolved UV-Vis spectra monitoring the response and hence, the redshift of a $TBA_xH_{1-x}TaP_2O_8$ thin film toward a short ethanol vapor pulse. The first to fifth order peaks are tracked throughout the visible region. Note that we clearly observe the third and fourth order Fabry-Pérot fringe in the visible region, even parts of the fifth order fringe are visible (see also Figure S4.14). b) Frames from two videos showing the response of $TBA_xH_{3-x}Sb_3P_2O_{14}$ (top) and $H_3Sb_3P_2O_{14}$ (bottom) toward a short ethanol vapor pulse. c) Frames from Video S4.3 showing the response of $TBA_xH_{1-x}TaP_2O_8$ thin film toward a short isopropanol vapor pulse.

4.1.3 Conclusion

In summary, we report the successful exfoliation of $HTaP_2O_8 \cdot 2H_2O$ with TBA and TBP into single layer nanosheets for the first time. The resulting sheets were spin-coated into optically homogeneous thin films to create Fabry-Pérot sensors. By comparing the response of $TBA_xH_{1-x}TaP_2O_8$ with those of $TBA_xH_{3-x}Sb_3P_2O_{14}$ and $H_3Sb_3P_2O_{14}$ toward vapors featuring different polarities, we demonstrate the strong impact of the intercalant on the sensor performance. In particular, we find that the presence of TBA substantially increases the sensitivity toward vapors of all polarities, with the largest effects seen for moderately polar and polar vapors. Therefore, solvent vapors with varying polarity and even solvent vapors with very similar polarities - such as *n*-octane, cyclohexane and toluene - can be distinguished optically with a single thin film device. Furthermore, the widened and chemically modified interlayer space of the nanosheets provides extremely fast response times for polar vapors on the millisecond timescale. Taken together, we present a versatile label-free optical sensing platform which shows potential as an alternative to optical sensors based on luminescent guest species or complex hybrid architectures. In particular, our approach provides a viable route to low-cost sensors, which do not rely on covalent modification of the host species, but can be easily tuned through non-covalent interactions between the host and guest species on the one hand, and between the guest species and the solvent vapor on the other hand. Ultimately, introducing suitably selected interlayer cations into nanosheet sensors may open new avenues to design single component sensors with unique selectivities for organic vapors, thus replacing or improving the currently used and more complex sensor arrays.

4.1.4 Acknowledgement

Financial support was granted by the Max Planck Society, the University of Munich (LMU), the Center for NanoScience (CeNS), and the Deutsche Forschungsgemeinschaft (DFG) through the Cluster of Excellence Nanosystems Initiative Munich (NIM). LMS acknowledges financial support by the Minerva Fast Track Fellowship. The authors thank Viola Duppel for TEM measurements and SEM cross-section images, Frank Adams and Helga Hoier for thin film XRD measurements, and Marie-Luise Schreiber for elemental analysis.

4.1.5 Bibliography

- [1] L. D. Bonifacio, D. P. Puzzo, S. Breslav, B. M. Willey, A. McGeer, G. A. Ozin, *Adv. Mater.* **2010**, *22*, 1351.
- [2] Z. Xie, K. Cao, Y. Zhao, L. Bai, H. Gu, H. Xu, Z.-Z. Gu, *Adv. Mater.* **2014**, *26*, 2413.
- [3] J.-S. Kim, H.-W. Yoo, H. O. Choi, H.-T. Jung, *Nano Lett.* **2014**, *14*, 5941.
- [4] H. Xu, P. Wu, C. Zhu, A. Elbaz, Z. Z. Gu, *J. Mater. Chem. C* **2013**, *1*, 6087.
- [5] P. Ganter, K. Szendrei, B. V. Lotsch, *Adv. Mater.* **2016**, *28*, 7436.
- [6] C. Fenzl, T. Hirsch, O. S. Wolfbeis, *Angew. Chem. Int. Ed.* **2014**, *53*, 3318.
- [7] G. Lu, J. T. Hupp, *J. Am. Chem. Soc.* **2010**, *132*, 7832.
- [8] F. K. Perkins, A. L. Friedman, E. Cobas, P. M. Campbell, G. G. Jernigan, B. T. Jonker, *Nano Lett.* **2013**, *13*, 668.
- [9] M. Tu, S. Wannapaiboon, K. Khaletskaia, R. A. Fischer, *Adv. Funct. Mater.* **2015**, *25*, 4470.
- [10] P. K. Kannan, D. J. Late, H. Morgan, C. S. Rout, *Nanoscale* **2015**, *7*, 13293.
- [11] K. Szendrei, P. Ganter, O. Sánchez-Sobrado, R. Eger, A. Kuhn, B. V. Lotsch, *Adv. Mater.* **2015**, *27*, 6341.
- [12] M. E. Calvo, S. Colodrero, N. Hidalgo, G. Lozano, C. Lopez-Lopez, O. Sanchez-Sobrado, H. Miguez, *Energy Environ. Sci.* **2011**, *4*, 4800.
- [13] J. Kobler, B. V. Lotsch, G. A. Ozin, T. Bein, *ACS Nano* **2009**, *3*, 1669.
- [14] G. Jiang, M. Golezdzinowski, F. J. E. Comeau, H. Zarrin, G. Lui, J. Lenos, A. Veileux, G. Liu, J. Zhang, S. Hemmati, J. Qiao, Z. Chen, *Adv. Funct. Mater.* **2016**, *26*, 1729.
- [15] J. A. Kelly, A. M. Shukaliak, C. C. Y. Cheung, K. E. Shopsowitz, W. Y. Hamad, M. J. MacLachlan, *Angew. Chem. Int. Ed.* **2013**, *52*, 8912.
- [16] M. Okaniwa, Y. Oaki, S. Kaneko, K. Ishida, H. Maki, H. Imai, *Chem. Mater.* **2015**, *27*, 2627.
- [17] M. Okaniwa, Y. Oaki, H. Imai, *Adv. Funct. Mater.* **2016**, *26*, 3463.
- [18] J. T. Robinson, F. K. Perkins, E. S. Snow, Z. Wei, P. E. Sheehan, *Nano Lett.* **2008**, *8*, 3137.
- [19] J. Feng, L. Peng, C. Wu, X. Sun, S. Hu, C. Lin, J. Dai, J. Yang, Y. Xie, *Adv. Mater.* **2012**, *24*, 1969.
- [20] S. Borini, R. White, D. Wei, M. Astley, S. Haque, E. Spigone, N. Harris, J. Kivioja, T. Ryhänen, *ACS Nano* **2013**, *7*, 11166.
- [21] S.-Y. Cho, Y. Lee, H.-J. Koh, H. Jung, J.-S. Kim, H.-W. Yoo, J. Kim, H.-T. Jung, *Adv. Mater.* **2016**, *28*, 7020.
- [22] D. Sarkar, X. Xie, J. Kang, H. Zhang, W. Liu, J. Navarrete, M. Moskovits, K. Banerjee, *Nano Lett.* **2015**, *15*, 2852.
- [23] S.-Y. Cho, S. J. Kim, Y. Lee, J.-S. Kim, W.-B. Jung, H.-W. Yoo, J. Kim, H.-T. Jung, *ACS Nano* **2015**, *9*, 9314.
- [24] Y. S. Kim, M. Liu, Y. Ishida, Y. Ebina, M. Osada, T. Sasaki, T. Hikima, M. Takata, T. Aida, *Nat. Mater.* **2015**, *14*, 1002.
- [25] R. Ma, T. Sasaki, *Adv. Mater.* **2010**, *22*, 5082.
- [26] J. N. Coleman, M. Lotya, A. O'Neill, S. D. Bergin, P. J. King, U. Khan, K. Young, A. Gaucher, S. De, R. J. Smith, I. V. Shvets, S. K. Arora, G. Stanton, H.-Y. Kim, K. Lee, G. T. Kim, G. S. Duesberg, T. Hallam, J. J. Boland, J. J. Wang, J. F. Donegan, J. C. Grunlan, G. Moriarty, A. Shmeliov, R. J. Nicholls, J. M. Perkins, E. M. Grieveson, K. Theuvsen, D. W. McComb, P. D. Nellist, V. Nicolosi, *Science* **2011**, *331*, 568.
- [27] V. Nicolosi, M. Chhowalla, M. G. Kanatzidis, M. S. Strano, J. N. Coleman, *Science* **2013**, *340*, 1226419.

- [28] S. Z. Butler, S. M. Hollen, L. Cao, Y. Cui, J. A. Gupta, H. R. Gutierrez, T. F. Heinz, S. S. Hong, J. Huang, A. F. Ismach, E. Johnston-Halperin, M. Kuno, V. V. Plashnitsa, R. D. Robinson, R. S. Ruoff, S. Salahuddin, J. Shan, L. Shi, M. G. Spencer, M. Terrones, W. Windl, J. E. Goldberger, *ACS Nano* **2013**, *7*, 2898.
- [29] C. N. R. Rao, H. S. S. Ramakrishna Matte, U. Maitra, *Angew. Chem. Int. Ed.* **2013**, *52*, 13162.
- [30] M. Xu, T. Liang, M. Shi, H. Chen, *Chem. Rev.* **2013**, *113*, 3766.
- [31] F. Bonaccorso, A. Bartolotta, J. N. Coleman, C. Backes, *Adv. Mater.* **2016**, *28*, 6136.
- [32] A. D. Dillon, M. J. Ghidui, A. L. Krick, J. Griggs, S. J. May, Y. Gogotsi, M. W. Barsoum, A. T. Fafarman, *Adv. Funct. Mater.* **2016**, *26*, 4162.
- [33] Z. S. Wu, K. Parvez, X. Feng, K. Müllen, *Nat. Commun.* **2013**, *4*, 2487.
- [34] F. Bonaccorso, A. Lombardo, T. Hasan, Z. Sun, L. Colombo, A. C. Ferrari, *Mater. Today* **2012**, *15*, 564.
- [35] X. Wang, Z. Xiong, Z. Liu, T. Zhang, *Adv. Mater.* **2015**, *27*, 1370.
- [36] D. Voiry, A. Goswami, R. Kappera, C. de Carvalho Castro e Silva, D. Kaplan, T. Fujita, M. Chen, T. Asefa, M. Chhowalla, *Nat. Chem.* **2015**, *7*, 45.
- [37] S. S. Chou, M. De, J. Kim, S. Byun, C. Dykstra, J. Yu, J. Huang, V. P. Dravid, *J. Am. Chem. Soc.* **2013**, *135*, 4584.
- [38] V. Georgakilas, M. Otyepka, A. B. Bourlinos, V. Chandra, N. Kim, K. C. Kemp, P. Hobza, R. Zboril, K. S. Kim, *Chem. Rev.* **2012**, *112*, 6156.
- [39] X. Chen, A. R. McDonald, *Adv. Mater.* **2016**, *28*, 5738.
- [40] H. Matsui, Y. Oaki, H. Imai, *Chem. Commun.* **2016**, *52*, 9466.
- [41] T. Gao, J. Gao, M. J. Sailor, *Langmuir* **2002**, *18*, 9953.
- [42] S. E. Létant, M. J. Sailor, *Adv. Mater.* **2001**, *13*, 335.
- [43] L. D. Bonifacio, B. V. Lotsch, D. P. Puzzo, F. Scotognella, G. A. Ozin, *Adv. Mater.* **2009**, *21*, 1641.
- [44] F. Geng, R. Ma, Y. Ebina, Y. Yamauchi, N. Miyamoto, T. Sasaki, *J. Am. Chem. Soc.* **2014**, *136*, 5491.
- [45] Y. Song, N. Iyi, T. Hoshida, T. C. Ozawa, Y. Ebina, R. Ma, N. Miyamoto, T. Sasaki, *Chem. Commun.* **2015**, *51*, 17068.
- [46] F. Geng, R. Ma, A. Nakamura, K. Akatsuka, Y. Ebina, Y. Yamauchi, N. Miyamoto, Y. Tateyama, T. Sasaki, *Nat. Commun.* **2013**, *4*, 1632.
- [47] F. Geng, R. Ma, Y. Yamauchi, T. Sasaki, *Chem. Commun.* **2014**, *50*, 9977.
- [48] M. Ogawa, K. Saito, M. Sohmiya, *Dalton Trans.* **2014**, *43*, 10340.
- [49] E. R. Kleinfeld, G. S. Ferguson, *Chem. Mater.* **1995**, *7*, 2327.
- [50] B. V. Lotsch, G. A. Ozin, *ACS Nano* **2008**, *2*, 2065.
- [51] B. V. Lotsch, G. A. Ozin, *Adv. Mater.* **2008**, *20*, 4079.
- [52] S. Oyetola, A. Verbaere, Y. Piffard, M. Tournoux, *Eur. J. Solid State Inorg. Chem.* **1988**, *25*, 259.
- [53] S. Oyetola, A. Verbaere, D. Guyomard, Y. Piffard, M. Tournoux, *Eur. J. Solid State Inorg. Chem.* **1989**, *26*, 175.
- [54] Y. Piffard, A. Verbaere, S. Oyetola, S. Deniard-Courant, M. Tournoux, *Eur. J. Solid State Inorg. Chem.* **1989**, *26*, 113.
- [55] J. Gao, T. Gao, Y. Y. Li, M. J. Sailor, *Langmuir* **2002**, *18*, 2229.
- [56] J.-C. P. Gabriel, F. Camerel, B. J. Lemalre, H. Desvaux, P. Davidson, P. Batail, *Nature* **2001**, *413*, 504.
- [57] F. Camerel, J. C. P. Gabriel, P. Batail, P. Panine, P. Davidson, *Langmuir* **2003**, *19*, 10028.
- [58] M. M. Mortland, S. Shaobai, S. A. Boyd, *Clays Clay Miner.* **1986**, *34*, 581.
- [59] R. K. Kukkadapu, S. A. Boyd, *Clays Clay Miner.* **1995**, *43*, 318.
- [60] R. M. Barrer, G. S. Perry, *J. Chem. Soc.* **1961**, 850.
- [61] R. M. Barrer, D. M. MacLeod, *Trans. Faraday Soc.* **1955**, *51*, 1290.
- [62] R. M. Barrer, J. S. S. Reay, *Trans. Faraday Soc.* **1957**, *53*, 1253.
- [63] R. M. Barrer, K. Brummer, *Trans. Faraday Soc.* **1963**, *59*, 959.
- [64] A. Weiss, *Angew. Chem.* **1963**, *75*, 113.
- [65] H.-R. Kim, K.-I. Choi, J.-H. Lee, S. A. Akbar, *Sens. Actuators, B* **2009**, *136*, 138.

- [66] Y. He, P. Tang, J. Li, J. Zhang, F. Fan, D. Li, *Mater. Lett.* **2016**, *165*, 50.
- [67] M. Cao, Y. Wang, T. Chen, M. Antonietti, M. Niederberger, *Chem. Mater.* **2008**, *20*, 5781.
- [68] J. Tan, X. Huang, *Sens. Actuators, B* **2016**, *237*, 159.
- [69] H.-R. Kim, K.-I. Choi, K.-M. Kim, I.-D. Kim, G. Cao, J.-H. Lee, *Chem. Commun.* **2010**, *46*, 5061.
- [70] V. Postica, I. Hölken, V. Schneider, V. Kaidas, O. Polonskyi, V. Cretu, I. Tiginyanu, F. Faupel, R. Adelung, O. Lupan, *Mater. Sci. Semicond. Process.* **2016**, *49*, 20.
- [71] Y. Sun, S. I. Shopova, G. Frye-Mason, X. Fan, *Opt. Lett.* **2008**, *33*, 788.
- [72] L. E. Humes, T. A. Busey, J. C. Craig, D. Kewley-Port, *Atten. Percept. Psychophys.* **2009**, *71*, 860.
- [73] T. L. Kelly, A. Garcia Segal, M. J. Sailor, *Nano Lett.* **2011**, *11*, 3169.

4.2 Supporting Information: Toward Tunable Photonic Nanosheet Sensors: Strong Influence of the Interlayer Cation on the Sensing Characteristics

4.2.1 Methods

Nanosheet synthesis

Nanosheets were synthesized in three steps: First, to obtain KTaP_2O_8 , Ta_2O_5 (99.85% Alfa Aesar), KNO_3 (99%, Merck), $\text{NH}_4\text{H}_2\text{PO}_4$ (98%+, Acros Organics) were ground in a stoichiometric ratio and heated up in a first step overnight at 250 °C and subsequently at 850 °C for two days with an intermediate grinding step after the first 24 h.^[1,2] For protonation 2 g of KTaP_2O_8 were treated with 250 mL 8 M HNO_3 (diluted 65 wt%, Merck), filtrated, washed with ethanol and dried at room temperature. To complete protonation, this step was repeated at least once to yield $\text{HTaP}_2\text{O}_8 \cdot 2 \text{H}_2\text{O}$.^[2] For exfoliation, 1.02 mmol $\text{HTaP}_2\text{O}_8 \cdot 2 \text{H}_2\text{O}$ were stirred either with TBAOH (tetrabutylammonium hydroxide 30-hydrate 98% , Sigma-Aldrich) or with TBPOH (tetrabutylphosphonium hydroxide, 40%wt, Sigma-Aldrich) (molar ratio 1:1) in an aqueous solution (concentration of 7.3 mmol L⁻¹). The resulting suspension was centrifuged at 3000 rpm to separate larger unexfoliated particles including the minor impurity phase, and later the nanosheet pellet was obtained by centrifugation at 24000 rpm for 25 min and subsequently dried at room temperature.

$\text{H}_3\text{Sb}_3\text{P}_2\text{O}_{14}$ nanosheets were obtained as described previously.^[3]

Colloidal suspensions preparation

Colloidal suspensions of $\text{H}_3\text{Sb}_3\text{P}_2\text{O}_{14}$ were obtained in a way similar to that described previously.^[3] $\text{H}_3\text{Sb}_3\text{P}_2\text{O}_{14}$ nanosheets were added to a mixture of water and ethanol (ratio 2:3, 40 mmol L⁻¹) and sonicated for 3.5 h.

Colloidal suspensions of $\text{TBA}_x\text{H}_{3-x}\text{Sb}_3\text{P}_2\text{O}_{14}$ were obtained by suspending $\text{H}_3\text{Sb}_3\text{P}_2\text{O}_{14}$ in aqueous ethanol (28.8 mmol L⁻¹). After sonicating for 2 h, 0.16 mmol TBAOH was added (ratio $\text{H}^+ : \text{TBA}$ 4:3). This mixture was then stirred for 1 h and sonicated for 2 h.

Colloidal suspensions of $\text{TBA}_x\text{H}_{1-x}\text{TaP}_2\text{O}_8$ and $\text{TBP}_x\text{H}_{1-x}\text{TaP}_2\text{O}_8$ were prepared by suspending $\text{TBA}_x\text{H}_{1-x}\text{TaP}_2\text{O}_8$ and $\text{TBP}_x\text{H}_{1-x}\text{TaP}_2\text{O}_8$ in aqueous ethanol. 39.5 mg of $\text{TBA}_x\text{H}_{1-x}\text{TaP}_2\text{O}_8$ or $\text{TBP}_x\text{H}_{1-x}\text{TaP}_2\text{O}_8$ were added to 2.6 mL of a water ethanol mixture (ratio 35:65), and subsequently either TBAOH (77.5 mg) or TBPOH (67.6 μL , 40%wt solution) were added. The suspension was then stirred for 1 h and sonicated for 2 h.

Thin film fabrication

All thin films were fabricated from the colloidal suspensions on silicon wafers (1.5 cm x 1.5 cm, 100 orientation) by spin-coating (WS-650S-NPP-Lite, Laurell Technologies Corporation). For all thin films an acceleration ramp of 10000 rpm s⁻¹, a spinning duration of 1 min, and 200 μL of the respective suspension was used. Thin films of $\text{H}_3\text{Sb}_3\text{P}_2\text{O}_{14}$ were spin-coated twice at 3500 rpm. Thin

films of $TBA_xH_{3-x}Sb_3P_2O_{14}$ were spin-coated at 1500-2000 rpm, $TBA_xH_{1-x}TaP_2O_8$ and $TBP_xH_{1-x}TaP_2O_8$ were spin coated between 1500-4000 rpm and 1500-3000 rpm, respectively.

4.2.2 Characterization

Morphology and structural characterization

PXRD patterns were collected in transmission geometry on a Stadi P diffractometer (STOE) working with Ge(111) monochromated $Mo-K_{\alpha 1}$ radiation ($\lambda = 70.926$ pm) or $Cu-K_{\alpha 1}$ radiation ($\lambda = 154.059$ pm).

Rietveld refinements of the nanosheet pellets were performed with the DiffracPlus TOPAS v4.2 software (Bruker AXS). A quasi single layer approach, similar as described in the literature, was used to approximate the turbostratic disorder. Due to preferred orientation, only $hk0$ reflections were observed, which allows for using a simplified model compared to the models described in the literature that also include modeling of the $00l$ reflections.^[4,5]

Thin film XRD patterns were recorded on a D8-Advance (Bruker) working with Ge(111) monochromated $Cu-K_{\alpha 1}$ radiation ($\lambda = 154.059$ pm) radiation or on a Empyrean (PANalytical) working with $Cu-K_{\alpha 1,2}$ radiation ($\lambda = 154.059$ pm, $\lambda = 154.442$ pm). Le Bail fits were performed with the DiffracPlus TOPAS v4.2 software (Bruker AXS).

EDX analysis of the bulk materials and nanosheet pellets were obtained with a Vega TS 5130 MM (Tescan) equipped with Si/Li detector (Oxford). TEM images and SAD patterns were acquired with a Phillips CM30 ST TEM (300 kV, LaB_6 cathode) equipped with a Gatan CCD camera.

AFM images were recorded with a MFP-3D (Oxford Instruments) working in non-contact mode under ambient conditions.

Cross-section images of the thin films were acquired with a Zeiss Merlin FE-SEM.

Optical characterization

Images of the thin film surface were acquired with an optical microscope (Olympus BX51), operating in reflection mode. Videos were recorded with a conventional smartphone camera.

Ellipsometric porosimetry measurements were carried out on a Sopra PS-1000 SAM (Semilab). The samples were equilibrated 15 minutes prior to measurements at all relative water vapor pressures. To obtain the RI and the layer thickness the obtained data were fitted with the software Sopra SEA (V. 1.4.12) using the model combination Cauchy and Lorentz.

For recording optical changes of the thin films toward humidity or organic vapors, the thin films were placed in a stainless steel chamber (ca. 6 mL residual volume) that has two basins with a volume of approximately 0.3 mL each, equipped with a transparent glass window. The basins were filled with saturated salt solutions (NaOH 8%, 43% K₂CO₃, 74% NaCl, 88% Sr(NO₃)₂, 95% KNO₃)^[6,7] or organic solvents at 20 °C. After a minimum equilibration time of 30 mins, UV-Vis spectra were recorded in the closed chamber. All UV-Vis spectra were acquired with a fiber optic spectrometer (USB4000-XR1-ES, Ocean Optics) attached to a microscope (BX51, Olympus) with normal incidence. The optical spectra were taken at the same spot for all thin films (1×1 mm² in area).

Short vapor pulses for dynamic measurements were created with a wash bottle (500 mL), which was filled with 15 mL of the respective solvent.

For cycling measurements a homebuilt setup was used, as described in ref [3] equipped with a Sensirion SHT 31 sensor for determination of the RH inside the chamber.

4.2.3 Additional data

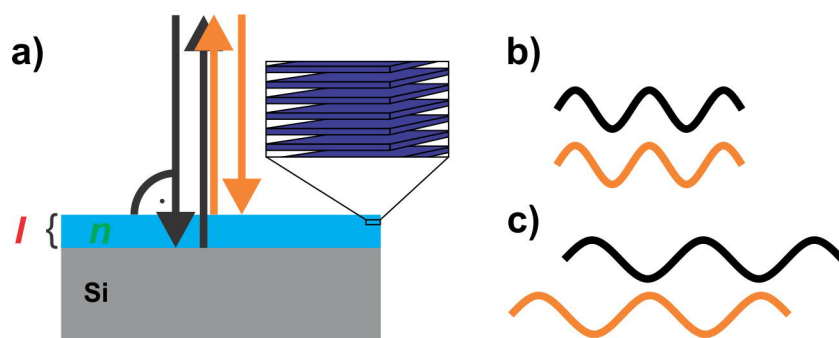


Figure S4.1. a) Schematic illustration of a Fabry-Pérot device based on nanosheets. l is the layer thickness, which consists of several nanosheets in our case, and n is the effective RI. b) Schematic illustration depicting constructive interference for the two outgoing beams for a wavelength λ_1 and c) destructive interference for a different wavelength λ_2 . The color of the Fabry-Pérot thin film device will depend on the wavelengths for which constructive interference are observed (see Equation 4.1 for more details).

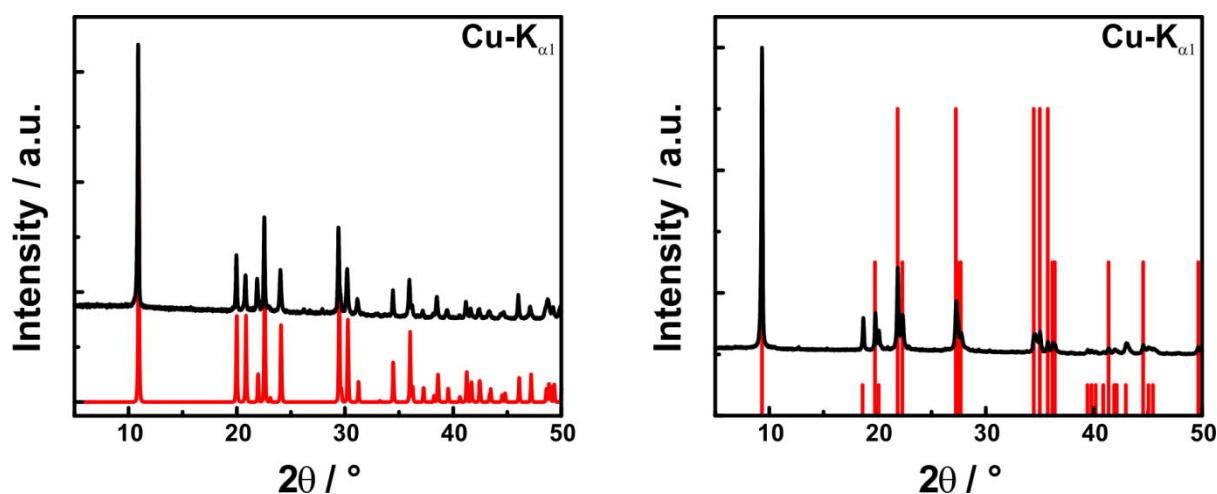


Figure S4.2. Experimental XRD patterns (in black) of KTaP_2O_8 (left) and $\text{HTaP}_2\text{O}_8 \cdot 2 \text{H}_2\text{O}$ (right) and reference XRD patterns from the literature (in red). Both compounds contain a minor impurity phase. The minor impurity phase is separated during the exfoliation step.

Table S4.1. EDX analysis of bulk compounds KTaP_2O_8 and $\text{HTaP}_2\text{O}_8 \cdot 2 \text{H}_2\text{O}$. For both compounds the theoretical values lie within the standard deviations of the experimental measurements.

	K Atom%	Ta Atom%	P Atom%	O Atom%	Calc. Formula
Theo. values	8.3	8.3	16.6	66.6	KTaP_2O_8
Exp. values	8.0 (4)	8.0 (6)	17.2 (9)	67 (2)	$\text{KTaP}_{2.16}\text{O}_{8.37}$
Theo. values		7.7	15.4	76.9	$\text{HTaP}_2\text{O}_8 \cdot 2 \text{H}_2\text{O}$
Exp. values		7.6(9)	16.2 (1.4)	76 (2)	$\text{HTaP}_{2.12}\text{O}_{9.97}$

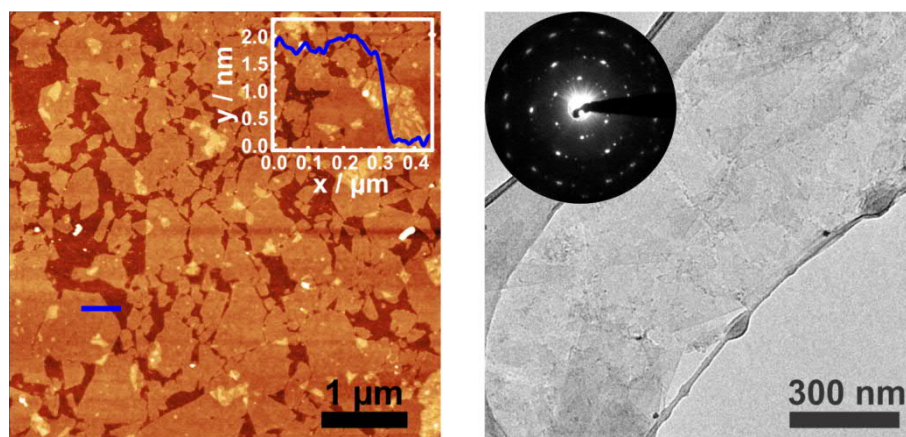


Figure S4.3. AFM image of $\text{TBP}_x\text{H}_{1-x}\text{TaP}_2\text{O}_8$ nanosheets with a corresponding height profile (left), and TEM image of $\text{TBP}_x\text{H}_{1-x}\text{TaP}_2\text{O}_8$ nanosheets with a representative SAD pattern (inset, right).

Table S4.2. Comparison of d -values obtained from XRD and SAD patterns for TBA and TBP exfoliated TaP_2O_8 nanosheets. Reflections marked with an asterisk are only weakly visible.

TaP_2O_8 nanosheets				
Miller indices	d value TBA SAD [\AA] (Figure 4.1)	d value TBA XRD [\AA] (Figure 4.1)	d value TBP SAD [\AA] (Figure S4.3)	d value TBP XRD [\AA] (Figure 4.1)
(10)	4.45	4.45	4.35	4.43
(11)	2.58	2.57	2.50	2.56
(20)	2.21*	2.22	2.16*	2.21
(21)	1.68	1.68	1.64	1.67
(30)	1.48	1.48	1.46	1.48
(22)	1.28	1.28	1.25	1.28
(31)		1.23		1.23

Table S4.3. EDX analysis of exfoliated $\text{TBA}_x\text{H}_{1-x}\text{TaP}_2\text{O}_8$ and $\text{TBP}_x\text{H}_{1-x}\text{TaP}_2\text{O}_8$ nanosheet pellets.

	Ta Atom%	P Atom%	O Atom%	Calc. Formula
Theo. values	9.1	18.2	72.7	$\text{TBA}_x\text{H}_{1-x}\text{TaP}_2\text{O}_8$
Exp. values	9.0 (1)	19.4 (5)	71.6 (5)	$\text{HTaP}_{2.15}\text{O}_{7.97}$
Theo. values	8.6	22.4	69.0	$\text{H}_{0.4}\text{TBP}_{0.6}\text{TaP}_2\text{O}_8$
Exp. values	8.4(5)	21.9(1.2)	69(2)	
Theo. values	8.8	21.0	70.2	$\text{H}_{0.6}\text{TBP}_{0.4}\text{TaP}_2\text{O}_8$

Table S4.4. Combustion and ICP analysis of $\text{TBA}_x\text{H}_{3-x}\text{Sb}_3\text{P}_2\text{O}_{14}$, $\text{TBA}_x\text{H}_{1-x}\text{TaP}_2\text{O}_8$ and $\text{TBP}_x\text{H}_{1-x}\text{TaP}_2\text{O}_8$. For the determination of x the relative ratio of every element in TBA ($\text{C}_{16}\text{H}_{36}\text{N}$) or TBP ($\text{C}_{16}\text{H}_{36}\text{P}$, except P) to Ta or Sb_3 was calculated. The slightly higher ratio of nitrogen compared to carbon through all the samples might be attributed to residual HNO_3 from the proton exchange step prior to exfoliation.

	C	N	H	Sb/Ta
wt% $\text{TBA}_x\text{H}_{3-x}\text{Sb}_3\text{P}_2\text{O}_{14}$	26.42	1.98	5.90	28.11
Determination of x for the different elements ($\text{C}_{16}\text{H}_{36}\text{N}$)	1.79	1.84	2.06	3
wt% $\text{TBA}_x\text{H}_{1-x}\text{TaP}_2\text{O}_8$	22.26	1.94	4.94	34.37
Determination of x for the different elements ($\text{C}_{16}\text{H}_{36}\text{N}$)	0.61	0.73	0.70	1
wt% $\text{TBP}_x\text{H}_{1-x}\text{TaP}_2\text{O}_8$	21.48	0.54	4.77	34.33
Determination of x for the different elements ($\text{C}_{16}\text{H}_{36}\text{P}$)	0.59	-	0.67	1

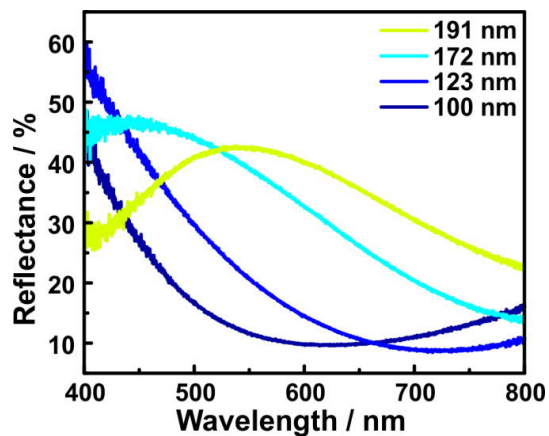


Figure S4.4. Corresponding UV-Vis spectra for the TBA_xH_{1-x}TaP₂O₈ thin film displayed in Figure 4.1. The film thicknesses given in the legend are related to film thicknesses determined by ellipsometry.

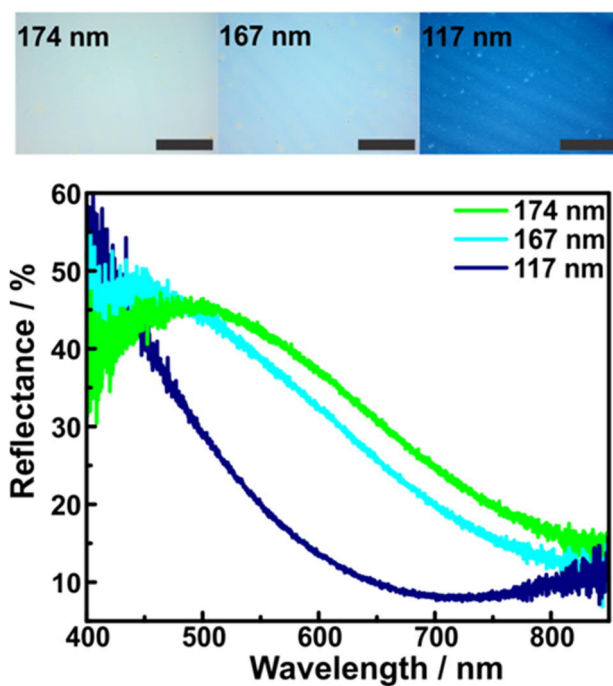


Figure S4.5. Tuning of TBP_xH_{1-x}TaP₂O₈ film thickness and thus the displayed color by varying the spin-coating speed. The legend displays the thicknesses obtained by ellipsometry.

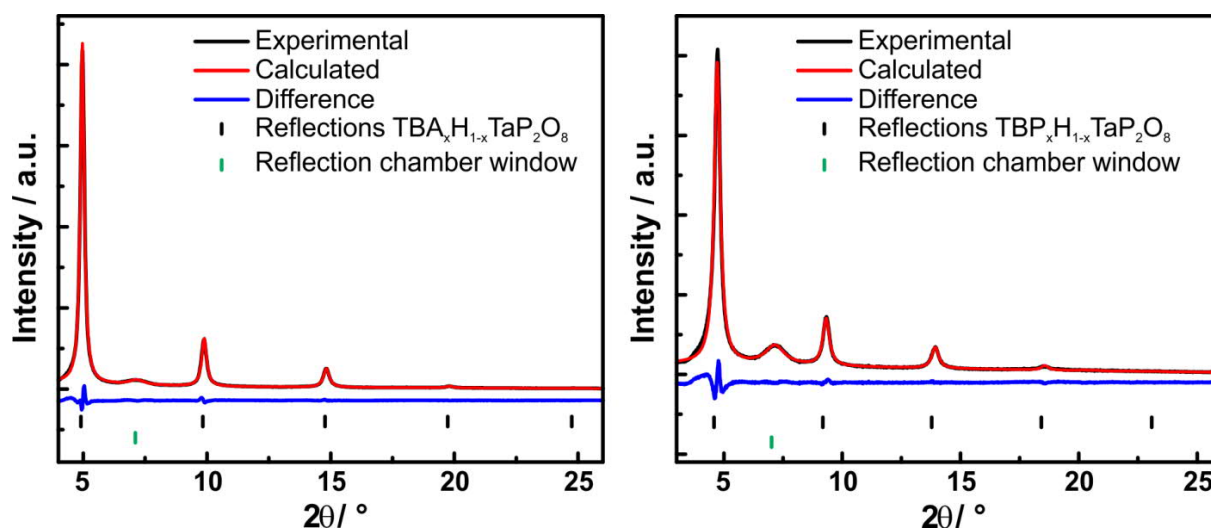


Figure S4.6. Le Bail fits of the thin film out-of-plane XRD pattern of Figure 4.1e ($\text{TBA}_x\text{H}_{1-x}\text{TaP}_2\text{O}_8$ and $\text{TBP}_x\text{H}_{1-x}\text{TaP}_2\text{O}_8$). The green line marks the reflection arising from the sample chamber window material.

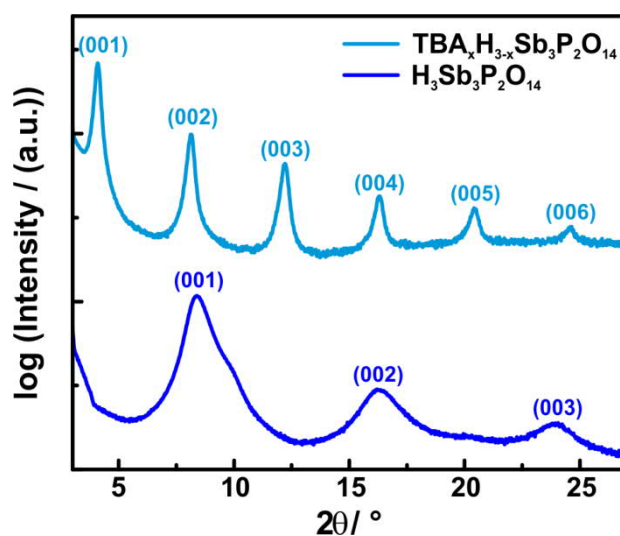


Figure S4.7. Indexed thin film out-of-plane XRD pattern of a $\text{H}_3\text{Sb}_3\text{P}_2\text{O}_{14}$ (dark blue, bottom) and a $\text{TBA}_x\text{H}_{3-x}\text{Sb}_3\text{P}_2\text{O}_{14}$ (light blue, top) thin film. The effect of the TBA intercalation is clearly visible as a shift in d -spacing of approximately 1.1 nm for the 001 reflection.

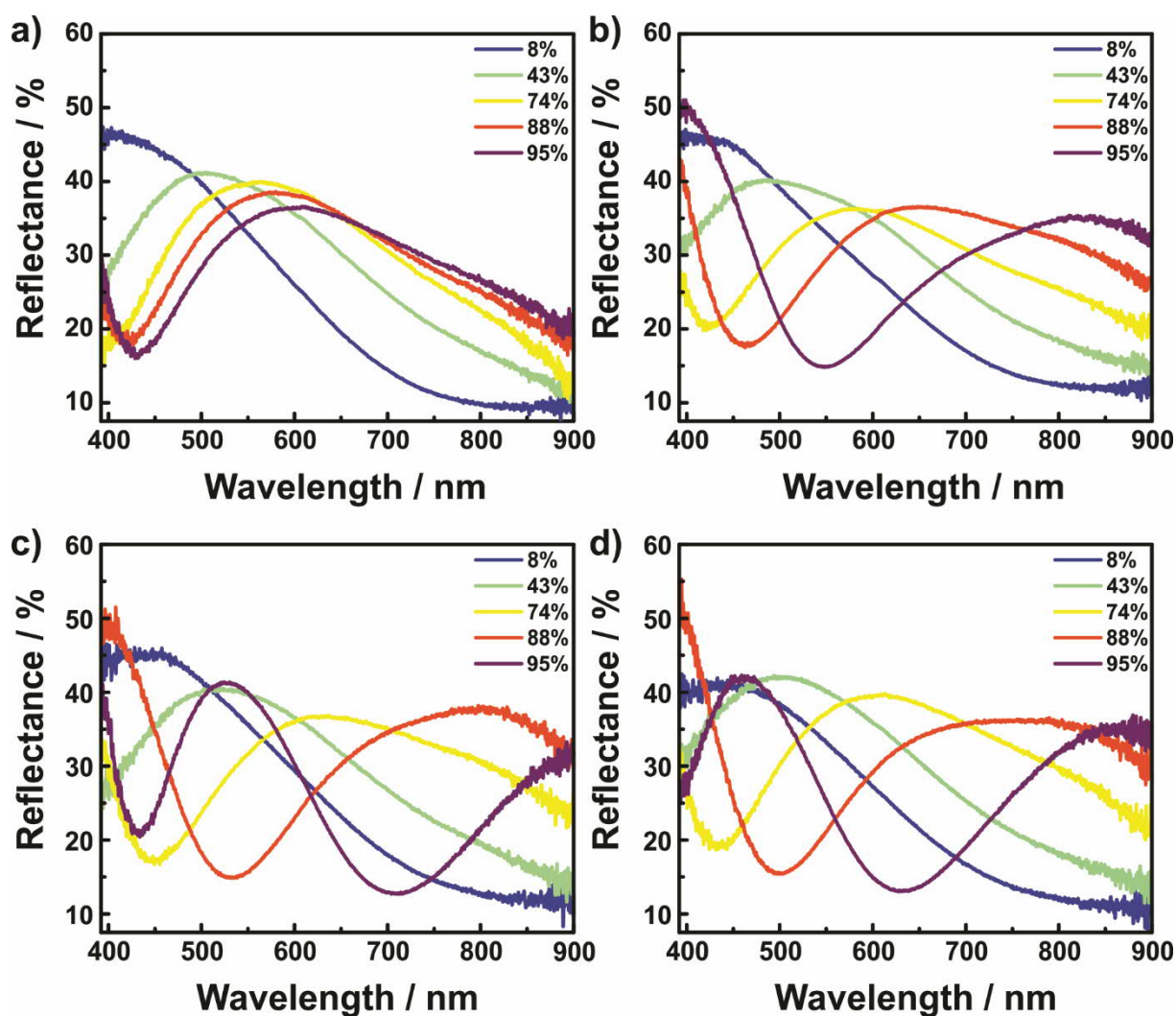


Figure S4.8. Humidity dependent UV-Vis spectra of a) $\text{H}_3\text{Sb}_3\text{P}_2\text{O}_{14}$, b) $\text{TBA}_x\text{H}_{3-x}\text{Sb}_3\text{P}_2\text{O}_{14}$, c) $\text{TBA}_x\text{H}_{1-x}\text{TaP}_2\text{O}_8$ and d) $\text{TBP}_x\text{H}_{1-x}\text{TaP}_2\text{O}_8$ thin films. A large difference in the optical shift is observed at 88% and 95% RH for samples with and without TBA or TBP. For corresponding optical microscope images see Figure 4.2, and for optical isotherms see Figure S4.9.

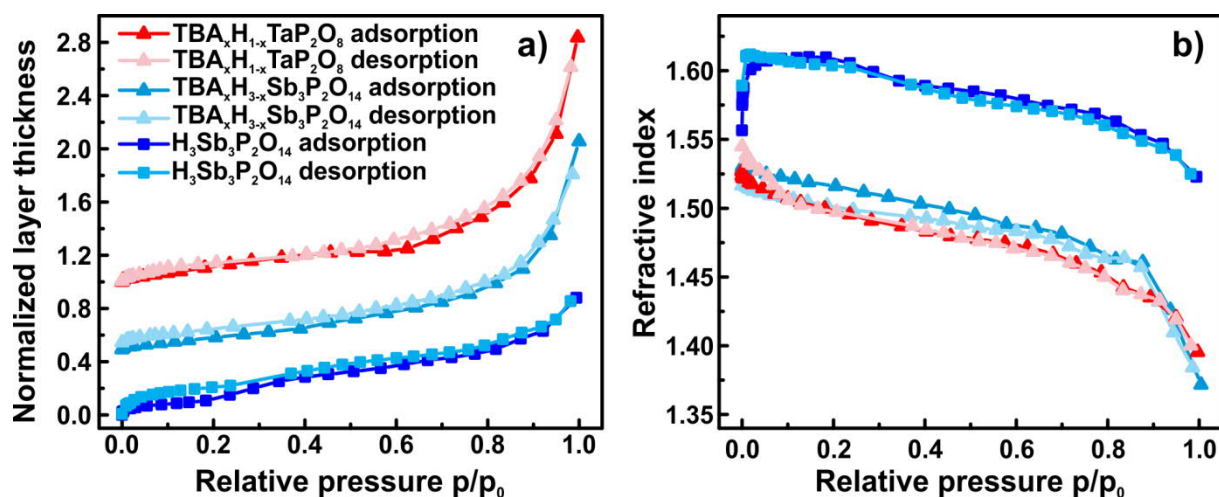


Figure S4.9. Optical isotherms of TBA_xH_{1-x}TaP₂O₈, TBA_xH_{3-x}Sb₃P₂O₁₄ and H₃Sb₃P₂O₁₄ nanosheets thin films measured by ellipsometric porosimetry. a) Normalized layer thickness change ($(l-l_0)/l_0$; note, that an offset of 0.5 was applied for each isotherm) and b) RI (at $\lambda=623$ nm) of the different nanosheet thin films measured at different relative pressures of water vapor. The measurements are in good agreement with Figure 4.2 and Figure S4.8. The optical isotherm of H₃Sb₃P₂O₁₄ has been reproduced from our previous publication, ref. [3].

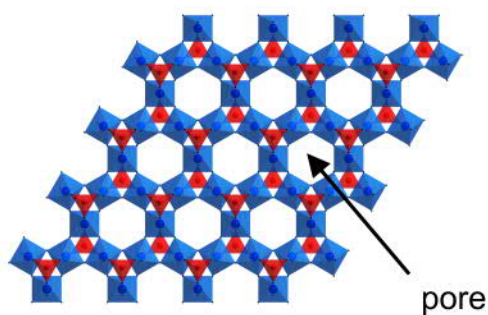


Figure S4.10. Structural pore of a Sb₃P₂O₁₄³⁻ nanosheet. SbO₆ octahedra in blue, PO₄ tetrahedra in red.

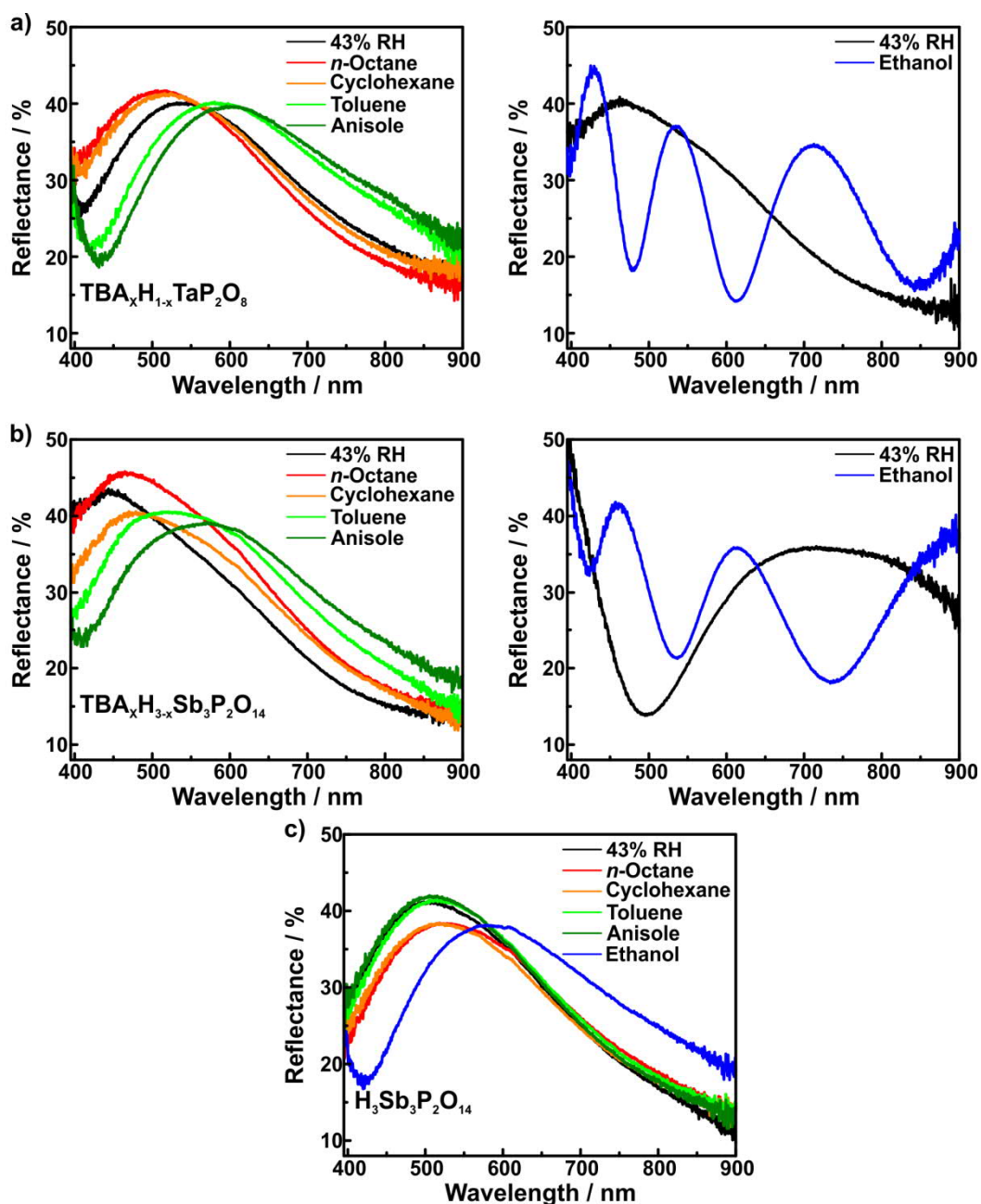


Figure S4.11. Optical response of a) $TBA_xH_{1-x}TaP_2O_8$, b) $TBA_xH_{3-x}Sb_3P_2O_{14}$ and c) $H_3Sb_3P_2O_{14}$ nanosheet thin films to saturated solvent vapors of *n*-octane, cyclohexane, toluene, anisole and ethanol. For comparison, the UV-Vis spectra obtained at 43% RH are shown as well. Note that for $H_3Sb_3P_2O_{14}$ only a very small difference in the spectra between *n*-octane, cyclohexane, toluene, and anisole is observed, whereas for the sample treated with TBA a clear difference between solvents of different polarity is seen.

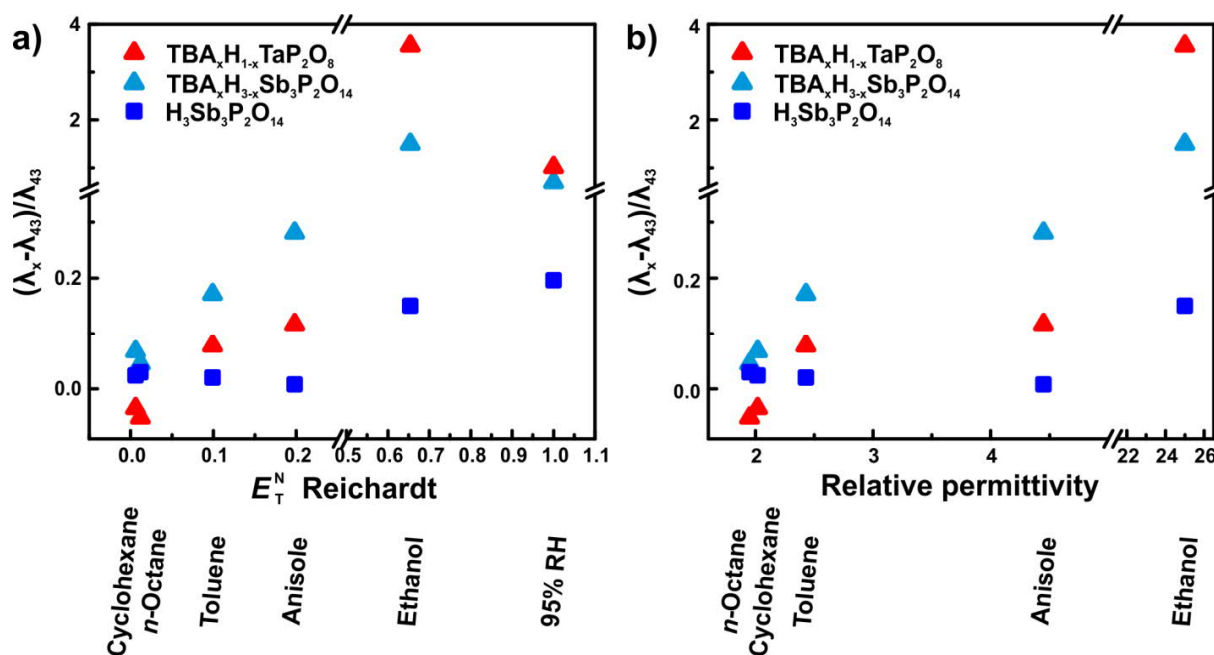


Figure S4.12. Normalized optical shift plotted as a function of solvent polarity. a) Optical shift plotted against the normalized Reichardt polarity scale E_T^N and b) against the relative permittivity, which is a good indicator of the solvent polarity. For the relative permittivity the points for water were not included in the plot, due to the very high relative permittivity.

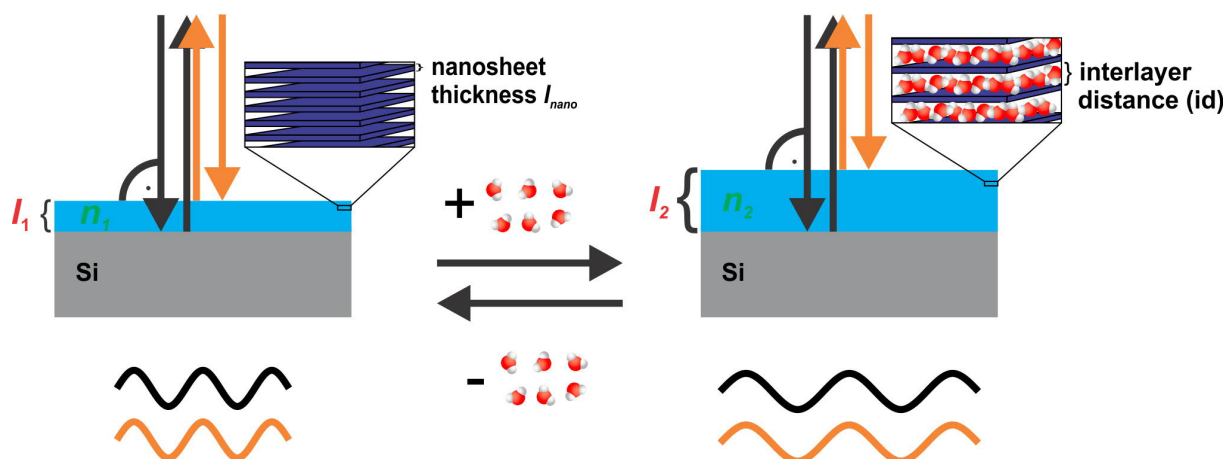


Figure S4.13. Schematic illustration describing the sensing principle of a nanosheet-based Fabry-Pérot device. For clarity, TBA is not depicted in the interlayer space. Upon intercalation of the analyte (here H₂O) into the interlayer space the interlayer distances (id) expands and the layer thickness changes from l_1 to l_2 . The layer thickness is expressed by: $l = k \cdot (l_{nano} + id) - id$. Here, k is the total number of single nanosheet layers that are stacked horizontally on the substrate, the sum of the single nanosheet thickness and the interlayer distance $l_{nano} + id$ corresponds to the (001) d -spacing. The change in layer thickness can be described as: $l_2 - l_1 = (k-1) \cdot (id_2 - id_1)$. Upon intercalation the effective RI can change. As the analytes have a lower RI compared to the nanosheet materials, the redshift is caused by the change in layer thickness (see Equation 4.1, $m\lambda = 2n_{eff}l$) rather than the RI (for the moderately polar and polar vapors). To specify, n_{eff} decreases upon adsorption of moderately polar and polar vapors, resulting in a decrease of λ (blueshift), whereas l increases, resulting in an increase of λ (redshift). But since $l_2/l_1 \gg n_1/n_2$ the net result is an increase in λ (redshift).

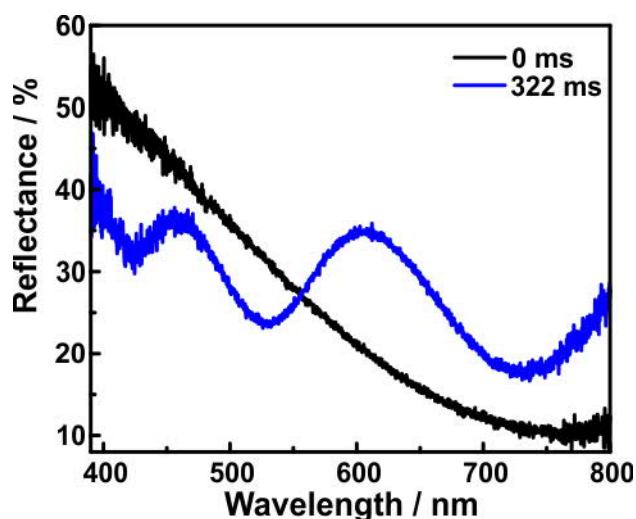


Figure S4.14. Single UV-Vis spectra of Figure 4.4a at 0 ms and after 322 ms. For 322 ms the maximum shift occurs, and the 4th and 3rd order Fabry-Pérot fringe are visible at 456 nm and 608 nm, respectively.

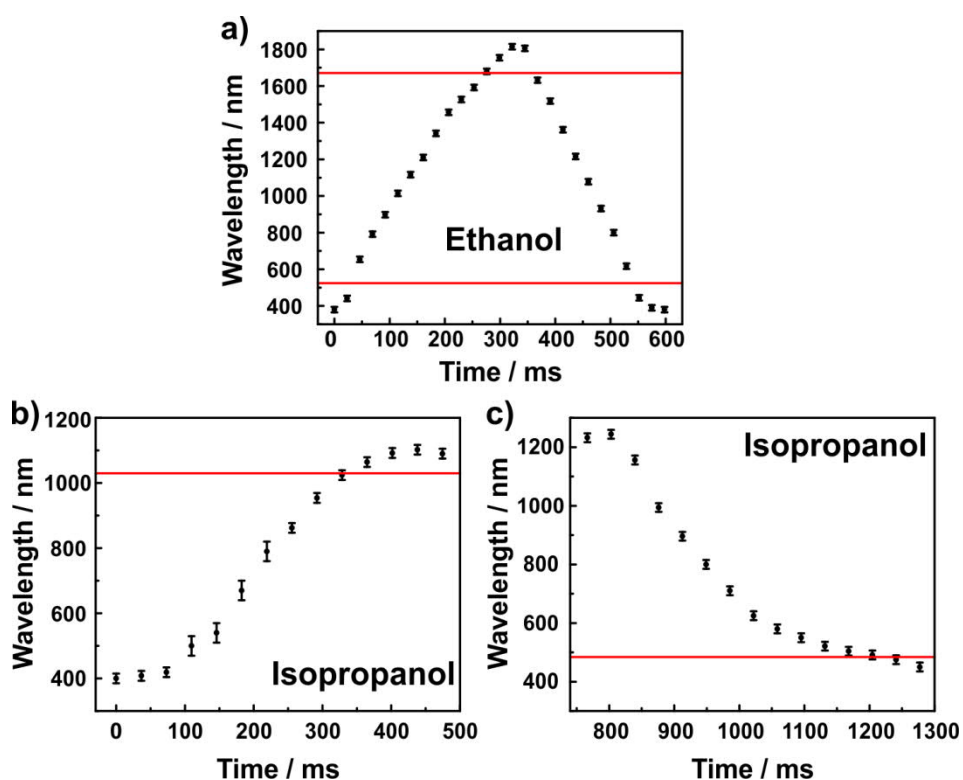


Figure S4.15: Determination of response and recovery time of a $\text{TBA}_x\text{H}_{1-x}\text{TaP}_2\text{O}_8$ Fabry-Pérot device toward ethanol and isopropanol (Figure 4.4a, Figure S4.18). a) Response and recovery time for ethanol. The upper lines indicate when 90% of the change in optical shift is reached, which is the response time, and the lower line indicates when 90% of the change in optical shift is reached for desorption, which is the recovery time. Determination of the response time (b) and of the recovery time (c) of isopropanol.

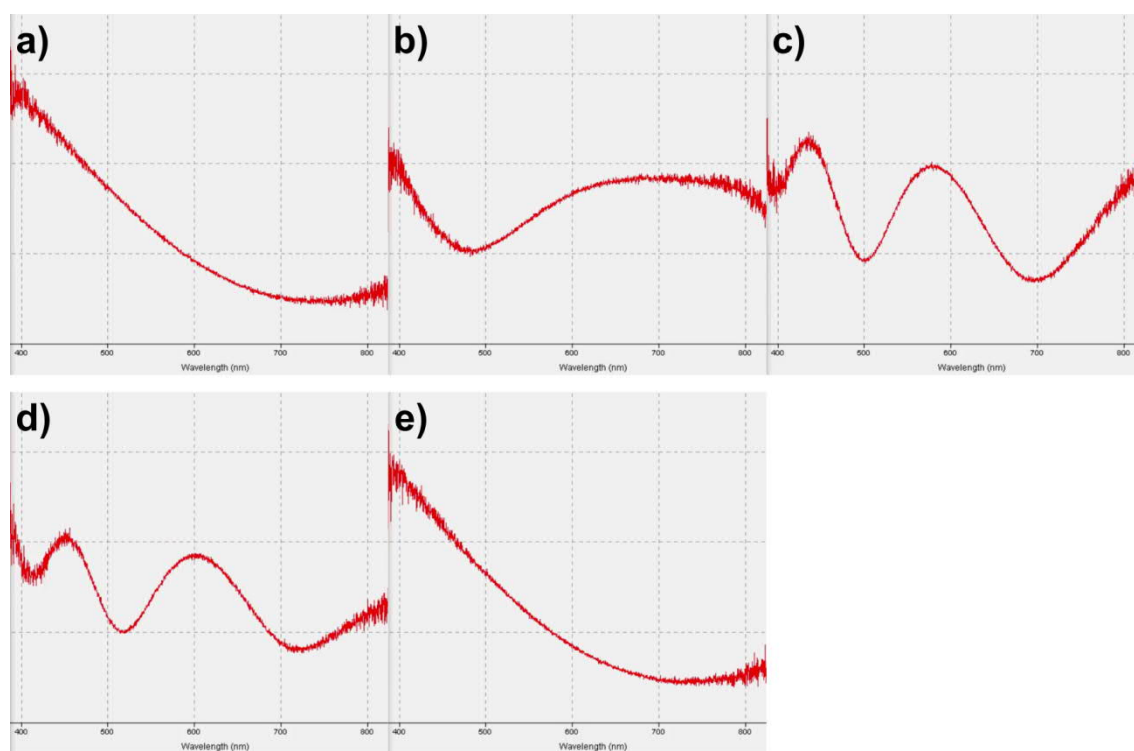


Figure S4.16. Frame series from Video S4.1. Time resolved response of a $\text{TBA}_x\text{H}_{1-x}\text{TaP}_2\text{O}_8$ thin film toward a short ethanol vapor pulse. Please see Video S4.1 for actual time resolution. The total shift and relaxation from a) to e) appears in less than 1 s.

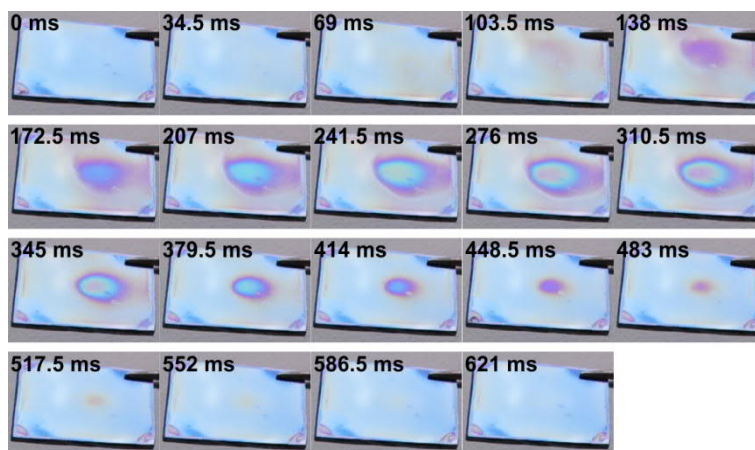


Figure S4.17. Response of $\text{TBA}_x\text{H}_{3-x}\text{Sb}_3\text{P}_2\text{O}_{14}$ thin film toward an ethanol vapor pulse from a wash bottle. Images are single frames from 29 fps video (Video S4.2). Note that the images of Figure 4.4b) top are from this consecutive image series (see also Video S4.2).

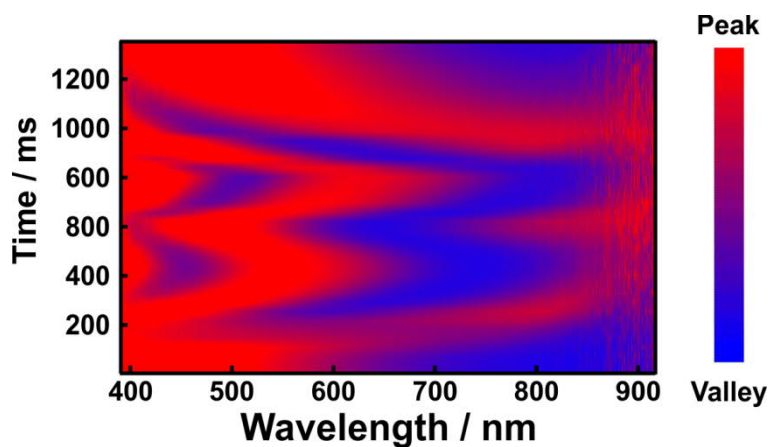


Figure S4.18. Time resolved response of a $\text{TBA}_x\text{H}_{1-x}\text{TaP}_2\text{O}_8$ thin film toward a short isopropanol vapor pulse. Note that we clearly observe the 2nd and 3rd order Fabry-Pérot fringe in the visible spectral region. The response also occurs in less than 500 ms.

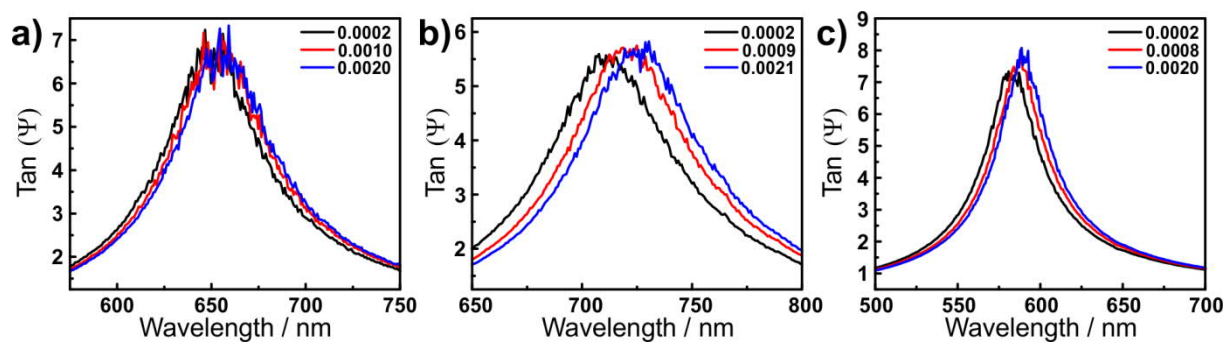


Figure S4.19. Minimum detectable concentration of ethanol for a) $\text{TBA}_x\text{H}_{1-x}\text{TaP}_2\text{O}_8$, b) $\text{TBA}_x\text{H}_{3-x}\text{Sb}_3\text{P}_2\text{O}_{14}$ and c) $\text{H}_3\text{Sb}_3\text{P}_2\text{O}_{14}$. For all of the sensors we can detect down to 200 ppm (p/p₀) ethanol, which is the lowest value reachable with our ellipsometer setup. Note that these measurements are ellipsometric raw data.

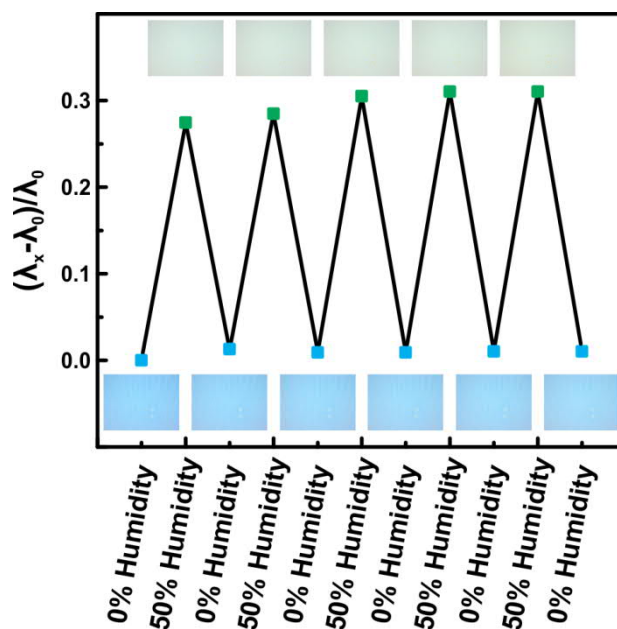


Figure S4.20. Cycling of a $\text{TBA}_x\text{H}_{3-x}\text{Sb}_3\text{P}_2\text{O}_{14}$ thin film between 0% and 50±1% RH.

Please, see Video S4.1-S4.4, which is available online.

<http://onlinelibrary.wiley.com/doi/10.1002/adma.201604884/abstract#footer-support-info>

Calculation S4.1:

Total optical shift in 322ms for a $TBA_xH_{1-x}TaP_2O_8$ thin film under ethanol vapor (see Figure 4.4a, Figure S4.14):

$$1824 \text{ nm} - 395 \text{ nm} = 1429 \text{ nm}$$

Optical Shift in nm ms^{-1} :

$$\frac{1429 \text{ nm}}{322 \text{ ms}} = 4.44 \text{ nm ms}^{-1}$$

Average time for human eye to detect two consecutive images 13 ms.^[8]

Optical shift in 13 ms:

$$4.44 \text{ nm ms}^{-1} \cdot 13 \text{ ms} = 57.72 \text{ nm}$$

Even shifts way below 57.72 nm can be detected with the naked eye without any problem.

Calculation S4.2:

Conservative estimation* of the percentage of film thickness change per ms with respect to starting thickness, assuming an average rate of change (Figure 4.4a):

Estimation of the thickness change caused by ethanol:

$$m\Delta\lambda = 2\Delta(nl)$$

with conservative estimation: $n_1 = n_2 = 1.5$

$$1824 \text{ nm} - 395 \text{ nm} = 2((l_2 \cdot 1.5) - (l_1 \cdot 1.5))$$

$$1429 \text{ nm} \cdot 3^{-1} = l_2 - l_1$$

$$476.33 \text{ nm} = l_2 - l_1$$

Estimation of film thickness prior to treatment:

$$X_1 = 2n_1l_1 \Rightarrow l_1 = \frac{X_1}{2n_1} \Rightarrow 395 \text{ nm} \cdot 3^{-1} = 131.67 \text{ nm}$$

Film thickness change per nm ms^{-1} and $\% \text{ ms}^{-1}$:

$$\frac{476.33 \text{ nm}}{322 \text{ ms}} = 1.48 \text{ nm ms}^{-1}$$

$$\frac{100\% \cdot 1.48 \text{ nm ms}^{-1}}{131.67 \text{ nm}} = 1.12\% \text{ ms}^{-1}$$

% change within 13 ms:

$$1.12\% \text{ ms}^{-1} \cdot 13 \text{ ms} = 14.56\%$$

*negative effect (blue shift) on the position of the Fabry-Pérot fringes for the change in RI due to decreasing effective RI by analyte intercalation and swelling is not included. Instead, the RI is set to 1.5. Since the RI decrease is not considered here, the percentage of thickness increase of the thin film is likely to be much higher.

4.2.4 Bibliography

- [1] S. Oyetola, A. Verbaere, Y. Piffard, M. Tournoux, *Eur. J. Solid State Inorg. Chem.* **1988**, 25, 259-278.
- [2] S. Oyetola, A. Verbaere, D. Guyomard, Y. Piffard, M. Tournoux, *Eur. J. Solid State Inorg. Chem.* **1989**, 26, 175-191.
- [3] K. Szendrei, P. Ganter, O. Sánchez-Sobrado, R. Eger, A. Kuhn, B. V. Lotsch, *Adv. Mater.* **2015**, 27, 6341-6348.
- [4] K. Ufer, G. Roth, R. Kleeberg, H. Stanjek, R. Dohrmann, J. Bergmann, *Z. Kristallogr.* **2004**, 219, 519-527.
- [5] X. Wang, J. Li, R. D. Hart, A. van Riessen, R. McDonald, *J. Appl. Crystallogr.* **2011**, 44, 902-910.
- [6] P. W. Winston, D. H. Bates, *Ecology* **1960**, 41, 232-237.
- [7] L. Greenspan, *J. Res. Nat. Bur. Stand.* **1977**, 81A, 89-96.
- [8] L. E. Humes, T. A. Busey, J. C. Craig, D. Kewley-Port, *Attention, Perception & Psychophysics* **2009**, 71, 860-871.

5 Controlling the interlayer cations in calcium niobate nanosheets thin films for sensing and μm scale patterning

5.1 Photocatalytic Nanosheet Lithography: Photolithography based on Organically Modified Photoactive 2D Nanosheets

Pirmin Ganter and Bettina V. Lotsch

published: *Angew. Chem. Int. Ed.* **2017**, *56*, 8389-8392.

DOI: 10.1002/anie.201703149

<http://onlinelibrary.wiley.com/doi/10.1002/anie.201703149/abstract>

Copyright © 2017 WILEY-VCH Verlag GmbH & Co. KGaA, Weinheim. Reproduced with the permission of WILEY-VCH.

Contribution of P.G: *P.G. carried out all the experiments. P.G. prepared all graphic material and performed the literature screening. In addition, P.G. wrote the major part of the manuscript.*

Abstract

Harvesting the properties of nanosheets is not only crucial from a fundamental perspective, but also for the development of novel functional devices based on 2D nanosheets. Herein, we demonstrate the processing of organically modified $\text{TBA}_x\text{H}_{1-x}\text{Ca}_2\text{Nb}_3\text{O}_{10}$ nanosheets into photonic thin films and study their colorimetric sensing properties in response to various aqueous and organic solvent vapors. Building on the enhanced solvent accessibility of TBA-containing nanosheets and their photocatalytic activity under UV irradiation, we develop a new concept for photocatalytic lithography using $\text{TBA}_x\text{H}_{1-x}\text{Ca}_2\text{Nb}_3\text{O}_{10}$ nanosheets as a negative photoresist to obtain high-fidelity micron-scale patterns of robust inorganic nanosheets. Photocatalytic nanosheet lithography (PNL) therefore adds a new resist-free, resource efficient direct patterning technique to the toolbox of photolithography.

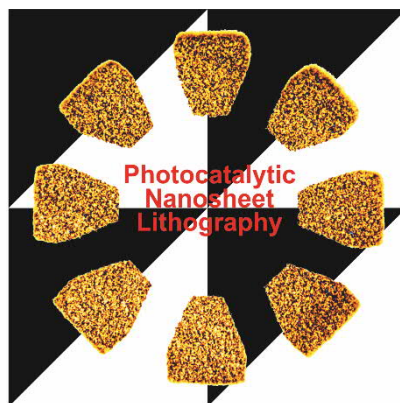


Table of Content: The pattern of little sheets: Combining the solvent-uptake capacity of organically modified $\text{TBA}_x\text{H}_{1-x}\text{Ca}_2\text{Nb}_3\text{O}_{10}$ nanosheets with their inherent photocatalytic activity imparts both vapor-sensing properties and enables their use as negative photoresists for micron-scale patterning.

5.1.1 Introduction

Recently, calcium niobate nanosheets derived from the DJ-type perovskite $\text{HCa}_2\text{Nb}_3\text{O}_{10}$ have developed into an ubiquitous building block for nanoarchitectonics,^[1-4] nanoelectronics,^[5-10] and beyond^[11-14] owing to their high structural definition and aspect ratio as well as their easy accessibility and handling.^[7, 15] Amongst others, calcium niobate nanosheets have been deployed as 2D building blocks in artificial heterostructures,^[15-17] as electron transport materials in solar cells^[14] and photocatalysts,^[11-13] or as ultrathin high- κ capacitors or gate insulators.^[5-10]

Following pioneering work by Sasaki and Mallouk on the exfoliation and utilization of 2D oxide nanosheets,^[1-3,18] Osterloh and co-workers demonstrated the vast potential of calcium niobate nanosheet suspensions in photocatalytic water splitting.^[11,12] While the large-band gap $\text{Ca}_2\text{Nb}_3\text{O}_{10}$ semiconductor nanosheets ($E_g = 3.5\text{-}3.6\text{ eV}$)^[11,19] produce hydrogen from pure water, the decomposition of TBA, which is commonly used as an EA, is another fingerprint of the photoactivity of calcium niobate under UV-illumination in air.^[12] Similar observations for titania nanosheets modified with organic cations were reported by Sasaki and co-workers earlier.^[20-22] This photodegradation of organic counterions was later used to pattern GO/PDDA/titania multilayer or titania thin films on the millimeter or hundreds of micron scale, respectively, using a shadow mask.^[23-25] However, being able to precisely sculpture nanosheet architectures with feature sizes smaller than 100 microns is highly desired for applications in integrated microelectronic circuits due to the ever increasing need for miniaturization.^[6,26] Recent attempts to pattern nanosheet thin films on the μm -scale were based on MoS_2 ,^[26] rGO,^[27] or GO.^[28] In these approaches the patterns are either obtained by laser patterning or by electrochemical microstamping.^[26-28] However, none of these latter methods utilizes the intrinsic properties of the nanosheets for pattern creation, and all of them rely on complex instrumentation for direct writing or stamping, which puts limitations on resolution, parallelization, and scale-up.

Apart from their known photocatalytic activity, calcium niobate nanosheets are promising candidates for ultrathin sensor devices and for high- κ -capacitors and gate devices owing to their molecularly thin thickness paired with high capacitance and large band gap.^[5-10] Therefore, the development of a straightforward, low-cost, and scalable patterning method for calcium niobate nanosheets is in high demand.

Herein, we exploit the colloidal nature of calcium niobate nanosheets to construct photonic thin films by spin-coating and study their response toward RH as well as saturated organic vapors. We then combine the enhanced solvent-accessibility of the organically modified sheets with their photocatalytic properties to photo-pattern thin film objects on the micrometer scale by using $\text{TBA}_x\text{H}_{1-x}\text{Ca}_2\text{Nb}_3\text{O}_{10}$ as a negative photoresist. To our knowledge, this is the first time that the inherent photoactivity of exfoliated inorganic nanosheets is used to mediate sub 100 micrometer pattern formation under UV irradiation with high fidelity, thus adding a new resist-free and direct patterning technique to the toolbox of photolithography.

5.1.2 Results and discussion

$\text{TBA}_x\text{H}_{1-x}\text{Ca}_2\text{Nb}_3\text{O}_{10}$ nanosheets were obtained from $\text{KCa}_2\text{Nb}_3\text{O}_{10}$ in a two-step process as described previously (see Experimental Details, and Table S5.1 and Figure S5.1 in the Supporting Information).^[19] The organically modified nanosheets exhibit a height of 2.6 nm (Figure 5.1a), which is in agreement with the XRD measurements (see below) and other data from the literature.^[19] The nanosheets were spincoated into optically homogenous films on silicon substrates as depicted in Figure 5.1b. Note that the color of the Fabry-Pérot thin films originates from interference, because the film has an optical thickness in the range of half of the wavelength of visible light,^[29] according to Equation 5.1:

$$2nl \cos(\theta) = m\lambda \quad (\text{Equation 5.1})$$

where n is the RI, l is the layer thickness, θ the angle of the refracted beam, m the spectral order and λ the wavelength.

The high degree of order perpendicular to the substrate is also illustrated by the fact that reflections up to the 11th order (0011) are observed in the out-of-plane XRD pattern (Figure 5.1c). A d -spacing of 2.74 nm can be extracted by a Pawley fit of the data (Figure S5.2 and Table S5.2), which is in good agreement with the combined $\text{Ca}_2\text{Nb}_3\text{O}_{10}^-$ nanosheet thickness of 1.5-1.6 nm^[6] and the height of a TBA^+ layer of around 1-1.1 nm.^[30] The inset in Figure 5.1c depicts a SEM cross-section image of the photonic thin film, highlighting the lateral homogeneity of the film on the micron-scale.

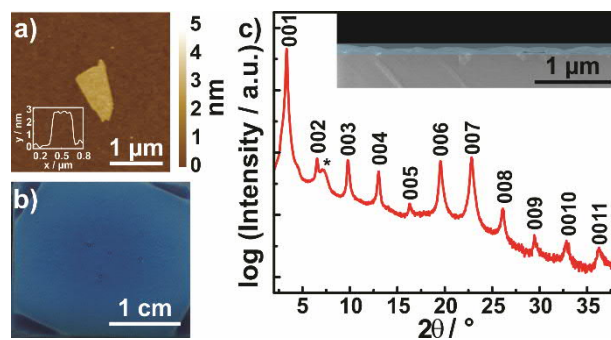


Figure 5.1. Characterization of $\text{TBA}_x\text{H}_{1-x}\text{Ca}_2\text{Nb}_3\text{O}_{10}$ nanosheets and thin films. a) AFM image of a single-layer $\text{TBA}_x\text{H}_{1-x}\text{Ca}_2\text{Nb}_3\text{O}_{10}$ nanosheet. Inset: height profile. b) Spin-coated thin film of $\text{TBA}_x\text{H}_{1-x}\text{Ca}_2\text{Nb}_3\text{O}_{10}$ nanosheets on a silicon substrate, showing the blue interference color. c) Out-of-plane XRD pattern of a $\text{TBA}_x\text{H}_{1-x}\text{Ca}_2\text{Nb}_3\text{O}_{10}$ thin film recorded with $\text{Cu-K}\alpha_1$ radiation. The broad reflection marked with an asterisk at around 7° stems from the sample chamber window material. Inset: a SEM cross-section of the $\text{TBA}_x\text{H}_{1-x}\text{Ca}_2\text{Nb}_3\text{O}_{10}$ thin film (middle, in blue; thickness ca. 100 nm).

The Fabry-Pérot films were exposed to vapors of varying RH or saturated organic solvent vapors in a closed system under static conditions (Figure 5.2 and Figure S5.3). Distinct color changes for varying RHs as well as organic vapors with different polarities are observed as shown by the microscope images in Figure 5.2 (bottom row). The shape of the normalized optical sensing response toward varying levels of RH (see Figure 5.2a) largely resembles the sensing behavior of the $\text{TBA}_x\text{H}_{1-x}\text{TaP}_2\text{O}_8$ and $\text{TBA}_x\text{H}_{3-x}\text{Sb}_3\text{P}_2\text{O}_{14}$, nanosheet films reported by us previously.^[29] This similarity points to the important role of the interlayer cation TBA^+ , which dominates the overall sensing behavior, rather than the host material itself: TBA acts as a gatekeeper for the swelling process in that it increases the interlayer distance, rendering the diffusion of larger molecules into the interlayer gallery space more facile. In addition, it slightly hydrophobizes the interlayer space, making the intercalation of moderately polar or unpolar molecules more favorable. At the same time, the TBA cations easily hydrate, thus extending the sensitivity range toward both polar and non-polar solvents and enhancing the overall swellability of the system (Figure 5.2b).^[29] Tuning the intrinsic polarity of the nanosheets by partial ion exchange of protons with TBA^+ therefore enables color-coded polarity differentiation of organic vapors in a fashion similar to the phosphate-based sensors developed by us previously.^[29,31,32]

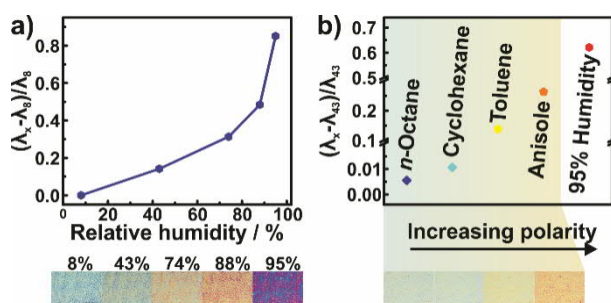


Figure 5.2. Colorimetric sensing of a) RH and b) organic vapors with $\text{TBA}_x\text{H}_{1-x}\text{Ca}_2\text{Nb}_3\text{O}_{10}$ thin films. Displayed is the normalized optical shift against the RH or the saturated vapor pressure of various solvents. Bottom row in (a) and (b) optical microscope images. The scale bar for the optical images is 200 μm . For the corresponding UV-Vis spectra see Figure S5.3.

In the next step we combine the enhanced solvent accessibility of the TBA-modified nanosheets with their inherent photoactivity to establish a new 2D platform for photocatalytic patterning. Photodegradation of TBA⁺ by calcium niobate under UV irradiation is ascribed to the light-induced generation of reactive oxygen species, especially superoxide radicals, which react with TBA under H abstraction to form H₂O₂.^[12] The degradation of the organic interlayer species will result in a decrease in the stacking distance as well as in the disappearance of characteristic C-H vibrations in the vibrational spectra. A decrease in the *d*-spacing and, hence, film thickness, is then expected to directly result in a color change of the thin film interference color according to Equation 5.1. Indeed, Figure 5.3b, d demonstrate the clearly visible color change upon irradiation of the film with a xenon lamp. The Xe lamp has a significant spectral contribution in the region below 380 nm, which is required for TBA decomposition. In addition, Raman measurements reveal decomposition of the TBA cations by the disappearance of the diagnostic C-H stretching vibration in the range between 2880 cm⁻¹ and 3050 cm⁻¹, which are clearly present in the TBA_xH_{1-x}Ca₂Nb₃O₁₀ bulk material as well as in the thin films before illumination (Figure 5.3a). Moreover, the *d*-spacing decreases by 1 nm (Figure 5.3c and Figure S5.4), confirming the loss of TBA in the interlayer space and its replacement by protons and NH₄⁺.^[5,6,9] Note that the final *d*-spacing of 1.7 nm is in good agreement with the stacking distances reported for UV-treated TBA-containing calcium niobate thin films (1.5-1.7 nm).^[6,9] Taking advantage of the local character of the light-induced TBA degradation, we use this novel photocatalytic lithography concept to pattern the thin films by illuminating only parts of the film surface through a shadow mask (Figure 5.3e). Exposure to UV light (Xe lamp, $\lambda < 380$ nm) results in thinner areas (golden, TBA-free) and thicker areas still containing TBA. Drawing on the sensing results (see Figure 5.2) from which swelling of the TBA intercalated samples in polar solvents is expected, we use washing with toluene or an acetone-water mixture to remove the non-exposed (i.e. TBA_xH_{1-x}Ca₂Nb₃O₁₀ containing) areas. The remaining patterns consist of regions of (NH₄)_xH_{1-x}Ca₂Nb₃O₁₀ nanosheet film (see Figure 5.3f). In essence, this process demonstrates that TBA_xH_{1-x}Ca₂Nb₃O₁₀ nanosheets can be used as a negative photoresist by combining the swellability of the organically modified nanosheets with their inherent photocatalytic activity under UV-light.

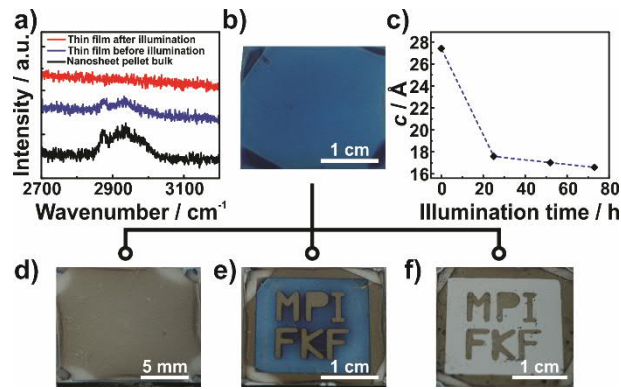


Figure 5.3. Photolithographic patterning of $\text{TBA}_x\text{H}_{1-x}\text{Ca}_2\text{Nb}_3\text{O}_{10}$ thin films. a) Raman measurements mapping the photodecomposition of TBA^+ under UV-illumination. The C-H stretching vibrations of the TBA is the dominant feature in the range between 2880 cm^{-1} and 3050 cm^{-1} . b) Image of the thin film before illumination. c) Change of the d -spacing with increasing illumination time. d) Thin film after illumination without a mask, e) after illumination with a shadow mask, and f) after removal of the unexposed area containing TBA ions (MPI FKF: Max-Planck-Institut für Festkörperforschung).

With a view toward potential applications of 2D materials in microelectronics, patterning on the μm -scale is key. To explore the potential of this technique for micron scale patterning, we applied a μm -scale mask to obtain high-fidelity micron-scale $(\text{NH}_4)_x\text{H}_{1-x}\text{Ca}_2\text{Nb}_3\text{O}_{10}$ features on a Si substrate (Figure 5.4, Figure S5.5 and S5.6). The oxide nanosheet patterns show a rather low line-edge roughness, considering the large lateral size of the nanosheets (see Figure 5.4d, e). Using this easy-to-implement and economical procedure under ambient conditions, we were able to obtain features with sizes smaller than $15 \times 10\ \mu\text{m}$ in lateral size, again demonstrating the ample potential of using $\text{TBA}_x\text{H}_{1-x}\text{Ca}_2\text{Nb}_3\text{O}_{10}$ as a negative photoresist for photolithographic patterning on the micron scale, and possibly beyond.

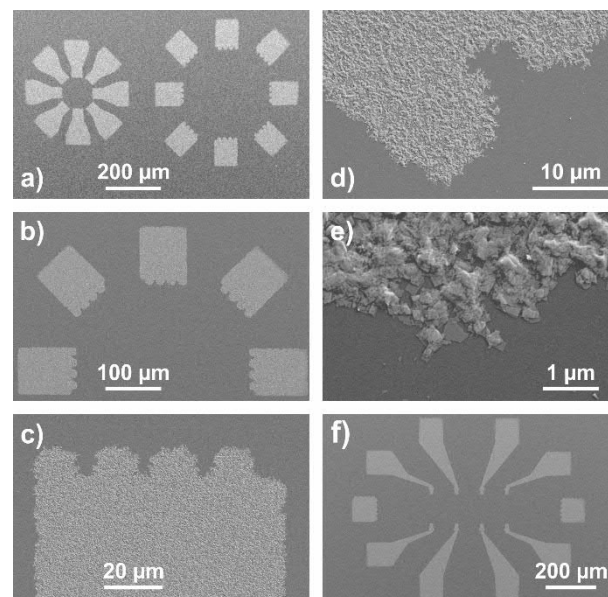


Figure 5.4. SEM images of micrometer scale patterns of $(\text{NH}_4)_x\text{H}_{1-x}\text{Ca}_2\text{Nb}_3\text{O}_{10}$. a)-e) magnification series of arbitrary nanosheet features and f) patterned electrode configuration. Note that the contours of individual nanosheets, the fundamental building block of the thin film structures, can clearly be observed in (e).

5.1.3 Conclusion

In conclusion, we have prepared photonic thin films based on exfoliated, organically modified $\text{TBA}_x\text{H}_{1-x}\text{Ca}_2\text{Nb}_3\text{O}_{10}$ nanosheets. The interaction of the films with various solvent vapors, resulting in swelling of the intergallery space during solvent uptake, was utilized to develop colorimetric sensors for humidity and organic-vapor detection based on Fabry-Pérot thin film interference. By combining the swellability of the organically modified nanosheets with their intrinsic photocatalytic activity, we further developed a new photolithographic concept for patterning photoresponsive nanosheets. In particular, we demonstrated the use of $\text{TBA}_x\text{H}_{1-x}\text{Ca}_2\text{Nb}_3\text{O}_{10}$ as a negative photoresist to create sub 100 micrometer scale patterns of $(\text{NH}_4)_x\text{H}_{1-x}\text{Ca}_2\text{Nb}_3\text{O}_{10}$ with low line-edge roughness in a straightforward and scalable development step. Since the calcium niobate nanosheets thus act both as the active component and a negative photoresist, this technique circumvents the use of sacrificial photoresists, which makes the overall process economical and resource efficient. While this is the first demonstration using exfoliated inorganic nanosheets as a photoresist, we expect this concept to be sufficiently general to transfer it to other photoactive 2D systems and to further reduce the feature sizes accessible by PNL to the submicron scale.

5.1.4 Acknowledgement

Financial support was granted by the Max Planck Society and the University of Munich (LMU). We thank Christine Stefani and Frank Adams for thin film XRD measurements, Armin Schulz for Raman spectroscopy and Viola Duppel for SEM and SEM cross-section measurements.

5.1.5 Bibliography

- [1] M. Fang, C. H. Kim, G. B. Saupe, H.-N. Kim, C. C. Waraksa, T. Miwa, A. Fujishima, T. E. Mallouk, *Chem. Mater.* **1999**, *11*, 1526-1532.
- [2] R. E. Schaak, T. E. Mallouk, *Chem. Mater.* **2000**, *12*, 2513-2516.
- [3] Y. Ebina, T. Sasaki, M. Harada, M. Watanabe, *Chem. Mater.* **2002**, *14*, 4390-4395.
- [4] T. Shibata, K. Fukuda, Y. Ebina, T. Kogure, T. Sasaki, *Adv. Mater.* **2008**, *20*, 231-235.
- [5] B.-W. Li, M. Osada, T. C. Ozawa, Y. Ebina, K. Akatsuka, R. Ma, H. Funakubo, T. Sasaki, *ACS Nano* **2010**, *4*, 6673-6680.
- [6] M. Osada, K. Akatsuka, Y. Ebina, H. Funakubo, K. Ono, K. Takada, T. Sasaki, *ACS Nano* **2010**, *4*, 5225-5232.
- [7] M. Osada, T. Sasaki, *Adv. Mater.* **2012**, *24*, 210-228.
- [8] Y.-H. Kim, H.-J. Kim, M. Osada, B.-W. Li, Y. Ebina, T. Sasaki, *ACS Appl. Mater. Interfaces* **2014**, *6*, 19510-19514.
- [9] C. Wang, M. Osada, Y. Ebina, B.-W. Li, K. Akatsuka, K. Fukuda, W. Sugimoto, R. Ma, T. Sasaki, *ACS Nano* **2014**, *8*, 2658-2666.
- [10] B.-W. Li, M. Osada, Y. Ebina, K. Akatsuka, K. Fukuda, T. Sasaki, *ACS Nano* **2014**, *8*, 5449-5461.
- [11] O. C. Compton, E. C. Carroll, J. Y. Kim, D. S. Larsen, F. E. Osterloh, *J. Phys. Chem. C* **2007**, *111*, 14589-14592.
- [12] O. C. Compton, F. E. Osterloh, *J. Phys. Chem. C* **2009**, *113*, 479-485.
- [13] E. M. Sabio, R. L. Chamousis, N. D. Browning, F. E. Osterloh, *J. Phys. Chem. C* **2012**, *116*, 3161-3170.
- [14] L. Chang, M. A. Holmes, M. Waller, F. E. Osterloh, A. J. Moule, *J. Mater. Chem.* **2012**, *22*, 20443-20450.
- [15] R. Ma, T. Sasaki, *Adv. Mater.* **2010**, *22*, 5082-5104.

- [16] B. V. Lotsch, *Annu. Rev. Mater. Res.* **2015**, *45*, 85-109.
- [17] C. Ziegler, S. Werner, M. Bugnet, M. Wörsching, V. Duppel, G. A. Botton, C. Scheu, B. V. Lotsch, *Chem. Mater.* **2013**, *25*, 4892-4900.
- [18] Y. Ebina, T. Sasaki, M. Watanabe, *Solid State Ionics* **2002**, *151*, 177-182.
- [19] K. S. Virdi, Y. Kauffmann, C. Ziegler, P. Ganter, P. Blaha, B. V. Lotsch, W. D. Kaplan, C. Scheu, *J. Phys. Chem. C* **2016**, *120*, 11170-11179.
- [20] T. Sasaki, Y. Ebina, K. Fukuda, T. Tanaka, M. Harada, M. Watanabe, *Chem. Mater.* **2002**, *14*, 3524-3530.
- [21] Y. Umemura, E. Shinohara, A. Koura, T. Nishioka, T. Sasaki, *Langmuir* **2006**, *22*, 3870-387.
- [22] M. Harada, T. Sasaki, Y. Ebina, M. Watanabe, *J. Photochem. Photobiol. A* **2002**, *148*, 273-276.
- [23] H.-B. Yao, L.-H. Wu, C.-H. Cui, H.-Y. Fang, S.-H. Yu, *J. Mater. Chem.* **2010**, *20*, 5190-5195.
- [24] G. Perotto, A. Antonello, D. Ferraro, G. Mattei, A. Martucci, *Mater. Chem. Phys.* **2013**, *142*, 712-716.
- [25] G. Perotto, M. Cittadini, H. Tao, S. Kim, M. Yang, D. L. Kaplan, A. Martucci, F. G. Omenetto, *Adv. Mater.* **2015**, *27*, 6728-6732.
- [26] L. Cao, S. Yang, W. Gao, Z. Liu, Y. Gong, L. Ma, G. Shi, S. Lei, Y. Zhang, S. Zhang, R. Vajtai, P. M. Ajayan, *Small* **2013**, *9*, 2905-2910.
- [27] L. Zhi-Bo, L. Li, X. Yan-Fei, L. Jia-Jie, Z. Xin, C. Shu-Qi, C. Yong-Sheng, T. Jian-Guo, *J. Opt.* **2011**, *13*, 085601.
- [28] K. Hu, L. S. Tolentino, D. D. Kulkarni, C. Ye, S. Kumar, V. V. Tsukruk, *Angew. Chem. Int. Ed.* **2013**, *52*, 13784-13788; *Angew. Chem.* **2013**, *125*, 14029-14033.
- [29] P. Ganter, L. M. Schoop, B. V. Lotsch, *Adv. Mater.* **2017**, *29*, 1604884.
- [30] Y. Song, N. Iyi, T. Hoshida, T. C. Ozawa, Y. Ebina, R. Ma, N. Miyamoto, T. Sasaki, *Chem. Commun.* **2015**, *51*, 17068-17071.
- [31] K. Szendrei, P. Ganter, O. Sánchez-Sobrado, R. Eger, A. Kuhn, B. V. Lotsch, *Adv. Mater.* **2015**, *27*, 6341-6348.
- [32] P. Ganter, K. Szendrei, B. V. Lotsch, *Adv. Mater.* **2016**, *28*, 7436-7442.

5.2 Supporting Information: Photocatalytic Nanosheet Lithography: Photolithography based on Organically Modified Photoactive 2D Nanosheets

5.2.1 Methods

$\text{KCa}_2\text{Nb}_3\text{O}_{10}$ was synthesized in a way similar to that described previously. In brief, K_2CO_3 (300 mg, 99%, Merck), Nb_2O_5 (1574 mg, 99.5%, Alfa Aesar), and CaCO_3 (798 mg, 99%, Grüssing) were heated to 1250 °C for 60 h. The product (1.2 g) was ion exchanged by stirring with 5 M HNO_3 (430 mL) for 4 days with daily renewal of the acid. The resulting powder $\text{HCa}_2\text{Nb}_3\text{O}_{10} \cdot 1.5 \text{H}_2\text{O}$ was dried at 100 °C to yield $\text{HCa}_2\text{Nb}_3\text{O}_{10} \cdot 0.5 \text{H}_2\text{O}$. For exfoliation the solid acid (788 mg) was stirred with tetra-*n*-butylammonium hydroxide 30-hydrate (TBAOH, 1200 mg 98%, Sigma-Aldrich) in water (206 mL). To remove unexfoliated material, the suspension was first centrifuged at 3000 rpm for 30 min and subsequently the supernatant solution was centrifuged at 24000 rpm for 25 min to yield the nanosheet pellet. The nanosheet pellet was dried overnight at room temperature.

The $\text{TBA}_x\text{H}_{1-x}\text{Ca}_2\text{Nb}_3\text{O}_{10}$ nanosheet pellet (50.4 mg) was dissolved with TBAOH 30-hydrate (77.5 mg) in a water-ethanol mixture (944 mL and 1680 mL, respectively). Subsequently, the sample was ultrasonicated for 4 h before spin-coating it (200 mL or 500 mL) on silicon substrates (1.5 x 1.5 cm or 2.5 x 2.5 cm, 100 orientation).

For recording optical changes of the thin films toward humidity or organic vapors, the films were placed in a stainless steel chamber (ca. 6 mL residual volume) that has two basins with a volume of approximately 0.3 mL each, equipped with a transparent glass window. The basins were filled with saturated salt solutions (NaOH 8%, 43% K_2CO_3 , 74% NaCl, 88% $\text{Sr}(\text{NO}_3)_2$, 95% KNO_3) or organic solvents at 20 °C. After a minimum equilibration time of 30 mins, UV-Vis spectra were recorded in the closed chamber.^[1]

For lithographic patterning thin films were placed either with or without a mask for at least 16 h under a xenon lamp (Newport, 300 W, 120 mW cm^{-2}). For removal of the $\text{TBA}_x\text{H}_{1-x}\text{Ca}_2\text{Nb}_3\text{O}_{10}$ regions the illuminated films were immersed in water acetone (1:3 volume ratio) mixture for 15 min.

5.2.2 Additional data

Table S5.1. EDX analysis of the bulk compounds $\text{KCa}_2\text{Nb}_3\text{O}_{10}$ and $\text{HCa}_2\text{Nb}_3\text{O}_{10} \cdot 1.5 \text{H}_2\text{O}$ as well as the nanosheet pellet $\text{TBA}_x\text{H}_{1-x}\text{Ca}_2\text{Nb}_3\text{O}_{10}$. Standard deviations in brackets. For all compounds the experimental data is very close to the theoretical composition.

	K Atom%	Ca Atom%	Nb Atom%	O Atom%	Calc. Formula
Theo. values	6.3	12.5	18.8	62.5	$\text{KCa}_2\text{Nb}_3\text{O}_{10}$
Exp. values	6.2 (3)	12.0(5)	18.8(1.3)	63(2)	$\text{KCa}_{1.9}\text{Nb}_3\text{O}_{10.2}$
Theo. values		12.1	18.2	69.7	$\text{HCa}_2\text{Nb}_3\text{O}_{10} \cdot 1.5 \text{H}_2\text{O}$
Exp. values		11.8 (1.3)	18.3 (1.7)	70(3)	$\text{HCa}_2\text{Nb}_{3.1}\text{O}_{10} \cdot 1.8 \text{H}_2\text{O}$
Theo. values		13.3	20.0	66.7	$\text{TBA}_x\text{H}_{1-x}\text{Ca}_2\text{Nb}_3\text{O}_{10}$
Exp. values		13.3(1)	21.1(1)	65.53(12)	$\text{TBA}_x\text{H}_{1-x}\text{Ca}_2\text{Nb}_{3.2}\text{O}_{9.8}$

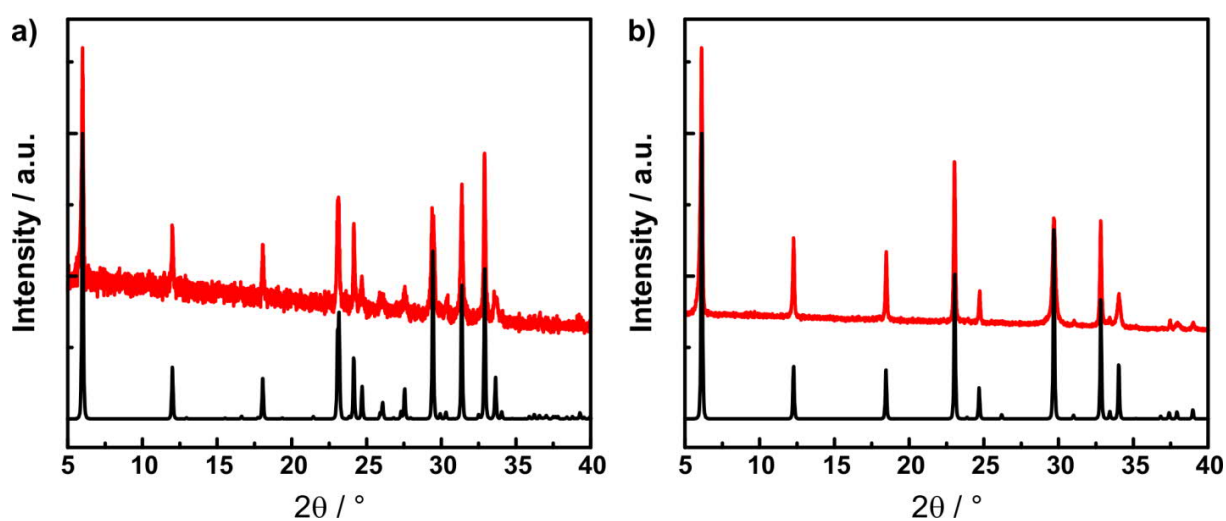


Figure S5.1. Experimental XRD patterns (in red) of $\text{KCa}_2\text{Nb}_3\text{O}_{10}$ (left) and $\text{HCa}_2\text{Nb}_3\text{O}_{10} \cdot 0.5 \text{H}_2\text{O}$ (right) and reference XRD patterns from the literature (in black). Both XRD patterns were recorded with $\text{Cu-K}\alpha_1$ radiation.

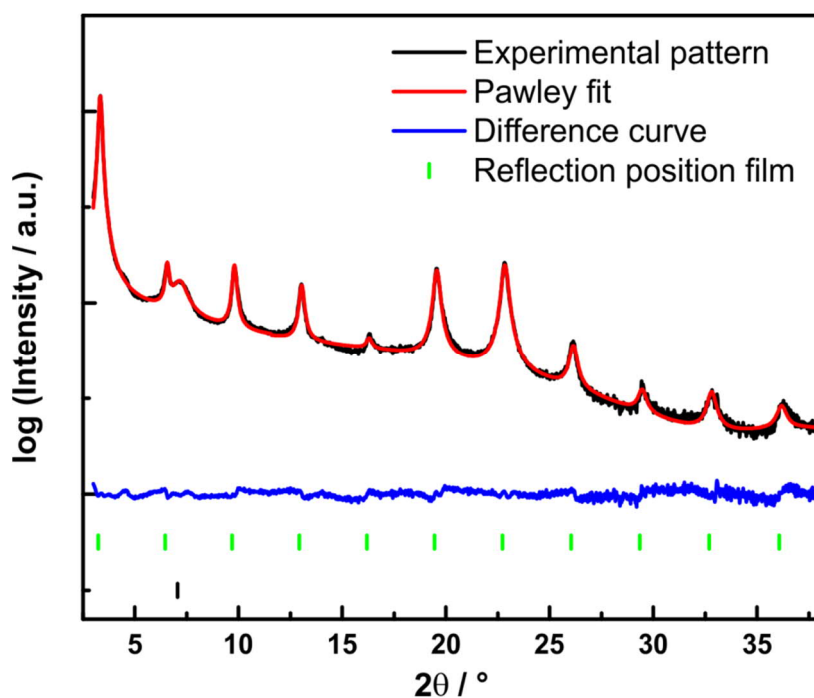


Figure S5.2. Pawley fit of the XRD out-of-plane pattern of the $\text{TBA}_x\text{H}_{1-x}\text{Ca}_2\text{Nb}_3\text{O}_{10}$ thin film displayed Figure 1c). The additional reflection marked with a black scatter at $7^\circ 2\theta$ stems from the sample chamber window material and was fitted as a single peak phase.

Table S5.2. Information on the Pawley fit of $\text{TBA}_x\text{H}_{1-x}\text{Ca}_2\text{Nb}_3\text{O}_{10}$ displayed in Figure S2.

Spacegroup	$P4/mbm$
$a = b / \text{\AA}^\#$	0.2
$c / \text{\AA}$	27.363(3)
R-exp / %*	1.45
R-p / %*	3.78
R-wp / %*	5.43
2θ range / °	3 - 38
Total parameters / thereof background including the single peak phase	25 / 9

Note as the diffraction pattern consists only of $00l$ reflections due to strongly preferred orientation of the nanosheets on the substrate, we used a very small a -axis to only obtain $00l$ reflection in the displayed 2θ range. The other option for fitting is to use the original cell parameters along with a strongly preferred sample orientation, which would only add additional parameters to the refinement.

*R-exp, R-p, R-wp as defined in TOPAS 4.2 (Bruker AXS).

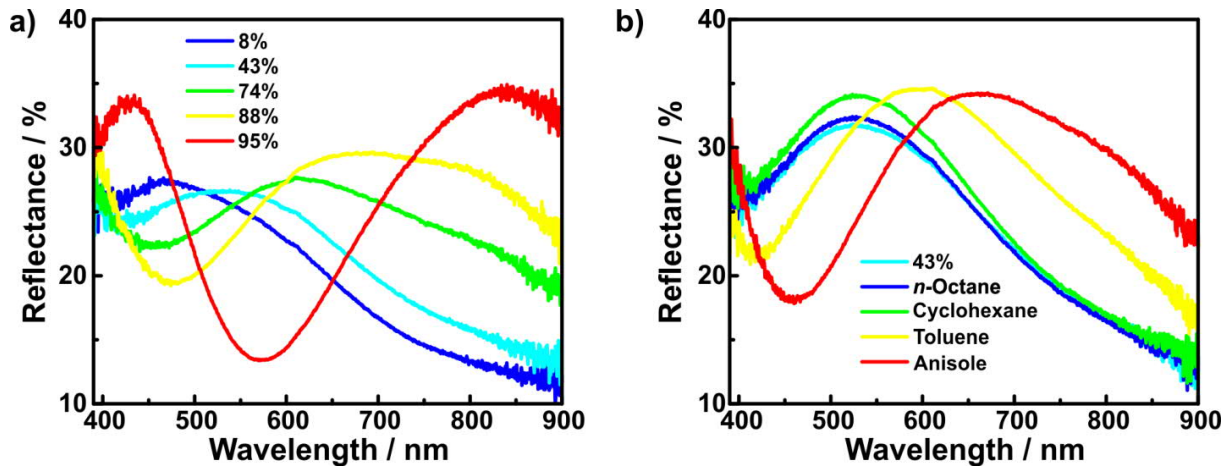


Figure S5.3. UV-Vis spectra of the $\text{TBA}_x\text{H}_{1-x}\text{Ca}_2\text{Nb}_3\text{O}_{10}$ thin films for a) exposure toward different RH levels and b) toward saturated vapors of organic solvents. For the normalized values and changes in color of the thin films see Figure 5.2.

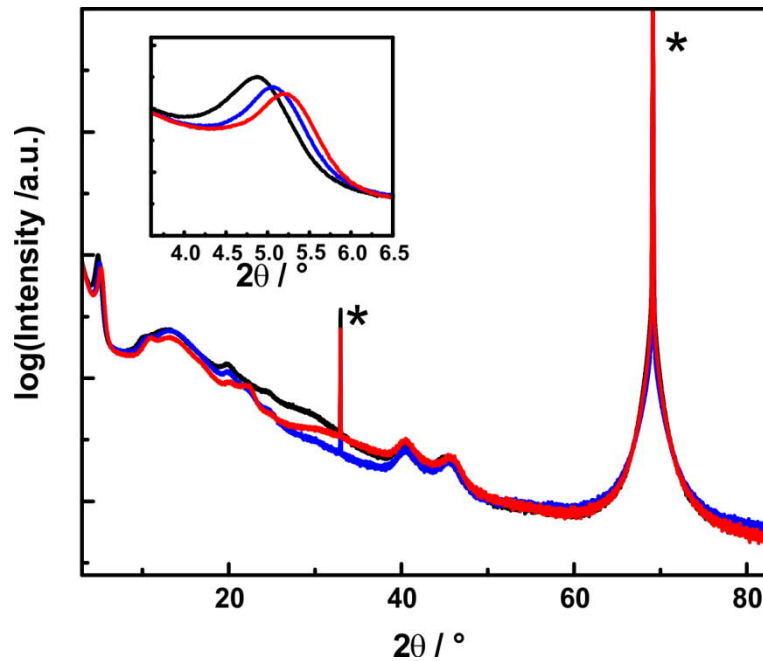


Figure S5.4. Thin film out-of-plane XRD pattern after 25 h (black), 52 h (blue) and 73 h (red) illumination time. The inset is a zoom of the range between 3.6° and 6.5° 2θ to illustrate the change over time more clearly (see also Figure 5.3c). The reflections marked with asterisks at 32.94° and 69.12° 2θ are due to the Si substrate and were used for pattern alignment. All XRD patterns were recorded with $\text{Cu-K}\alpha_1$ radiation.

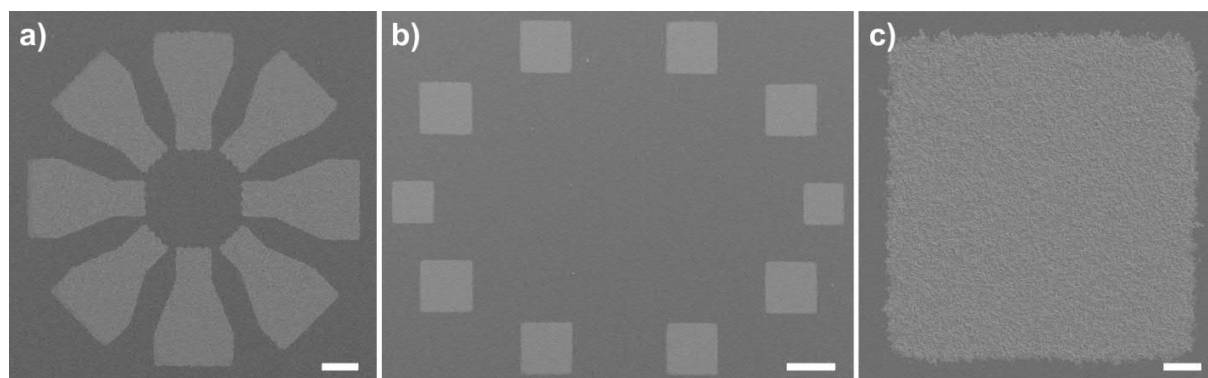


Figure S5.5. Additional SEM images of photolithographic patterns of $(\text{NH}_4)_x\text{H}_{1-x}\text{Ca}_2\text{Nb}_3\text{O}_{10}$ obtained through PNL. a) Magnification of Figure 5.4a) (main text), b) SEM image of a square pattern and c) magnification of a single square. Scale bar in a) 40 μm , b) 100 μm and c) 10 μm .

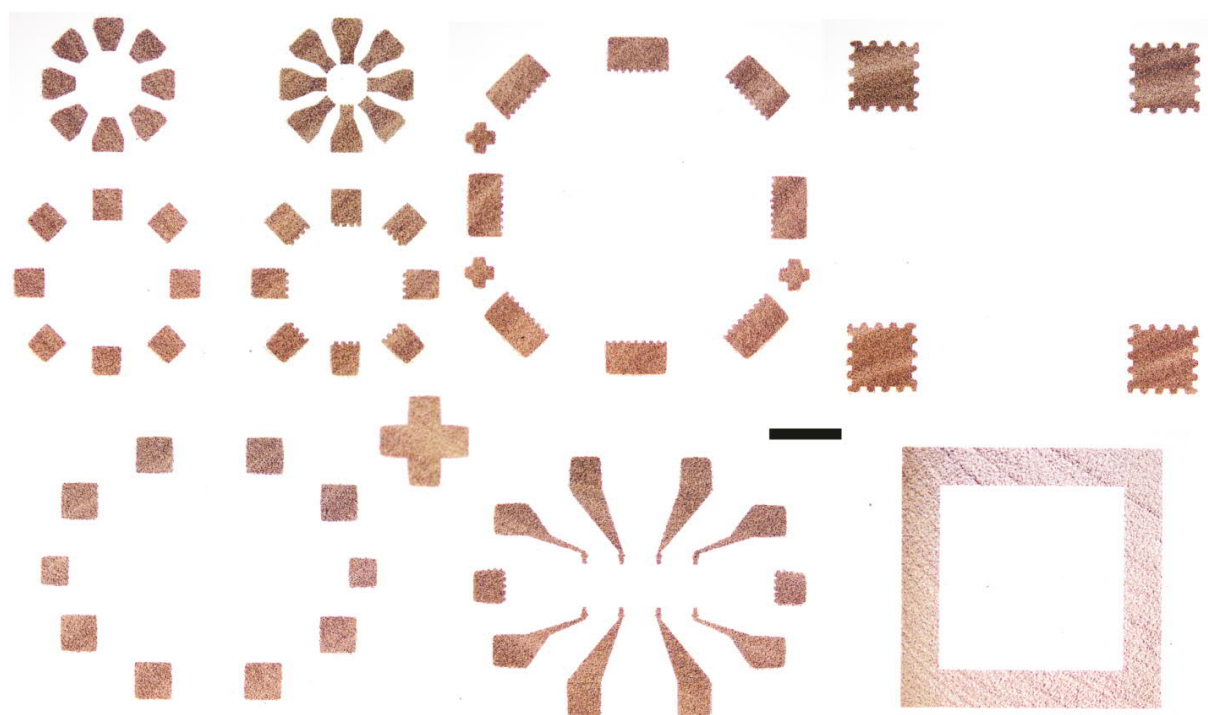


Figure S5.6. Optical microscope images of arbitrary structures obtained by PNL. The scale bar is 200 μm . Note that the large circle consisting of three crosses and several rectangles is equivalent to the mask shape, i.e. the mask also contained three crosses rather than four.

5.2.3 Bibliography

- [1] P. Ganter, L. M. Schoop, B. V. Lotsch, *Adv. Mater.* **2017**, *29*, 1604884.

6 Vapor-phase alkylamine intercalation: A smart, versatile and colorful way for sensor modification

6.1 Vapor-Phase Amine Intercalation for the Rational Design of Photonic Nanosheet Sensors

Pirmin Ganter, Leslie M. Schoop, Marie Däntl, and Bettina V. Lotsch

published: *Chem. Mater.* **2018**, *30*, 2557-2565.

DOI: 10.1021/acs.chemmater.7b04828

<https://pubs.acs.org/doi/10.1021/acs.chemmater.7b04828>

Reprinted with permission from P. Ganter, L. M. Schoop, M. Däntl, and B. V. Lotsch, *Chem.Mater.* **2018**, *30*, 2557-2565. Copyright © 2018 American Chemical Society.

Contribution of P.G.: *P.G. carried out all the experiments and wrote the major part of the manuscript. P.G. also carried out the literature screening and preparation of graphical material.*

Abstract

The development of vapor sensors with tunable sensitivity and selectivity is highly desirable because of the manifold applications ranging from air quality monitoring to food control. The design of such sensors remains, however, a great challenge. Here, we address this challenge by intercalating primary and tertiary alkylamines with varying alkyl chain lengths into $\text{H}_3\text{Sb}_3\text{P}_2\text{O}_{14}$ nanosheet-based Fabry-Pérot interference sensors. As the sensors are photonic in nature, the different amines can be distinguished based on their intercalation time and optical shift. Since the amines are protonated during intercalation and therefore trapped, this allows us to use amine modification as the basis for creating optical sensors. Intercalation of different amines gradually and widely tunes the sensor's sensitivity and selectivity to various analytes. This adjustment of sensing properties allows us to construct a sensor array on a single chip, which can distinguish different VOCs. The color change of this sensor array upon exposure to solvent vapors can be tracked with the naked eye, making this system a promising platform for the high-fidelity identification of volatile compounds. The sensor design protocol presented herein is straightforward and robust and can be transferred to other nanosheet-based devices for the rational tuning of their vapor-sensing properties and beyond.

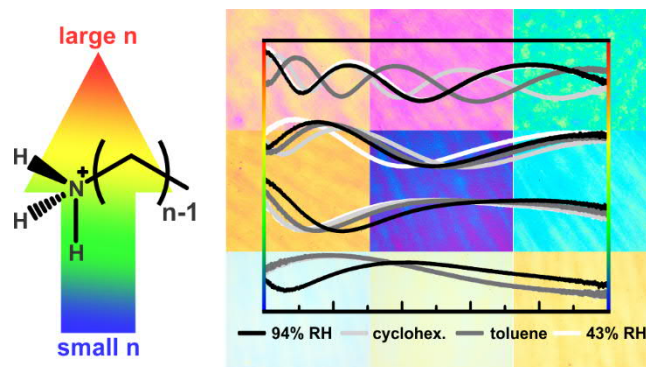


Table of Content: An approach toward rationally designed nanosheet-based Fabry-Pérot sensors by vapor-phase amine intercalation is presented. Amine intercalation into photonic nanostructures was used for the spatio-temporal monitoring of the intercalation process and to fabricate tunable photonic vapor sensors. Pairing the latter with spatially confined intercalation, an array sensor for the high-fidelity optical differentiation of various vapors is demonstrated.

6.1.1 Introduction

Fine-tuning of a vapor sensor's sensitivity and selectivity over a broad analyte range is a key challenge in fundamental science, and at the same time, of enormous commercial interest.^[1-14] To date, vapor sensors derived from layered materials have shown first promising performances, but their rational development is still in its infancy.^[5,12-18] Among the techniques that can be used to tune the properties of layered materials, ion exchange and intercalation have stood out as efficient, yet simple means of chemical modification of the host material.^[19-39] For example, thermal,^[19,20] magnetic,^[21] superconducting,^[22-24] optical,^[25] electrochemical,^[26,27] sensing,^[28-32] catalytic,^[33] and many other properties have previously been altered by intercalation methods. Additionally, intercalating ions into layered materials or exchange for bulky interlayer ions can also be used to delaminate layered systems into single layer nanosheets.^[40-42]

Apart from studying the fundamental properties of nanosheets, their assembly into novel functional architectures, and the modification of their properties by introducing intercalants into such 2D nanosheet-based structures, has triggered significant research interest.^[40,43-58] Toward this end, the real time, *in situ* monitoring of such intercalation processes is of particular interest.^[47,48,56,58] So far, little is known about the tunability of nanosheet-based vapor sensors by intercalation or ion exchange,^[6,59] despite promising studies on intercalated layered bulk oxide materials.^[28-31] Moreover, fundamental work emphasizes the pivotal role of intercalated cations for swelling and delamination.^[60,61] For instance, Sasaki and co-workers were able to show how intercalated ions affect the crystal stability of $\text{H}_{0.8}[\text{Ti}_{1.2}\text{Fe}_{0.8}]\text{O}_4 \cdot \text{H}_2\text{O}$ and demonstrated that intercalated short primary and tertiary amines can cause a 100-fold, reversible swelling of the material, ultimately leading to delamination of the layered material in water.^[60,61] Furthermore, Imai and co-workers used ion exchange methods with long-chained alkylamines to achieve exfoliation of different layered oxides in non-polar solvents.^[62,63]

With respect to ion exchange and intercalation effects on vapor sensing, we recently reported on the strong influence of the interlayer cation TBA on the sensing characteristics of nanosheet-based Fabry-Pérot sensors.^[6,59] We were able to show that their sensitivity, selectivity and response time is significantly improved by the presence of TBA, suggesting that the interlayer cation dominates the sensing response.^[6,59] However, this approach has certain limitations, for example, little sensitivity and selectivity toward non-polar analytes due to the restricted number of ammonium and phosphonium ions that can be introduced by ion exchange.^[6,59] Nevertheless, modification of the active sensing material by ion exchange and intercalation is complementary to other approaches aiming to tune the sensitivity and selectivity of electrical, electrochemical and photonic sensors based on 2D materials and photonic vapor sensors in general,^[2-5,64-70] these mainly focus on the introduction of completely new materials^[65,66] or on the covalent modification of known ones,^[2-5] their decoration with metal NPs,^[67-69] or the design of complex hierarchical structures.^[9,70] Although the *de novo* synthesis of stimuli-responsive materials suffers from multiple optimization steps, the others strategies are limited by complex fabrication procedures or low levels of tunability or both. In contrast, covalently modified photonic vapor sensors typically exhibit tunable selectivity but show limited sensitivity since they operate based on RI changes,^[2-4] rendering additional statistical readout methods, such as PCA, necessary for the differentiation of vapors.^[2,4] Because at their current development state all of the above methods have certain shortcomings, it is highly desirable to develop generic techniques that allow for the straightforward adjustment and modification of a sensor's selectivity and sensitivity while allowing for easy scale-up.

In this work, we show that many primary and tertiary alkylamines as well as aminoalcohols can be intercalated into $\text{H}_3\text{Sb}_3\text{P}_2\text{O}_{14}$ photonic thin films swiftly *via* the vapor-phase. Each amine leads to distinct optical shifts and intercalation times, thus providing a color-coded fingerprint characteristic of each chemical modification of the photonic thin film. A convenient feature of our photonic device is therefore the possibility to optically track the intercalation process in real time and locally resolved through changes in the interference color occurring upon intercalation. Since the amines are trapped as ammonium ions in the interlayer space, the amine-modified photonic films are robust and reusable, which are important ingredients for their use as sensors. By varying the alkyl chain length or adding functional groups, we demonstrate that we can rationally tailor the sensor's selectivity and sensitivity toward various analytes. Finally, by combining vapor-phase intercalation with the amine-specific local modification of the sensing properties, we create a single-chip array sensor, which because of its high selectivity and sensitivity allows for both naked eye readout of analyte detection and readout with a commercial webcam.

6.1.2 Results and discussion

An overview of the experimental procedures is displayed in Scheme S6.1 (Supporting Information) and Figure 6.1. $\text{H}_3\text{Sb}_3\text{P}_2\text{O}_{14}$ nanosheets were prepared and spin-coated to form Fabry-Pérot thin films as described previously (Scheme S6.1).^[6,15] Building on our results on the strong influence of the interlayer cation TBA on the sensing characteristics^[6,59] and inspired by the feasibility of intercalating various amines into layered bulk materials,^[71-75] we decided to intercalate primary and tertiary alkylamines into photonic $\text{H}_3\text{Sb}_3\text{P}_2\text{O}_{14}$ nanosheet-based thin films to study their sensing characteristics (Figure 6.1). As evident from Figure 6.1, the vapor-phase amine intercalation into $\text{H}_3\text{Sb}_3\text{P}_2\text{O}_{14}$ thin films is a *post-film* fabrication modification approach which is efficient and at the same time allows for additional sensor design capabilities. It also increases the possibilities for applications compared to our previous approach relying on solution-based ion exchange methods which were applied before film fabrication.^[6,59]

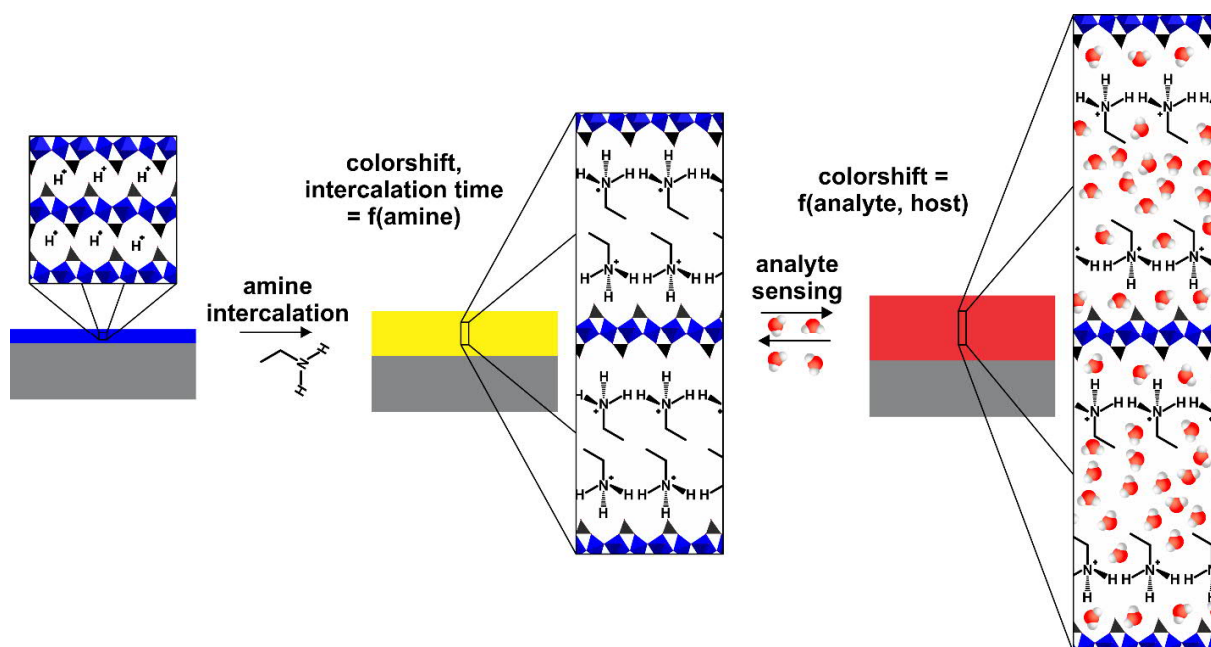


Figure 6.1. Schematic overview of the amine intercalation process and optical sensing. The amine intercalation process into photonic thin films occurs *via* an acid-base reaction, which causes a change in the film thickness and, hence, structural color. Note that the last image on the right shows a simplified picture of the interlayer gallery upon analyte intercalation.

During the vapor phase intercalation process of primary and tertiary alkylamines into the solid acid, that is, the proton-bearing nanosheets, an acid-base reaction occurs where the alkylamines are protonated to form ammonium ions and are therefore trapped in the interlayer space.^[61,73,74]



The intercalation is accompanied by an increase of the interlayer distance,^[29,74] which in turn results in an increase in the overall film thickness. According to Equation 6.1, this should result in a change of the structural color according to the interference condition under perpendicular illumination:^[6]

$$m\lambda = 2n_{eff}l = 2n_{eff}cg \quad (\text{Equation 6.1})$$

Here, m is the spectral order, λ the wavelengths that allow for constructive interference, n_{eff} the effective RI, and l the film thickness, which is given by the stacking distance c times the number of nanosheet layers g .

As expected, upon amine intercalation we clearly observe distinct color changes in the photonic films (Figure 6.2a). XRD shows a linear shift of the $00l$ stacking reflection and thus the interlayer distance with increasing chain length of the primary alkyl amines (Figure 6.2b, Figure S6.1). Similarly, the normalized first order interference band in the UV-Vis spectra shifts linearly with alkyl chain length between ethylamine and tetradecylamine (Figure 6.2c, Figure S6.2). Note that, for the photonic thin films displayed in Figure 6.2a, the color is determined only by the first order band for short alkyl chains (up to $n=4$), whereas for longer chain lengths, the colors are determined by interference of higher order bands. The range of color modulation shown here is among the widest reported so far for a photonic material.^[76,77]

From the slope of the stacking distance versus alkyl chain length relation, we can extract the increase in the interlayer distance per carbon atom. For the primary alkylamines, we find an increase in layer distance of $2.03 \pm 0.02 \text{ \AA}$ per carbon atom. This is similar to other reported values for layered bulk materials intercalated with primary alkylamines, which are in the range of 1.9-2.3 \AA per carbon atom and are assigned to a tilted bilayer arrangement of the amines in the interlayer space.^[74] Therefore, by comparison to literature values, we can deduce that bilayers of amines are present in the interlayer space. This is also supported by the elemental analysis results (see Table S6.1), which indicate a value of three primary amines per $\text{H}_3\text{Sb}_3\text{P}_2\text{O}_{14}$ formula unit. The area of at least 55.8 \AA^2 covered by three primary amines^[74] is thereby too large to match the area of 44.2 \AA^2 provided by the $\text{H}_3\text{Sb}_3\text{P}_2\text{O}_{14}$ formula unit if a monolayer arrangement is assumed and, hence, bilayers are formed. Moreover, we can calculate the tilting angle of the primary amines in the interlayer space, which is 53.1° (for calculation of the tilting angle see Figure S6.3).^[74] Amine intercalation is thus a straightforward and easy method to modify nanosheet-based photonic thin films and to distinguish between different primary alkylamines.

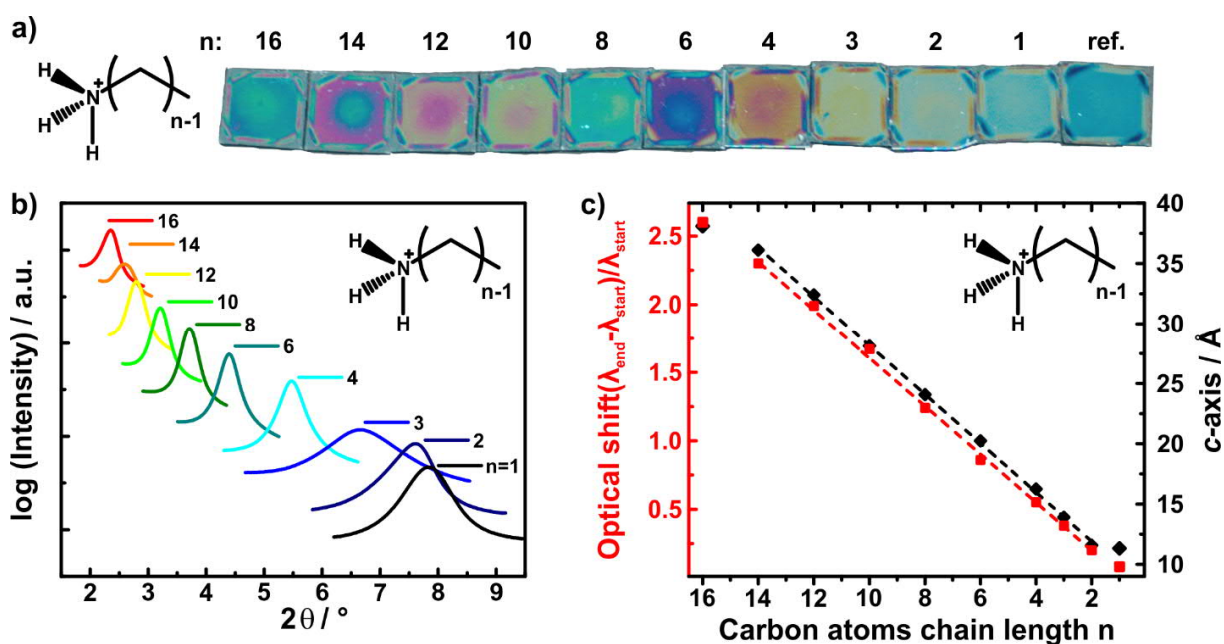


Figure 6.2. Characterization of $H_{3-x}(NH_3(CH_2)_{n-1}CH_3)_xSb_3P_2O_{14}$ thin films. a) Optical image of spin-coated, primary alkylamine-intercalated Fabry-Pérot thin films (UV-Vis spectra before and after intercalation are shown in Figure S6.2). Note that the circular color gradient visible in several films is due to the gradient in film thickness resulting from the spin-coating process, which translates into the amine-intercalated system. b) 001 reflection of the out-of-plane XRD patterns. For complete XRD patterns see Figure S6.1. c) Correlation plot of the stacking distance and the normalized optical shift which is extracted from the UV-Vis spectra versus the number of carbon atoms in the alkyl chain.

The technical relevance of differentiating and identifying amine vapors,^[78,79] along with the peculiar swelling behavior of (tertiary) dimethylalkylamines^[61] prompted us to study the intercalation behavior of these amines and to compare them to that of the primary amines. We again observe a linear trend in the optical shift, as well as the 001 reflection, with increasing alkyl chain lengths (Figure S6.4, S6.5 and S6.6). Thus, dimethylalkylamines, just as alkylamines, can also be distinguished based on their optical shift. In this case, we obtain an increase of $1.05 \pm 0.03 \text{ \AA}$ per carbon atom, which points to a monolayer arrangement with a tilting angle of 55.8° . The monolayer arrangement is also supported by the results of the elemental analysis (Table S6.1). Two tertiary amines are found per formula unit $H_3Sb_3P_2O_{14}$. As the area provided by a $H_3Sb_3P_2O_{14}$ formula unit is sufficient to accommodate two tertiary amines, monolayer formation seems likely. The different arrangement of the tertiary amines compared to the primary amines could stem from altered interactions between the amine groups and the P-O groups of the nanosheets since the two additional methyl groups weaken the hydrogen bonds and favor interactions between the alkyl chains.

However, since the optical shifts and stacking distances are rather similar for the tertiary and primary amines with $n = 4$, it is practical to identify another parameter to clearly differentiate between all primary and tertiary amines. Since the color of the film changes upon intercalation, this allows us to monitor the intercalation process in real time by tracking the color change over time (Video S6.1). Thus, as displayed in Figure 6.3a) and b), *n*-butylamine (BA) and *N,N*-dimethylbutylamine (DMBA)

can be clearly distinguished based on the time needed for the intercalation process of the respective amines to be completed.

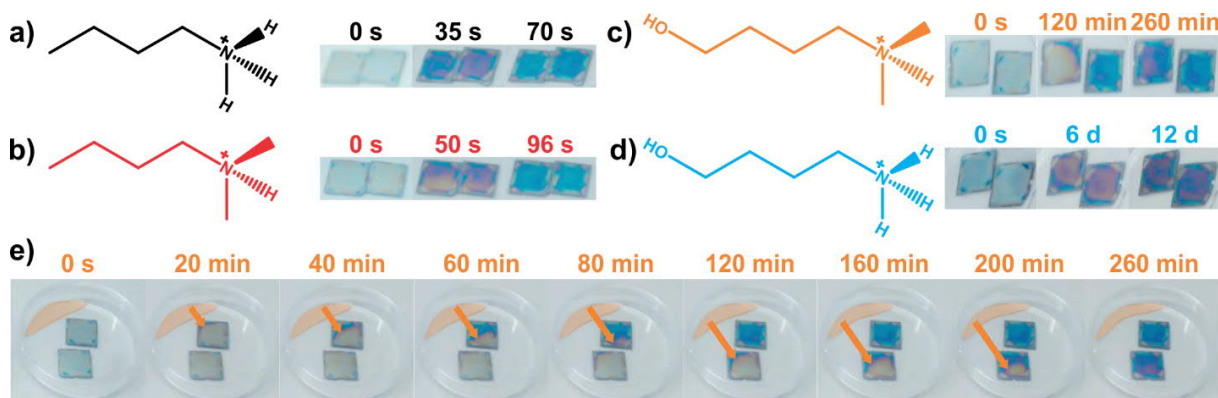


Figure 6.3. Time resolved amine intercalation into photonic thin films. Intercalation of a) *n*-butylamine, b) *N,N*-dimethylbutylamine, c) 4-(dimethylamino)-1-butanol, and d) 4-amino-1-butanol into two thin films per amine to visualize the spatial extent of amine intercalation (see Video S6.1, Figure S6.7). Ammonium cations are sketched on the left because the amines get protonated in the interlayer space. e) Detailed time-resolved intercalation of 4-(dimethylamino)-1-butanol illustrating the spatially resolved progression of the structural color change. The area of the evaporating aqueous amine solution is highlighted in light orange and the propagation of the amine intercalation front with orange arrows.

To demonstrate the scope of amine vapor differentiation, we additionally intercalated 4-amino-1-butanol (BAOH) as well as 4-(dimethylamino)-1-butanol (DMBAOH) and recorded the optical changes (Figure 6.3c, d). For these hydroxyl-group bearing compounds, we found considerably longer intercalation times, which are on the order of several hours (DMBAOH) or even days (BAOH). The boiling points of the different intercalants, which can be viewed as an approximation of the vapor pressure, correlate with the increasing intercalation times (see Table S6.2). This does not only demonstrate that a large range of chemically different amines carrying functional groups can be intercalated but also that it is possible to differentiate such amines based on their optical shift and the time scale of the intercalation process, which can be followed optically.

Analyzing the intercalation process displayed in Figure 6.3, Figure S6.7, and Video S6.1 in more detail, some further observations can be made: We can localize the exact area where the amines are vaporizing (Figure 6.3e, Video S6.1), as the intercalation commences in the area of the thin film facing toward the spot where the liquid amines were deposited. Because of this locally resolved, large response of the film to the amine vapor, nanosheet thin film devices can potentially be used to quickly and reliably find leaks of amine-containing gases. On a more fundamental level, tracking amine intercalation optically with high spatial resolution is the first step to the direct macroscopic visualization of intercalation processes occurring at the atomic level.

Having developed an easy method for the differentiation of various amines based on the irreversible intercalation into photonic thin films, we can now proceed to use these permanent modifications for the development of functional, that is, chemically selective sensors. Using different amines, we are

able to modify the host (intercalated $\text{H}_3\text{Sb}_3\text{P}_2\text{O}_{14}$) - guest (analytes) interactions and to tune the selectivity, defined as the discrimination capability of the sensor toward analytes.^[67,80,81] To demonstrate the gradual tunability of the photonic nanosheet sensors, we analyzed the effect of the increasing alkyl chain length ($n = 1 - 16$) of intercalated primary alkylamines on the reversible sensing response toward vapors of 94% RH, saturated toluene and saturated cyclohexane (Figure 6.4a, Figure S6.8-6.10, Video S6.2-6.4). For hosts intercalated with short alkylamine chain lengths, we observe a strong response toward saturated polar vapors, and a weak response toward saturated non-polar and moderately polar vapors, as would be expected. With increasing alkyl chain lengths, especially for $n \geq 4$, this property gradually reverses and stronger responses toward non-polar and moderately polar vapors are observed. This can be easily explained by the effect of the increasing alkyl chain lengths, rendering the interlayer space more hydrophobic and, therefore, gradually enhancing the selectivity toward more non-polar analytes. This is also in agreement with observations made for the exfoliation of amine-intercalated bulk materials, where intercalated short-chained amines can lead to exfoliation in water, whereas long-chained amines can lead to exfoliation in moderately polar solvents.^[61-63] To further illustrate the potential of amine-intercalated nanosheet sensors, we additionally exposed the dodecylamine- and hexadecylamine-intercalated thin films toward ethanol, anisole, and *n*-octane vapor (Figure S6.11), as well as the hexadecylamine-intercalated sample toward mixtures of anisole and toluene vapor (Figure S6.12). All of the pure solvent vapors as well as anisole and toluene mixtures can be clearly distinguished. Remarkably, the optical shift is nearly linear for the mixture series of anisole and toluene. To verify the fast response (defined as the time to reach 90% of the signal change)^[82] and recovery times, and also the cyclability, we recorded time-dependent UV-Vis spectra for representative samples intercalated with ethylamine and decylamine (Figure S6.10, Video S6.2-S6.4). We observe subsecond response and recovery times toward saturated vapor streams of cyclohexane (response time: 840 ms, recovery time: 510 ms), toluene (response time, 510 ms; recovery time, 720 ms) for the decylamine-intercalated sample and water (response time, 600 ms; recovery time, 930 ms) for the ethylamine-intercalated sample (see Figure S6.10, Video S6.2-6.4). These response and recovery times are faster compared to most other nanosheet-based or other photonic sensors, which exhibit response times on the order of several seconds.^[2,4,12-14]

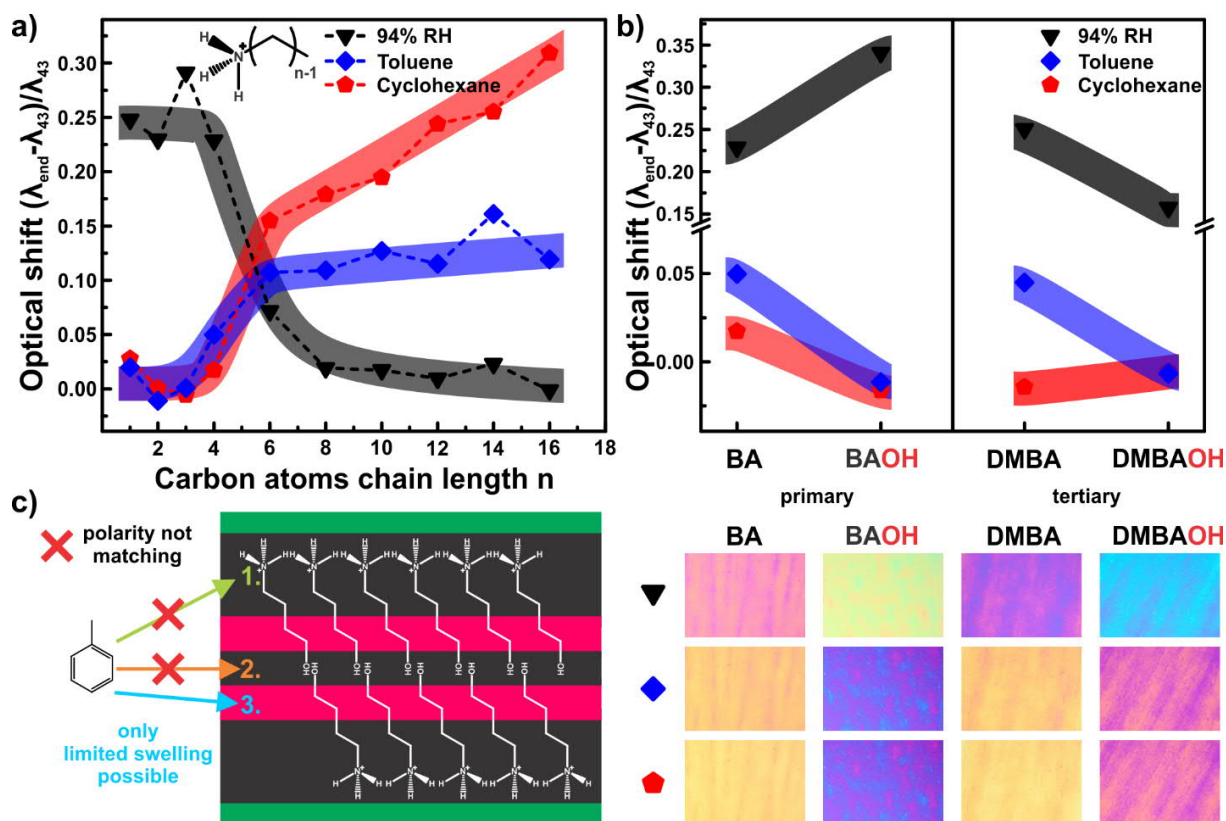


Figure 6.4. Gradual tuning of the properties of photonic nanosheet sensors. Influence of the alkyl chain length as well as the hydroxy functional group on the sensitivity and selectivity of photonic nanosheet sensors toward vapors of varying polarity. a) Influence of the alkyl chain length of primary alkylamines, displayed in terms of the normalized optical shift, which is expressed here by $(\lambda_{\text{end}} - \lambda_{43}) / \lambda_{43}$ with λ_{end} and λ_{43} being the first order band maximum position of the saturated vapor atmosphere and that of 43% RH, respectively, toward polar (94% RH), moderately polar (saturated toluene), and non-polar vapor (saturated cyclohexane). b) Impact of the introduction of an OH functional group on *n*-butylamine and *N,N*-dimethylbutylamine toward the same vapors as in a). The bottom part in b) displays optical images of the thin film surface capturing the color change under exposure to the different vapors. c) Possible mechanism for toluene vapor intercalation, assuming an intercalated bimolecular amine layer for rationalizing the differences caused by introducing a hydroxyl functional group on the amines. The polar region is drawn in black, the non-polar region in red, and the $\text{Sb}_3\text{P}_2\text{O}_{14}^{3-}$ layers in green. The labels 1-3 are further explained in the text.

To demonstrate the long-term stability of the intercalation modification, we recorded videos of the responses of ethylamine-, butylamine-, and decylamine-intercalated sensors toward different vapors, including H_2O , toluene, and cyclohexane, after storing the sensors in ambient air for 10 months (see Video S6.5-S6.7). Notably, the responses are still fast enough to track lateral movement of the vapor streams in real time without any delay. In addition, the response and selectivity shown in the videos (Videos S6.5-S6.7) closely resemble the data shown in Figure 6.4a: Ethylamine- and butylamine-modified thin films show a pronounced response toward H_2O vapor and no response toward toluene and cyclohexane, whereas the decylamine-modified films exhibit a large response toward cyclohexane and a medium one to toluene, but no response toward humidity.

To demonstrate the additional degrees of freedom in tailoring the vapor response, we analyzed the sensing response of BA-, BAOH-, DMBA- and DMBAOH-modified nanosheets toward vapors of

varying polarity (Figure 6.4b, Figure S6.13). We observe that the introduction of a hydroxyl group has a pronounced effect on the selectivity of the sensing response, for primary and tertiary amines alike. While without the functional group, responses toward moderately polar vapors such as toluene are observable for BA and DMBA (See Figure 6.4b), introducing a hydroxyl group almost entirely suppresses the sensing response toward toluene vapor. Figure 6.4c shows a plausible mechanism for the interaction of toluene vapor with an alkanolamine-modified film, assuming a bimolecular amine layer in the interlayer space. When entering the interlayer space, the analyte encounters three regions for interaction with the host lattice: 1) The region close to the ammonium group and the inorganic layers, which is hydrophilic; 2) the central part close to the functional hydroxyl groups facing each other, which is hydrophilic as well, and 3) the area in which the alkyl chains interact, which is hydrophobic. Since 1) and 2) are polar regions while toluene is only moderately polar, it is rather unlikely that intercalation will take place in these regions. Therefore, only area 3) remains as valid option. However, the presence of this region depends on the alkyl chain length and is essentially absent in short-chain amines. For amines with sufficiently large chain lengths, however, the sensor is not able to swell along the *c*-axis as the hydrophilic areas are fixed by hydrogen bonding along the stacking distance. Thus, in addition to the alkyl chain length as tunable parameter, the deliberate introduction of a functionalized amine can be used to tailor the properties of photonic thin film sensors.

Using the concepts outlined above, we proceeded to design an array sensor that responds differently to various solvent vapors. To keep the setup as simple as possible, we intercalated different amines into a single nanosheet thin film by using a mask (see Scheme S6.2). This is a significant advance compared to other approaches^{6,59} since this approach allows us to locally tune the chemical properties in single thin films, and therefore array design and nanostructuring becomes possible.

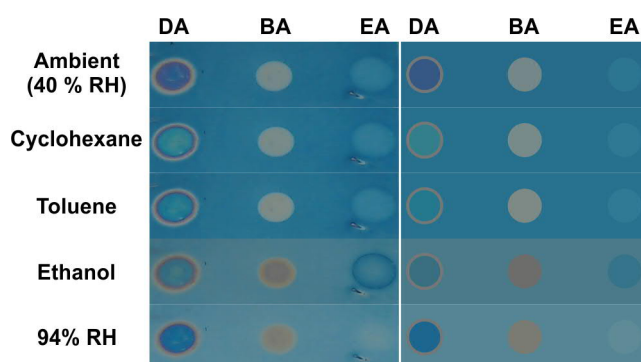


Figure 6.5. Response of the array sensor fabricated by local amine modification of $\text{H}_3\text{Sb}_3\text{P}_2\text{O}_{14}$ nanosheets toward saturated organic vapors as well as humidity. The sensor array consists of decylamine (DA), butylamine (BA) and ethylamine (EA) intercalated into $\text{H}_3\text{Sb}_3\text{P}_2\text{O}_{14}$ and the pristine $\text{H}_3\text{Sb}_3\text{P}_2\text{O}_{14}$ as background. On the left the actual sensing response is displayed, whereas on the right the corresponding averaged RGB images for each analyte are displayed. Once obtained, the averaged RGB images can be utilized for analyte identification similar to the color coded legend of a pH-indicator paper for pH identification.

As can be seen in Figure 6.5, we were able to intercalate three different primary alkylamines, each at different locations, into a $\text{H}_3\text{Sb}_3\text{P}_2\text{O}_{14}$ thin film on a Si substrate. The choice of the three alkylamines is based on their chemical properties, using ethylamine (EA) as a short-chained hydrophilic intercalant, butylamine (BA) as an intermediate intercalant, and decylamine (DA) as long-chained hydrophobic intercalant. Exposing the array sensor toward different solvent vapors results in clear, distinct, and reversible color changes and in a characteristic color pattern for each vapor (Figure 6.5). More generally, each vapor analyte can clearly be grouped into either hydrophilic or non-hydrophilic analytes as judged by the response of the pristine or butylamine-intercalated spots. Because of the selection of amines with a large enough sensitivity, our sensor array can be readout with the naked eye or with a cheap, commercial webcam, circumventing further data processing such as PCA. This is a significant improvement with respect to other photonic vapor sensors.^[2,4] Taking the characteristic color pattern and the naked eye readout into account, the sensor array can be viewed as test strip for detecting solvents vapors. This utility might be applied for example in laboratories to identify unlabeled solvents.

In contrast to previous approaches based on 2D materials,^[6,12-14,16,67-69] we are now able to rationally design sensors that can be tuned to maximize the response to a certain solvent vapor. Therefore, our approach to locally modify the sensing response of the photonic nanosheets based on amine intercalation provides a viable alternative to other optical sensors that for example are based on metalloporphyrins or other chemical sensors with an optical readout.^[1,10,78]

6.1.3 Conclusion

In summary, we showed that amines can be intercalated into photonic thin films consisting of $\text{H}_3\text{Sb}_3\text{P}_2\text{O}_{14}$ nanosheets *via* the gas phase. Because of the photonic nature of the thin films, the intercalation process can be tracked in real time by monitoring the color changes, and different amines

can be distinguished based on the dual readout of optical shift and intercalation time. The locally resolved, color-coded amine intercalation observed through thin film interference presents a new route toward studying microscopic diffusion processes by a straightforward optical readout, which ultimately may be used to visually address questions concerning the interaction and intercalation mechanisms of analytes in nanostructures. In addition, the thin film devices can be used to spot sources of amine vapors, which may be a convenient tool, for example, for finding leakages of amines in amine-treating processes for contaminant removal.

Putting the chemical modifications introduced by the amine vapors to use, the amine-modified thin films can also be applied as extremely fast solvent vapor sensors with a large dynamic range. Since many different amines can be intercalated, it is possible to gradually fine-tune the sensor's sensitivity and selectivity. Combining the advantage of vapor-phase intercalation with the option to choose from various amines with gradually different properties, we constructed an easy-to-implement, low-cost array sensor that shows a high-fidelity visual color readout for analytes of different polarity. Since the color response can be read out with the bare eye, it can thus be used as a test strip for easy identification of VOCs. Since the same and similar amines can be intercalated into various other layered materials,^[73] the concept developed herein is sufficiently generic to be transferred to other nanosheet-based systems. Amine intercalation in nanosheet-based systems can further be utilized as a tool to tune and diversify the chemical properties of other thin film systems beyond sensing, including porous thin films for catalysis or molecular sieve adsorbents, where amine intercalation is a crucial step for synthesizing such materials.^[32,33,72,83,84]

6.1.4 Acknowledgement

Financial support was granted by the Max Planck Society, the University of Munich (LMU), the Center for NanoScience (CeNS), and the Deutsche Forschungsgemeinschaft (DFG) through the Cluster of Excellence Nanosystems Initiative Munich (NIM). L.M.S. acknowledges financial support by the Minerva fast track fellowship. The authors thank Christine Stefani for thin film XRD measurements, Marie-Luise Schreiber for elemental analysis and Willi Hölle for the support with the home-built measurement chamber.

6.1.5 Bibliography

- [1] N. A. Rakow, K. S. Suslick, *Nature* **2000**, *406*, 710-713.
- [2] L. D. Bonifacio, D. P. Puzzo, S. Breslav, B. M. Willey, A. McGeer, G. A. Ozin, *Adv. Mater.* **2010**, *22*, 1351-1354.
- [3] L. D. Bonifacio, G. A. Ozin, A. C. Arsenault, *Small* **2011**, *7*, 3153-3157.
- [4] Z. Xie, K. Cao, Y. Zhao, L. Bai, H. Gu, H. Xu, Z.-Z. Gu, *Adv. Mater.* **2014**, *26*, 2413-2418.
- [5] J.-S. Kim, H.-W. Yoo, H. O. Choi, H.-T. Jung, *Nano Lett.* **2014**, *14*, 5941-5947.
- [6] P. Ganter, L. M. Schoop, B. V. Lotsch, *Adv. Mater.* **2017**, *29*, 1604884.
- [7] M. Tu, S. Wannapaiboon, K. Khaletskaya, R. A. Fischer, *Adv. Funct. Mater.* **2015**, *25*, 4470-4479.
- [8] R. A. Potyrailo, *Angew. Chem., Int. Ed.* **2006**, *45*, 702-723.

- [9] R. A. Potyrailo, R. K. Bonam, J. G. Hartley, T. A. Starkey, P. Vukusic, M. Vasudev, T. Bunning, R. R. Naik, Z. Tang, M. A. Palacios, M. Larsen, L. A. Le Tarte, J. C. Grande, S. Zhong, T. Deng, *Nat. Commun.* **2015**, *6*, 7959.
- [10] J. R. Askim, M. Mahmoudi, K. S. Suslick, *Chem. Soc. Rev.* **2013**, *42*, 8649-8682.
- [11] J. H. Lee, B. Fan, T. D. Samdin, D. A. Monteiro, M. S. Desai, O. Scheideler, H.-E. Jin, S. Kim, S.-W. Lee, *ACS Nano* **2017**, *11*, 3632-3641.
- [12] X. Liu, T. Ma, N. Pinna, J. Zhang, *Adv. Funct. Mater.* **2017**, *27*, 1702168.
- [13] W. Yang, L. Gan, H. Li, T. Zhai, *Inorg. Chem. Front.* **2016**, *3*, 433-451.
- [14] S. Yang, C. Jiang, S.-h. Wei, *Appl. Phys. Rev.* **2017**, *4*, 021304.
- [15] K. Szendrei, P. Ganter, O. Sánchez-Sobrado, R. Eger, A. Kuhn, B. V. Lotsch, *Adv. Mater.* **2015**, *27*, 6341-6348.
- [16] P. Ganter, K. Szendrei, B. V. Lotsch, *Adv. Mater.* **2016**, *28*, 7436-7442.
- [17] S.-Y. Cho, S. J. Kim, Y. Lee, J.-S. Kim, W.-B. Jung, H.-W. Yoo, J. Kim, H.-T. Jung, *ACS Nano* **2015**, *9*, 9314-9321.
- [18] S. Borini, R. White, D. Wei, M. Astley, S. Haque, E. Spigone, N. Harris, J. Kivioja, T. Ryhänen, *ACS Nano* **2013**, *7*, 11166-11173.
- [19] C. Wan, X. Gu, F. Dang, T. Itoh, Y. Wang, H. Sasaki, M. Kondo, K. Koga, K. Yabuki, G. J. Snyder, R. Yang, K. Koumoto, *Nat. Mater.* **2015**, *14*, 622-627.
- [20] G. Zhu, J. Liu, Q. Zheng, R. Zhang, D. Li, D. Banerjee, D. G. Cahill, *Nat. Commun.* **2016**, *7*, 13211.
- [21] J. Wontcheu, W. Bensch, M. Wilkening, P. Heitjans, S. Indris, P. Sideris, C. P. Grey, S. Mankovsky, H. Ebert, *J. Am. Chem. Soc.* **2008**, *130*, 288-299.
- [22] R. Zhang, J. Waters, A. K. Geim, I. V. Grigorieva, *Nat. Commun.* **2017**, *8*, 15036.
- [23] M. Burrard-Lucas, D. G. Free, S. J. Sedlmaier, J. D. Wright, S. J. Cassidy, Y. Hara, A. J. Corkett, T. Lancaster, P. J. Baker, S. J. Blundell, S. J. Clarke, *Nat. Mater.* **2013**, *12*, 15-19.
- [24] M. S. Dresselhaus, *MRS Bull.* **1987**, *12*, 24-28.
- [25] J. A. Wilson, A. D. Yoffe, *Adv. Phys.* **1969**, *18*, 193-335.
- [26] J. Luo, W. Zhang, H. Yuan, C. Jin, L. Zhang, H. Huang, C. Liang, Y. Xia, J. Zhang, Y. Gan, X. Tao, *ACS Nano* **2017**, *11*, 2459-2469.
- [27] M. Ghidui, S. Kota, J. Halim, A. W. Sherwood, N. Nedfors, J. Rosen, V. N. Mochalin, M. W. Barsoum, *Chem. Mater.* **2017**, *29*, 1099-1106.
- [28] A. Weiss, E. Michel, A. Weiss, *Angew. Chem.* **1961**, *73*, 707-707.
- [29] A. Weiss, *Angew. Chem., Int. Ed.* **1963**, *2*, 134-144.
- [30] Y. Yan, T. Bein, *Chem. Mater.* **1993**, *5*, 905-907.
- [31] G. Alberti, M. Casciola, U. Costantino, R. Vivani, *Adv. Mater.* **1996**, *8*, 291-303.
- [32] T. E. Mallouk, J. A. Gavin, *Acc. Chem. Res.* **1998**, *31*, 209-217.
- [33] T. J. Pinnavaia, *Science* **1983**, *220*, 365-371.
- [34] R. Schöllhorn, *Chem. Mater.* **1996**, *8*, 1747-1757.
- [35] J. P. Motter, K. J. Koski, Y. Cui, *Chem. Mater.* **2014**, *26*, 2313-2317.
- [36] K. P. Chen, F. R. Chung, M. Wang, K. J. Koski, *J. Am. Chem. Soc.* **2015**, *137*, 5431-5437.
- [37] J. S. Kang, M. Ke, Y. Hu, *Nano Lett.* **2017**, *17*, 1431-1438.
- [38] Y. Wang, E. Delahaye, C. Leuvrey, F. Leroux, P. Rabu, G. Rogez, *Inorg. Chem.* **2016**, *55*, 4039-4046.
- [39] M. S. Dresselhaus, *Intercalation in Layered Materials* Plenum Press, New York, **1986**.
- [40] R. Ma, T. Sasaki, *Adv. Mater.* **2010**, *22*, 5082-5104.
- [41] V. Nicolosi, M. Chhowalla, M. G. Kanatzidis, M. S. Strano, J. N. Coleman, *Science* **2013**, *340*, 1226419.
- [42] S. Jeong, D. Yoo, M. Ahn, P. Miró, T. Heine, J. Cheon, *Nat. Commun.* **2015**, *6*, 5763.
- [43] J. Wan, S. D. Lacey, J. Dai, W. Bao, M. S. Fuhrer, L. Hu, *Chem. Soc. Rev.* **2016**, *45*, 6742-6765.
- [44] F. Bonaccorso, A. Bartolotta, J. N. Coleman, C. Backes, *Adv. Mater.* **2016**, *28*, 6136-6166.
- [45] R. Ma, T. Sasaki, *Acc. Chem. Res.* **2015**, *48*, 136-143.

- [46] J. Yao, K. J. Koski, W. Luo, J. J. Cha, L. Hu, D. Kong, V. K. Narasimhan, K. Huo, Y. Cui, *Nat. Commun.* **2014**, *5*, 5670.
- [47] W. Bao, J. Wan, X. Han, X. Cai, H. Zhu, D. Kim, D. Ma, Y. Xu, J. N. Munday, H. D. Drew, M. S. Fuhrer, L. Hu, *Nat. Commun.* **2014**, *5*, 4224.
- [48] A. M. Dimiev, G. Ceriotti, N. Behabtu, D. Zakhidov, M. Pasquali, R. Saito, J. M. Tour, *ACS Nano* **2013**, *7*, 2773-2780.
- [49] J. J. Cha, K. J. Koski, K. C. Y. Huang, K. X. Wang, W. Luo, D. Kong, Z. Yu, S. Fan, M. L. Brongersma, Y. Cui, *Nano Lett.* **2013**, *13*, 5913-5918.
- [50] T. H. Bointon, I. Khrapach, R. Yakimova, A. V. Shytov, M. F. Craciun, S. Russo, *Nano Lett.* **2014**, *14*, 1751-1755.
- [51] S. Stankovich, D. A. Dikin, O. C. Compton, G. H. B. Dommett, R. S. Ruoff, S. T. Nguyen, *Chem. Mater.* **2010**, *22*, 4153-4157.
- [52] D. Weber, L. M. Schoop, V. Duppel, J. M. Lippmann, J. Nuss, B. V. Lotsch, *Nano Lett.* **2016**, *16*, 3578-3584.
- [53] M. R. Lukatskaya, O. Mashtalir, C. E. Ren, Y. Dall'Agnese, P. Rozier, P. L. Taberna, M. Naguib, P. Simon, M. W. Barsoum, Y. Gogotsi, *Science* **2013**, *341*, 1502-1505.
- [54] K. Lu, Z. Hu, Z. Xiang, J. Ma, B. Song, J. Zhang, H. Ma, *Angew. Chem., Int. Ed.* **2016**, *55*, 10448-10452.
- [55] Y. Yu, F. Yang, X. F. Lu, Y. J. Yan, Y.-H. Cho, L. Ma, X. Niu, S. Kim, Y.-W. Son, D. Feng, S. Li, S.-W. Cheong, X. H. Chen, Y. Zhang, *Nat. Nanotechnol.* **2015**, *10*, 270-276.
- [56] F. Xiong, H. Wang, X. Liu, J. Sun, M. Brongersma, E. Pop, Y. Cui, *Nano Lett.* **2015**, *15*, 6777-6784.
- [57] W. M. R. Divigalpitya, R. F. Frindt, S. R. Morrison, *Science* **1989**, *246*, 369-371.
- [58] M. Kühne, F. Paolucci, J. Popovic, P. M. Ostrovsky, J. Maier, J. H. Smet, *Nat. Nanotechnol.* **2017**, *12*, 895-900.
- [59] P. Ganter, B. V. Lotsch, *Angew. Chem. Int. Ed.* **2017**, *56*, 8389-8392.
- [60] F. Geng, R. Ma, A. Nakamura, K. Akatsuka, Y. Ebina, Y. Yamauchi, N. Miyamoto, Y. Tateyama, T. Sasaki, *Nat. Commun.* **2013**, *4*, 1632.
- [61] F. Geng, R. Ma, Y. Ebina, Y. Yamauchi, N. Miyamoto, T. Sasaki, *J. Am. Chem. Soc.* **2014**, *136*, 5491-5500.
- [62] M. Honda, Y. Oaki, H. Imai, *Chem. Mater.* **2014**, *26*, 3579-3585.
- [63] M. Honda, Y. Oaki, H. Imai, *Chem. Commun.* **2015**, *51*, 10046-10049.
- [64] J. Kobler, B. V. Lotsch, G. A. Ozin, T. Bein, *ACS Nano* **2009**, *3*, 1669-1676.
- [65] A. Ranft, F. Niekietel, I. Pavlichenko, N. Stock, B. V. Lotsch, *Chem. Mater.* **2015**, *27*, 1961-1970.
- [66] Y.-n. Wu, F. Li, W. Zhu, J. Cui, C.-a. Tao, C. Lin, P. M. Hannam, G. Li, *Angew. Chem., Int. Ed.* **2011**, *50*, 12518-12522.
- [67] S.-Y. Cho, H.-J. Koh, H.-W. Yoo, H.-T. Jung, *Chem. Mater.* **2017**, *29*, 7197-7205.
- [68] S.-Y. Cho, H.-J. Koh, H.-W. Yoo, J.-S. Kim, H.-T. Jung, *ACS Sens.* **2017**, *2*, 183-189.
- [69] K. Y. Ko, J.-G. Song, Y. Kim, T. Choi, S. Shin, C. W. Lee, K. Lee, J. Koo, H. Lee, J. Kim, T. Lee, J. Park, H. Kim, *ACS Nano* **2016**, *10*, 9287-9296.
- [70] T. L. Kelly, A. G. Sega, M. J. Sailor, *Nano Lett.* **2011**, *11*, 3169-3173.
- [71] R. M. Tindwa, D. K. Ellis, G.-Z. Peng, A. Clearfield, *J. Chem. Soc., Faraday Trans. 1* **1985**, *81*, 545-552.
- [72] A. Galarneau, A. Barodawalla, T. J. Pinnavaia, *Nature* **1995**, *374*, 529.
- [73] G. Lagaly, *Solid State Ionics* **1986**, *22*, 43-51.
- [74] F. Menéndez, A. Espina, C. Trobajo, J. Rodríguez, *Mater. Res. Bull.* **1990**, *25*, 1531-1539.
- [75] A. Espina, E. Jaimez, S. A. Khainakov, C. Trobajo, J. R. García, J. Rodríguez, *Chem. Mater.* **1998**, *10*, 2490-2496.
- [76] Y. Kang, J. J. Walsh, T. Gorishnyy, E. L. Thomas, *Nat. Mater.* **2007**, *6*, 957-960.
- [77] K. Sano, Y. S. Kim, Y. Ishida, Y. Ebina, T. Sasaki, T. Hikima, T. Aida, *Nat. Commun.* **2016**, *7*, 12559.
- [78] N. A. Rakow, A. Sen, M. C. Janzen, J. B. Ponder, K. S. Suslick, *Angew. Chem., Int. Ed.* **2005**, *44*, 4528-4532.
- [79] M. Comes, M. D. Marcos, R. Martínez-Mañez, F. Sancenón, J. Soto, L. A. Villaescusa, P. Amorós, D. Beltrán, *Adv. Mater.* **2004**, *16*, 1783-1786.

- [80] F. K. Perkins, A. L. Friedman, E. Cobas, P. M. Campbell, G. G. Jernigan, B. T. Jonker, *Nano Lett.* **2013**, *13*, 668-673.
- [81] S.-Y. Cho, Y. Lee, H.-J. Koh, H. Jung, J.-S. Kim, H.-W. Yoo, J. Kim, H.-T. Jung, *Adv. Mater.* **2016**, *28*, 7020-7028.
- [82] J. G. Calvert, *Pure Appl. Chem.* **1990**, *62*, 2167-2219.
- [83] P. Olivera-Pastor, P. Maireles-Torres, E. Rodríguez-Castellón, A. Jiménez-López, T. Cassagneau, D. J. Jones, J. Rozière, *Chem. Mater.* **1996**, *8*, 1758-1769.
- [84] S. Letaïef, M. A. Martín-Luengo, P. Aranda, E. Ruiz-Hitzky, *Adv. Funct. Mater.* **2006**, *16*, 401-409.

6.2 Supporting Information: Vapor-Phase Amine Intercalation for the Rational Design of Photonic Nanosheet Sensors

6.2.1 Methods

Nanosheet synthesis and spin coating

KNO₃ (99 %, Merck), Sb₂O₃ (99.6%, Alfa Aesar), and NH₄H₂PO₄ (98%+, Acros Organics) were used to synthesize K₃Sb₃P₂O₁₄ as described elsewhere.^[1,2] K₃Sb₃P₂O₁₄ was protonated, exfoliated, dried, dissolved in a water-ethanol mixture, ultrasonicated, and spin-coated on Si wafers (1.5 cm x 1.5 cm up to 5 cm x 5 cm) into thin films as reported previously (Scheme S6.1).^[1,2]

Amine intercalation

The H₃Sb₃P₂O₁₄ nanosheet-based thin films with thicknesses in the range of 130-160 nm were subsequently intercalated with various amines (Figure 6.1). For this procedure the films were exposed to the amine vapors. The amines with $n \leq 4$ (methylamine, 40 wt% solution in water, Acros Organics; ethylamine, 70% in water, Acros Organics; *n*-propylamine, 99%, Merck; *n*-butylamine, 99+%, Alfa Aesar; *N,N*-dimethylbutylamine, 99%, Sigma-Aldrich; 4-amino-1-butanol, 98%, Sigma-Aldrich; 4-(dimethylamino)-1-butanol, 97%, Sigma-Aldrich) were diluted to 1 mol L⁻¹ aqueous solutions, and the amines with $n > 4$ (*n*-hexylamine, 99%, Acros Organics; *n*-octylamine, 99+%, Acros Organics; *n*-dodecylamine, 99%, Acros Organics; dodecylamine, 98%, Sigma-Aldrich; tetradecylamine, 98%, Acros Organics; hexadecylamine, 90%, Sigma-Aldrich; *N,N*-dimethylhexylamine, 99%, Acros Organics; *N,N*-dimethyloctylamine, 97%, Acros Organics; *N,N*-dimethyldecylamine, 98%, Sigma-Aldrich) were used without further dilution. For intercalation, the thin films were placed in a plastic or glass Petri dish together with a small amount of amine (ca. 800 μ L in the case of liquid amine and ca. 100 mg in the case of a solid amine). In the case of long-chained amines (dodecylamine, tetradecylamine, hexadecylamine, and *N,N*-dimethyldecylamine) the glass Petri dishes were heated up to 80 °C to promote intercalation. Note that the intercalation of tetradecylamine as well as hexadecylamine takes up to 72 h. In all cases, the end of the intercalation process is indicated by a uniformly colored film.

For tracking the intercalation of amines with $n = 4$, *n*-butylamine, *N,N*-dimethylbutylamine, 4-amino-1-butanol, and 4-(dimethylamino)-1-butanol, in real time (Figure 6.3), 800 μ L of the 1 mol L⁻¹ solution of the respective amine was placed inside a Petri dish (diameter 5.5 cm) together with two H₃Sb₃P₂O₁₄ thin films. The real-time videos capturing the intercalation process (see Video S6.1) were acquired with a commercial webcam (Logitech, C920).

To determine how much amine intercalates per formula unit H₃Sb₃P₂O₁₄, nanosheet pellets were exposed to amine (ethylamine, *n*-butylamine, *n*-octylamine, *N,N*-dimethylbutylamine, *N,N*-dimethylhexylamine, and *N,N*-dimethyloctylamine) vapors for 14 days and subsequently their composition was analyzed.

Note that most of the amines used in this work are irritating and corrosive and some are even toxic.

Sensing with amine modified thin films

For recording optical changes of the amine-modified thin films toward vapors of varying polarity, the thin films were placed in a stainless steel chamber (ca. 6 mL residual volume) that has two basins with a volume of approximately 0.3 mL each, equipped with a transparent glass window. The basins were filled with saturated salt solutions (43% RH K_2CO_3 ; 94% RH KNO_3) or pure organic solvents (toluene, 99.5%, Merck; cyclohexane, 99.98%, Acros Organics; anisole, 99%, Acros Organics; *n*-octane, 98%+, Alfa Aesar) or their mixtures at 20 °C. After a minimum equilibration time of 30 min, UV-Vis spectra were recorded in the closed chamber.

Dynamic vapor pulses were created with the help of wash bottles. About 25 mL of the respective liquid analyte (toluene, 99.5%, Merck; cyclohexane, 99.98%, Acros Organics; ethanol, 99.8%, Carl Roth; deionized water) was placed in a 500 mL wash bottle. The inside nozzle was placed in the vapor phase above the liquid, making sure that only vapor is transferred outside. The response of the thin films to these vapor pulses were recorded with a UV-Vis spectrometer or webcam.

Array sensor fabrication and sensing

For the creation of the array (see also Scheme S6.2), a $\text{H}_3\text{Sb}_3\text{P}_2\text{O}_{14}$ thin film of 2 cm x 2 cm size was covered with a mask having three holes. Sequentially, one area (hole in the mask) of the thin film after the other was exposed to one of the amine vapors (ethylamine, *n*-butylamine, and *n*-decylamine). To control the area that is exposed through the mask by an amine Scotch tape was used (s. Scheme S6.2). For ethylamine and *n*-butylamine, a 1 mol L⁻¹ aqueous solution was used and in the case of *n*-decylamine the pure amine was used. Additionally, the amines were heated up to 40 °C for ethylamine and *n*-butylamine, and to 70 °C for *n*-decylamine to promote intercalation. The array containing the three amines was placed in the stainless steel chamber described earlier. The basins were filled with saturated salt solutions (43% RH K_2CO_3 ; 94% RH KNO_3) or organic solvents (toluene, 99.5%, Merck; cyclohexane, 99.98%, Acros Organics; ethanol, 99.8%, Carl Roth) at 20 °C. After a minimum equilibration time of 30 min, images were recorded with a webcam (Logitech, C920).

6.2.2 Characterization

X-ray

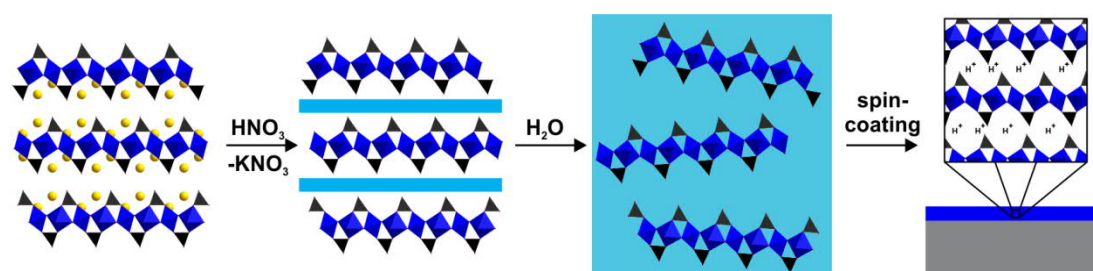
XRD patterns of the thin films were recorded on a D8-Advance (Bruker) working with Ge(111) monochromated Cu-K $_{\alpha 1}$ radiation ($\lambda = 154.059$ pm), equipped with a Vântec detector.

UV-Vis

All UV-Vis spectra were acquired with a fiber optic spectrometer (USB4000-XR1-ES, Ocean Optics) attached to a microscope (BX51, Olympus) with normal incidence. The optical spectra were taken at the same spot for all thin films (1×1 mm² in area).^[1-3]

UV-Vis spectra were acquired for every primary and tertiary alkylamine before and after intercalation for at least four spots on two thin films in total. The presented data in Figure 6.2c) and Figure S6.6 is the average optical shift from these measurements. Representative spectra before and after intercalation for the alkylamines are shown in Figure S6.2 and S6.5.

6.2.3 Additional data



Scheme S6.1. From bulk material to thin films. Solid state synthesis of $\text{K}_3\text{Sb}_3\text{P}_2\text{O}_{14}$, followed by ion exchange with nitric acid and subsequent exfoliation in water and spin-coating into photonic thin films on a Si substrate.

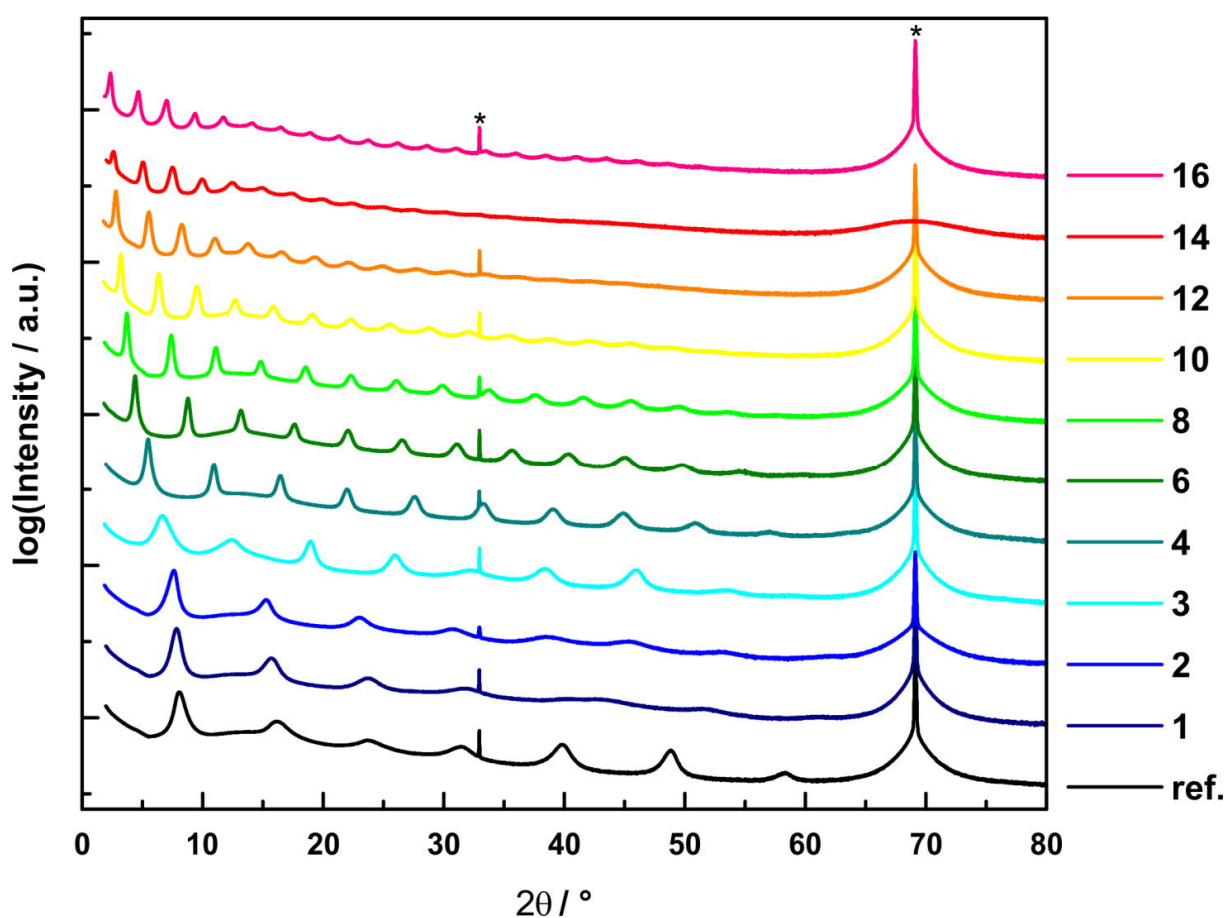


Figure S6.1. Complete out-of-plane XRD patterns of the thin films $\text{H}_{3-x}(\text{NH}_3(\text{CH}_2)_{n-1}\text{CH}_3)_x\text{Sb}_3\text{P}_2\text{O}_{14}$ with $n = 1-16$ and, for reference, $\text{H}_3\text{Sb}_3\text{P}_2\text{O}_{14}$. The reflections marked with asterisks at 32.94 and 69.12 2θ are due to the Si substrate and were used for pattern alignment.

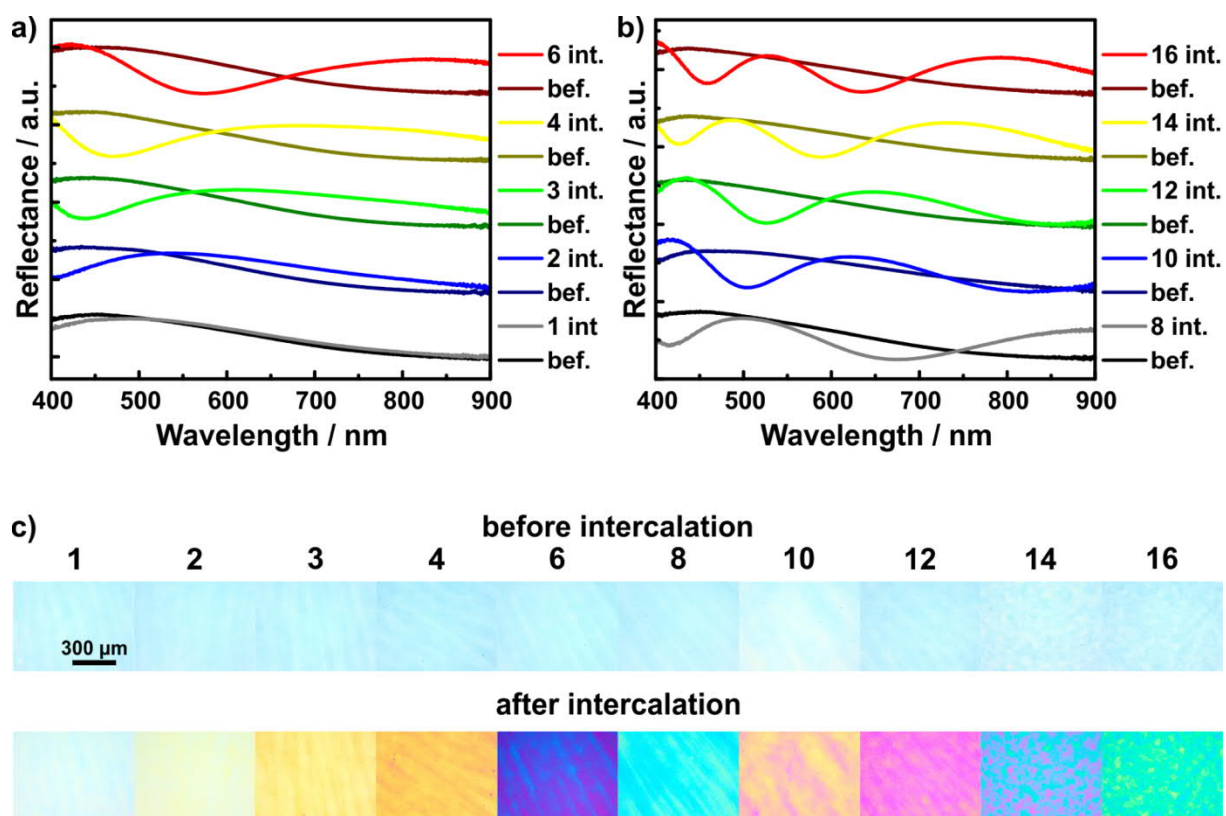


Figure S6.2. UV-Vis spectra and corresponding microscope images of $H_{3-x}(NH_3(CH_2)_{n-1}CH_3)_xSb_3P_2O_{14}$ with $n = 1-16$ thin films. UV-Vis spectra before and after intercalation for $n = 1-6$ a) and $n = 8-16$ b). In c) the corresponding light microscope images before and after intercalation are displayed. All images have the same dimensions.

Table S6.1. Results of the elemental analysis for $H_{3-x}(NH_3(CH_2)_n-1CH_3)_xSb_3P_2O_{14}$ ($n = 2, 4, 8$) and $H_{3-x}((CH_3)_2NH(CH_2)_n-1CH_3)_xSb_3P_2O_{14}$ ($n = 4, 6, 8$) in order to determine the number of amine molecules per formula unit of antimony phosphate, x . A value of $x \approx 3$ for primary and $x \approx 2$ for tertiary amines is found, pointing toward a bilayer and a monolayer arrangement, respectively. The increasing x values (higher density of amines in the interlayer space) with increasing alkyl chain length might be a consequence of the increasing attractive hydrophobic interactions with increasing alkyl chain length, leading to a filling of the remaining available interlayer space.

	Sb / wt%	P / wt%	C / wt%	N / wt%	H / wt%	x
$H_{3-x}(NH_3(CH_2)CH_3)_xSb_3P_2O_{14}$	45.15	7.78	8.06	5.25	3.23	2.8
$H_{3-x}(NH_3(CH_2)_3CH_3)_xSb_3P_2O_{14}$	40.60	7.01	15.32	4.59	4.22	2.9
$H_{3-x}(NH_3(CH_2)_7CH_3)_xSb_3P_2O_{14}$	31.38	5.55	31.46	4.70	6.64	3.7
$H_{3-x}((CH_3)_2NH(CH_2)_3CH_3)_xSb_3P_2O_{14}$	42.72	7.30	14.63	3.27	4.24	1.9
$H_{3-x}((CH_3)_2NH(CH_2)_5CH_3)_xSb_3P_2O_{14}$	38.56	6.60	19.80	3.39	4.92	2.1
$H_{3-x}((CH_3)_2NH(CH_2)_7CH_3)_xSb_3P_2O_{14}$	33.75	5.84	26.54	3.55	5.96	2.5

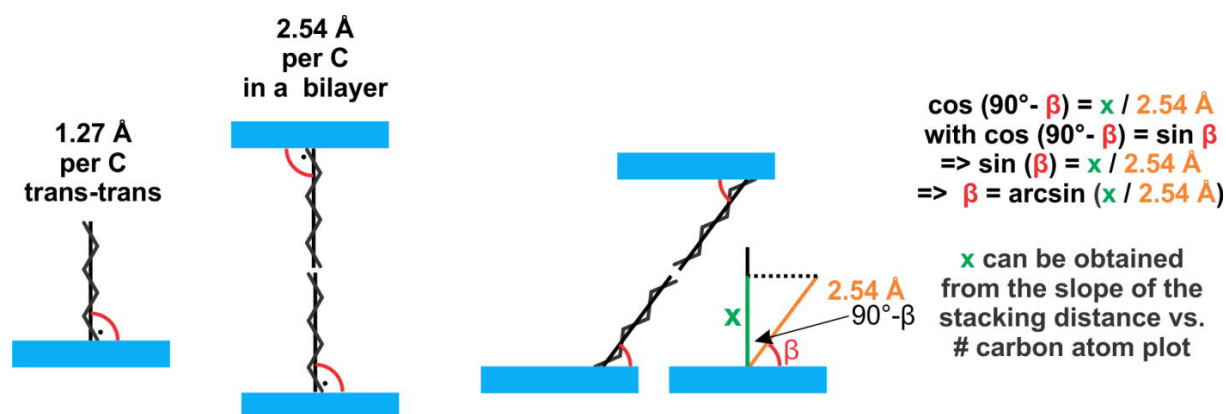


Figure S6.3. Considerations for tilting angle calculation in a bilayer (see also ref. 1 in the SI). The value of 1.27 Å per carbon atom in a trans-trans chain conformation were obtained from the literature.^[4]

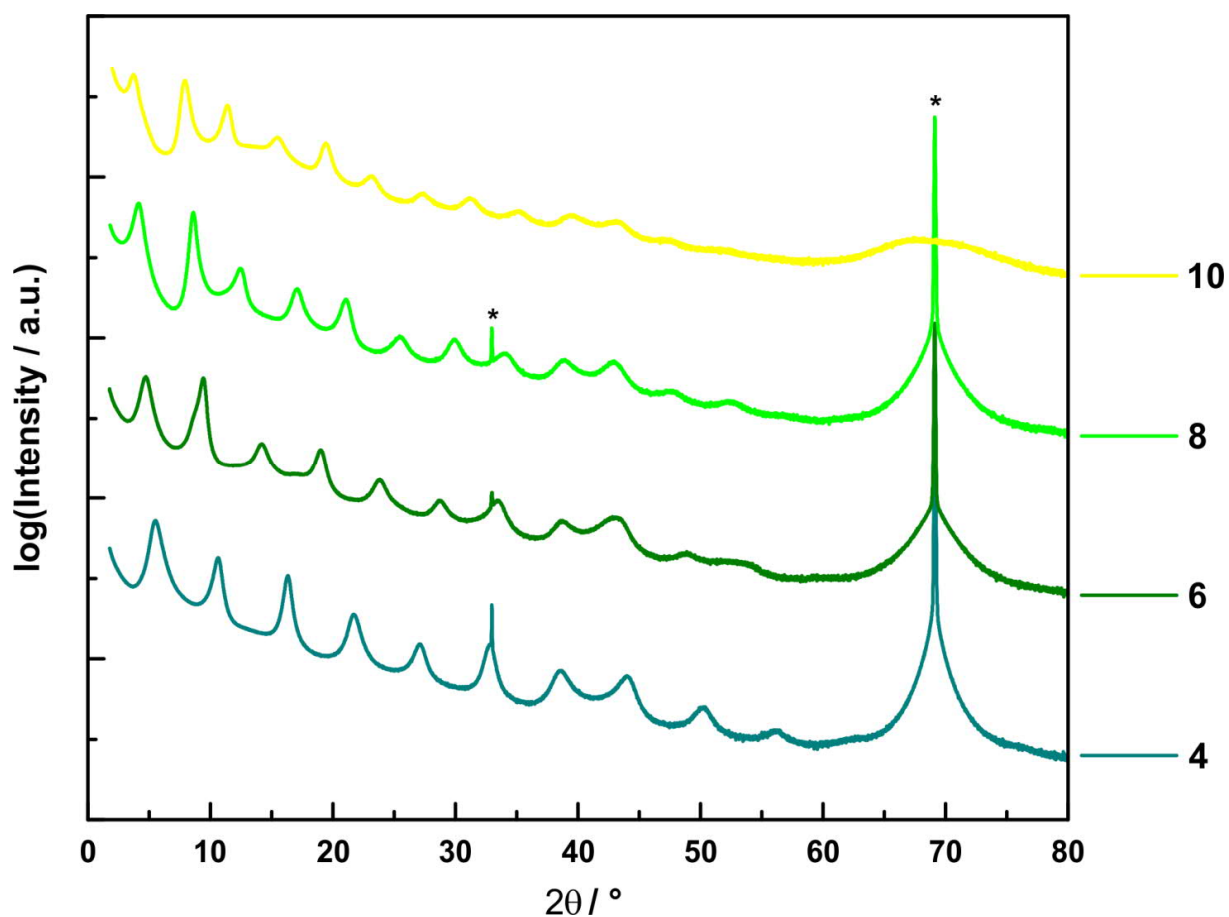


Figure S6.4. Out-of-plane XRD patterns of $\text{H}_{3-x}((\text{CH}_3)_2\text{NH}(\text{CH}_2)_{n-1}\text{CH}_3)_x\text{Sb}_3\text{P}_2\text{O}_{14}$ thin films for $n = 4-10$. The reflections marked with asterisks at 32.94 and 69.12 2θ are due to the Si substrate and were used for pattern alignment.

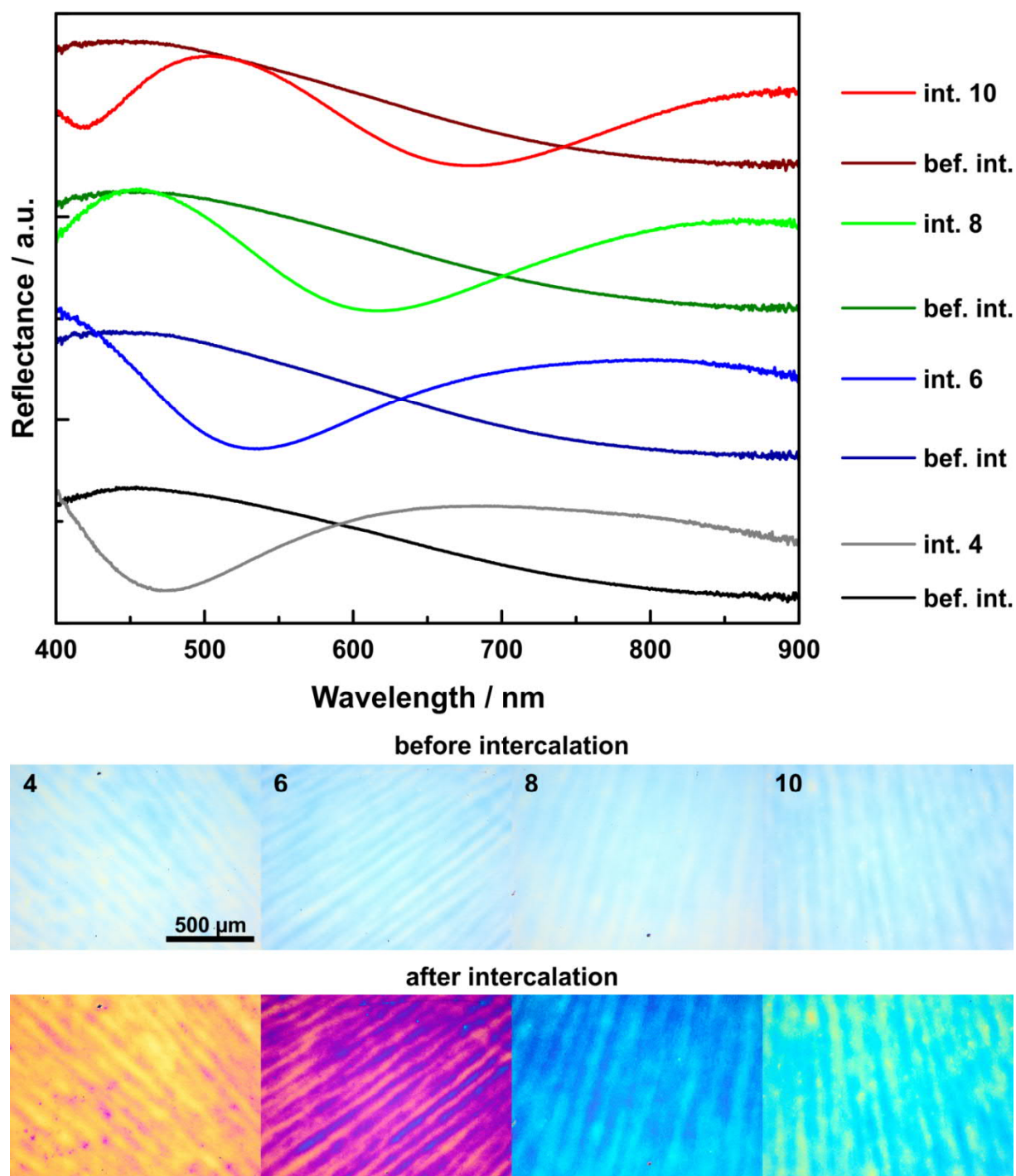


Figure S6.5. Representative UV-Vis spectra and corresponding microscope images of the $H_{3-x}((CH_3)_2NH(CH_2)_{n-1}CH_3)_xSb_3P_2O_{14}$ films with $n = 4-10$ before (bef. int.) and after intercalation (int. n). All optical microscope images have the same dimensions.

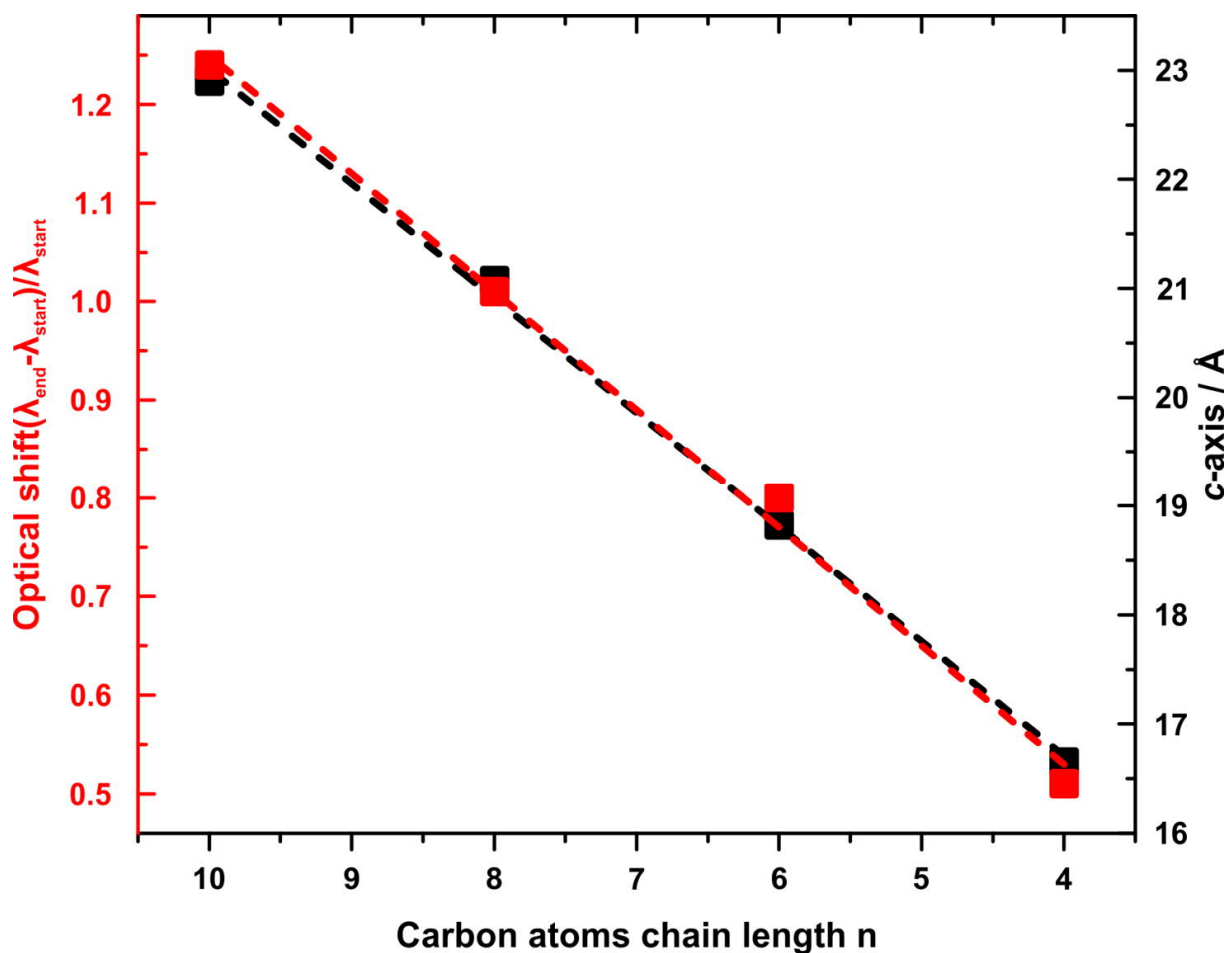


Figure S6.6. Correlation plot of the stacking distance (Figure S6.4) as well as the normalized optical shift, which is extracted from the UV-Vis spectra (Figure S6.5), versus the number of carbon atoms in the alkyl chain for $H_{3-x}((CH_3)_2NH(CH_2)_{n-1}CH_3)_xSb_3P_2O_{14}$ thin films.

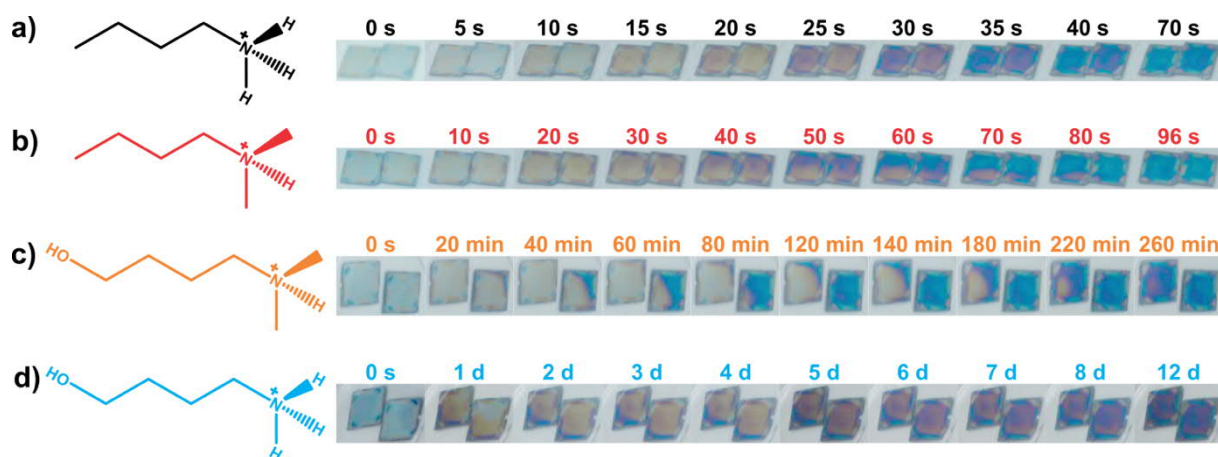


Figure S6.7. Additional data of the time resolved amine intercalation into photonic thin films compared to Figure 6.3a)-d). Intercalation of a) *n*-butylamine, b) *N,N*-dimethylbutylamine, c) 4-(dimethylamino)-1-butanol, and d) 4-amino-1-butanol into two thin films per amine (see Video S6.1). Ammonium cations are sketched on the left because the amines get protonated in the interlayer space.

Table S2. Boiling points of BA, DMBA, DMBAOH and BAOH.

Amine	Boiling point / °C
BA	78 ^[5]
DMBA	95 ^[6]
DMBAOH	177-179 ^[7]
BAOH	204-206 ^[8]

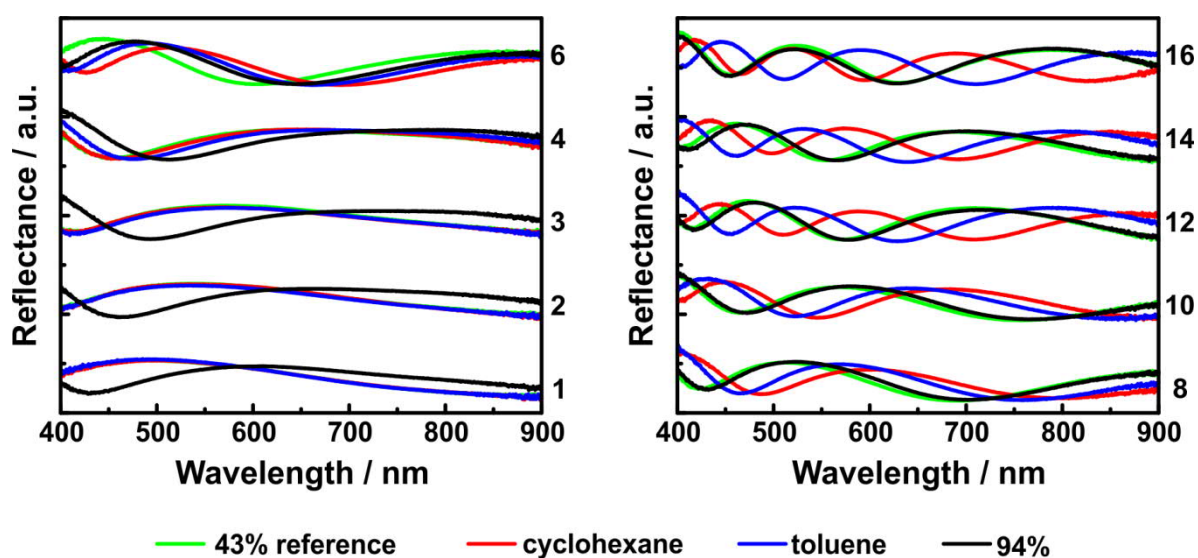


Figure S6.8. UV-Vis spectra illustrating the influence of the alkyl chain length in $H_{3-x}(NH_3(CH_2)_{n-1}CH_3)_xSb_3P_2O_{14}$ ($n = 1-16$) thin films on the response toward polar 94% RH, saturated moderately polar toluene vapor as well as unpolar cyclohexane vapor. For reference the response toward 43% RH is also displayed. See also Figure 6.4a for data analysis.

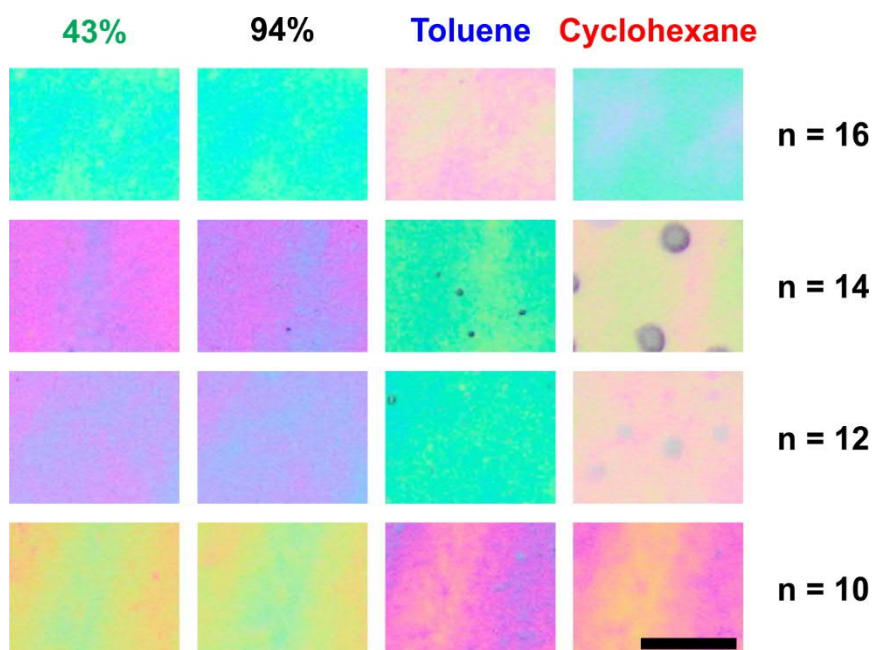


Figure S6.9. Optical response of $H_{3-x}(NH_3(CH_2)_{n-1}CH_3)_xSb_3P_2O_{14}$ ($n = 10, 12, 14, 16$) thin films toward toluene, cyclohexane, 43% and 94% RH. The images correspond to the spectra and data shown in Figures 6.4a and S6.8. The scale bar is 50 μm .

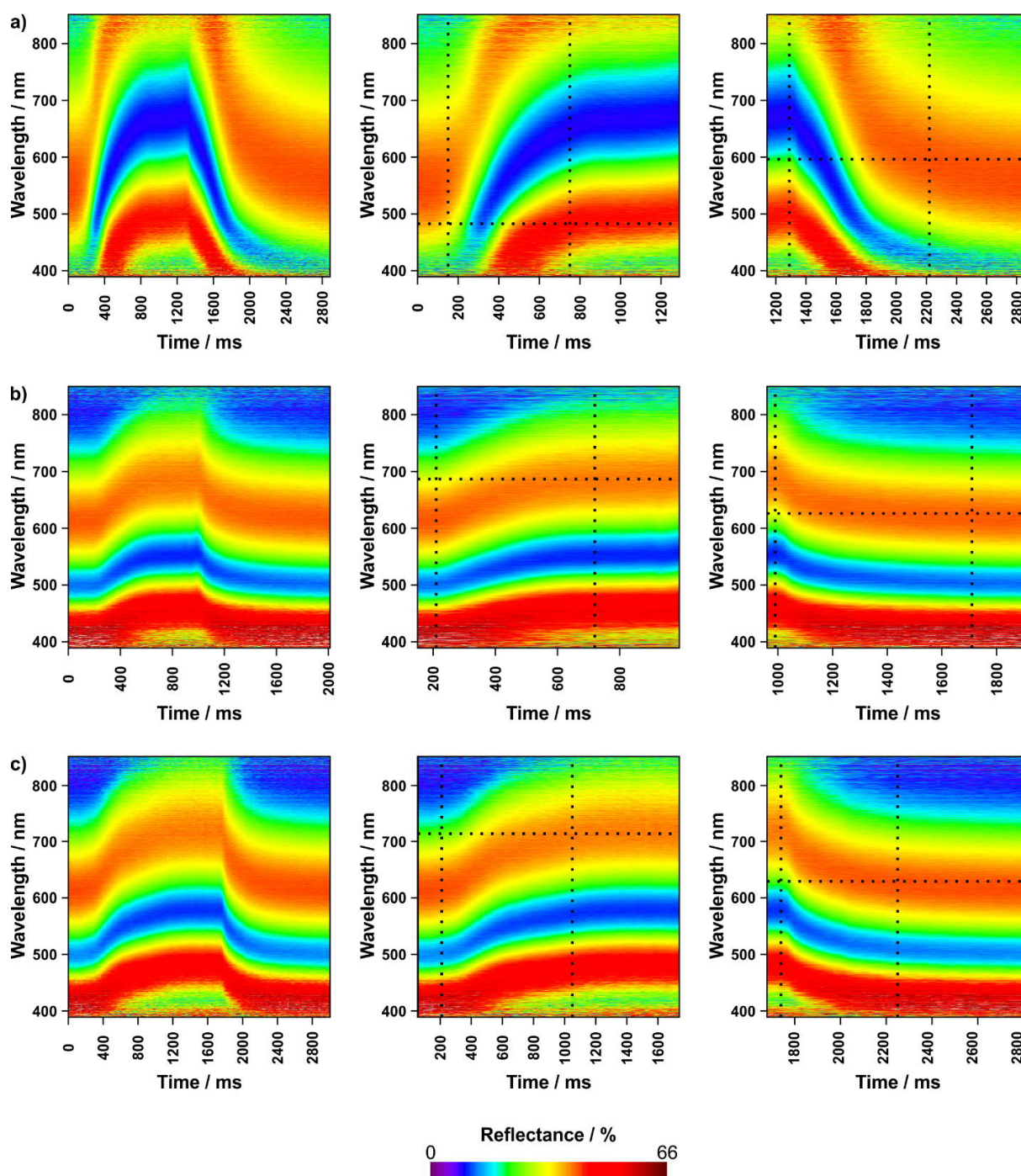


Figure S6.10. Time resolved UV-Vis spectra for the determination of the response and recovery times (see dashed lines) for $\text{H}_{3-x}(\text{NH}_3(\text{CH}_2)_{n-1}\text{CH}_3)_x\text{Sb}_3\text{P}_2\text{O}_{14}$ $n = 4, 10$. The response and recovery times are defined as the time to reach 90% of the signal change. The horizontal line indicates the position to reach 90% of the signal change and the first vertical line indicates the start of the stimuli change, while the second vertical line indicates the time at which 90% of the signal change is completed. Therefore, the response and recovery times are given as the difference between the two vertical lines. Determination of the response and recovery times toward almost saturated a) water vapor for the ethylamine intercalated sample, b) and c) toluene and cyclohexane, respectively, for the decylamine intercalated sample. As in a) the first order interference band shifts out of the detectable region the second order was additionally used to determine the response and recovery times. See also Video S6.2-6.4 for the cycling experiments.

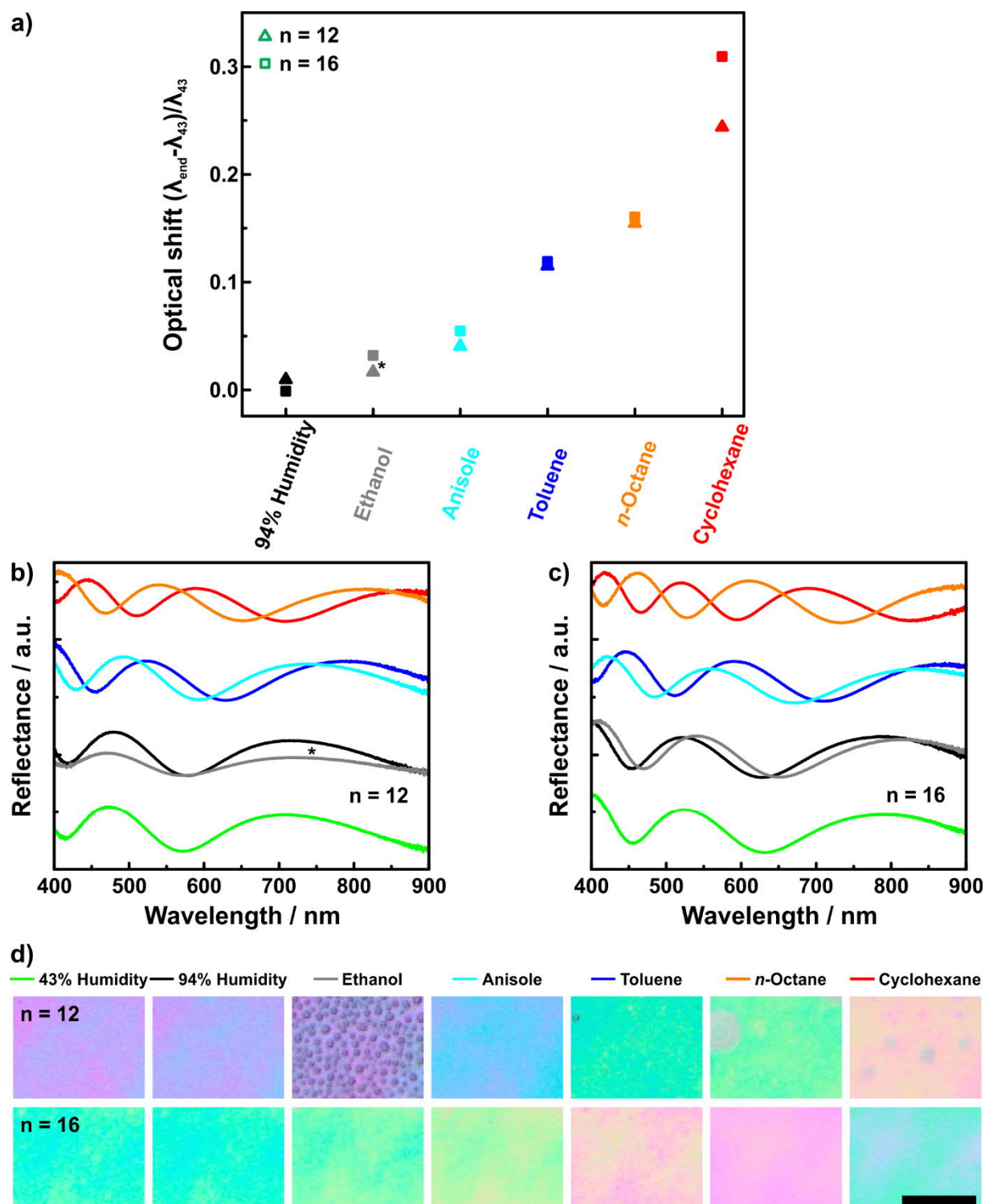


Figure S11. Response of the $H_{3-x}(NH_3(CH_2)_n-CH_3)_xSb_3P_2O_{14}$ ($n = 12, 16$) thin films toward 43% RH, 94% RH, ethanol, anisole, toluene, *n*-octane and cyclohexane vapor. a) Summary plot showing the normalized optical shift toward different analytes for the dodecylamine ($n = 12$, triangles) and hexadecylamine ($n = 16$, squares) intercalated samples. In b) for $n = 12$ and c) for $n = 16$ the corresponding UV-Vis spectra are depicted. In d) the corresponding light microscope images are shown. The scale bar is 50 μm . Note that for ethanol vapor and $n = 12$ pronounced condensation occurred, which lead to data that cannot be interpreted unambiguously (light gray, marked with an asterisk).

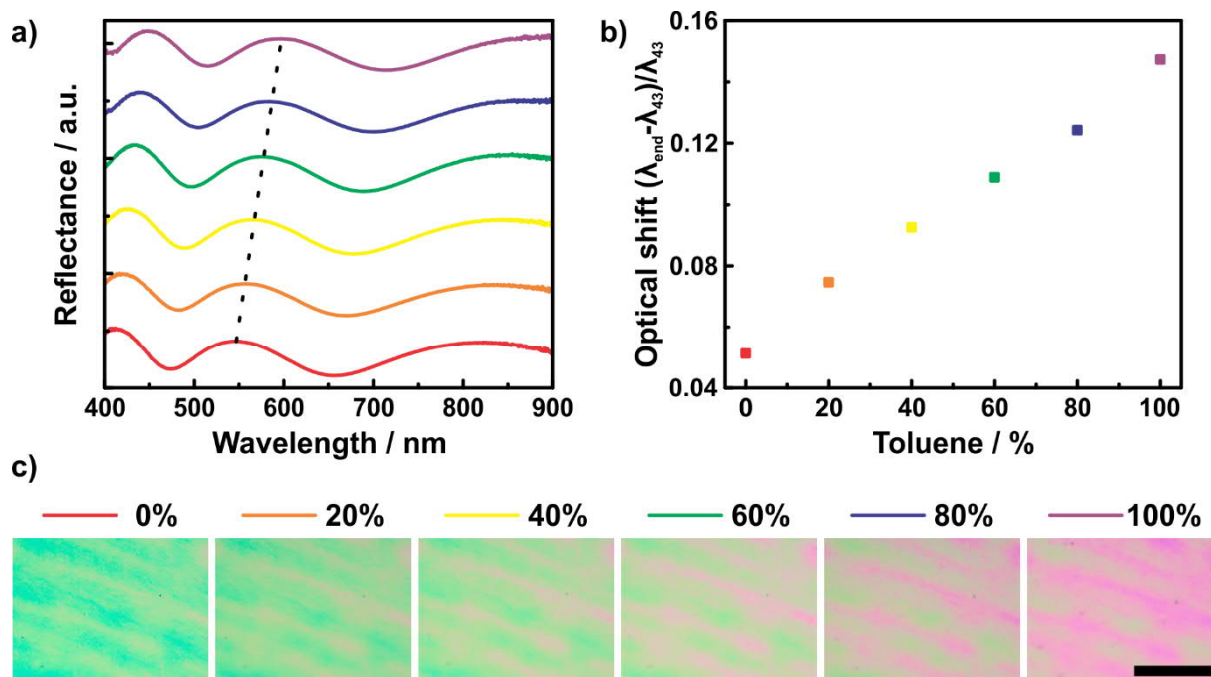


Figure S6.12. Response of a hexadecylamine intercalated $\text{H}_3\text{Sb}_3\text{P}_2\text{O}_{14}$ thin film toward vapor mixtures of anisole and toluene. a) UV-Vis spectra upon exposure toward mixtures of toluene (T) and anisole (A) vapor (100% A (bottom), 80% A + 20% T, 60% A + 40% T, 40% A + 60% T, 20% A + 80% T, 100% T (top)). The dashed line indicates the redshift of the third order interference band with increasing amount of toluene. b) Normalized optical shift summarizing the spectral data given in a). c) Corresponding light microscope images illustrating the gradual color change of the thin film upon exposure to mixtures with a varying anisole to toluene ratio. The scale bar is 200 μm .

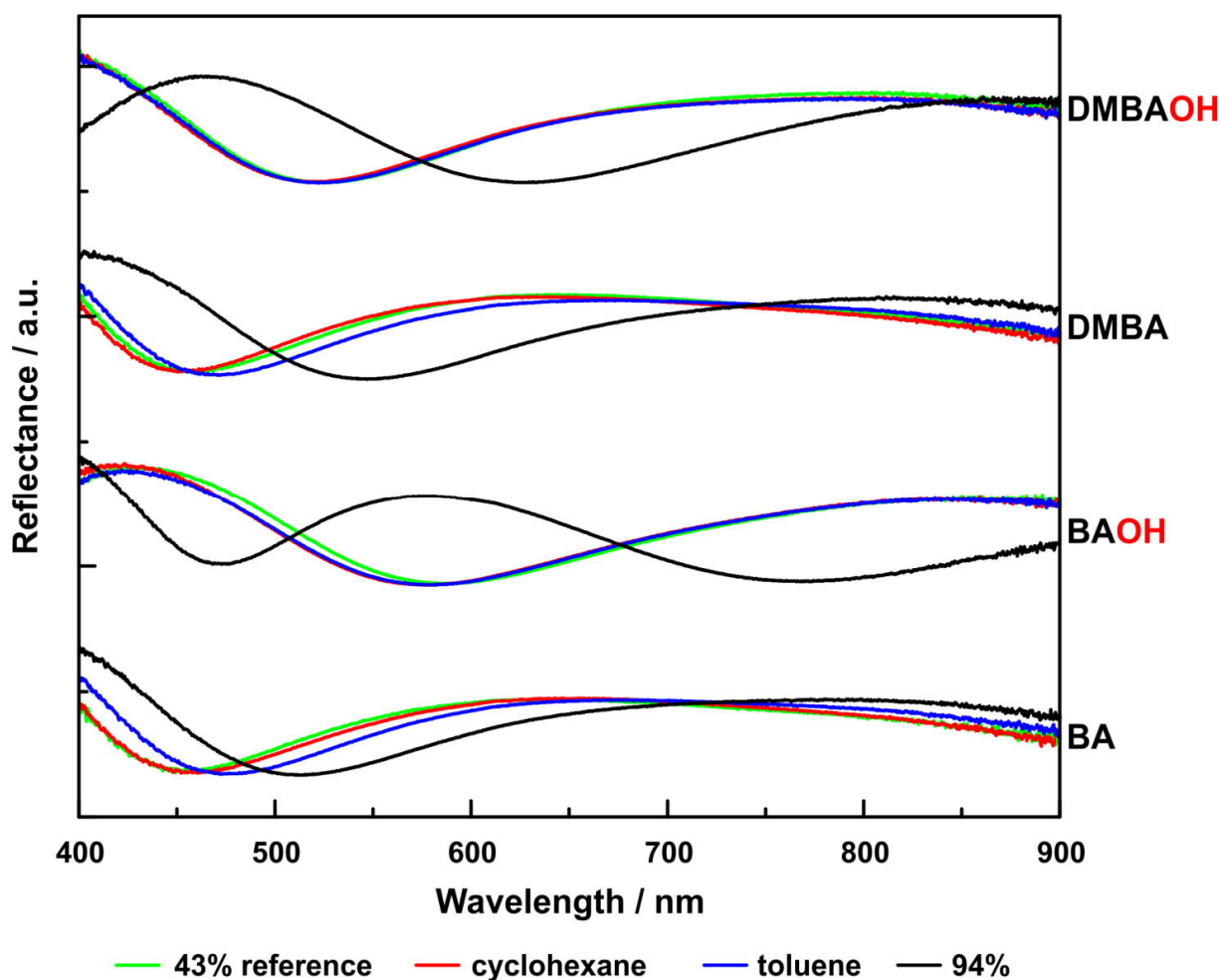
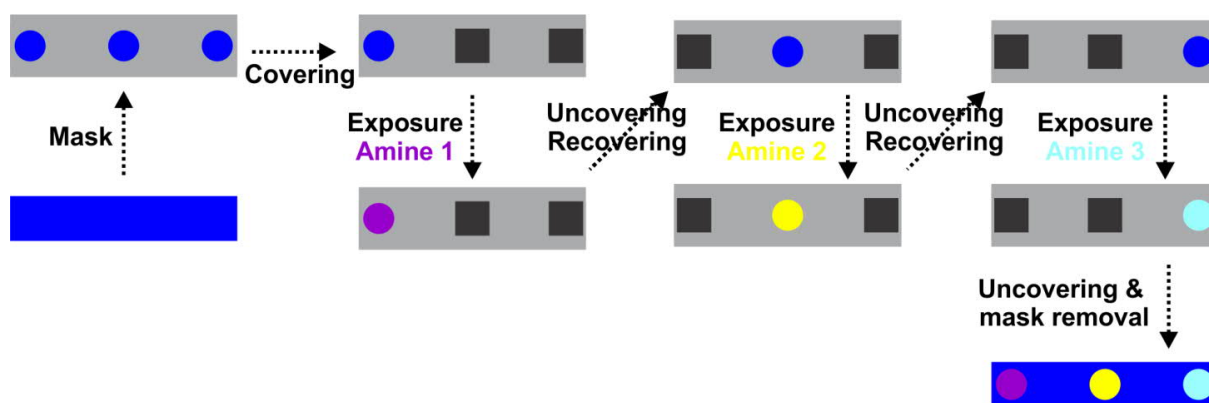


Figure S6.13. UV-Vis spectra corresponding to Figure 6.4b, showing the response of BA, BAOH, DMBA and DMBAOH intercalated $\text{H}_3\text{Sb}_3\text{P}_2\text{O}_{14}$ thin films, toward 94% RH and saturated vapors of toluene and cyclohexane. For reference also the spectra for 43% RH are depicted. Note that the difference for cyclohexane (red curves) and toluene (blue curves) can clearly be seen for films intercalated with BA and DMBA, whereas there is almost no difference for BAOH and DMBAOH intercalated films between the responses toward these vapors.



Scheme S6.2. Sequential preparation of the array sensor with a viewing direction toward the surface of the thin film. In a first step, a mask is applied to the $\text{H}_3\text{Sb}_3\text{P}_2\text{O}_{14}$ thin film. Subsequently certain holes in the mask are covered with scotch tape, and then the thin film is exposed to vapor of an amine and afterwards the scotch tape is removed. The last three steps can be repeated with other amines as depicted. By intercalating various amines in different areas in the same $\text{H}_3\text{Sb}_3\text{P}_2\text{O}_{14}$ thin film this procedure yields an array sensor.

See also Video S6.1-6.7 available at <https://pubs.acs.org/doi/suppl/10.1021/acs.chemmater.7b04828>

Video S6.1 is shown at four times the original speed, whereas Video S6.2-S6.7 are shown in real-time.

6.2.4 Bibliography

- [1] P. Ganter, L. M. Schoop, B. V. Lotsch, *Adv. Mater.* **2017**, *29*, 1604884.
- [2] K. Szendrei, P. Ganter, O. Sánchez-Sobrado, R. Eger, A. Kuhn, B. V. Lotsch, *Adv. Mater.* **2015**, *27*, 6341-6348.
- [3] P. Ganter, K. Szendrei, B. V. Lotsch, *Adv. Mater.* **2016**, *28*, 7436-7442.
- [4] F. Menéndez, A. Espina, C. Trobajo, J. Rodríguez, *Mater. Res. Bull.* **1990**, *25*, 1531-1539.
- [5] R. P. Koob, J. G. Miller, A. R. Day, *J. Am. Chem. Soc.* **1951**, *73*, 5775-5777.
- [6] H. T. Clarke, *J. Chem. Soc., Trans.* **1913**, *103*, 1689-1704.
- [7] T. N. De Castro Dantas, J. P. Laval, A. Lattes, *Phosphorus Sulfur Relat. Elem.* **1982**, *13*, 97-105.
- [8] E. D. Bergmann, A. Kaluszyner, *Recl. Trav. Chim. Pays-Bas Belg.* **1959**, *78*, 331-336.

7 The silver exfoliation route

7.1 A New Fabrication Method for Single-Layer Nanosheets by Silver-Assisted Exfoliation

Pirmin Ganter, Christian Ziegler,* Anne T. Friedrichs, Viola Duppel,
Christina Scheu, and Bettina V. Lotsch*

published: *ChemNanoMat* **2017**, 3, 411-414.

DOI: 10.1002/cnma.201700067

<http://onlinelibrary.wiley.com/doi/10.1002/cnma.201700067/full>

*equally contributed

Copyright © 2017 WILEY-VCH Verlag GmbH & Co. KGaA, Weinheim. Reproduced with the permission of WILEY-VCH.

Contribution of P.G.: *P.G. exfoliated and characterized the AgTaP₂O₈ phase, and wrote the major part of the publication. P.G. also carried out the image editing as well as literature screening.*

Abstract

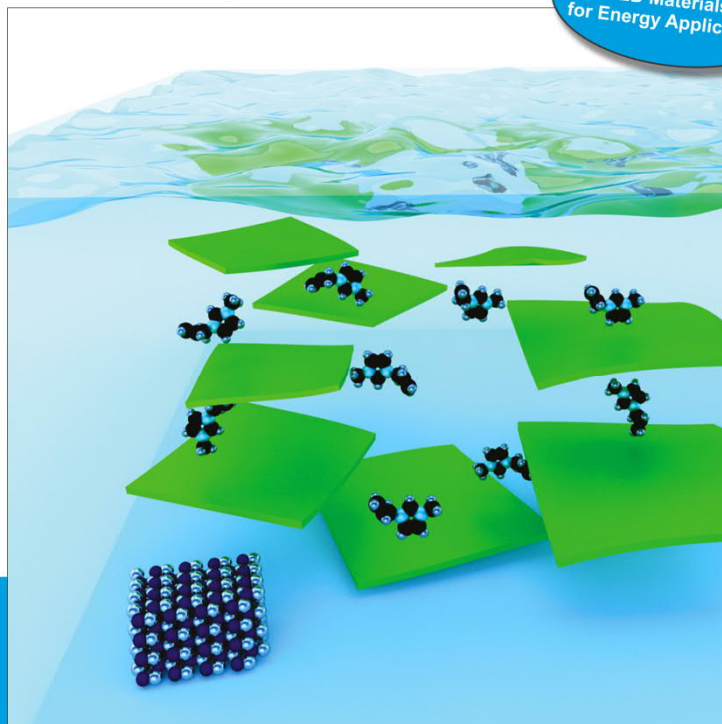
The discovery of 2D forms of matter, pioneered by graphene, has not only triggered new insights into fundamental physics but also pushed the limits of miniaturization. To process nanosheets into ultrathin functional devices, the development of scalable exfoliation routes is of key interest. Here, we demonstrate for the first time a mild, yet highly effective silver-ion-based exfoliation route for layered transition metal oxides. Single layer transition metal oxide nanosheets were obtained by applying silver ion exchange and subsequent treatment of the silver-intercalated phases with an aqueous suspension containing organic iodides. This generic exfoliation route can be widely applied also to acid-sensitive materials and allows the modification of the nanosheets with non-conventional organic ligands, which owing to their chemical functionality may be used to tailor the optoelectronic and surface properties of the nanosheet-ligand hybrid.

CHEMNANOMAT

CHEMISTRY OF NANOMATERIALS FOR ENERGY, BIOLOGY AND MORE

www.chemnanomat.org

Special Issue:
2D Materials
for Energy Applications



6/03
2017

A Journal of



A sister journal of Chemistry – An Asian Journal
and the Asian Journal of Organic Chemistry

Front Cover:

B. V. Lotsch *et al.*
A New Fabrication Method for Single-Layer Nanosheets
by Silver-Assisted Exfoliation

WILEY-VCH

Front Cover: A new way toward single-layer nanosheets: The novel silver-assisted exfoliation route described in this work utilizes the formation of highly insoluble silver iodide as driving force for the exfoliation of silver transition metal oxides with organic iodides. This method not only broadens the scope of organic exfoliation agents but allows for the judicious introduction of functional ligands which can be used to tailor the properties of the nanosheets. Moreover, the silver-assisted route is exceptionally mild and hence may be used to exfoliate acid-sensitive systems, which are not accessible by conventional acid-assisted exfoliation protocols, thus enlarging the portfolio of existing nanosheets. More information can be found in the Communication by B. V. Lotsch *et al.* on page 411 in Issue 6, 2017 (DOI: 10.1002/cnma.201700067). Cover design by P. Ganter.



Table of Content: A generic silver-based exfoliation route for layered transition metal oxides is demonstrated. Single layer oxide nanosheets were obtained by ion exchange and exfoliation of Ag-intercalated layered oxides with organic iodides. The mild conditions and functional-group tolerance of this method significantly expand the scope of accessible hybrid 2D materials.

7.1.1 Introduction

The development of novel exfoliation routes for layered materials is of immense interest due to the broad range of applications ranging from fundamental physics to processing nanosheets into ultrathin functional devices.^[1-15] Current solvent-based exfoliation can be grouped into either chemical or mechanical exfoliation methods (see Figure S7.1 in the Supporting Information).^[8] As every exfoliation method brings its own set of distinct advantages, but also limitations in terms of the compounds it can be used for,^[2,4,8,10,16,17] the improvement of existing and the development of new exfoliation routes is highly desirable to expand the scope of accessible nanosheet systems.^[7,9,11,12,14,18-23]

Current solvent-based approaches allowing for a high yield of single nanosheets largely rely on chemical exfoliation strategies.^[16,24] The most common wet chemical exfoliation routes can be classified as either redox-mediated or ion exchange delamination methods.^[8,16] The group of redox-mediated exfoliation includes^[25] for example the alkali metal redox-mediated intercalation into layered dichalcogenides with subsequent delamination in an appropriate solvent.^[22] For TMOs the most often applied delamination strategies utilize interlayer ion exchange to render the interlayer gallery more accessible to solvents and, ultimately, osmotic swelling. Examples include the alkylamine exchange and exfoliation in non-polar solvents^[20,26] or the cation-proton exchange upon acid treatment with subsequent reaction of the protons with quaternary ammonium hydroxides, most commonly TBAOH.^[2,16,24] The driving force behind the exfoliation with TBAOH and other bulky hydroxides is the acid-base reaction (i.e., neutralization) in the interlayer space followed by osmotic swelling in water due to the higher concentration of TBA ions in the interlayer space.^[2,16,24] However, a strong acid in a rather high concentration (5M-8M) is required for a successful ion exchange, limiting this exfoliation process to acid-stable compounds.

Nanosheets exfoliated with an organic EA such as TBA can be considered as a “hybrid” material, the properties of which are determined by both the inorganic nanosheet “core” and by the outer organic

“shell”.^[20,26] The profound influence of the organic EA was illustrated by Imai and co-workers who showed that the band gap of $\text{Ti}_{1-x}\text{O}_2^{4x-}$ nanosheets can be shifted by 0.2 eV using a long chain primary alkylamine EA.^[20] Along similar lines, we recently showed that the EA TBAOH has significant impact on the swelling properties and hence, sensing characteristics, of antimony phosphate nanosheet-based Fabry-Pérot sensors.^[27] The impact of the EA on the properties of the nanosheets motivates our attempt to enlarge the portfolio of suitable EAs, as they can ultimately be used for the direct modification of the properties of the nanosheets.^[19,20,26,27]

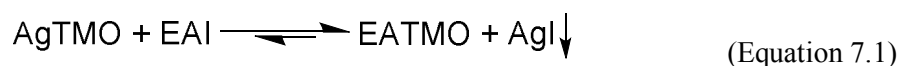
In this work, we present the first silver-ion based exfoliation route for TMOs, which significantly expands the scope of EA to unconventional organic surfactants. The broad range of applicability to different types of oxide and phosphate nanosheets is demonstrated by delaminating $\text{AgLaNb}_2\text{O}_7$, $\text{AgCa}_2\text{Nb}_3\text{O}_{10}$ and AgTaP_2O_8 with Ch, AMI or TBA iodide into single-layer nanosheets of similar quality compared to the conventional proton exchange exfoliation route.

7.1.2 Results and discussion

The exfoliation was carried out in three steps and is shown in Scheme 7.1. First, the starting materials KLaNb_2O_7 , $\text{KCa}_2\text{Nb}_3\text{O}_{10}$ and KTaP_2O_8 were synthesized as described previously^[27-29] and their identity was confirmed by PXRD and EDX spectroscopy (see Table S7.1 and Figure S7.2). The silver-exchanged compounds $\text{AgLaNb}_2\text{O}_7$, $\text{AgCa}_2\text{Nb}_3\text{O}_{10}$ and AgTaP_2O_8 were obtained by treatment of the potassium compounds in an AgNO_3 melt at 260 °C as described in the literature.^[30,31] The completeness of the ion exchange was verified by EDX and PXRD (see Supporting Information). Note that from EDX analysis of $\text{AgCa}_2\text{Nb}_3\text{O}_{10}$ we can exclude the formation of $\text{Ag}_{1.1}\text{Ca}_{0.9}[\text{Ca}_{0.6}\text{Ag}_{0.9}\text{Nb}_3\text{O}_{10}]$ during the Ag exchange, in contrast to what was suggested by Boltersdorf and Maggard.^[31]

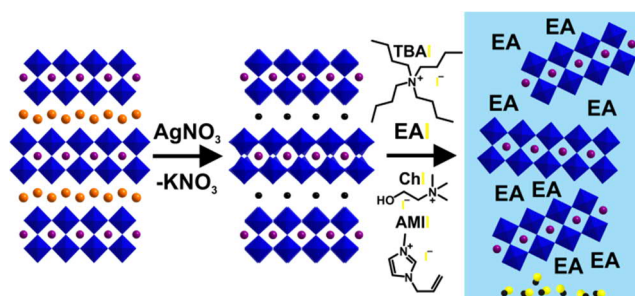
For exfoliation the compounds were stirred or shaken in a 1:1 molar ratio with the iodide salts of the respective EAs (EAI) in water (7-12 mmol L⁻¹).

Upon treatment with the iodide salts ChI, AMII and TBAI, the onset of AgI formation is indicated by precipitation of yellow colored particles. AgI is almost insoluble in water (solubility product 8.5×10^{-17}),^[32] hence Ag^+ is removed from the interlayer space according to the following Equation 7.1:



This reaction provides the driving force for the exchange of Ag for the organic cations Ch, AMI and TBA in the interlayer space, which likely leads to osmotic swelling with water and, ultimately, delamination by applying some weak mechanical force, for instance stirring or shaking. Since the Ag-exfoliation route is similar to conventional acid-mediated exfoliation in that it takes advantage of a chemical reaction between the interlayer cation (Ag^+ or H^+) and the anion of the EA (I^- or OH^-) with high thermodynamic driving force,^[2,16,24] this points toward a more general concept for chemically

inducing exfoliation based on Pearson's concept of HSAB: Here, the soft Ag^+ reacts with soft I^- to form the highly insoluble precipitate AgI , while in the acid-mediated case the hard H^+ and hard OH^- combination yields H_2O , likewise with a strongly negative reaction enthalpy.^[33,34]



Scheme 7.1. Schematic of the exfoliation process via the silver exfoliation route. Example of the delamination of KLaNb_2O_7 (NbO_6 octahedra in blue, La in purple, K in orange, Ag in black, I in yellow). In the first step, the bulk potassium compounds are ion exchanged in an AgNO_3 melt and are exfoliated with an EA - AMI, Ch or TBA iodide - in the second step. During the exfoliation step insoluble AgI is formed, which is the main driving force for exfoliation.

To yield mainly single layer nanosheets, the unexfoliated material as well as the AgI particles were removed by centrifugation at 3000-6000 rpm. Note that a similar centrifugation step is applied in the acid route. The supernatant containing the nanosheets was collected and analyzed by TEM and AFM. We also exfoliated HLaNb_2O_7 and $\text{HCa}_2\text{Nb}_3\text{O}_{10}$ with TBAOH (see details in Supporting Information) and compared it to $\text{AgLaNb}_2\text{O}_7$ and $\text{AgCa}_2\text{Nb}_3\text{O}_{10}$ nanosheets exfoliated with TBAI (see Figure 7.1, Figure S7.3) to ensure that the Ag-exfoliation route yields nanosheets of similar quality compared to the H-route. Both methods indeed furnish nanosheets of similar size and thickness. The thickness determined by AFM amounts to 1.7-1.9 nm and 2.8-2.9 nm for $\text{TBALaNb}_2\text{O}_7$ and $\text{TBACa}_2\text{Nb}_3\text{O}_{10}$ nanosheets, respectively. These thicknesses are expectedly larger than the respective crystallographic thicknesses (1.05 nm and 1.44 nm, respectively) owing to the TBA and water molecules surrounding the nanosheets. The d -values extracted from the SAED patterns are within the range of experimental errors for the different exfoliation methods (see Table S7.2). For the SAED pattern, TEM and AFM images of TBAI exfoliated TaP_2O_8^- see Figure S7.4.

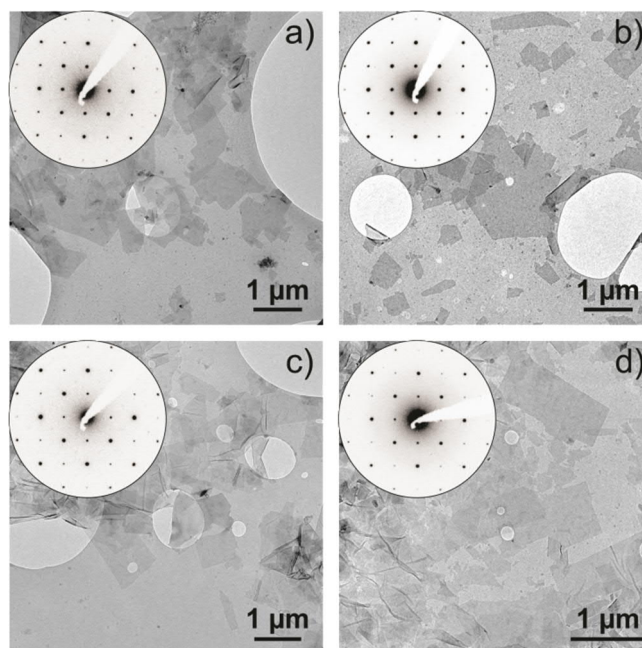


Figure 7.1. Comparison of TEM images and representative SAED patterns taken along the [001] zone axis of $\text{TBACa}_2\text{Nb}_3\text{O}_{10}$ and $\text{TBALaNb}_2\text{O}_7$ nanosheets. The nanosheets were obtained from a) $\text{AgCa}_2\text{Nb}_3\text{O}_{10}$, b) $\text{HCa}_2\text{Nb}_3\text{O}_{10}$, c) $\text{AgLaNb}_2\text{O}_7$ and d) HLaNb_2O_7 by exfoliation with TBAI for the silver phases and TBAOH for the solid acids.

For exfoliation of $\text{AgLaNb}_2\text{O}_7$, $\text{AgCa}_2\text{Nb}_3\text{O}_{10}$ and AgTaP_2O_8 with ChI and AMII we also observe the formation of single layer nanosheets as confirmed by AFM and TEM (Figure 7.2). The d -values obtained from the SAED patterns are in agreement with the ones obtained from the TBA-exfoliated samples (see Table S7.2, S7.4 and S7.5). The height measured by AFM is around 1.9-2.2 nm for $\text{LaNb}_2\text{O}_7^-$, 2.2-2.4 nm for $\text{Ca}_2\text{Nb}_3\text{O}_{10}^-$ and 1.2-1.5 nm for TaP_2O_8^- , which is in agreement with the height measured for the TBA-exfoliated samples (see Table S7.3).

Up to now both AMI^[35] and Ch^[36] have only been used in very specialized exfoliation procedures limited either by the range of applicable compounds or the complicated exfoliation process resulting mainly in multilayer nanosheets. The Ag-route therefore allows the easy introduction of exotic EAs as a ligand shell. At the same time, the Ag-route avoids the extensive use of strong acids which is necessary using conventional methods to obtain the intermediate, protonated solid acid and, hence, might be applied to acid-sensitive systems. Moreover, it does not require the use of organic hydroxides, which are less common as compared to the iodides.

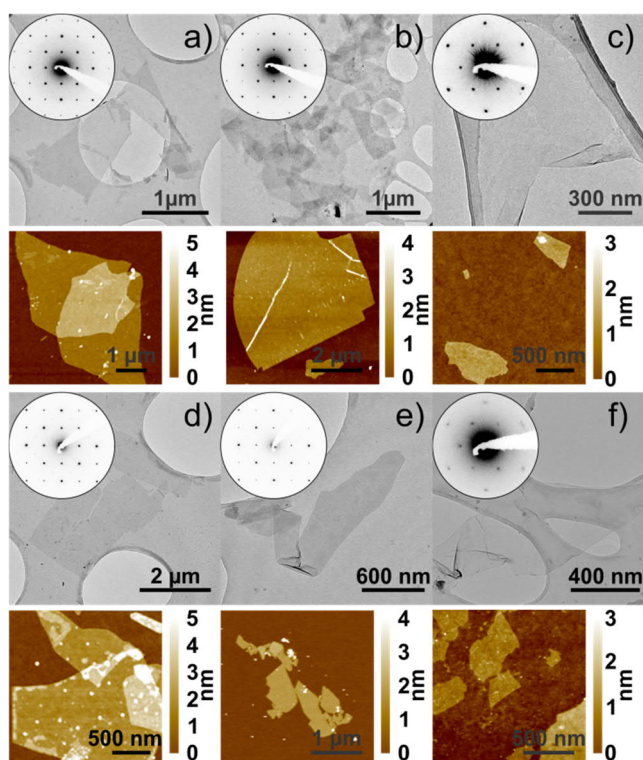


Figure 7.2. AFM, TEM images and SAED patterns of AgCa₂Nb₃O₁₀, AgLaNb₂O₇ and AgTaP₂O₈ exfoliated with ChI (a), b and c), respectively) and AMI (d), e) and f), respectively).

7.1.3 Outlook

In summary, we have introduced a novel silver-ion based exfoliation route for TMOs to obtain single-layer nanosheets. The silver-ion delamination route is an alternative to the conventional H-route using strong acids to generate the protonated oxides as intermediates. However, in contrast to the H-route it allows the use of exotic EAs, which owing to their chemical functionality may be beneficial for introducing functional groups into the ligand shell of the nanosheets. This in turn bodes well for the development of a new generation of versatile nanosheet building blocks for nanoarchitectonics^[37] as well as for various other applications.

7.1.4 Acknowledgement

Financial support was granted by the Max Planck Society, the University of Munich (LMU), the Center for NanoScience (CeNS), and the Deutsche Forschungsgemeinschaft (DFG) through the Cluster of Excellence Nanosystems Initiative Munich (NIM).

7.1.5 Bibliography

- [1] Editorial, *Nat. Mater.* **2017**, *16*, 155.
- [2] R. Ma, T. Sasaki, *Adv. Mater.* **2010**, *22*, 5082-5104.
- [3] M. Osada, T. Sasaki, *Adv. Mater.* **2012**, *24*, 210-228.
- [4] S. Z. Butler, S. M. Hollen, L. Cao, Y. Cui, J. A. Gupta, H. R. Gutiérrez, T. F. Heinz, S. S. Hong, J. Huang, A. F. Ismach, E. Johnston-Halperin, M. Kuno, V. V. Plashnitsa, R. D. Robinson, R. S. Ruoff, S. Salahuddin, J. Shan, L. Shi, M. G. Spencer, M. Terrones, W. Windl, J. E. Goldberger, *ACS Nano* **2013**, *7*, 2898-2926.
- [5] M. Xu, T. Liang, M. Shi, H. Chen, *Chem. Rev.* **2013**, *113*, 3766-3798.
- [6] C. N. R. Rao, H. S. S. Ramakrishna Matte, U. Maitra, *Angew. Chem. Int. Ed.* **2013**, *52*, 13162-13185; *Angew. Chem.* **2013**, *125*, 13400-13424.
- [7] J. N. Coleman, M. Lotya, A. O'Neill, S. D. Bergin, P. J. King, U. Khan, K. Young, A. Gaucher, S. De, R. J. Smith, I. V. Shvets, S. K. Arora, G. Stanton, H.-Y. Kim, K. Lee, G. T. Kim, G. S. Duesberg, T. Hallam, J. J. Boland, J. J. Wang, J. F. Donegan, J. C. Grunlan, G. Moriarty, A. Shmeliov, R. J. Nicholls, J. M. Perkins, E. M. Grieveson, K. Theuvsissen, D. W. McComb, P. D. Nellist, V. Nicolosi, *Science* **2011**, *331*, 568-571.
- [8] V. Nicolosi, M. Chhowalla, M. G. Kanatzidis, M. S. Strano, J. N. Coleman, *Science* **2013**, *340*, 1226419.
- [9] K. R. Paton, E. Varrla, C. Backes, R. J. Smith, U. Khan, A. O'Neill, C. Boland, M. Lotya, O. M. Istrate, P. King, T. Higgins, S. Barwich, P. May, P. Puczkarski, I. Ahmed, M. Moebius, H. Pettersson, E. Long, J. Coelho, S. E. O'Brien, E. K. McGuire, B. M. Sanchez, G. S. Duesberg, N. McEvoy, T. J. Pennycook, C. Downing, A. Crossley, V. Nicolosi, J. N. Coleman, *Nat. Mater.* **2014**, *13*, 624-630.
- [10] F. Bonaccorso, A. Bartolotta, J. N. Coleman, C. Backes, *Adv. Mater.* **2016**, *28*, 6136-6166.
- [11] G. Bepete, E. Anglaret, L. Ortolani, V. Morandi, K. Huang, A. Pénicaud, C. Drummond, *Nat. Chem.* **2017**, *9*, 347-352.
- [12] P. L. Cullen, K. M. Cox, M. K. Bin Subhan, L. Picco, O. D. Payton, D. J. Buckley, T. S. Miller, S. A. Hodge, N. T. Skipper, V. Tileli, C. A. Howard, *Nat. Chem.* **2017**, *9*, 244-249.
- [13] K. Manna, H.-N. Huang, W.-T. Li, Y.-H. Ho, W.-H. Chiang, *Chem. Mater.* **2016**, *28*, 7586-7593.
- [14] A. Molle, J. Goldberger, M. Houssa, Y. Xu, S.-C. Zhang, D. Akinwande, *Nat. Mater.* **2017**, *16*, 163-169.
- [15] M. Chhowalla, H. S. Shin, G. Eda, L.-J. Li, K. P. Loh, H. Zhang, *Nat. Chem.* **2013**, *5*, 263-275.
- [16] R. Ma, T. Sasaki, *Acc. Chem. Res.* **2015**, *48*, 136-143.
- [17] C. Tan, H. Zhang, *Nat. Commun.* **2015**, *6*, 7873.
- [18] J. Xuan, Z. Wang, Y. Chen, D. Liang, L. Cheng, X. Yang, Z. Liu, R. Ma, T. Sasaki, F. Geng, *Angew. Chem. Int. Ed.* **2016**, *55*, 14569-14574; *Angew. Chem.* **2016**, *128*, 14789-14794.
- [19] F. Geng, R. Ma, Y. Yamauchi, T. Sasaki, *Chem. Commun.* **2014**, *50*, 9977-9980.
- [20] M. Honda, Y. Oaki, H. Imai, *Chem. Mater.* **2014**, *26*, 3579-3585.
- [21] A. Jawaid, J. Che, L. F. Drummy, J. Bultman, A. Waite, M.-S. Hsiao, R. A. Vaia, *ACS Nano* **2017**, *11*, 635-646.
- [22] J. Zheng, H. Zhang, S. Dong, Y. Liu, C. Tai Nai, H. Suk Shin, H. Young Jeong, B. Liu, K. Ping Loh, *Nat. Commun.* **2014**, *5*, 2995.
- [23] J. Thompson, A. Crossley, P. D. Nellist, V. Nicolosi, *J. Mater. Chem.* **2012**, *22*, 23246-23253.
- [24] T. Maluangnont, K. Matsuba, F. Geng, R. Ma, Y. Yamauchi, T. Sasaki, *Chem. Mater.* **2013**, *25*, 3137-3146.
- [25] D. Weber, L. M. Schoop, V. Duppel, J. M. Lippmann, J. Nuss, B. V. Lotsch, *Nano Lett.* **2016**, *16*, 3578-3584.
- [26] M. Honda, Y. Oaki, H. Imai, *Chem. Commun.* **2015**, *51*, 10046-10049.

- [27] P. Ganter, L. M. Schoop, B. V. Lotsch, *Adv. Mater.* **2017**, *29*, 1604884.
- [28] C. Ziegler, S. Werner, M. Bugnet, M. Wörsching, V. Duppel, G. A. Botton, C. Scheu, B. V. Lotsch, *Chem. Mater.* **2013**, *25*, 4892-4900.
- [29] M. Sato, J. Abo, T. Jin, M. Ohta, *J. Alloys Compd.* **1993**, *192*, 81-83.
- [30] M. Sato, J. Watanabe, K. Uematsu, *J. Solid State Chem.* **1993**, *107*, 460-470.
- [31] J. Boltersdorf, P. A. Maggard, *ACS Catal.* **2013**, *3*, 2547-2555.
- [32] A. F. Holleman, E. Wiberg, *Lehrbuch der Anorganischen Chemie, 101st ed.*, Walter de Gruyter, Berlin&New York, **1995**.
- [33] R. G. Pearson, *J. Am. Chem. Soc.* **1963**, *85*, 3533-3539.
- [34] R. G. Parr, R. G. Pearson, *J. Am. Chem. Soc.* **1983**, *105*, 7512-7516.
- [35] B. Zhang, W. Ning, J. Zhang, X. Qiao, J. Zhang, J. He, C.-Y. Liu, *J. Mater. Chem.* **2010**, *20*, 5401-5403.
- [36] A. M. Abdelkader, I. A. Kinloch, *ACS Sustainable Chem. Eng.* **2016**, *4*, 4465-4472.
- [37] K. Ariga, Q. Ji, W. Nakanishi, J. P. Hill, M. Aono, *Mater. Horiz.* **2015**, *2*, 406-413.

7.2 Supporting Information: A New Fabrication Method for Single-Layer Nanosheets by Silver-Assisted Exfoliation

7.2.1 Methods

Bulk material

KCa₂Nb₃O₁₀ was synthesized by heating K₂CO₃ (99 %, Merck), CaCO₃ (99 %, Grüssing) and Nb₂O₅ (99.5 %, Alfa Aesar) in a 0.6:2:1.5 molar ratio at 1200 °C for 60 h.^[1] KLaNb₂O₇ was obtained by heating K₂CO₃ (99 %, Merck), La(OH)₃ (99.95%, Alfa Aesar) and Nb₂O₅ (99.5%, Alfa Aesar) in 0.6:1:1 molar ratio at 1200 °C for 60 h.^[2] The excess of 20% K₂CO₃ is used to compensate for the loss due to volatilization. KTaP₂O₈ was synthesized by heating Ta₂O₅ (99.85% Alfa Aesar), KNO₃ (99%, Merck), NH₄H₂PO₄ (98%+, Acros Organics) in a first step overnight at 250 °C and subsequently at 850 °C for 48 h.^[3]

Cation exchange

For the silver exchange KCa₂Nb₃O₁₀, KLaNb₂O₇ and KTaP₂O₈ were treated in excess of molten AgNO₃ at 260 °C for 12-24 h.^[4,5] In the case of KTaP₂O₈ a 16-fold excess and for the other compounds a 4-fold molar excess of AgNO₃ was used. After the reaction, the cation-silver exchanged materials were washed with distilled water and dried at 60 °C.

For the proton exchange 2 g of KCa₂Nb₃O₁₀ or KLaNb₂O₇ were treated with 5M HNO₃ for 5-7 days with daily renewal of the acid. After the exchange the two materials were filtered, washed with water and dried at 60 °C over night^[1]

Exfoliation

The silver phases (AgLaNb₂O₇, AgCa₂Nb₃O₁₀ and AgTaP₂O₈) were exfoliated with tetra-*n*-butylammonium iodide (TBAI, C₁₆H₃₆IN, 99%, Sigma-Aldrich), 1-allyl-3-methylimidazolium iodide (AMII, C₇H₁₁IN₂, 98%, Sigma-Aldrich) or choline iodide (ChI, C₅H₁₄INO, 98%, Alfa Aesar) in a 1:1 molar ratio (concentration 7-12 mmol L⁻¹). Exfoliation was achieved by either stirring, in the case of AgTaP₂O₈, or shaking, for AgLaNb₂O₇ and AgCa₂Nb₃O₁₀, for several days in the dark. The solid acid phases HCa₂Nb₃O₁₀ and HLaNb₂O₇ were exfoliated with tetra-*n*-butylammonium hydroxide (TBAOH, 98%, Sigma-Aldrich) in a 1:1 molar ratio (concentration 7.3 mmol L⁻¹).^[1] For further characterization the suspensions were centrifuged between 3000-6000 rpm for 30 min to remove non-exfoliated material.

7.2.2 Characterization

XRD:

PXRD patterns of the bulk materials, cation- or silver-exchanged were recorded on a Huber G670 Guinier imaging plate diffractometer (Cu $K_{\alpha 1}$ -radiation, $\lambda = 154.059$ pm, Ge(111)-monochromator) or on a D8-Advance (Bruker) working with Ge(111) monochromated Cu- $K_{\alpha 1}$ radiation ($\lambda = 154.059$ pm).

EDX:

Composition of bulk materials, cation-, or silver-exchange materials was determined by SEM coupled with EDX spectroscopy. Either a JSM-6500F electron microscope (JOEL Ltd) or a Vega TS 5130 MM (Tescan) both equipped with an EDX detector (Oxford) were used.

AFM:

AFM topography measurements of the nanosheetes were performed with a MFP-3D Standalone AFM (Asylum Research) operated in tapping mode.

TEM:

TEM samples were prepared by dropping a diluted (1:100-200) colloidal nanosheet suspension onto copper or gold grids coated with a lacey or holey carbon film, respectively. A Philips CM30 ST microscope (300 kV, LaB6 cathode, Royal Philips Electronics) was used for imaging and obtaining SAED pattern of the nanosheets.

7.2.3 Additional data

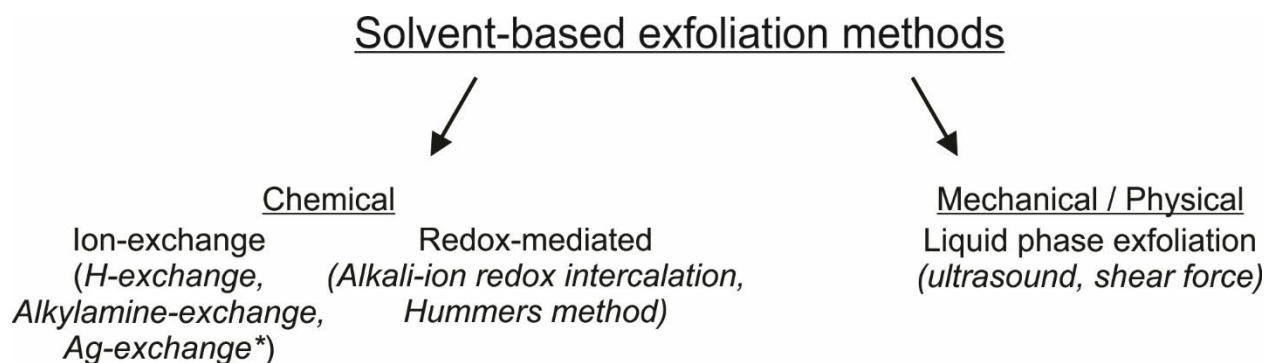


Figure S7.1. Schematic overview of the two main groups of solvent-based exfoliation. The asterisk marks the exfoliation route added in this work.

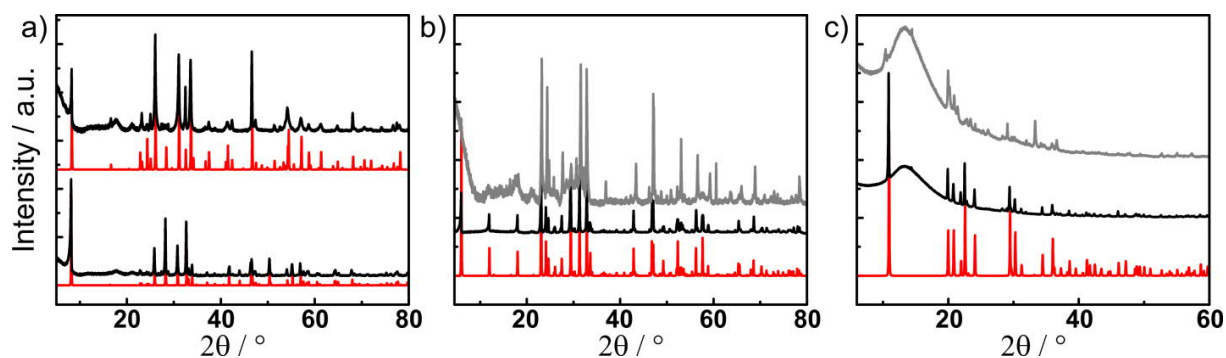


Figure S7.2. PXRD pattern of a) KLaNb_2O_7 (bottom) and $\text{AgLaNb}_2\text{O}_7$ (top). In both cases the reference is in red and the measured experimental XRD pattern in black. b) PXRD pattern of bottom $\text{KCa}_2\text{Nb}_3\text{O}_{10}$ (black) with its reference pattern (red) as well as the pattern of $\text{AgCa}_2\text{Nb}_3\text{O}_{10}$ (light gray). c) PXRD pattern of KTaP_2O_8 (black) with its reference pattern (red) as well as the pattern of AgTaP_2O_8 (light gray). Note that KTaP_2O_8 as well as AgTaP_2O_8 contain a minor impurity phase of TaPO_5 , which is separated during the centrifugation step. The broad reflections in a) and b) at around $18^\circ 2\theta$ and $23^\circ 2\theta$ are due to the polyester mounting foil in the XRD setup and the broad reflection in c) at around $13^\circ 2\theta$ from the sample holder material.

Table S7.1. SEM-EDX quantification data of bulk, cation-proton and cation-silver exchanged lanthanum niobates, calcium niobates or tantalum phosphate, respectively. The theoretical formula is compared to the experimental formula determined by the element specific signals given in atomic%. Note that the higher oxygen content for the Ag-exchanged and H-exchanged phases most likely results from the presences of additional water molecules.

Theoretical formula						Experimental formula
	K	Ag	La	Nb	O	
KLaNb ₂ O ₇	8.6	-	8.0	16.6	66.8	KLaNb ₂ O ₈
HLaNb ₂ O ₇	0.3	-	7.2	14.9	77.6	(H)LaNb ₂ O _{10.4}
AgLaNb ₂ O ₇	-	6.2	6.0	13.4	74.4	Ag _{0.9} La _{0.9} Nb ₂ O _{11.1}
	K	Ag	Ca	Nb	O	
KCa ₂ Nb ₃ O ₁₀	5.6	-	10.9	16.9	66.6	KCa ₂ Nb ₃ O _{10.7}
HCa ₂ Nb ₃ O ₁₀	-	-	11.9	18.2	69.9	(H)Ca ₂ Nb ₃ O _{11.5}
AgCa ₂ Nb ₃ O ₁₀	-	5.3	11.0	17.1	66.6	Ag _{0.9} Ca _{1.9} Nb ₃ O _{11.7}
	K	Ag	Ta	P	O	
KTaP ₂ O ₈	7.6		8.1	16.2	68.2	KTa _{0.9} P ₂ O _{8.4}
AgTaP ₂ O ₈		6.7	7.4	14.3	71.7	Ag _{0.9} TaP ₂ O ₁₀

Table S7.2. Most prominent *d*-spacings and corresponding (*hkl*) values observed by SAED of *TBALa*Nb₂O₇ and *TBACa*₂Nb₃O₁₀ nanosheets after exfoliation *via* the silver or proton route. The SAED patterns of the exfoliated nanosheets were indexed by assuming a tetragonal unit cell for LaNb₂O₇ based on the tetragonal unit cell of the parent material AgLaNb₂O₇. Likewise, a monoclinic unit cell was assumed for the Ca₂Nb₃O₁₀ nanosheets due to the monoclinic symmetry of the parent material KCa₂Nb₃O₁₀.

	(200)	(220)	(420)
Ag: <i>TBALa</i> Nb ₂ O ₇	3.88	2.73	1.72
H: <i>TBALa</i> Nb ₂ O ₇	3.92	2.75	1.74
	(200)	(220)	(420)
Ag: <i>TBACa</i> ₂ Nb ₃ O ₁₀	3.88	2.76	1.73
H: <i>TBACa</i> ₂ Nb ₃ O ₁₀	3.85	2.72	1.73

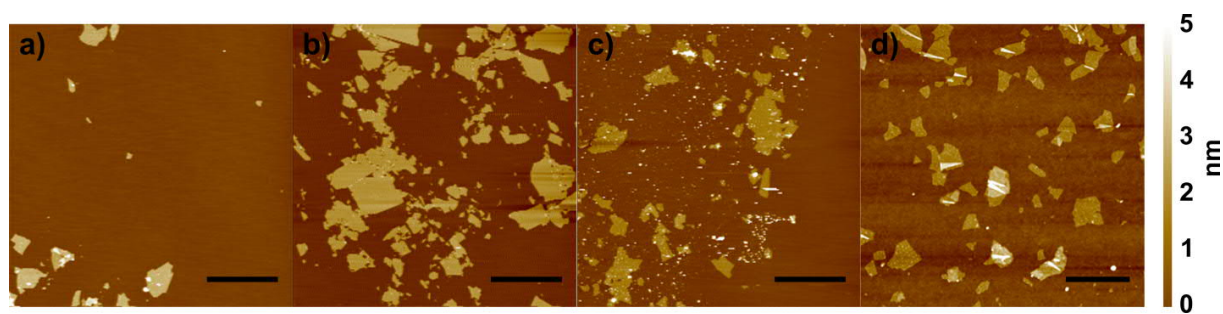


Figure S7.3. Comparison of the AFM images of TBACa₂Nb₃O₁₀ and TBALaNb₂O₇ nanosheets. The nanosheets were obtained from a) AgCa₂Nb₃O₁₀, b) HCa₂Nb₃O₁₀, c) AgLaNb₂O₇ and d) HLaNb₂O₇ by exfoliation with TBAI for the silver phases and TBAOH for the solid acid compounds. The scale bar is 5 μm in a), b) and c) and 1 μm in d).

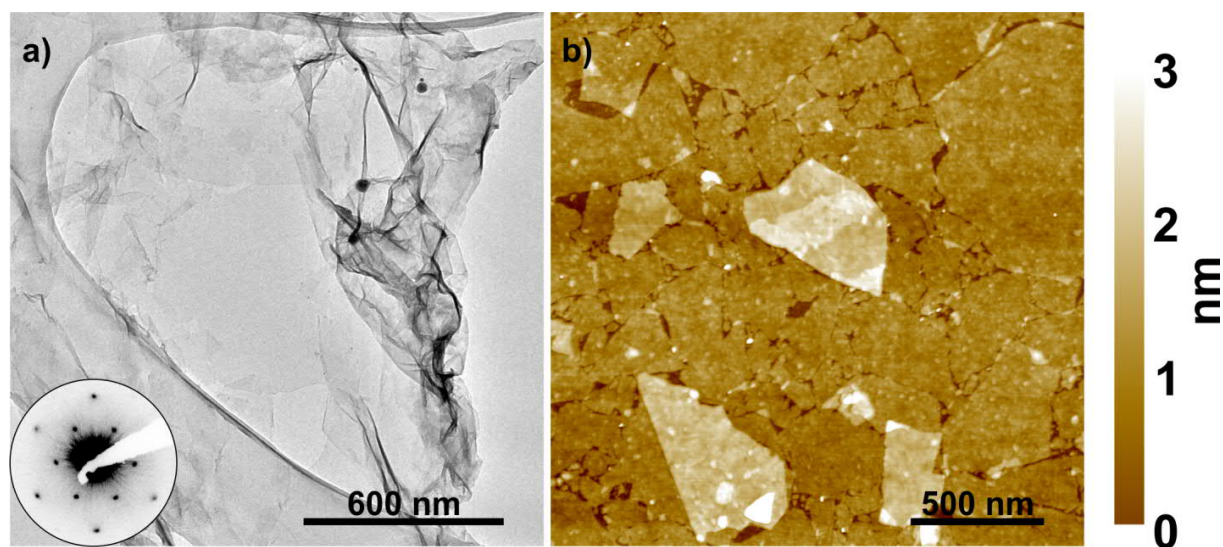


Figure S7.4. a) TEM image as well as SAED pattern in [001] zone axis and b) AFM image of TBATaP₂O₈ nanosheets exfoliated by the silver route.

Table S7.3. Comparison of measured AFM thicknesses with their standard deviation in brackets. Each value was obtained by at least measuring over three different nanosheets. For comparison, the value of HTaP₂O₈ exfoliated with TBAOH is taken from the literature.^[3] Note that the thicknesses can slightly deviate due to the different sizes of the EAs and their arrangement around the nanosheets. The sample marked with an asterisk was cleaned with water to remove the excess of the EA prior to AFM measurement.

Compounds / EAs	TBAOH	TBAI	ChI	AMI
HCa ₂ Nb ₃ O ₁₀ & AgCa ₂ Nb ₃ O ₁₀	2.79(11)	2.94(16)	2.31(11)*	2.31(13)
HLaNb ₂ O ₇ & AgLaNb ₂ O ₇	1.71(9)	1.81(1)	2.16(16)	1.97(4)
HTaP ₂ O ₈ & AgTaP ₂ O ₈	1.31(16)	1.37(16)	1.46(9)	1.22(11)

Table S7.4. Most prominent *d*-spacings and corresponding (*hkl*) values of the TBATaP₂O₈ nanosheets observed by SAED after exfoliation *via* the silver route as compared to the proton route from the literature.^[3] Note that the SAED patterns were indexed based on a trigonal unit cell.^[3]

	(100)	(110)	(210)
Ag: TBATaP ₂ O ₈	4.35	2.53	1.65
H: TBATaP ₂ O ₈	4.45	2.58	1.68

Table S7.5. Most prominent distances and corresponding (*hkl*) values observed by SAED of ChLaNb₂O₇, AMLaNb₂O₇, ChCa₂Nb₃O₁₀, AMCa₂Nb₃O₁₀, ChTaP₂O₈ and AMITaP₂O₈ nanosheets after exfoliation *via* the silver route.

	(200)	(220)	(420)
ChLaNb ₂ O ₇	3.92	2.73	1.73
AMLaNb ₂ O ₇	3.90	2.74	1.74
	(200)	(220)	(420)
ChCa ₂ Nb ₃ O ₁₀	3.85	2.71	1.73
AMCa ₂ Nb ₃ O ₁₀	3.87	2.73	1.73
	(100)	(110)	(210)
ChTaP ₂ O ₈	4.37	2.54	1.66
AMITaP ₂ O ₈	4.37	2.53	1.65

7.2.4 Bibliography

- [1] C. Ziegler, S. Werner, M. Bugnet, M. Wörsching, V. Duppel, G. A. Botton, C. Scheu, B. V. Lotsch, *Chem. Mater.* **2013**, 25, 4892-4900.
- [2] M. Sato, J. Abo, T. Jin, M. Ohta, *J. Alloys Compd.* **1993**, 192, 81-83.
- [3] P. Ganter, L. M. Schoop, B. V. Lotsch, *Adv. Mater.* **2017**, 29, 1604884.
- [4] M. Sato, J. Watanabe, K. Uematsu, *J. Solid State Chem.* **1993**, 107, 460-470.
- [5] J. Boltersdorf, P. A. Maggard, *ACS Catal.* **2013**, 3, 2547-2555.

8 Conclusion and outlook

8.1 Conclusion

Despite the outstanding properties of nanosheets, nanosheet-based devices are absent in our everyday life. This circumstance is due to the lack of synchronizing efficient delamination methods with high control, scalable positioning methods and versatile modification strategies. By advancing and improving delamination, positioning and modification of oxide and phosphate nanosheets and by identifying potential areas of applications, this thesis was targeted to bridge the gap for these nanosheets toward practical applications.

In Chapter 2 and 3 $\text{H}_3\text{Sb}_3\text{P}_2\text{O}_{14}$ and HSbP_2O_8 nanosheets were successfully processed into thin films and Bragg stacks. These thin film devices were identified as high performance photonic and electrochemical vapors sensors showing extraordinary performances, such as high sensitivities and fast response times. These outstanding sensor characteristics enabled their utilization as sensors for trace amounts of water and TPI. Moreover, the highly acidic interlayer space of the nanosheets enabled the differentiation of various protic vapors.

Realizing that the interlayer environment in the nanosheet-based thin film sensors controls the sensor characteristics, the interlayer environment was modified (Chapter 4, 5 and 6). The interlayer environment was tuned and tailored with ion exchange as well as vapor-phase intercalation. Both non-covalent strategies resulted in faster response times, tunable selectivities and enhanced sensitivities of the sensors. While both strategies are effective, the vapor-phase amine intercalation approach is more versatile and straightforward being a post film fabrication modification. The post film fabrication intercalation method allowed the intercalation of various amines into photonic nanosheet-based sensors and their differentiation based on their intercalation time and optical shift. In addition, it enabled the area-resolved tracking of the intercalation process in real-time, which is beneficial for locating the amine vapor source and study fundamental intercalation kinetics and mechanisms. Furthermore, the vapor-phase amine intercalation in combination with a mask allowed selective area resolved intercalation of amines into the thin film. This area-resolved intercalation of amines was utilized for the straightforward construction of an array sensor, which enabled the distinction of various vapors with the naked eye.

Besides spatially controlling the interlayer environment, photodecomposition of interlayer species was utilized to tune the interlayer space in an area resolved manner (see Chapter 5). The locally controlled photodecomposition was achieved by UV-light illumination of $\text{TBA}_x\text{H}_{1-x}\text{Ca}_2\text{Nb}_3\text{O}_{10}$ thin films through a mask, leading to $(\text{NH}_4)_x\text{H}_{1-x}\text{Ca}_2\text{Nb}_3\text{O}_{10}$ in the exposed areas. As the swelling and delaminating properties of the thin film strongly depend on the intercalated cations, the $\text{TBA}_x\text{H}_{1-x}\text{Ca}_2\text{Nb}_3\text{O}_{10}$ (masked areas) of the thin film could be easily washed off while the $(\text{NH}_4)_x\text{H}_{1-x}\text{Ca}_2\text{Nb}_3\text{O}_{10}$ areas remained on the substrate. Therefore, $\text{TBA}_x\text{H}_{1-x}\text{Ca}_2\text{Nb}_3\text{O}_{10}$ acted as negative photoresists. Due to the described characteristics, we named this method *photocatalytic nanosheet lithography* (PNL). With PNL we were able to obtain features with lateral sizes as small as $\sim 10\ \mu\text{m}$. The control of lateral sizes

of $(\text{NH}_4)_x\text{H}_{1-x}\text{Ca}_2\text{Nb}_3\text{O}_{10}$ structures is of high interest as the material is a good high- k dielectric with potential applications in capacitors and transistors.

Besides effective positioning and modification of nanosheets, the development of new solvent-based exfoliation routes and improving of existing ones is highly desirable. In Chapter 7, the development of a silver-assisted exfoliation route is reported. This new exfoliation method is utilizing the formation of highly water insoluble AgI as the driving force for delamination. This exfoliation route has the advantages of allowing the use of various exfoliation agents (EAs) and avoiding the use of strong acids for delamination. The applicability of a wide range of EAs is desirable as the nanosheet properties can be tremendously altered by the used EA. The avoidance of strong acids can lead to the delamination of acid-sensitive materials. In addition, from a fundamental perspective the development of new exfoliation routes helps to identify general exfoliation principles.

In summary, the results obtained in the current thesis in the field of delamination, positioning and modification of oxide and phosphate nanosheets represent a significant step toward the utilization of these nanosheets in devices for practical applications, especially in the field of vapor sensing. Although this thesis could not completely resolve all of the grand challenges on the way towards commercial application, it nevertheless triggered significant interest from industry in the nanosheet topic.

8.2 Outlook

The results and advancements in the field of nanosheet synthesis, positioning and modification achieved in this thesis provide a sound and solid foundation for further investigations. These further investigations, inspired by or directly evolving from this thesis, have the capability, on the one hand, to bridge the gap toward industrial applications and on the other hand, to gain an even deeper fundamental understanding of the properties and processes of nanosheet-based structures.

In the following, an overview of the most promising approaches are presented.

The vapor-phase amine intercalation presented in Chapter 6 opens up new opportunities in the field of nanosheet-based sensing. Intercalation of biogenic and other amines into photonic structures enables their optical detection. Detection of such analytes is relevant for various applications. These include the detection of trace amounts of isobutylamine, *o*-toluidine and aniline in medical diagnostics (Figure 8.1a),^[1] cadaverine and putrescine in food freshness monitoring (Figure 8.1b),^[1-4] or amphetamine^[5,6] and methylhexanamine^[7,8] to verify abuse of performance enhancing drugs (see Figure 8.1c). First steps toward the detection of these amines are underway. The results obtained so far are promising as they can be intercalated in high concentrations, and micromolar and nanomolar concentrations of other amines can also be detected. Besides the detection of amines by intercalation, amine intercalation can also be used to modify the sensing properties (see Chapter 6).

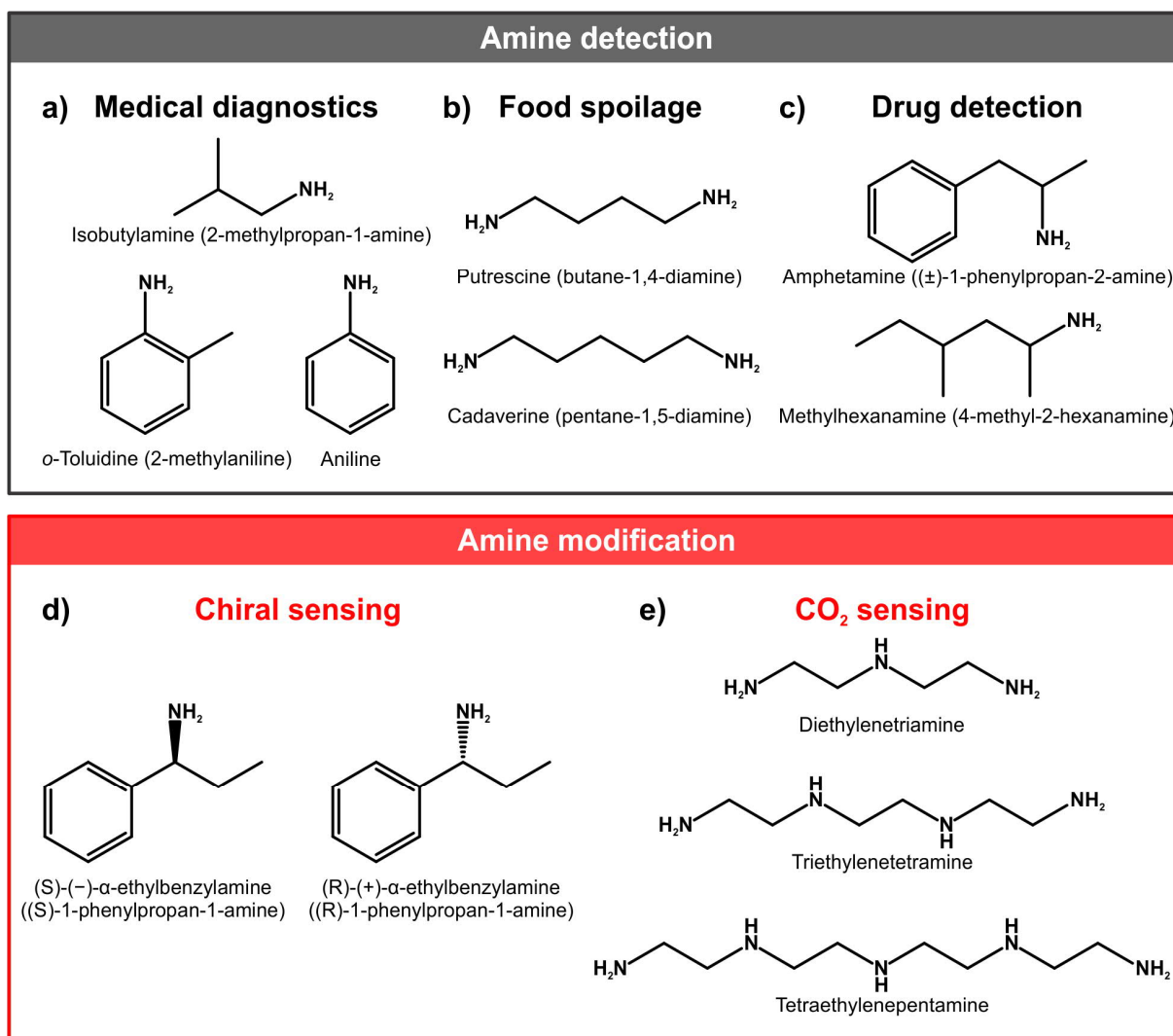


Figure 8.1. Overview of promising amines to be detected, a) - c), and useable compounds for sensor modification, d), e).

In addition to the amines shown in Chapter 6, also chiral amines and polyamines can be intercalated, offering further tailoring of the nanosheet-based sensor toward analytes. The intercalation of chiral amines, such as (S)-(-)- α -ethylbenzylamine and (R)-(+)- α -ethylbenzylamine, might allow to distinguish enantiomers of analyte molecules (Figure 8.1d). Instead, intercalation of polyamines might be utilized for CO₂ sensing. Possible candidates of polyamines for CO₂ sensing are diethylenetriamine, triethylenetetramine, and tetraethylenepentamine (Figure 8.1e).

Besides modification by ion exchange and intercalation (Chapter 4 and 6), nanosheet properties can be also tailored by covalent modification. There are several ways for example of modifying α -Zr(HPO₄)₂ bulk material and some of the corresponding nanosheets reported in the literature.^[9] Modification can be achieved with alkoxy and chlorosilanes,^[10,11] epoxides^[12,13] and isocyanates,^[14] as well as grafting with poly N-isopropylacrylamide (PNIPAM)^[15,16] by a radical mechanism (Figure 8.2). Another way to yield covalently modified α -Zr(HPO₄)₂ is by using phosphonic acid or phosphoric acid esters during the synthesis instead of phosphoric acid.^[9] As the phosphate nanosheets investigated in this thesis are closely related to α -Zr(HPO₄)₂, it might be possible to transfer these modifications to HSbP₂O₈,

$\text{H}_3\text{Sb}_3\text{P}_2\text{O}_{14}$ and HTaP_2O_8 nanosheets (s. Chapter 1). Even the functionalization by phosphonic acid or phosphoric acid esters might be transferred, as a similar reaction pathway exists also for obtaining HSbP_2O_8 .^[17]

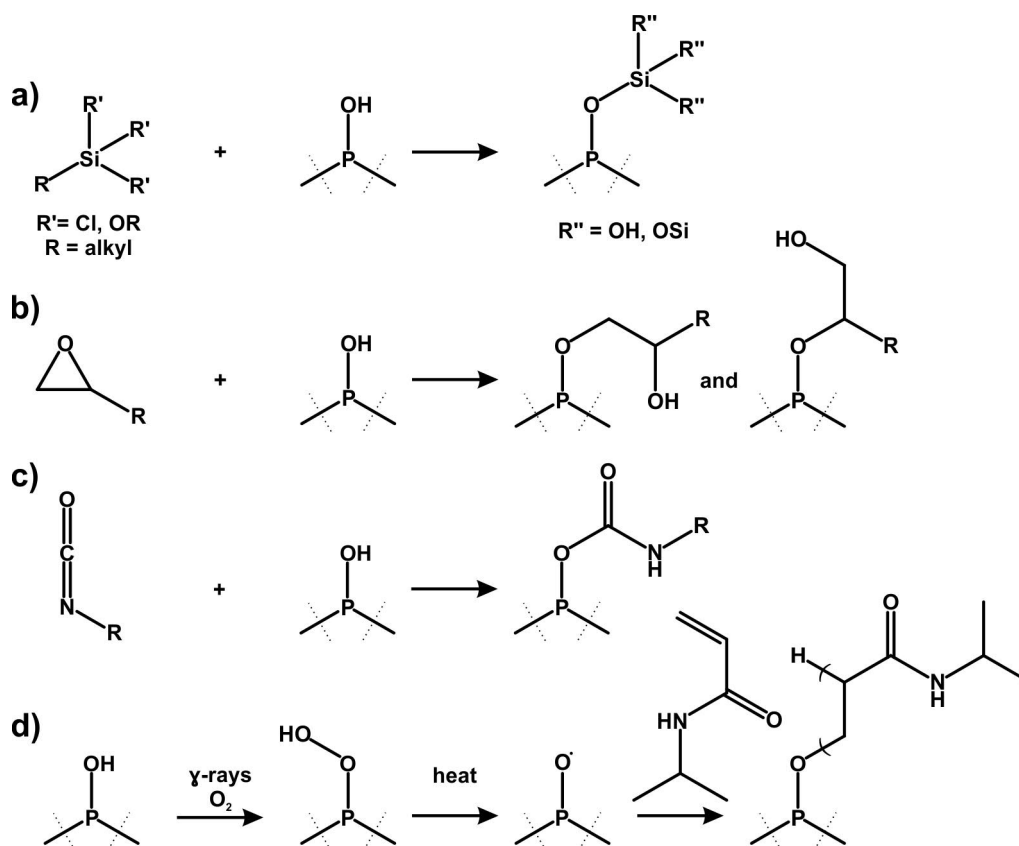


Figure 8.2. Covalent modification strategies for $\alpha\text{-Zr}(\text{HPO}_4)_2$. Modification with a) chloro or alkoxy silanes, b) epoxides, c) isocyanates, and d) by a radical mechanism. Note that by the reaction with epoxides two different products can be obtained.

In addition to their application in gas and vapor sensing devices, nanosheet-based photonic sensors can be utilized for temperature sensing. Therefore, they have to be stored in sealed containers with defined humidity conditions. Upon heating, water deintercalates from the interlayer space. This deintercalation causes an overall decrease in thin film thickness and hence, color change. Promising first results indicate that these color changes are reversible, showing only a small hysteresis and almost linear d -spacing change up to temperature of 60 or 90 °C, depending on the type of nanosheets. Further in-depth studies including temperature dependent XRD studies under defined RH conditions, as well as temperature dependent AFM and UV-Vis studies, are considered.

As shown in Chapter 5, the concept of controlling the interlayer environment can be extended also to control the positioning of nanosheets. Inspired by the PNL project and mask-based vapor-phase amine intercalation approach, it should be possible to create isolated amine intercalated nanosheet-based structures on a substrate. Indeed, preliminary experiments show that if we start from a $\text{H}_3\text{Sb}_3\text{P}_2\text{O}_{14}$ thin film intercalated with long chain alkylamine in certain areas, we are able to remove the non intercalated areas of $\text{H}_3\text{Sb}_3\text{P}_2\text{O}_{14}$ simply by washing the sample with water, leaving only the primary

alkylamine intercalated areas on the substrates (Figure 8.4a). Even a lift-off resulting in a freestanding amine intercalated $\text{H}_3\text{Sb}_3\text{P}_2\text{O}_{14}$ thin film should be feasible by spin-coating the $\text{H}_3\text{Sb}_3\text{P}_2\text{O}_{14}$ layer on a water soluble layer on a substrate with subsequent vapor-phase amine intercalation (Figure 8.4c). The water soluble layer can, for instance, be based on $\text{Li}_2\text{Sn}_2\text{S}_5$ nanosheets as these nanosheets are not intercalating amines over the vapor-phase.

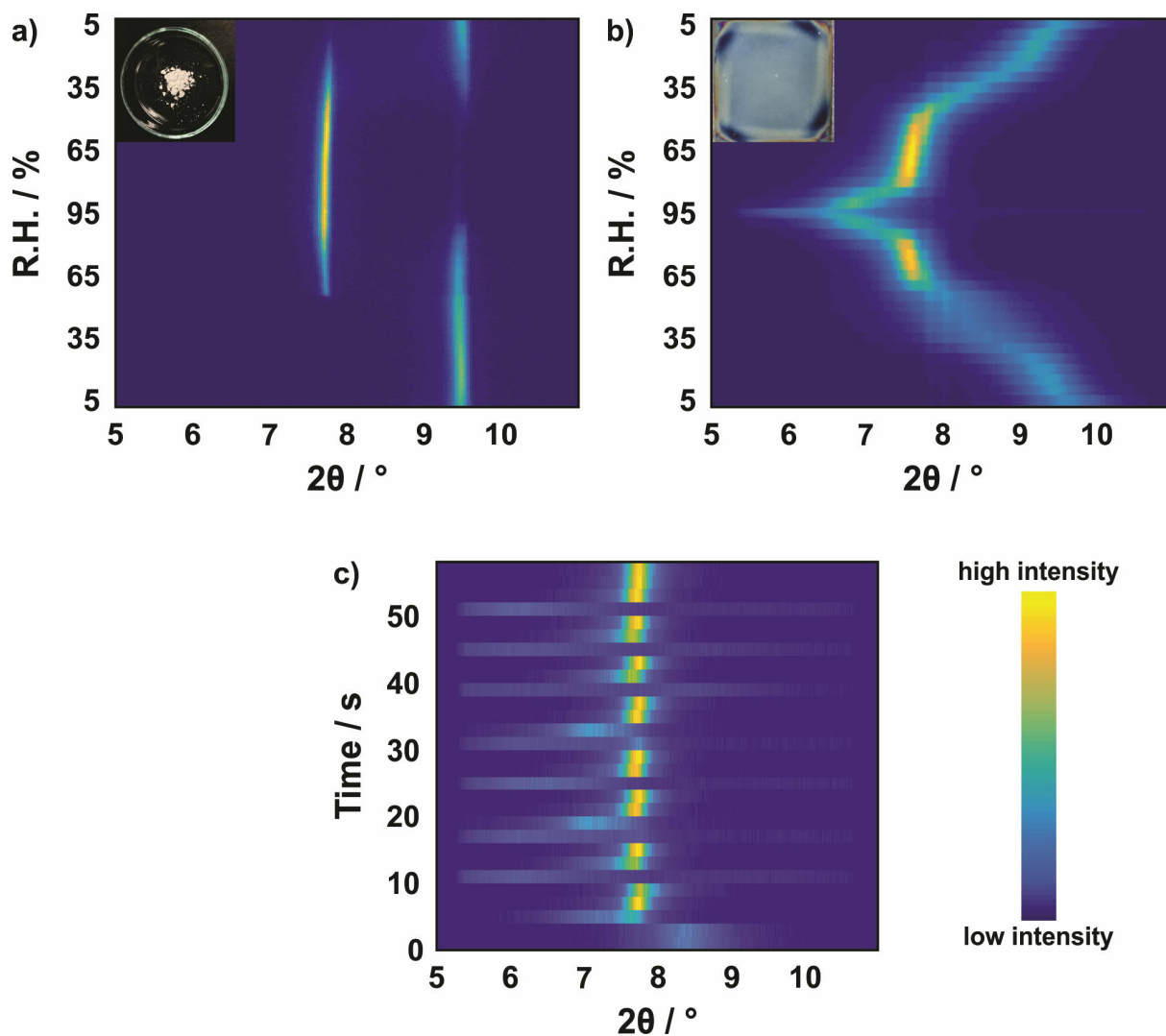


Figure 8.3. Influence of the sample morphology on the 001 d -spacing response toward humidity. d -spacing response toward 5% RH steps from 5%-95%-5% for a) the $\text{H}_3\text{Sb}_3\text{P}_2\text{O}_{14}$ bulk material and b) the $\text{H}_3\text{Sb}_3\text{P}_2\text{O}_{14}$ nanosheet-based thin film measured with *in situ* XRD. In the insets, images of the sample morphologies are shown. The $\text{H}_3\text{Sb}_3\text{P}_2\text{O}_{14}$ nanosheet-based thin film shows a continuous, higher sensitivity, smaller hysteresis compared to $\text{H}_3\text{Sb}_3\text{P}_2\text{O}_{14}$ bulk material. Moreover, for the thin film morphology also the 5% RH steps are resolved. c) Tracking of exhaled human breath by out-of-plane XRD with the $\text{H}_3\text{Sb}_3\text{P}_2\text{O}_{14}$ nanosheet-based thin film. To the best of my knowledge, for the first time human breathing events are clearly resolved by XRD.^[18]

The described properties of the photonic nanosheet-based thin films are also interesting for fundamental studies. Fundamental studies currently conducted by us investigate the impact of the morphology change, bulk material versus nanosheet thin film, and amine modification on the analyte

uptake at the atomic scale by *in situ* XRD measurements. Our observations so far indicate that, if a bulk material is delaminated into small sized nanosheets and subsequently assembled into a thin film, the swelling properties change from a stepwise to a continuous response with an increased sensitivity, which is highly beneficial for sensing (Figure 8.3a, b). Besides the continuous *d*-spacing response, the observed *d*-spacing changes are very fast (Figure 8.3c). The tracking of human breath with XRD in real time illustrates the rapid *d*-spacing changes caused by intercalation and deintercalation of analyte molecules in the interlayer space (Figure 8.3c). Moreover, amine modification does not alter the continuous and fast swelling, but enhances the sensitivity, *i.e.* percentage of *d*-spacing change, toward analytes. The combination of fast continuous *d*-value changes paired with the tunability of these systems makes them superior candidates for sensors compared to, for example, breathing metal organic frameworks (MOFs).^[19]

In addition, to study the interaction of analytes with functionalized structures, analyzing the functionalization step of photonic nanosheet-based structures itself can deliver fundamental insights. The $\text{H}_3\text{Sb}_3\text{P}_2\text{O}_{14}$ nanosheet-based photonic thin films enable direct optical tracking of the intercalation process. Optical studies in combination with *in situ* XRD measurements can provide useful area resolved information on the mechanism of the intercalation process as well as its kinetics. The obtained results so far indicate that the intercalation mechanism is different for long and short chained alkylamines. In addition, it depends on the type of alkylamine, for instance, primary or tertiary amines (Figure 8.4d).

Besides functionalization with one amine at one area and studying its intercalation process, also the understanding of more complex intercalation processes are of fundamental interest. For example, the question remains, what is happening if two amines are subsequently intercalated at the same area? Is a co-intercalation taking place or a replacement reaction? Besides being of fundamental interest this question is also of practical interest as area resolved intercalation allows the creation of complex nanostructures with area tunable properties. Our results so far strongly indicate that a replacement is taking place. A replacement allows, for instance, the straightforward construction of complex structures like “nanopyramids” or “nanoamphitheatres” (s. Figure 8.4a, b).

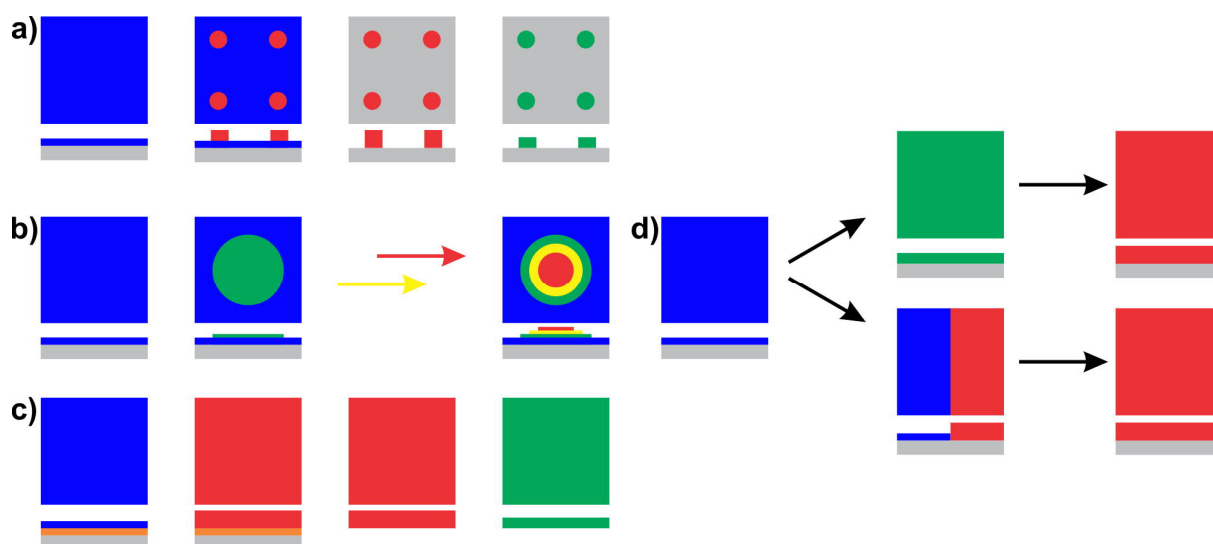


Figure 8.4. Schematic illustration of step-wise amine intercalation strategies and the distinct intercalation mechanism observed. a) Utilization of vapor-phase amine intercalation to create hydrophobic areas (red) in the thin film, followed by developing with water and subsequent replacement with other amines. This leads to isolated tunable amine intercalated nanosheet-based structures on a substrate. b) Utilization of amine replacement and area resolved intercalation to create complex structures, here a nanopyramide. c) Utilization of amine intercalation with a water-soluble layer (orange). Upon amine intercalation in the $\text{H}_3\text{Sb}_3\text{P}_2\text{O}_{14}$ layer the water-soluble layer can be dissolved, leading to a freestanding nanosheet-based thin film. Note that it is possible to combine a) and b) with c) and therefore, freestanding complex nanosheet-based structures are within reach. d) Highlighting the different intercalation mechanisms observed. Small amines intercalate evenly over the whole film (top), whereas large amines start to intercalate at one area (bottom). In the latter case, one can see an intercalation front moving through the thin film. Grey, Si substrate, orange, water soluble layer (e.g. $\text{Li}_2\text{Sn}_2\text{S}_5$), blue, pristine $\text{H}_3\text{Sb}_3\text{P}_2\text{O}_{14}$ nanosheet-based thin film, green, yellow and red, $\text{H}_3\text{Sb}_3\text{P}_2\text{O}_{14}$ nanosheet-based thin film intercalated with different amines.

Looking forward, the huge efforts around the world in nanosheet research and the outstanding properties of nanosheets will most likely result in nanosheet-based technology becoming part of our everyday life within years.

8.3 Bibliography

- [1] N. A. Rakow, A. Sen, M. C. Janzen, J. B. Ponder, K. S. Suslick, *Angew. Chem., Int. Ed.* **2005**, *44*, 4528-4532.
- [2] J. Brockgreitens, A. Abbas, *Compr. Rev. Food Sci. Food Saf.* **2016**, *15*, 3-15.
- [3] S. F. Liu, A. R. Petty, G. T. Sazama, T. M. Swager, *Angew. Chem., Int. Ed.* **2015**, *54*, 6554-6557.
- [4] H. Yang, D. Kim, J. Kim, D. Moon, H. S. Song, M. Lee, S. Hong, T. H. Park, *ACS Nano* **2017**, *11*, 11847-11855.
- [5] S. Bashiri, E. Vessally, A. Bekhradnia, A. Hosseinian, L. Edjlali, *Vacuum* **2017**, *136*, 156-162.
- [6] A. Hackner, S. Beer, G. Müller, T. Fischer, S. Mathur, *Sens. Actuators, B* **2012**, *162*, 209-215.
- [7] A. Lisi, N. Hasick, R. Kazlauskas, C. Goebel, *Drug Test. Anal.* **2011**, *3*, 873-876.
- [8] Y. Zhang, R. M. Woods, Z. S. Breitbach, D. W. Armstrong, *Drug Test. Anal.* **2012**, *4*, 986-990.
- [9] B. M. Mosby, A. Diaz, A. Clearfield, *Dalton Trans.* **2014**, *43*, 10328-10339.
- [10] A. Díaz, B. M. Mosby, V. I. Bakhmutov, A. A. Martí, J. D. Batteas, A. Clearfield, *Chem. Mater.* **2013**, *25*, 723-728.
- [11] Y. Zhou, R. Huang, F. Ding, A. D. Brittain, J. Liu, M. Zhang, M. Xiao, Y. Meng, L. Sun, *ACS Appl. Mater. Interfaces* **2014**, *6*, 7417-7425.

- [12] B. M. Mosby, A. Diaz, V. Bakhmutov, A. Clearfield, *ACS Appl. Mater. Interfaces* **2014**, *6*, 585-592.
- [13] M. Casciola, D. Capitani, A. Donnadio, G. Munari, M. Pica, *Inorg. Chem.* **2010**, *49*, 3329-3336.
- [14] A. F. Mejia, A. Diaz, S. Pullela, Y.-W. Chang, M. Simonetty, C. Carpenter, J. D. Batteas, M. S. Mannan, A. Clearfield, Z. Cheng, *Soft Matter* **2012**, *8*, 10245-10253.
- [15] X. Wang, D. Zhao, I. B. N. Medina, A. Diaz, H. Wang, A. Clearfield, M. S. Mannan, Z. Cheng, *Chem. Commun.* **2016**, *52*, 4832-4835.
- [16] X. Wang, M. Zeng, Y.-H. Yu, H. Wang, M. S. Mannan, Z. Cheng, *ACS Appl. Mater. Interfaces* **2017**, *9*, 7852-7858.
- [17] A. Winkler, E. Thilo, *Z. Anorg. Allg. Chem.* **1966**, *346*, 92-112.
- [18] M. Däntl, Master thesis, University of Munich (LMU), **2017**.
- [19] E. J. Carrington, C. A. McAnally, A. J. Fletcher, S. P. Thompson, M. Warren, L. Brammer, *Nat. Chem.* **2017**, *9*, 882.

9 Appendix

9.1 Table of Abbreviations

Abbreviation	Description
1D	one-dimensional
2D	two-dimensional
3D	three-dimensional
α -Zr(HPO ₄) ₂	α -zirconium phosphate
A	anisole
AFM	atomic force microscopy
AMI	1-allyl-3-methylimidazolium
BA	<i>n</i> -butylamine
BAOH	4-amino-1-butanol
BP	Bragg peak
BS	Bragg stack
Ch	choline
DA	decylamine
DJ	Dion-Jacobson
DMAE	2-(dimethylamino)ethanol
DMBA	<i>N,N</i> -dimethylbutylamine
DMBAOH	4-(dimethylamino)-1-butanol
DTA	differential thermal analysis
EA (Chapter 6)	ethylamine
EA (except of Chapter 6)	exfoliation agent
EDX	energy dispersive X-ray
eLbL	electrostatic layer-by-layer
FET	field effect transistor
GO	graphene oxide
HSAB	hard and soft acids and bases
IR	infrared
IUPAC	International Union of Pure and Applied Chemistry
LB	Langmuir-Blodgett
MPI FKF	Max-Planck-Institut für Festkörperforschung
MOF	metal organic framework
NMR	nuclear magnetic resonance
NP	nanoparticle
PC	photonic crystal
PCA	principal component analysis
PNIPAM	poly N-isopropylacrylamide
PNL	photocatalytic nanosheet lithography
PXRD	powder X-ray diffraction
rGO	reduced graphene oxide
RH	relative humidity

RI	refractive index
SAD	selected area diffraction
SAED	selected area electron diffraction
SEM	scanning electron microscopy
T	toluene
TBA	tetrabutylammonium
TBP	tetrabutylphosphonium
TEM	transmission electron microscopy
TGA	thermogravimetric analysis
TMA	tetramethylammonium
TMD	transition metal dichalcogenide
TMO	transition metal oxide
TPI	touchless positioning interfaces
UV	ultraviolet
Vis	visible
VOCs	volatile organic compounds
wt	weight
XRD	X-ray diffraction

9.2 List of Publications

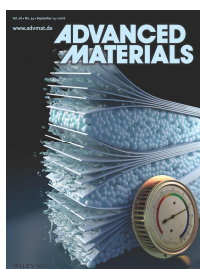
Published as part of this thesis:

1. **Touchless Optical Finger Motion Tracking Based on 2D Nanosheets with Giant Moisture Responsiveness**

K. Szendrei,* P. Ganter,* O. Sánchez-Sobrado, R. Eger, A. Kuhn, B. V. Lotsch, *Adv. Mater.* **2015**, *27*, 6341-6348.

2. **Towards the Nanosheet-Based Photonic Nose: Vapor Recognition and Trace Water Sensing with Antimony Phosphate Thin Film Devices**

P. Ganter,* K. Szendrei,* B. V. Lotsch, *Adv. Mater.* **2016**, *28*, 7436-7442.



3. **Toward Tunable Photonic Nanosheet Sensors: Strong Influence of the Interlayer Cation on the Sensing Characteristics**

P. Ganter, L. M. Schoop, B. V. Lotsch, *Adv. Mater.* **2017**, *29*, 1604884.

4. **Photocatalytic Nanosheet Lithography: Photolithography based on Organically Modified Photoactive 2D Nanosheets**

P. Ganter, B. V. Lotsch. *Angew. Chem. Int. Ed.* **2017**, *56*, 8389-8392.

5. **A New Fabrication Method for Single-Layer Nanosheets by Silver-Assisted Exfoliation**

P. Ganter,* C. Ziegler,* A. T. Friedrichs, V. Duppel, C. Scheu, B. V. Lotsch, *ChemNanoMat* **2017**, *3*, 411-414.



6. **Vapor-Phase Amine Intercalation for the Rational Design of Photonic Nanosheet Sensors**

P. Ganter, L. M. Schoop, M. Däntl, B. V. Lotsch, *Chem. Mater.* **2018**, *30*, 2557-2565.

Published not as part of this thesis:

- 1. Electronic structure of $\text{KCa}_2\text{Nb}_3\text{O}_{10}$ as envisaged by density functional theory and valence electron energy loss spectroscopy**
K. S. Viridi, Y. Kauffmann, C. Ziegler, P. Ganter, W. D. Kaplan, B. V. Lotsch, P. Blaha, C. Scheu, *Phys. Rev. B* **2013**, *87*, 115108.
- 2. Layered germanium tin antimony tellurides: element distribution, nanostructures and thermoelectric properties**
S. Welzmler, T. Rosenthal, P. Ganter, L. Neudert, F. Fahrnbauer, P. Urban, C. Stiewe, J. de Boor, O. Oeckler, *Dalton Trans.* **2014**, *43*, 10529-10540.
- 3. Nanostructured rocksalt-type solid solution series $(\text{Ge}_{1-x}\text{Sn}_x\text{Te})_n\text{Sb}_2\text{Te}_3$ ($n = 4, 7, 12; 0 \leq x \leq 1$): Thermal behavior and thermoelectric properties**
T. Rosenthal, L. Neudert, P. Ganter, J. de Boor, C. Stiewe, O. Oeckler, *J. Solid State Chem.* **2014**, *215*, 231-240.
- 4. In Search of Aluminum Hexathiohypodiphosphate: Synthesis and Structures of ht-ALPS_4 , lt-ALPS_4 , and $\text{Al}_4(\text{P}_2\text{S}_6)_3$**
Kuhn, R. Eger, P. Ganter, V. Duppel, J. Nuss, B. V. Lotsch, *Z. Anorg. Allg. Chem.* **2014**, *640*, 2663-2668.
- 5. Nanocellulose-Templated Porous Titania Scaffolds Incorporating Presynthesized Titania Nanocrystals**
A. Ivanova, M. C. Fravventura, D. Fattakhova-Rohlfing, J. Rathouský, L. Movsesyan, P. Ganter, T. J. Savenije, T. Bein, *Chem. Mater.* **2015**, *27*, 6205-6212.
- 6. Band gap extraction from individual two-dimensional perovskite nanosheets using valence electron energy loss spectroscopy**
K. Viridi, Y. Kauffmann, C. Ziegler, P. Ganter, P. Blaha, B. V. Lotsch, W. D. Kaplan, C. Scheu, *J. Phys. Chem. C* **2016**, *120*, 11170-11179.
- 7. Selectivity, cycling stability and temperature dependence of touchless finger motion tracking devices based on 1D photonic crystal**
K. Szendrei, P. Ganter, B. V. Lotsch, *Proc. SPIE* **2016**, 9885.

8. Ultra-thin Relative Humidity Sensors for Hybrid System-in-Foil Applications

M. Elsobky, B. Albrecht, H. Richter, J. N. Burghartz, P. Ganter, K. Szendrei, B. V. Lotsch, IEEE Sensors **2017**. DOI:10.1109/ICSENS.2017.8234298

9.3 Patents

K. Szendrei, P. Ganter, O. Sanchez-Sobrado, A. Kuhn, B. V. Lotsch, **Gas and vapor sensing devices based on 2D nanosheet material**, European Patent Application No. 14200 196.5

9.4 Contribution to conferences

Toward Tunable Photonic Nanosheet Sensors (oral presentation)

P. Ganter, *Functional Materials Seminar*, Stuttgart **2017**.

Toward rational designed photonic nanosheet sensors (poster presentation)

P. Ganter, L. M. Schoop, B. V. Lotsch, *JSPS Core-to-Core Workshop: Novel Quantum and Functional Materials – Design and Synthesis*, Stuttgart **2017**.

Amine intercalation for the rational design of photonic nanosheet sensors (poster presentation)

P. Ganter, L. M. Schoop, B. V. Lotsch, *Stuttgart Nanodays Workshop*, Munich **2017**.

Stimuli-responsive nanosheet thin film sensors (poster presentation)

P. Ganter, K. Szendrei, D. Weber, B. V. Lotsch, *80. Jahrestagung der DPG und DPG-Frühjahrstagung*, Regensburg **2016**.